

STUDIES ON ADVANCED MATERIALS FOR HYDROGEN STORAGE

By

SEEMITA BANERJEE

Enrolment No. CHEM01200804001

Bhabha Atomic Research Centre, Mumbai

A thesis submitted to the

Board of Studies in Chemical Sciences

In partial fulfillment of requirements

For the Degree of

DOCTOR OF PHYLOSOPHY

of

HOMI BHABHA NATIONAL INSTITUTE



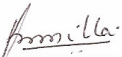
March, 2013

Homi Bhabha National Institute

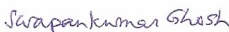
Recommendations of the Viva Voce Board

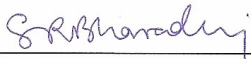
As members of the Viva Voce Board, we certify that we have read the dissertation prepared by Mrs. Seemita Banerjee entitled "Study on Advanced Materials for Hydrogen Storage" and recommend that it may be accepted as fulfilling the dissertation requirement for the Degree of Doctor of Philosophy.


Chairman: Dr. D. Das Date: 01.03.2013


Convener: Dr. C. G. S. Pillai Date: 01-03-2013


External Examiner: Prof. G. P. Das Date: 01-03-2013


Member: Dr. S. K. Ghosh Date: 01-03-2013

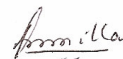

Member: Dr. S. R. Bharadwaj Date: 01-03-2013

Final approval and acceptance of this dissertation is contingent upon the candidate's submission of the final copies of the dissertation to HBNI.

I hereby certify that I have read this dissertation prepared under my direction and recommended that it can be accepted as fulfilling the dissertation requirement.

Date 1-3-2013

Place Trombay, Mumbai



Dr. C. G. S. Pillai

STATEMENT BY AUTHOR

This dissertation has been submitted in partial fulfillment of requirements for an advanced degree at Homi Bhabha National Institute (HBNI) and is deposited in the Library to be made available to borrowers under rules of the HBNI.

Brief quotations from this dissertation are allowable without special permission, provided that accurate acknowledgement of source is made. Requests for permission for extended quotation from or reproduction of this manuscript in whole or in part may be granted by the Competent Authority of HBNI when in his or her judgment the proposed use of the material is in the interests of scholarship. In all other instances, however, permission must be obtained from the author.

Seemita Banerjee

DECLARATION

I, hereby declare that the investigation presented in the thesis has been carried out by me. The work is original and has not been submitted earlier as a whole or in part for a degree / diploma at this or any other Institution / University.

Seemita Banerjee

Dedicated

To my Family

ACKNOWLEDGEMENTS

I wish to record my deep sense of gratitude and sincere thanks to my research guide, **Dr. C. G. S. Pillai**, Former Head, Material Chemistry Section, Chemistry Division for his unstinted inspiration, invaluable guidance, encouragement, keen interest, good wishes and valuable suggestions throughout my entire research tenure. I am also grateful to him for critically reviewing this thesis.

It gives me immense pleasure to acknowledge to my research co-guide **Dr. (Mrs) K. Shashikala**, & **Dr. C. Majumder** of Chemistry Division, for critically evaluating my research activities time to time and also for providing the laboratory & computational facilities and several valuable suggestions for completion of this work.

It is also my great pleasure to thank **Dr. S. K. Sarkar**, Director Chemistry Group, **Dr. T. Mukherjee**, Former Director, Chemistry Group, **Dr. V. K. Jain**, Head Chemistry Division, **Dr. D. Das**, Former Head, Chemistry Division, & **Dr. V. Sudarsan**, Head Material Chemistry Section, for their encouragement and support in carrying out the research work.

It is my great privilege to acknowledge **Dr. S. K. Ghosh**, Head, TCS, **Dr. (Mrs.) S. Bharadwaj** and **Dr. A. K. Taygi**, Chemistry Division for critically evaluating my research activities time to time as members of the HBNI doctoral committee and providing valuable suggestions for completion of this work.

I express my sincere thanks to **Dr. S. Nigam**, for his help in computational study. I also express my thanks to **Dr. M. R. Pai**, **Dr. S. Varma**, **Mr. Dheeraj Jain**, **Mr. J. Nurwad**, **Dr. P. Sengupta** for providing me different experimental facilities like temperature programmed desorption, differential thermal calorimetry, scanning electron microscope, electron probe micro analyzer and **members of Computer Centre, BARC** is highly acknowledged for providing ANUPAM parallel computing facility and ready help over the years.

It is a great pleasure to acknowledge my lab mates **Mr. Asheesh Kumar** and **Ms. Priyanka Das** for helping me and providing kind support and encouragement during my research work. I am also thankful to all my **Chemistry Division colleagues** and **staff members** for their support at different times.

I wish to express my sincere gratitude and indebtedness to **my parents, parents-in-law** for their blessings, **brothers** and other **family members** for their love and support to me.

Finally, I am extremely thankful to my husband **Dr. Atindra Mohan Banerjee** and little daughter **Asmita Banerjee** for all their love and understanding.

CONTENTS

	Page No.
SYNOPSIS	<i>i</i>
LIST OF FIGURES	<i>xxiii</i>
LIST OF TABLES	<i>xxxvii</i>
CHAPTER I	1
Introduction	
1.1 Hydrogen as Energy Carrier	4
1.2 Hydrogen Production Methods	6
1.2.1 Hydrogen production from water	7
1.3 Different Hydrogen Storage Methods	9
1.3.1 Storage of hydrogen in gaseous form	10
1.3.2 Storage in liquid form	11
1.3.3 Solid state hydrogen storage materials	12
1.3.3.1 Storage of hydrogen in the form of metallic hydride	12
1.3.3.2 Hydrogen storage in carbon based material	23
1.3.3.3 Other solid state hydrogen storage systems	26
1.4 Objective and Scope of the Present Thesis	30
CHAPTER II	33
Instrumentation & Experimental Methods	
2.1 Arc Melting Setup	34
2.2 Sievert's Type Setup	35

2.3 Hydrogen Estimation Setup	38
2.4 X-Ray Diffraction (XRD)	39
2.5 Scanning Electron Microscope (SEM), Energy Dispersive X-ray (EDX)	44
2.6 Electron Probe Micro Analyser (EPMA)	46
2.7 Mössbauer Spectroscopy	48
2.7.1 Isomer shift	49
2.7.2 Quadrupole splitting	50
2.7.3 Magnetic hyperfine interaction	52
2.8 Thermo Gravimetric Analyser (TGA)	53
2.9 Differential Thermal Analyser (DTA)	54
2.10 Differential Scanning Calorimeter (DSC)	55
2.11 Temperature Programmed Desorption (TPD)	56
CHAPTER III	59
Effect of Substitution on Hydrogen Storage Properties of Ti-V-Fe System	
3.1 Experimental Details	63
3.2 Results and Discussions	65
3.2.1 Hydrogen storage properties of $Ti_{1-x}VFe_x$ ($x = 0.1, 0.15, 0.2, 0.4$) and Ti-V-Fe-Cr alloys	66
3.2.1.1 The structural aspects of the alloys and the hydrides	66
3.2.1.2 The hydrogen absorption behavior of Ti-V-Fe alloys	71
3.2.1.3 Desorption characteristics of the alloys	76
3.2.1.4 Summary	80
3.2.2 Hydrogen absorption characteristics of Zr substituted $Ti_{0.85}VFe_{0.15}$ alloy	81
3.2.2.1 Crystal structure	81
3.2.2.2 Hydrogen absorption properties	83

3.2.2.3	Mössbauer study	86
3.2.2.4	Temperature programmed desorption study	88
3.2.2.5	Summary	89
3.2.3	Hydrogen absorption studies on Ce substituted $Ti_{0.85}VFe_{0.15}$	89
3.2.3.1	Structural characterization	90
3.2.3.2	Micro chemical analysis using EPMA	92
3.2.3.3	Hydrogen absorption characteristics	94
3.2.3.4	Electrochemical characterization	97
3.2.3.5	Summary	99
3.4	Conclusion	100
CHAPTER IV		101
Hydrogen Storage Studies on Ti-V-Cr Based Systems		
4.1	Experimental Details	103
4.2	Results & Discussions	105
4.2.1	Hydrogen storage properties of Zr doped TiVCr alloys	105
4.2.1.1	Crystal structure of the alloys	105
4.2.1.2	Hydrogen absorption studies on different compositions	106
4.2.1.3	Crystal structure of the hydrides	109
4.2.1.4	Temperature programmed desorption study	111
4.2.1.5	Summary	112
4.2.2	Hydrogen storage characteristics and cyclic study of Ti_2VCr alloy	113
4.2.2.1	Crystal structure	113
4.2.2.2	Hydrogen absorption study	115
4.2.2.3	Cyclic hydrogen absorption–desorption characteristics of Ti_2VCr	117
4.2.2.4	Morphology	118

4.2.2.5 Hydrogen desorption study	119
4.2.2.6 Summary	121
4.3 Conclusion	121
CHAPTER V	123
Vanadium Substituted ZrFe₂ as Laves Phase Hydrogen Storage Material	
5.1 Experimental Details	128
5.2 Results and Discussion	129
5.2.1 Compositional studies	129
5.2.2 Crystal structure of the alloys and their corresponding hydrides	130
5.2.3 Hydrogen absorption studies of different compositions	135
5.2.4 Temperature programmed desorption	139
5.3 Conclusion	140
CHAPTER VI	
Theoretical Methodology	143
6.1 The Schrödinger Equation	144
6.2 Born-Oppenheimer Approximation	145
6.3 Wave Function Based Calculations	146
6.4 Density Functional Theory	147
6.4.1 The Energy Functional	148
6.4.2 Limitations of DFT	150
6.5 Exchange Correlation Functions	151
6.5.1 Local density approximation (LDA)	151
6.5.2 Generalized gradient approximation	152
6.6 Basis Set	153
6.6.1 Slater type orbital (STO)	154

6.6.2 Gaussian-type orbital (GTO)	<i>155</i>
6.6.3 Plane wave basis set	<i>159</i>
6.7 Pseudo-potential Approximation	<i>160</i>
6.8 Modeling of Periodic System	<i>164</i>
6.9 Calculation of Physical Properties	<i>165</i>
6.9.1 Density of state	<i>165</i>
6.9.2 Charge analysis	<i>166</i>
CHAPTER VII	<i>179</i>
Hydrogen Storage in Magnesium Based Systems	
7.1 Hydrogen Adsorption and Diffusion Properties of the Transition Metal Doped Mg(0001) Surface	<i>171</i>
7.1.1 Computational details	<i>172</i>
7.1.2 Results & discussions	<i>175</i>
7.1.2.1 Thermodynamic and kinetic stability of M atoms (Ti, V and Ni) on the Mg(0001) surface	<i>175</i>
7.1.2.2 Interaction of hydrogen with clean Mg surface and M doped Mg surface (dopants are at the surface layer)	<i>179</i>
7.1.2.3 Interaction of hydrogen with M (M = Ti, V and Ni) doped Mg surface (dopants are at the second layer)	<i>188</i>
7.1.2.4 Relative stability of Mg surface after substitution of V and Ni	<i>199</i>
7.1.2.5 Interaction of hydrogen with most stable Mg ₅₈ VNi Surface	<i>192</i>
7.1.3 Summary	<i>198</i>
7.2 Hydrogen Adsorption and Desorption Properties of Ti Doped Mg Clusters	<i>200</i>
7.2.1 Computational methodology	<i>201</i>
7.2.2 Results & discussion	<i>202</i>

7.2.2.1	Optimization of the geometry of Mg ₅₅ cluster & Ti doped Mg ₅₅ cluster	202
7.2.2.2	Interaction of hydrogen with Mg ₅₅ and TiMg ₅₄ clusters	207
7.2.2.3	Geometry and stability of smaller Ti doped Mg Clusters	213
7.2.2.4	Hydrogenation on TiMg ₈ cluster	218
7.2.2.5	Comparison of hydrogen absorption behavior of the Mg clusters with Mg(0001) surface	221
7.2.3	Summery	222
7.3	Conclusion	223
CHAPTER VIII		227
Hydrogen Storage in Carbon Based Systems		
8.1	Hydrogen adsorption behavior of alkali & alkaline earth metal doped corannulene	229
8.1.1	Theoretical Methodology	231
8.1.2	Result and Discussion	232
8.1.2.1	Doping of alkali (Li ⁺ , Na ⁺ , K ⁺) and alkaline earth metal (Be ²⁺ , Mg ²⁺ , Ca ²⁺) ions on the corannulene ring	232
8.1.2.2	Interaction with hydrogen molecule	237
8.1.3	Summary	246
8.2	Hydrogen Storage on SiC Nanostructures	247
8.2.1	Computational details	250
8.2.2	Result and Discussion	251
8.2.2.1	Calculations on SiC graphene Like Sheet	251
8.2.2.2	Calculations on Single walled (10, 0) SiC nanotube	264
8.2.3	Summary	270
8.3	Interaction of Hydrogen with Metallo-Carbohedrenes	271
8.3.1	Theoretical methodology	273

8.3.2 Result and discussion	274
8.3.2.1 Geometry and energetics	274
8.3.2.2 Interaction of hydrogen molecules with M_8C_{12} cluster	276
8.3.2.3 Hydrogen desorption behavior	280
8.3.3 Summary	282
8.4 Conclusion	283
CHAPTER IX	285
Conclusion	
REFERENCES	291
LIST OF PUBLICATIONS	331

SYNOPSIS

In recent years, research in materials science has shown a rapid expansion toward discoveries of suitable materials for sustainable energy. A hydrogen economy is proposed to solve the ill effects of using hydrocarbon fuels in transportation and other end-use applications, where carbon is released to the atmosphere. In this context the storage of hydrogen poses the biggest challenge in a new hydrogen economy because the storage medium must meet the requirements of high gravimetric and volumetric density, fast kinetics and favorable thermodynamics [1-5]. Although molecular hydrogen has very high energy density on a mass basis, as a gas, at ambient conditions, it has very low energy density by volume. If it is to be used as fuel stored on board in the vehicle, pure hydrogen gas must be pressurized or liquefied, which in addition to being energy intensive will also bring complications in terms of safety aspects. Considering all these issues, solid-state materials offer a practical alternative, and a lot of efforts have been devoted in finding efficient solid state hydrogen storage materials.

There are different candidate materials for solid state hydrogen storage [6-12]. The most conventional and practical one is metal hydride, where different transition metal based and light weight alloys are being considered. Transition metal based alloys are quite promising for their good hydrogen absorption desorption kinetics and favorable thermodynamics whereas light metal alloys shows higher hydrogen absorption capacity but unfavorable kinetics and thermodynamics. The suitability of alloys for hydrogen storage applications can be judged from their hydrogen storage properties such as hydrogen reversible capacity, plateau pressure, plateau slope, hysteresis, sorption kinetics and thermodynamics of dissolved hydrogen.

Other exclusively studied hydrogen storage materials include metal organic framework, carbon nanostructures etc. Metal organic frameworks (MOF) can absorb hydrogen by physisorption, but it requires operating at cryogenic condition. Carbon nano structures are one of the most promising solid-state materials for hydrogen storage because of its porosity, high surface area and high gravimetric hydrogen storage properties. Nanotubes, nano scrolls, nano fibers, fullerenes and graphene sheets are among the different well studied structures. Though the experimental results obtained for hydrogen storage on carbon nanotubes are contradictory because of the presence of metal nano particle impurities and defect structures but still theoretical and experimental research is going on to see its nature of interaction with hydrogen, curvature effect and the effect of doping on the hydrogen absorption properties.

In the present scenario there is a need for the development of hydrogen storage materials with high gravimetric and volumetric hydrogen storage capacity and fast enough kinetics of loading and unloading of hydrogen gas. Existing drawbacks of transition metal based systems should be addressed carefully and meticulously to minimize the practical difficulties. A systematic research work is required on the determination of hydrogen storage capacities, isotherms, and critical thermodynamic and kinetic properties of different solid state hydrogen storage materials using different experimental techniques and improvement upon them. To make the hydrogen economy viable, another principle goal should be the understanding of physical and chemical properties of efficient light weight hydrogen storage materials, especially magnesium, which can provide platform for experimental studies. Till now no hydrogen storage material could show performances close to practical requirements. Therefore in addition to the existing hydrogen storage materials, there is an urgent need to explore new materials with improved performances compared to the existing one. Among various ways, theoretical

modeling of materials is one of the most cost effective routes to explore new materials with tunable properties.

In the present thesis the focus has been made on the investigation of the absorption and desorption behavior of hydrogen on metal and carbon based systems using both experimental and theoretical techniques. For this purpose, the hydrogen storage properties of various transition metal based elements were investigated in detail using different experimental techniques. Along with that, the first principle based calculations were done on magnesium based system to see the effect of size and transition metal doping on the hydrogen absorption properties. Also calculations were carried out on carbon based nanomaterials to find prospective new hydrogen storage systems. The total work of the thesis has been described in nine chapters as outlined below.

Chapter I: Introduction

This chapter gives a broad review on hydrogen as an alternative, clean and renewable energy carrier. Different hydrogen storage methods are discussed with special emphasis on solid state hydrogen storage materials. The special aspects of different solid state materials as hydrogen storage media and the requirements for vehicular and other applications are discussed subsequently. The thermodynamics of hydrogen absorption is also explained elaborately. A brief overview is presented on the role of doping elements on the hydrogen storage properties. Finally the aim and scope of the present thesis is addressed.

Chapter II: Instrumentation and Experimental Methods

This chapter deals with the experimental techniques employed for the synthesis, characterization and evaluation of the hydrogen storage properties of the alloys. All the

transition metal based alloys were prepared by melting the high purity constituent elements in stoichiometric ratio, in DC arc melting furnace under Ar atmosphere in a water cooled Cu hearth. The Sievert's type volumetric hydrogen storage setup, which had been developed in our laboratory, was used for the synthesis of the hydrides. The methods used for the activation of the alloys before hydride formation is also presented. The procedure to measure the pressure composition isotherm and hydrogen absorption kinetics in the Sievert's type setup is discussed in detail. Various characterisation techniques were used for the characterization of the alloys as well as the hydrides during the present work, this includes X-Ray Diffraction (XRD), Scanning Electron Microscopy (SEM), Energy Dispersive X-ray (EDX), Mössbauer, Electron Probe Micro-analyzer (EPMA) and temperature programmed desorption (TPD). A brief account of these techniques is presented in this chapter.

Chapter III: Effect of Substitution on Hydrogen Storage Properties of Ti-V-Fe System

Ti-V based alloys are considered to be promising third generation hydrogen storage materials due to their high hydrogen storage capacity. They have a great potential to replace the AB₅ types of alloys in the hydrogen compressor systems [13]. But Ti-V alloys suffer from certain disadvantages, such as, rigorous activation prior to hydrogen absorption, slow kinetics, sloping plateaus and high desorption temperature for the complete desorption of the stored hydrogen. Substitution of a small amount of transition elements like Fe, Co, Ni, Mn or Cr changes the hydrogen absorption characteristics of Ti-V system drastically [14-16]. In this work, to improve the performances of Ti-V system, Ti was partially replaced by Fe and the hydrogen absorption properties of Ti_{1-x}VFe_x ($x = 0.0, 0.1, 0.15, 0.2$ and 0.4) alloys were investigated in detail. Fe substituted Ti-V alloys were characterized by XRD and EPMA. It is evident from Fig. 1, that except Ti_{0.85}VFe_{0.15}, all the other Ti-V-Fe compositions are having mixed phase structure

composed of a body centered cubic (bcc) phase and a secondary C14 Laves phase, with bcc as the major phase. The composition, $Ti_{0.85}VFe_{0.15}$ contains single phase bcc structure. The lattice parameter of the bcc phase decreases with increasing Fe substitution due to the smaller atomic radius of Fe as compared to that of Ti and V (Ti: 1.47\AA , V: 1.34\AA , Fe: 1.26\AA). The corresponding hydride structures were found to have face centered cubic (fcc) structure and the lines corresponding to the secondary phase were not seen in the XRD patterns of the hydrides.

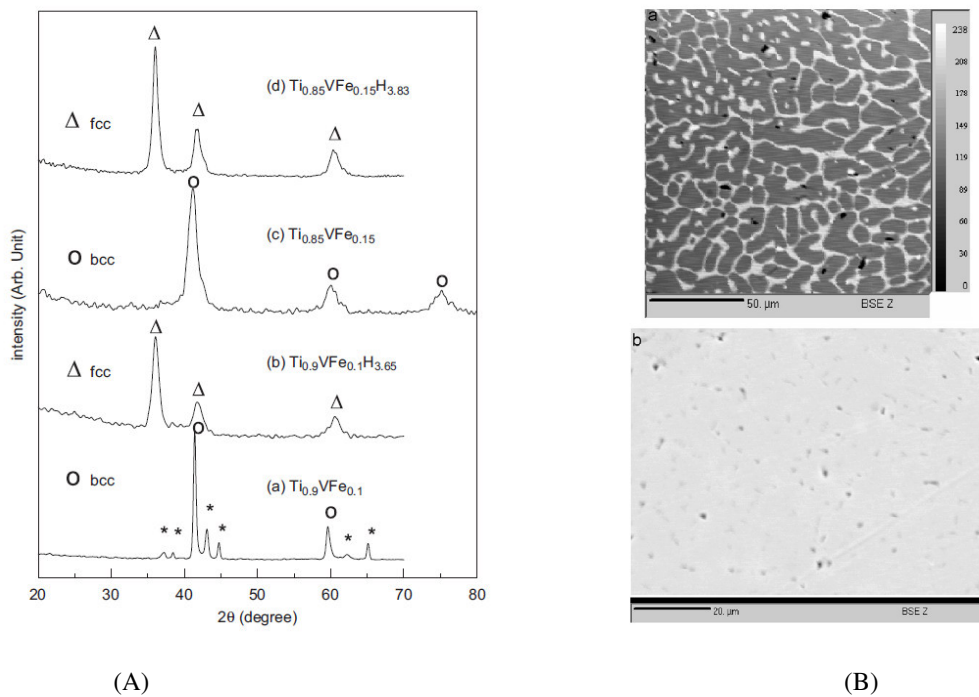


Fig. 1 (A) X-ray diffraction patterns for: (a) $Ti_{0.9}VFe_{0.1}$, (b) $Ti_{0.9}VFe_{0.1}H_{3.65}$, (c) $Ti_{0.85}VFe_{0.15}$, and (d) $Ti_{0.85}VFe_{0.15}H_{3.83}$ (the lines corresponding to the secondary phase are marked by ‘*’) (B) Electron micrographs for: (a) $Ti_{0.9}VFe_{0.1}$ and (b) $Ti_{0.85}VFe_{0.15}$ alloys

The pressure composition isotherm and kinetics of all the alloys were evaluated and the hydrogen storage capacities of $Ti_{1-x}VFe_x$ alloys as a function of Fe content, x , are shown in Fig. 2. It is seen that the hydrogen storage capacity of $Ti_{1-x}VFe_x$ increases with Fe content up to $x = 0.15$, but further increase in the Fe content brings down the hydrogen storage capacity drastically. At a high Fe concentration, the bcc phase was found to coexist with the secondary phase. The

amount of the hydrogen absorbed in this series of alloys is closely related with the amount of bcc phase present. The bcc phase in Ti–V system is reported to absorb more hydrogen than the secondary phase [17]. The composition $\text{Ti}_{0.85}\text{VFe}_{0.15}$ was found to have single phase bcc structure and it shows the maximum storage capacity of 3.7 wt. % among the various Ti–V–Fe compositions studied in this work.

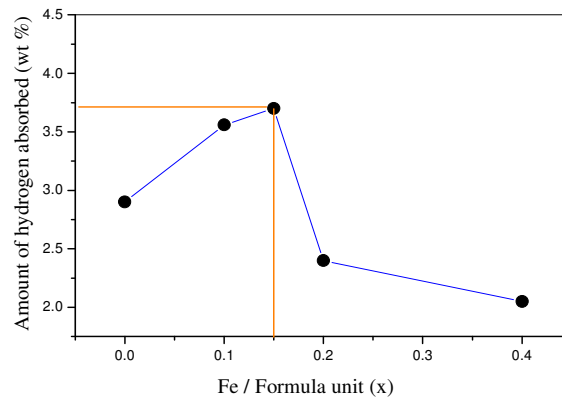


Fig. 2 Variation of hydrogen absorption capacity with respect to the Fe content in $\text{Ti}_{1-x}\text{VFe}_x$ alloys ($x = 0.0, 0.1, 0.15, 0.2$ and 0.4)

The desorption profiles of the saturated hydrides reveal that with increasing Fe concentration the hydrogen desorption temperature decreases. This may be attributed to the fact that with increasing Fe concentration the relative stability of the hydrides decreases and hence the hydrogen desorption takes place at a lower temperature.

Further, to see the effect of Cr substitution on the activation performance, the compositions $\text{Ti}_{0.85}\text{VFe}_{0.15}$ and $\text{Ti}_{0.80}\text{VFe}_{0.20}$ were modified by chromium substitution (60 at. %) in place of V. It is found that the storage capacity decreases with Cr substitution but there was no observable change in the absorption plateau pressure up to 373 K. Among the two compositions, $\text{Ti}_{0.8}\text{V}_{0.4}\text{Fe}_{0.2}\text{Cr}_{0.6}$ was found to absorb hydrogen without any prior activation. It is reported that

the presence of C14 Laves phase in Ti-based bcc alloy helps in the easy activation of the alloys [18]. The XRD of the above two compositions also confirms the presence of a secondary C14 hexagonal Laves phase along with the bcc phase. Thermal desorption studies showed a sharper desorption profile for the Cr containing hydride as compared to the Cr-free hydride.

The hydrogen absorption properties of $\text{Ti}_{0.85}\text{VFe}_{0.15}$ alloy was modified by Zr substitution (5 at. %) at V site to ease the activation as it is known that small amount of Zr substitution ease activation before hydrogen absorption. The alloys and the corresponding hydrides were characterized by X-ray diffraction and Mössbauer spectroscopy. The crystal structure (Fig. 3) shows that 5 at. % of Zr substitution in place of vanadium results in a bi-phasic structure consisting mainly C15 cubic Laves phase along with V based bcc solid solution. The lattice parameter of the C15 cubic Laves phase was found to be 7.36 Å. It may be noted that the C15 cubic Laves phase structure remains unchanged on hydrogenation of $\text{Ti}_{0.85}\text{V}_{0.95}\text{Fe}_{0.15}\text{Zr}_{0.05}$ alloy though there is an appreciable shift in the peak positions to lower 2-theta values indicating volume expansion due to hydrogenation.

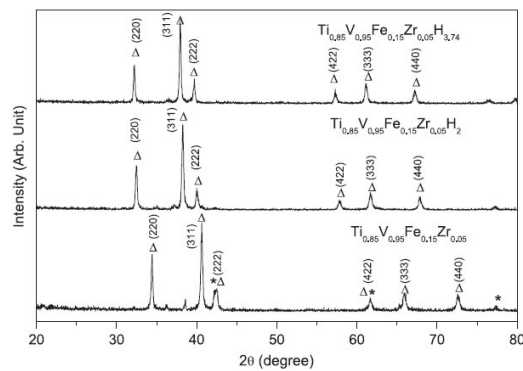


Fig. 3 XRD patterns of $\text{Ti}_{0.85}\text{V}_{0.95}\text{Fe}_{0.15}\text{Zr}_{0.05}$, $\text{Ti}_{0.85}\text{V}_{0.95}\text{Fe}_{0.15}\text{Zr}_{0.05}\text{H}_2$ and $\text{Ti}_{0.85}\text{V}_{0.95}\text{Fe}_{0.15}\text{Zr}_{0.05}\text{H}_{3.74}$. (Δ C15 Laves phases, * V based bcc solid solution).

Comparing the hydrogen absorption capacity and the hydrogen desorption properties of $\text{Ti}_{0.85}\text{V}_{0.95}\text{Fe}_{0.15}\text{Zr}_{0.05}$ with those of $\text{Ti}_{0.85}\text{VFe}_{0.15}$, it was found that the Zr substitution improves the hydrogen absorption–desorption characteristics of $\text{Ti}_{0.85}\text{VFe}_{0.15}$ alloy by decreasing the hysteresis loss without affecting the maximum hydrogen storage capacity considerably. The effective hydrogen storage capacity was found to improve by 5 at. % of Zr substitution in place of V. The increase in the effective hydrogen storage capacity can be attributed to the fact that Zr substituted alloy has an additional site (as shown in the TPD profile in Fig. 4), which desorbs hydrogen at a lower temperature as compared to Ti–V–Fe system.

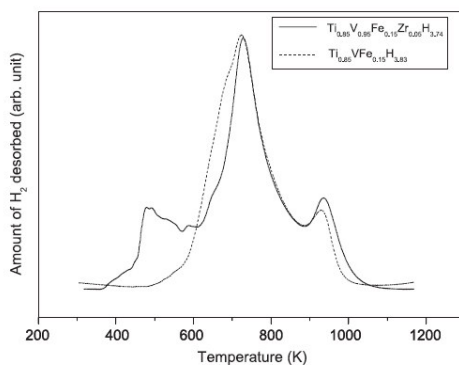


Fig. 4 TPD profiles of the hydrides $\text{Ti}_{0.85}\text{VFe}_{0.15}\text{H}_{3.83}$ and $\text{Ti}_{0.85}\text{V}_{0.95}\text{Fe}_{0.15}\text{Zr}_{0.05}\text{H}_{3.74}$

The effect of Ce substitution on the microstructure, hydrogen absorption properties, peak current of hydrogen absorption and electrochemical behaviour of $\text{Ti}_{0.85}\text{VFe}_{0.15}$ system was also investigated. Substitution of Ce (2 and 5 at. %) for Ti improves the hydrogen absorption capacity of $\text{Ti}_{0.85}\text{VFe}_{0.15}$ alloy. The maximum storage capacity of $\text{Ti}_{0.85}\text{VFe}_{0.15}$, $\text{Ti}_{0.83}\text{Ce}_{0.02}\text{VFe}_{0.15}$ and $\text{Ti}_{0.80}\text{Ce}_{0.05}\text{VFe}_{0.15}$ alloys were found to be 3.7, 4.02 and 3.92 wt. %, respectively. The ease of activation of Ti-V-Fe system was found to improve by Ce substitution. EPMA studies showed the presence of CeO_2 phase in Ce-substituted alloys along with a third phase. The CeO_2 phase is responsible for the easy activation of the alloy as it suppresses TiO_2 phase formation.

Electrochemical studies showed increased exchange current density for Ce doped alloy indicating improved electrochemical activity for the hydrogen electrode reactions.

Chapter IV: Hydrogen Storage Studies on Ti-V-Cr Based System

This chapter deals with the hydrogen storage properties of Zr substituted TiVCr alloy. Stoichiometric TiVCr from the Ti-V-Cr series is reported to exhibit good hydrogen absorption capacity in the previous studies [19]. However, hydrogenation of TiVCr is reported to result in phase separation into TiH_2 and $TiCr_{1.8}H_{5.3}$ when subjected to cyclic hydrogenation-dehydrogenation process [20]. In our work, the hydrogen absorption and desorption characteristics of $Ti_{1-x}Zr_xVCr$ with $x = 0, 0.05, 0.10$ and 1.0 were studied as an attempt to express the phase separation. The maximum storage capacities of these alloys, as a function of Zr substitution, were found to be 3.64, 3.53, 2.93 and 2.16 wt. %, respectively. While TiVCr crystallized in bcc structure, ZrVCr found to have a C15 cubic Laves phase structure and the intermediate compositions with $x = 0.05$ and 0.1 showed the presence of a small amount of $ZrCr_2$ along with the main bcc phase. A small amount of Zr substitution (5 at. %) for Ti decreases the storage capacity of TiVCr system marginally, but TiH_2 phase separation is suppressed, possibly leading to better cyclic hydrogen absorption capacity. Hysteresis was found to be less for Zr substituted systems. With further increase in the Zr concentration, the hydrogen storage capacity was found to decrease considerably due to the formation of the secondary Laves phase in addition to the bcc phase. Temperature programmed desorption studies showed the presence of an additional desorption site at lower temperature for Zr substituted hydrides, which desorb hydrogen at lower temperature as compared to the hydride of TiVCr, indicating higher effective hydrogen storage capacity for Zr substituted systems.

In the second part of the chapter the hydrogen absorption-desorption properties and the cyclic stability of Ti_2VCr alloy are discussed in detail. This alloy shows quite high hydrogen absorption capacity with a maximum storage capacity of 4.37 wt. %. The plateau pressure was found to be less than 0.02 atm. at room temperature, indicating that this alloy forms a stable hydride at room temperature. The cyclic hydrogen absorbing ability decreased progressively during the first few cycles and after that it remains almost constant. The alloy shows maximum 3.5 wt. % hydrogen absorption capacity after few cycles. The kinetics of hydrogen absorption was found to be fast for Ti_2VCr alloy without any incubation time. The desorption capacity of Ti_2VCr hydride were measured by heating the sample at different temperatures. It was found that the hydrogen desorption capacity at room temperature is only 1 wt. % which increases with increase in temperature. In the DSC analysis the multi-cycled hydride showed hydrogen desorption at a lower temperature as compared to uncycled hydride of Ti_2VCr . This may be due to the fact that with increase in cycling the particle size of the hydride decreases. Due to the high storage capacity, the studied alloy can be used in Ni-MH batteries, though the desorption temperature is quite high for the practical application. To take care of this aspect, further modification was done by substitution of 5 at. % Co and Ni, for Ti. The results show that, with Ni substitution though there is a marginal decrease in the storage capacity, but there is a decrease in hydrogen desorption temperature by 75 K.

Chapter V: Vanadium Substituted $ZrFe_2$ as a Laves Phase Hydrogen Storage Material

AB_2 Laves phases are a class of alloy that is considered to be promising candidates as hydrogen storage materials and negative electrodes for Ni-MH batteries. It is well known that many of the pseudo binary compounds like AB_2 show excellent hydrogen absorption-desorption properties and can be considered as potential hydrogen storage materials [21, 22]. Many of them

can absorb three hydrogen atoms per molecule and exhibit a desorption plateau pressure of around 1 atm. at room temperature. Recently, interest has been focused on Zr-based AB₂ alloys, because of their good storage capacity, fast kinetics and easy activation. Among this series, ZrFe₂ intermetallic compound is having a C15 Laves phase structure (MgCu₂ type) with lattice parameter of 7.064 Å. At ambient conditions, it can absorb only a small amount of hydrogen to form a solid solution with composition ZrFe₂H_{0.16}. In the present work, we substituted different amount of V for Fe in ZrFe₂, and demonstrated its effect on the phase formation, hydrogen absorption desorption properties, hydrogen absorption capacity and thermodynamic stability. The compositions studied were ZrFe_{1.8}V_{0.2}, ZrFe_{1.6}V_{0.4}, ZrFe_{1.4}V_{0.6} and ZrFe_{1.2}V_{0.8}. From the structural analysis it was observed that with increase in the V content, the C15 cubic structure transforms into C14 hexagonal structure. While ZrFe_{1.8}V_{0.2} shows a C15 cubic Laves phase structure with lattice parameter of 7.085 Å, other compositions with V content ≥ 0.4 shows C14 type hexagonal structures. It was also observed that, with an increase in the V content the cell volume increases. All the hydrides show similar structure as their parent alloys with an increase in the lattice parameter.

It was found that with the increase in V content the hydrogen absorption capacity increases significantly due to the decrease in the 3d occupation number in the transition elements. The pressure composition isotherms was studied at 300 K, 323 K, 350 K and 373K temperatures respectively using a Sievert's type set up. It was found that ZrFe_{1.2}V_{0.8} absorbs maximum amount of hydrogen within this series to form ZrFe_{1.2}V_{0.8}H_{3.78} at around 20 atm. pressures and it shows a very low absorption plateau around zero atm. at room temperature. The other hydrides, i.e., ZrFe_{1.8}V_{0.2}, ZrFe_{1.6}V_{0.4} and ZrFe_{1.4}V_{0.6}, absorb 2.52, 3.26 and 3.61 H/formula unit, respectively. The plateau pressure for hydrogen absorption decreases significantly with increase

in the V content, indicating higher thermodynamic stability of the hydrides. The formation enthalpies of the hydrides were found out from the van't Hoff plot and it was found that with increase in the V content the formation enthalpy becomes more and more negative indicating more stable hydrides. The increase in the stability of the hydrides with V substitution was also reflected in the temperature programmed desorption profile, which shows that with increase in the V content the desorption temperature increases.

Chapter VI: Theoretical Methodology

This chapter deals with the computational methods used for the first principles based calculations on Mg and carbon based systems. This chapter provides a short overview of quantum chemical electronic structure methods namely, Hartree Fock, and Density Functional theory (DFT). The fundamentals of Hartree-Fock method, post Hartree-Fock and the associated approaches were discussed. The formation of density functional theory and its advantages over wave function based methods for electronic structure calculation in larger systems are discussed. The basic concept of Nudged Elastic Band (NEB) method is introduced, which has been used for the calculation of activation barrier for the dissociation of hydrogen molecules towards hydrogen atoms and subsequent diffusion of hydrogen atoms on Mg surfaces and nano-clusters. Finally some of the technical details and parameters used in these calculations, viz. initial guess wave function or basis set, pseudo-potentials, simulation cell, geometry optimization techniques, utilized computer systems configuration etc. is illustrated in this chapter

Chapter VII: Hydrogen Storage in Mg Based System

Magnesium based systems are considered as one of the most promising hydrogen storage materials because of its low cost and high hydrogen storage capacity. Ideally, it can absorb 7.66 wt. % of hydrogen, which is sufficiently high for on board hydrogen storage [23]. But the

problems with magnesium are high thermal stability of the magnesium hydride and its slow kinetics of hydrogen absorption and desorption in bulk Mg [24]. On reaction with hydrogen at extreme condition, Mg forms MgH_2 and the heat of formation was estimated to be -76 kJ/mole of H_2 . [25]. Due to such higher stability of MgH_2 , the hydrogen desorption occurs at a temperature of around 360°C , which is very high for practical applications. It was found that ball milling of Mg can improve the hydrogen absorption-desorption kinetics by a factor of 10. It is also reported that transition metal elements can act as a catalyst for the adsorption of hydrogen on the Mg surface, thus improving the kinetics of hydrogen adsorption. Here, an attempt was made to provide such an understanding by first-principles calculations to investigate the structure and stability of Mg(0001) surface doped with M atoms ($\text{M} = \text{Ti}, \text{V}, \text{and Ni}$) and their interaction with hydrogen molecule. The chapter deals with the interaction behavior of a hydrogen molecule on the Mg(0001) surface doped with three different transition metal atoms ($\text{M} = \text{Ti}, \text{V}, \text{and Ni}$). In the first part of the work we investigated the stability of these M atoms at different layers of the Mg surface, and in the second part we calculated the interaction energy of hydrogen on the surfaces and the energy barriers for the dissociation of molecular hydrogen into atomic form and subsequent diffusion of atomic hydrogen when the M atoms are at the top surface and in the bulk. From the calculation, it was concluded that the substitutional energies of all the M elements are negative, indicating that M atom doping is thermodynamically favorable (Fig. 5).

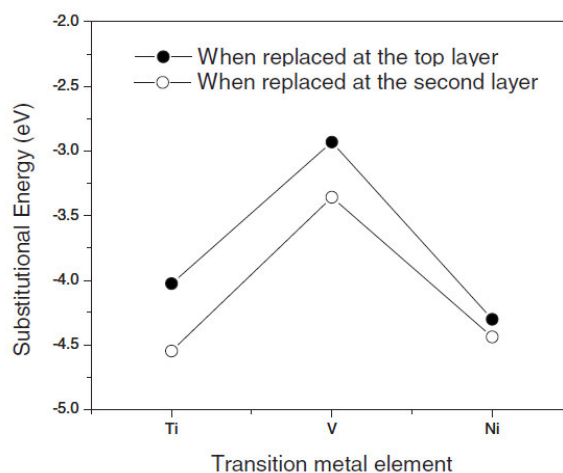


Fig. 5 Comparison of stability for the substitution of *M* (Ti, V, and Ni) atoms at the top (solid circle) and second (open circle) layers.

More importantly, it was seen that all the *M* atoms prefer to substitute one of the Mg atoms from the second layer than that from the top surface layer. However, the relative stability in the first and second layers differs for different transition metal elements. For Ti and V the differences in energy are almost 0.52 and 0.425 eV, respectively, and in the case of Ni it is 0.13 eV only.

The interaction of molecular hydrogen was seen with all the transition metal (Ti, V, Ni) doped Mg surfaces, when the *M* atom remains in the first and second layer of the surface and the results are represented in the tabular form in Table 1.

The interaction of a hydrogen molecule with doped Mg surface suggests that when the impurity atoms are on the top layer they behave as good catalyst for hydrogen dissociation and the dissociative chemisorption of hydrogen molecule occurs spontaneously on the catalytic site. The dissociated hydrogen atoms occupy the fcc or hcp holes depending on the nature of *M* atom. However, they restrict the movement of hydrogen atoms further as the diffusion barrier is quite high. Here the diffusion of hydrogen atoms is the rate limiting step. The situation is reversed

when the M atoms substituted one of the Mg atoms from the second layer. In this case the dissociation of hydrogen molecule is controlled by a high activation barrier but once the hydrogen is absorbed the mobility of the hydrogen atoms on the surface is easier than the previous case. In this case, the dissociation process is the rate limiting step.

Table 1 Calculation of interaction energy of hydrogen and different activation barriers

Surface	Substitution at the first surface			Substitution at the second surface		
	Hydrogen adsorption energy (eV)	Activation barrier for dissociation (eV)	Activation barrier for diffusion (eV)	Hydrogen adsorption energy (eV)	Activation barrier for dissociation (eV)	Activation barrier for diffusion (eV)
Pure Mg surface	-0.07	0.97	0.26	-	-	-
Ti doped Mg surface	-0.61	Almost nil	0.96	-0.27	0.81	0.73
V doped Mg surface	-0.67	Almost nil	0.73	-0.41	0.62	0.83
Ni doped Mg surface	-0.37	0.12	0.43	0.09	0.78	0.22

From the above calculations, we understood the behavior hydrogen on the metal doped Mg surfaces and inferred that the most desirable situation could be, if we can use two dopants, each substituting one Mg atom from the first layer and the second layer. So we investigated the structure and stability of the Mg(0001) surface doped with V and Ni atoms and its interaction with hydrogen molecules. For this purpose, first we calculated the stability of the doubly doped Mg surface by placing the dopants at different layers and found the most stable configuration, where V and Ni are placed in the second and first layer, respectively. Once the preferred location was established through stability criteria, we investigated the dissociative chemisorptions of

hydrogen molecule followed by diffusion of hydrogen atoms on the doubly doped Mg surface. It was found that the most stable state is one where the hydrogen atoms absorb into two nearby hcp positions and one hydrogen atom is nearer to the V atom (Fig. 6). Moreover, from the projected density of states (PDOS) of the system we found that the d PDOS of V changed significantly after the interaction with hydrogen, which suggests that there is a strong influence of V atom, also for the dissociation of hydrogen molecule. The dissociation activation barrier for the hydrogen molecule on the doubly doped structure was found to be quite low (Fig. 7). The stabilization of Ni in the first layer enhances the direct interaction of hydrogen, which results in significant lowering of the dissociation energy barrier, the most desirable property of hydrogen storage. The presence of V atom at the subsurface layer not only stabilizes Ni at the surface layer but also facilitates dissociative chemisorptions of the hydrogen molecule on the catalytic site of Mg(0001) surface. After dissociation of hydrogen molecule into two hydrogen atoms at the catalytic site in the Mg(0001) surface, two hydrogen atoms show different activation barriers for diffusion depending upon their positions. The hydrogen atom, which is away from the V atom, shows a lower diffusion barrier compared to the other hydrogen atom as a result of the lower influence of the V atom.

In the final part of the chapter, discusses the hydrogen adsorption properties of Mg cluster using first principle calculations to reveals the effect of finite size. Our calculations clearly showed that Mg₅₅ cluster has less activation barrier for dissociation of hydrogen molecule than bulk Mg, hence enabling hydrogen dissociation at lower temperatures. The effect of Ti doping on the hydrogen adsorption properties of Mg₅₅ cluster was also established, and we find that when Ti is substituted in the Mg₅₅ cluster then, it preferably goes at the middle layer and it can decrease the dissociation barrier further by activating the surface Mg atom. The

overall decrease in the activation barrier in this case is 40% compared to pure Mg bulk. The *ab-initio* molecular dynamics calculations showed that at 300 K the Mg–H is elongated sufficiently and starts a flip-flop motion on the surface, which can be viewed as the onset of hydrogen diffusion, a preliminary step for desorption. As currently, high desorption temperatures are a major impediment; hence the projected shift toward more favorable operation temperatures is crucial for the application of Mg as a reversible hydrogen storage material.

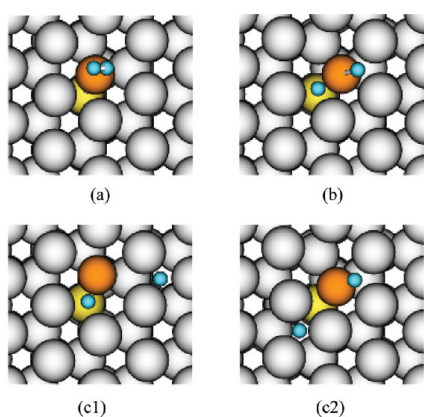


Fig. 6 Hydrogen dissociation and diffusion on the most stable $Mg_{58}VNi(0001)$ surface as represented by the initial state (a), after dissociation of hydrogen molecule (b), and after diffusion of hydrogen atoms (c1 and c2). The gray, yellow and orange balls indicate Mg, V and Ni atoms, respectively. The small balls indicate hydrogen

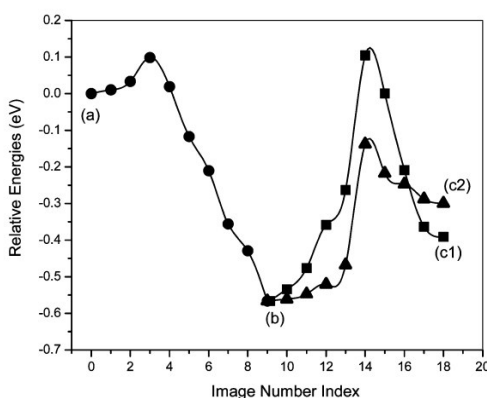


Fig. 7 Minimum energy path (MEP) for the dissociation (indicated by circles) of hydrogen molecule and diffusion (indicated by squares and triangles) of hydrogen atom on the $Mg_{58}VNi$ surface. The relative energies of the initial state, after dissociation of hydrogen molecule on the surface, and after diffusion of hydrogen atoms on the surface are marked by (a), (b), and (c), respectively

Chapter VIII: Hydrogen Adsorption on Carbon Based System

In this chapter we have discussed three systems namely corannulene, SiC nano-materials and metallo-carbohedrene for their hydrogen adsorption properties. Using density functional theory, we investigated the hydrogen uptake capacity of alkali (Li^+ , Na^+ and K^+) and alkaline earth metal ion (Be^{2+} , Mg^{2+} and Ca^{2+}) doped corannulene molecules. The results showed that all

metal ions bind the corannulene ring through charge transfer complex formation. Moreover, the site preference of metal ion adsorption depends on the size of the cation. While the larger size cation prefers to bind on the concave surface, the smaller cation stabilizes on the convex surface. Subsequently, we carried out the interaction of molecular hydrogen with the clean and doped corannulene complexes. Where as, the bare corannulene absorbs hydrogen very weakly, a significant improvement of H₂ binding energy on the doped corannulene was observed. This was attributed to the charge-induced polarization of the H-H bond. Based on the binding energy and hydrogen uptake considerations, it is inferred that Na⁺ doped corannulene is the best candidate among all metal ions considered here.

In the second part of the chapter we report the hydrogen adsorption behavior of two SiC nanostructures; a planar sheet and a nanotube (10, 0) of 1nm diameter, decorated by Ti atoms on it. The lowest energy structure of the Ti adsorbed SiC sheet shows that Ti atom distorts the sheet in such a way that one of the Si atoms goes down the plane and bind with nearest three C atoms. The interaction of this Ti decorated sheet with hydrogen suggests that each Ti atom can bind up to four hydrogen molecules (all hydrogen are adsorbed in the molecular form) with an average binding energy of 0.37 eV. For SiC nanotube, the adsorption of Ti favors the hexagonal hollow site. Moreover, on interaction of this Ti decorated tube with hydrogen, the dissociation of the first hydrogen molecule occurs first and thereafter it adsorbs hydrogen in the molecular form. The average binding energy of hydrogen molecules on this Ti decorated tube was estimated to be 0.65 eV. Based on these results, we inferred that the Ti decorated SiC nanostructures moderately bind with hydrogen molecules (within the energy window for hydrogen storage materials) and therefore, can be considered as one of the potential hydrogen storage material.

The hydrogen adsorption properties of the metallo-carbohedrene (met-car) having a formula M_8C_{12} ($M = Sc, Ti, V$) was also discussed in his chapter. In the work the tetrahedron (T_d) geometry of met-car was considered and the stabilization energies of the pure met-car clusters were compared. In Ti_8C_{12} cluster, each corner Ti atoms can bind three molecules of hydrogen, where as each face Ti atom can bind with one molecule of hydrogen. So total 16 molecular hydrogen can get absorbed on met-car by physisorption. Along with that, six hydrogen molecules get dissociated and absorbed as hydrogen atom on six C-C bond. Considering all the hydrogen atoms, the hydrogen adsorption capacity of Ti_8C_{12} cluster was found to be 15.06 wt. %. The hydrogen adsorption behavior of Ti_8C_{12} was compared with that of the Sc_8C_{12} and V_8C_{12} clusters. Molecular dynamics simulation were carried out to see the desorption behavior of hydrogen molecules.

Chapter IX: Conclusion/Highlights of the Present Work

This chapter discusses the summery and out come of the present thesis and also the scope for the future work both with experiment and theoretical tools. During the present thesis, different experimental techniques have been used for the determination of hydrogen storage capacities, isotherms, and critical thermodynamic and kinetic properties of solid state hydrogen storage materials. During the course of the work, several transition metal based alloys have been identified, modified by proper substitution and the results provide a suitable database for the appropriate choice of hydrogen storage materials. Further the theoretical calculations in the thesis provide proper understanding of physical and chemical properties for efficient hydrogen storage materials, which can give insight for experimental studies. In order to further explore new materials with higher hydrogen storage capacities, theoretical modeling has been carried out on carbon based system using electronic structure theory. The present work can be extended by

different other modification experimentally, and the verification of the theoretical data by experimental methods. However, efforts are to be continued, using both experimental and theoretical tools, to find newer hydrogen storage materials with suitable thermodynamics and kinetics properties, which can store higher amount of hydrogen.

References

- (1) J. Alper, *Science* **299**, 1686 (2003).
- (2) R. D. Cortright, R. R. Davada, and J. A. Dumesic, *Nature (London)* **418**, 964 (2002).
- (3) P. Chen, Z. Xiang, J. Z. Luo, and K. L. Tan, *Nature (London)* **420**, 302 (2002).
- (4) N. L. Rosi, J. Eckert, M. Eddaoudi, D. T. Vodak, J. Kim, M. O'Keefe, and O. M. Yaghi, *Science* **300**, 1127 (2003).
- (5) L. Schlappbach and A. Züttel, *Nature (London)* **414**, 353 (2001).
- (6) A. Züttel, P. Sudan, Ph. Maunon, T. Kiyobayashi, Ch. Emmenegger, L. Schlappbach. *Int J Hydrogen Energy* **27**, 203 (2002).
- (7) L. Zaluski, A. Zaluska, J. O. Ström-Olsen, *J Alloys Compds.* **253-254**, 70 (1997).
- (8) R. Genma, N. Okada, T. Sobue, H. H. Uchida, *Int J Hydrogen Energy* **31**, 309 (2006).
- (9) G. Sandrock, K. Gross, G. Thomas, *J Alloys Compds.* **339**, 299 (2002).
- (10) J. Li, S. Cheng, Q. Zhao, P. Long, D. Dong, *Int J Hydrogen Energy* **34**, 1377 (2009).
- (11) S. J. Yang, J. H. Cho, K. S. Nahm, C. R. Park, *Int J Hydrogen Energy* **35**, 13062 (2010).
- (12) B. Sakintuna, L. D. Farida, H. Michael. *Int J Hydrogen Energy* **32**, 1121 (2007).
- (13) T. Kuriwa, T. Tamura, T. Amemiya, T. Fuda, A. Kamegawa, H. Takamura. et al. *J Alloys Compd.* **293-295**, 433 (1999).
- (14) K. Nomura, E. Akiba, *J Alloys Compd.* **231**, 513 (1995).
- (15) A. Kagawa, E. Ono, T. Kusakabe, Y. Sakamoto, *J Less-Common Met* **64**, 172 (1991).

- (16) E. Akiba, H. Iba, *Intermetallics* **6**, 461 (1998).
- (17) M. Okada, T. Kuriwa, T. Tamura, H. Takamura, A. Kamagawa, *J Alloys Compd.* **330–332**, 511 (2002).
- (18) X. B. Yu, J. Z. Chen, B. J. Xia, N. X. Xu, *J Alloys Compd* **29**, 1377 (2004)
- (19) J-Y. Wang, R-R. Jeng, J-K. Nieh, S. Lee, S-L. Lee, H-Y. Bor, *Int J Hydrogen Energy* **32**, 3959 (2007).
- (20) H. C .Lin, K. M. Lin, K. C. Wu, H. H. Hsiung, H. K. Tsai, *Int J Hydrogen Energy* **32**, 4966 (2007).
- (21) Y.S. Choi, D.J. Lee, Y.W. Park, *J Alloys Compd* **231**, 176 (1995).
- (22) I. Nowik, I. Jacob, R. Moreh, *Phys. Rev. B*, **47**, 723 (1993).
- (23) A. Zaluska, L. Zaluski, and J. O. Strob-Olsen, *Appl. Phys. A: Mater. Sci. Process.* **72**, 157 (2001).
- (24) M. Tsuda, W. A. Dinõ, H. Nakanishi, and H. Kasai, *J. Phys. Soc. Jpn.* **73**, 2628 (2004).
- (25) Y. Fukai, *The Metal-Hydrogen System: Basic Bulk Properties* (Springer- Verlag, Berlin, 1993).

LIST OF FIGURES

Figure Number	Figure Captions	Page Number
Fig. 1.1	<i>Estimation of world energy demand and available energy form conventional sources. [Adapted from http://www.plasma.inpe.br]</i>	2
Fig. 1.2	<i>Increase in global average temperature with increase in the CO₂ emission [Adapted from http://www.zfact.com]</i>	3
Fig. 1.3	<i>Comparison of specific energies of different hydrocarbon fuels with that of hydrogen.</i>	5
Fig. 1.4	<i>The gravimetric storage capacities of hydrogen in different form [Adapted from www.slowmovingwater.com/hydrides2.htm]</i>	10
Fig. 1.5	<i>Mechanism of metal hydride formation</i>	14
Fig. 1.6	<i>A typical pressure composition isotherm showing the hydrogen absorption-desorption profile</i>	16
Fig. 1.7	<i>Schematic PCT diagram at different temperature ($T_1 < T_2 < T_3 < T_4 < T_c$), and the van't Hoff plot</i>	18
Fig. 2.1	<i>The chamber of the arc furnace used during the study</i>	35
Fig. 2.2	<i>Sievert's type hydriding setup</i>	36
Fig. 2.3	<i>The schematic diagram of the estimation set up used during the study</i>	39
Fig. 2.4	<i>A simplified diagram of the X-Ray diffractometer</i>	40
Fig. 2.5	<i>Characteristic X-ray of metallic Cu</i>	41

Fig. 2.6	<i>Depiction of different phenomena occurring on interaction of electron beam with specimen</i>	45
Fig. 2.7	<i>Operating principle of EPMA</i>	47
Fig. 2.8	<i>Simple Mössbauer spectrum from identical source and absorber</i>	49
Fig. 2.9	<i>Quadrupole splitting for a 3/2 to 1/2 transition</i>	51
Fig. 2.10	<i>Magnetic splitting of the nuclear energy levels</i>	53
Fig. 2.11	<i>The simplified diagram of a TG apparatus</i>	54
Fig. 2.12	<i>The schematic diagram of DTA/DSC</i>	56
Fig. 2.13	<i>Schematic for the TPDRO – 1100 instrument</i>	57
Fig. 3.1	<i>The structure of (a) the monohydride (hydrogen atoms occupying the octahedral sites) and (b) the dihydride (hydrogen atoms occupying the tetrahedral sites).</i>	61
Fig. 3.2	<i>Transformation of the bcc alloy structure towards the fcc hydride structure.</i>	61
Fig. 3.3	<i>X-ray diffraction patterns for (a) $Ti_{0.9}VFe_{0.1}$ (b) $Ti_{0.9}VFe_{0.1}H_{3.65}$ (c) $Ti_{0.85}VFe_{0.15}$ and (d) $Ti_{0.85}VFe_{0.15}H_{3.83}$</i>	67
Fig. 3.4	<i>Electron micrographs for (a) $Ti_{0.9}VFe_{0.1}$ and (b) $Ti_{0.85}VFe_{0.15}$ (c) $Ti_{0.8}VFe_{0.2}$ and (d) $Ti_{0.6}VFe_{0.4}$ alloys</i>	69
Fig. 3.5	<i>(a) Ti Kα and Fe Kα X-ray line profiles (b) Electron micrographs for $Ti_{0.9}VFe_{0.1}$ alloys showing the relative concentrations of Fe metal in the bcc and secondary phase.</i>	70
Fig. 3.6	<i>Pressure-composition absorption curves for $Ti_{1-x}VFe_x$ ($x = 0, 0.1, 0.15, 0.2$ and 0.4) alloys at room temperature.</i>	71

Fig. 3.7	<i>Pressure-composition absorption curves for $Ti_{1-x}VFe_x$ ($x = 0, 0.1, 0.15, 0.2$ and 0.4) alloys at different temperatures.</i>	72
Fig. 3.8	<i>Variation of hydrogen absorption capacity with respect to the Fe content in $Ti_{1-x}VFe_x$ alloys ($x = 0.0, 0.1, 0.15, 0.2$ and 0.4)</i>	73
Fig. 3.9	<i>Pressure-composition diagram of $Ti_{0.85}V_{0.4}Fe_{0.15}Cr_{0.6}$ and $Ti_{0.8}V_{0.4}Fe_{0.2}Cr_{0.6}$ alloy.</i>	75
Fig. 3.10	<i>Thermal desorption profiles of (a) $Ti_{0.8}VFe_{0.2}H_{2.5}$ (b) $Ti_{0.9}VFe_{0.1}H_{3.65}$.</i>	77
Fig. 3.11	<i>Thermal desorption profiles of (a) $Ti_{0.9}VFe_{0.1}H_{3.65}$ (b) $Ti_{0.9}VFe_{0.1}D_{3.65}$</i>	78
Fig. 3.12	<i>Thermal desorption profiles of $Ti_{0.8}V_{0.4}Fe_{0.2}Cr_{0.6}H_{1.55}$, $Ti_{0.8}V_{0.4}Fe_{0.2}Cr_{0.6}D_{1.55}$ and $Ti_{0.8}VFe_{0.2}H_{2.5}$.</i>	79
Fig. 3.13	<i>XRD patterns of $Ti_{0.85}VFe_{0.15}$ alloy and the hydride $Ti_{0.85}VFe_{0.15}H_{3.83}$.</i>	82
Fig. 3.14	<i>XRD patterns of $Ti_{0.85}V_{0.95}Fe_{0.15}Zr_{0.05}$, $Ti_{0.85}V_{0.95}Fe_{0.15}Zr_{0.05}H_2$ and $Ti_{0.85}V_{0.95}Fe_{0.15}Zr_{0.05}H_{3.74}$.</i>	82
Fig. 3.15	<i>Kinetic study of $Ti_{0.85}VFe_{0.15}$ and $Ti_{0.85}V_{0.95}Fe_{0.15}Zr_{0.05}$ alloys at room temperature and 20 atm. hydrogen pressure (Recorded after one absorption desorption cycle).</i>	84
Fig. 3.16	<i>PCT curves of $Ti_{0.85}VFe_{0.15}$ at room temperature and 373 K</i>	85
Fig. 3.17	<i>PCT curves of $Ti_{0.85}V_{0.95}Fe_{0.15}Zr_{0.05}$ at room temperature and 373 K.</i>	85
Fig. 3.18	<i>Room temperature Mössbauer spectra of $Ti_{0.85}VFe_{0.15}$ and $Ti_{0.85}VFe_{0.15}H_{3.83}$.</i>	87

Fig. 3.19	<i>Room temperature Mössbauer spectra of $Ti_{0.85}V_{0.95}Fe_{0.15}Zr_{0.05}$ and $Ti_{0.85}V_{0.95}Fe_{0.15}Zr_{0.05}H_{3.74}$.</i>	87
Fig. 3.20	<i>TPD profiles of the hydrides $Ti_{0.85}VFe_{0.15}H_{3.83}$ and $Ti_{0.85}V_{0.95}Fe_{0.15}Zr_{0.05}H_{3.74}$.</i>	88
Fig. 3.21	<i>X-ray diffraction patterns of $Ti_{0.85-x}Ce_xVFe_{0.15}$ alloys with $x = 0, 0.02$ and 0.05.</i>	90
Fig. 3.22	<i>X-ray diffraction patterns of 2 at. % Ce substituted alloy $Ti_{0.83}Ce_{0.02}VFe_{0.15}$ and its hydride $Ti_{0.83}Ce_{0.02}VFe_{0.15}H_{4.26}$.</i>	91
Fig. 3.23	<i>Electron micrographs of (a) $Ti_{0.85}VFe_{0.15}$ and (b) $Ti_{0.83}Ce_{0.02}VFe_{0.15}$, respectively.</i>	93
Fig. 3.24	<i>(a) Ce La, (b) Ti Ka and (c) V Ka X-ray line scans showing compositional variations among different phases of $Ti_{0.83}Ce_{0.02}VFe_{0.15}$ alloy.</i>	94
Fig. 3.25	<i>Kinetic study on $Ti_{0.85}VFe_{0.15}$, $Ti_{0.83}Ce_{0.02}VFe_{0.15}$ and $Ti_{0.80}Ce_{0.05}VFe_{0.15}$ alloys.</i>	95
Fig. 3.26	<i>Pressure-composition isotherms of $Ti_{0.85-x}Ce_xVFe_{0.15}$ ($x = 0, 0.02$ and 0.05) alloys at room temperature.</i>	96
Fig. 3.27	<i>Current versus time characteristics of $Ti_{0.85}VFe_{0.15}$ and $Ti_{0.83}Ce_{0.02}VFe_{0.15}$ alloys.</i>	98
Fig. 3.28	<i>Measured impedance data plots of $Ti_{0.85}VFe_{0.15}$ and $Ti_{0.83}Ce_{0.02}VFe_{0.15}$ alloys. Inset shows the equivalent circuit used for fitting the data. R_1 is the contact resistance, L_1 is the inductance, $R_2//Q_1$ represent the charge transfer resistance at the electrode electrolyte interface.</i>	98

Fig. 4.1	<i>X-ray diffraction patterns of $Ti_{1-x}Zr_xVCr$ alloys ($x = 0.0, 0.05, 0.1$ and 1.0).</i>	105
Fig. 4.2	<i>X-ray diffraction patterns of the hydrides: (a) $TiVCrH_{5.7}$, (b) $Ti_{0.95}Zr_{0.05}VCrH_{5.6}$, (c) $Ti_{0.9}Zr_{0.1}VCrH_{4.7}$ and (d) $ZrVCrH_{4.28}$.</i>	105
Fig. 4.3	<i>P-C isotherms for $Ti_{1-x}Zr_xVCr$ alloys ($x = 0.0, 0.05, 0.1$ and 1.0) at room temperature.</i>	108
Fig. 4.4	<i>Kinetic study of the alloys at room temperature and 20 atm. hydrogen pressure. (Recorded after one absorption-desorption cycle).</i>	109
Fig. 4.5	<i>X-ray diffraction pattern of $TiVCr$ hydride (prepared by dehydrogenation at 673 K followed by hydrogenation at room temperature) showing TiH_2 phase and the fcc $TiVCrH_{5.7}$ without TiH_2 phase separation.</i>	110
Fig. 4.6	<i>Temperature programmed desorption profiles of the hydrides: (a) $TiVCrH_{5.7}$, (b) $Ti_{0.95}Zr_{0.05}VCrH_{5.6}$, (c) $Ti_{0.9}Zr_{0.1}VCrH_{4.7}$ and (d) $ZrVCrH_{4.28}$.</i>	111
Fig. 4.7	<i>X-ray diffraction patterns of Ti_2VCr alloys and $Ti_2VCrH_{9.5}$.</i>	114
Fig. 4.8	<i>EDX mapping of Ti_2VCr alloy.</i>	115
Fig. 4.9	<i>P-C isotherms of Ti_2VCr alloy at 298 K and 373 K.</i>	116
Fig. 4.10	<i>Kinetic study of Ti_2VCr at room temperature and 20 atm hydrogen pressure. (Recorded after one absorption-desorption cycle).</i>	116
Fig. 4.11	<i>Cyclic hydrogen absorption capacity of Ti_2VCr alloy at room temperature up to 10th cycle.</i>	117

Fig. 4.12	<i>SEM micrographs of (a) The Ti_2VCr alloy (b) after initial hydrogen absorption (c) hydride after one cycle and (d) hydride after 10th cycle.</i>	118
Fig. 4.13	<i>Amount of hydrogen desorbed (wt. %) of Ti_2VCr at different temperature.</i>	119
Fig. 4.14	<i>TG-DTA curve of Ti_2VCr uncycled hydride.</i>	120
Fig. 4.15	<i>DSC graph of Ti_2VCr of (a) uncycled hydride and (b) multi-cycled hydride (after 10th cycle).</i>	120
Fig. 5.1	<i>Structure models of the (a) C14, (b) C36 and (c) C15 polytypic crystal structures of Laves phases. A & B atoms are represented by black & grey colours, respectively.</i>	124
Fig. 5.2	<i>(a) The C15 Laves phase structure, where the larger and smaller balls represent A and B atoms, respectively.</i>	126
Fig. 5.3	<i>The EDX mapping of $ZrFe_{2-x}V_x$ ($x = 0.2, 0.4, 0.6, 0.8$) alloys.</i>	130
Fig. 5.4	<i>The X-Ray diffraction profile of alloys. The numbers in the parenthesis represent the respective lattice planes.</i>	131
Fig. 5.5	<i>Variation of lattice volume with the V substitution. The variation in volume both for the C14 and C15 structures are shown separately.</i>	132
Fig. 5.6	<i>The X-Ray diffraction profile of the saturated hydrides of the alloys.</i>	133
Fig. 5.7	<i>The SEM pictures of the hydrides after four absorption desorption cycle (a-d). (a) $ZrFe_{1.8}V_{0.2}H_{2.52}$ (b) $ZrFe_{1.6}V_{0.4}H_{3.26}$ (c) $ZrFe_{1.4}V_{0.6}H_{3.61}$ (d) $ZrFe_{1.4}V_{0.8}H_{3.78}$ (e) The cracks formed on</i>	134

ZrFe_{1.8}V_{0.2} surface during interaction with hydrogen.

- Fig. 5.8** *The pressure composition isotherm of (a) ZrFe_{1.8}V_{0.2} (b) ZrFe_{1.6}V_{0.4} (c) ZrFe_{1.4}V_{0.6} and (d) ZrFe_{1.2}V_{0.8} at 298 and 373 K.* **137**
- Fig. 5.9** *Van't Hoff plots for ZrFe_{2-x}V_x.* **138**
- Fig. 5.10** *The variation of enthalpy of formation of ZrFe_{2-x}V_x (x = 0.2, 0.4, 0.6, 0.8).* **138**
- Fig. 5.11** *Temperature programmed desorption profile of the air exposed hydrides of ZrFe_{1.8}V_{0.2}, ZrFe_{1.6}V_{0.4}, ZrFe_{1.4}V_{0.6} and ZrFe_{1.2}V_{0.8} hydrides.* **140**
- Fig. 6.1** *The pseudo potential concept.* **161**
- Fig. 6.2** *Pseudo potential wave functions.* **162**
- Fig. 7.1** *Structures of (a) unit cell of bulk Mg, (b) unit cell of bulk β-MgH₂.* **170**
- Fig. 7.2** *Surface calculation with five layers of surface atoms using different super cells.* **174**
- Fig. 7.3** *Transition metal doped Mg surface. (a) The M is doped at the top layer of the surface (b) the M doped at the second layer of the surface.* **175**
- Fig. 7.4** *Substitution for different M atoms when they are placed at first and second layer.* **176**
- Fig. 7.5** *Interaction of hydrogen with the clean Mg surface.* **179**
- Fig. 7.6** *Hydrogen dissociation and diffusion on the pure Mg surface as viewed from the top. (a) Initial state, (b) After dissociation of hydrogen molecule and (c) After diffusion of hydrogen atom.* **180**

- Fig. 7.7** *The minimum energy path for hydrogen dissociation and diffusion on the pure Mg surface. IS = Initial State, DS = After dissociation of hydrogen, FS = Final state after diffusion of hydrogen, TS1 = First transition state, TS2 = Second transition state.* **181**
- Fig. 7.8** *Hydrogen dissociation and diffusion (A) Ti, (B) V and (C) Ni doped Mg surface when the substituent elements remains in the top layer as viewed from the top. 1) Initial State, (2) After dissociation of hydrogen, and (3) After diffusion of hydrogen.* **182**
- Fig. 7.9** *NEB profiles for the dissociation and diffusion of hydrogen on the clean and doped Mg surface when M (Ti, V, and Ni) atoms are on the surface layer. The symbols “solid circle”, “solid triangle”, “hollow circle” and “hollow triangle” represent the clean, and Ti, V, and Ni doped Mg surface, respectively. The relative energies of the initial state, after dissociation of hydrogen molecule on the surface, and after diffusion of hydrogen atoms on the surface are marked by (a), (b) and (c), respectively.* **183**
- Fig. 7.10** *Geometry of hydrogen dissociation and diffusion on the Ti doped Mg surface when Ti is in the second layer as represented by initial State (a), after dissociation of hydrogen (b) and (c) and after diffusion of hydrogen (d).* **184**
- Fig. 7.11** *NEB profile for hydrogen dissociation and diffusion on the Ti doped Mg surface when Ti is in the second layer as represented by initial state (a), after dissociation of hydrogen (b) and (c) and after diffusion of hydrogen (d).* **185**
- Fig. 7.12** *NEB profile for hydrogen dissociation and diffusion on the V doped Mg surface when V is in the second layer as represented by initial state (a), after dissociation of hydrogen (b) and (c) and* **187**

after diffusion of hydrogen (d).

- Fig. 7.13** NEB profile for hydrogen dissociation and diffusion on the Ni doped Mg surface when Ni is in the second layer as represented by initial State (a), after dissociation of hydrogen (b) and (c) and after diffusion of hydrogen (d). **187**
- Fig. 7.14** V and Ni doped at different layer of Mg(0001) surface, when V and Ni are not occupying the nearby positions. The yellow and orange balls indicate V and Ni atoms, respectively. (a), (b), (c) and (d) indicate V1Ni1, V2Ni2, V1Ni2 and V2Ni1 respectively. **190**
- Fig. 7.15** V and Ni doped at different layer of Mg(0001) surface, when V and Ni substitute two Mg atoms from the adjacent position. The gray, yellow and orange balls indicate Mg, V and Ni atoms, respectively. (a), (b), (c) and (d) indicate V1Ni1, V2Ni2, V1Ni2 and V2Ni1 respectively. **192**
- Fig. 7.16** Possible absorption sites of the hydrogen atoms after dissociation on the V and Ni doped Mg(0001) surface. The small balls indicate hydrogen atoms. **193**
- Fig. 7.17** Hydrogen dissociation and diffusion on the most stable Mg₅₈VNi(0001) surface as represented by initial state (a), after dissociation of hydrogen molecule (b) and after diffusion of hydrogen atoms (c1 and c2). **195**
- Fig. 7.18** Projected densities of states for H₂ dissociating over Ni and V doped Mg surface as a function of the energy. While figures (a), (b), and (c) represent the PDOS of H, Ni, and V before interaction (initial state), figures (d), (e), and (f) represent the PDOS of H, Ni, V after hydrogen absorption. The s and d orbitals are represented by blue and red lines, respectively. **196**

- Fig. 7.19** *NEB profiles for the dissociation and diffusion of hydrogen on the $Mg_{55}VNi$ surface when Ni atom is at the first layer and V atom is at the second layer. The relative energies of the initial state, after dissociation of hydrogen molecule on the surface, and after diffusion of hydrogen atoms on the surface are marked by (a), (b) and (c), respectively.* **198**
- Fig. 7.20** *The equilibrium structure of the Mg_{55} cluster. Blue, green, red and yellow colors represent center Mg atom (Mg1), one of the 12 Mg atoms at the middle layer (Mg2), one of the 12 Mg atoms at the surface at the top of 12 vertices (Mg3), and one of the Mg atoms at the center of 30 edges of the icosahedron (Mg4), respectively.* **204**
- Fig. 7.21** *The spin density distribution of (a) Mg_{55} and (b) $TiMg_{54}$ cluster (Ti remains at the middle layer). Dark and light colors represent higher and lower values, respectively.* **206**
- Fig. 7.22** *The density of state of one of the surface Mg atom for Mg_{55} cluster and $TiMg_{54}$ cluster (Ti remains at the middle layer). Green and blue colors indicate the contribution from s and p orbital, respectively. The pink line indicates the Fermi level.* **207**
- Fig. 7.23** *(a) The images of Mg_{55} through out the reaction path. The bond distance of H-H bond was indicated on each image showing the dissociation of the hydrogen molecule towards hydrogen atoms. (b) NEB profiles for the dissociation of hydrogen molecule on pure Mg_{55} cluster and $TiMg_{54}$ clusters when Ti atom remains at four different positions.* **210**
- Fig. 7.24** *The density of state of Ti atom of $TiMg_{54}$ cluster when Ti atom remains at four different positions. The sup, ddn etc represents s* **211**

spin up, d spin down respectively.

Fig. 7.25	<i>Molecular Dynamics Calculation at 100 K, 200 K and 300 K on HMg₅₅H cluster. (a) The equilibrium structure of HMg₅₅H and (b) variation of Mg–H(2) distance at different temperatures.</i>	212
Fig. 7.26	<i>The optimized geometries of TiMg_n clusters.</i>	215
Fig. 7.27	<i>The variation of binding energy/atom with increasing number of Mg atom.</i>	217
Fig. 7.28	<i>The variation of second difference in energy with the increasing number of Mg atom.</i>	218
Fig. 7.29	<i>Interaction of hydrogen molecule with the TiMg₈ cluster in the perpendicular and parallel direction and the final geometry after interaction.</i>	219
Fig. 7.30	<i>NEB profile for the dissociation of hydrogen molecule on the TiMg₈ cluster.</i>	221
Fig. 8.1	<i>Optimized geometries of the corannulene molecule and metal-corannulene complexes.</i>	233
Fig. 8.2	<i>Comparison of binding energies and charge transfer of alkali and alkaline earth metal ions with corannulene molecule.</i>	235
Fig. 8.3	<i>Binding of hydrogen molecule with clean corannulene ring in the perpendicular orientation.</i>	237
Fig. 8.4	<i>Optimized geometry of metal ions-hydrogen complexes.</i>	239
Fig. 8.5	<i>Binding energy of hydrogen molecules with the bare metal ions.</i>	241
Fig. 8.6	<i>Charge transfer by the metal atom after interaction with hydrogen molecules.</i>	241

Fig. 8.7	<i>Optimized geometries of the hydrogenated alkali and alkaline metal doped corannulene.</i>	244
Fig. 8.8	<i>Binding energy of hydrogen molecules with the metal ion-corannulene complexes.</i>	245
Fig. 8.9	<i>Charge on the metal atom in corannulene-metal ion complexes after interaction with hydrogen molecules.</i>	246
Fig. 8.10	<i>(a) The structure of SiC sheet with alternative Si (bigger atom) and C atoms (smaller atom). (b) The charge density distribution on the SiC sheet. The darker color and lighter color indicate higher charge and lesser charge respectively. Figure shows higher charge on the C atom and lower charge on the Si atom.</i>	251
Fig. 8.11	<i>(a) The total density of state (DOS) of the graphene like SiC sheet. (b) The DOS of the Si atoms. (c) The DOS of the C atoms. The darker and the lighter color in the DOS of Si & C atoms represent the s- and p-orbital respectively.</i>	252
Fig. 8.12	<i>The chair conformer of SiCH. (a) The top view and (b) the side view.</i>	254
Fig. 8.13	<i>The stirrup conformer of SiCH. (a) The top view and (b) the side view.</i>	254
Fig. 8.14	<i>The twist conformer of SiCH. (a) The top view and (b) the side view.</i>	255
Fig. 8.15	<i>The puckered conformer of SiCH. (a) The top view and (b) the side view.</i>	256
Fig. 8.16	<i>The boat conformer of SiCH. (a) The top view and (b) the side view.</i>	256

Fig. 8.17	<i>The density of states of different conformers of fully hydrogenated SiC honeycomb structure.</i>	258
Fig.8.18	<i>Molecular dynamics simulation showing the average relaxation of C-H, Si-H and Si-C bonds at 300 K with 5-ps time period and 1-fs time step.</i>	259
Fig. 8.19	<i>Ti doped SiC graphene like sheet. (a) Different probable positions for Ti doping. [1) on top of the Si atom, 2) on top of the C atom, 3) at the hexagonal site and 4) at the bridged position] (b) The top view of the SiC sheet after doping with Ti atom. (c) Side view of the SiC sheet after doping with Ti atom.</i>	260
Fig. 8.20	<i>(a) The total density of state (DOS) of the Ti doped SiC sheet. (b) The DOS of the Ti atoms.</i>	261
Fig. 8.21	<i>Pictorial diagram showing the interaction of hydrogen molecules one by one with Ti@SiC_sh. (a) top view (b) side view.</i>	263
Fig. 8.22	<i>SiC (10,0) zigzag nanotube. (a) Transverse view (b) Longitudinal view.</i>	265
Fig. 8.23	<i>(a) The total density of state (DOS) of SiC nanotube. (b) The DOS of the Si atoms. (c) DOS of the C atoms.</i>	266
Fig. 8.24	<i>Doping of Ti atom on the SiC nano tube.</i>	266
Fig. 8.25	<i>(a) Total density of state (DOS) of the Ti doped SiC (10,0) nanotube. (b) The DOS of the Ti atom.</i>	267
Fig. 8.26	<i>The optimized geometry of Ti doped SiC nanotube when it interacts with four hydrogen molecules.</i>	268
Fig. 8.27	<i>The projected density of state of the Ti d-orbital. (a) Ti atom is doped on the Si atom of SiC sheet. (b) Ti atom is doped in the</i>	269

hexagonal site of SiC nanotube.

- Fig. 8.28** *Discovery of metallocarbohedrene by mass spectrometric study by Guo & Castleman.* **272**
- Fig. 8.29** *The geometry of Ti_8C_{12} cluster. The red balls and the blue balls represent Ti and carbon atoms respectively.* **274**
- Fig. 8.30** *Density of state of Ti_8C_{12} cluster.* **276**
- Fig. 8.31** *16 hydrogen molecules absorbed in Ti_8C_{12} cluster. Each corner and side centered Ti atoms absorbs three and one hydrogen molecules respectively.* **277**
- Fig. 8.32** *Comparison of density of state between Ti_8C_{12} and $16H_2@Ti_8C_{12}$. For comparison purpose the Fermi energy has been set at zero.* **278**
- Fig. 8.33** *Geometry of Ti_8C_{12} cluster after addition of hydrogen on the C sites. (a) and (b) represents the geometry of the cluster after addition of hydrogen on the C atom, and geometry of the cluster after full coverage with hydrogen respectively.* **279**
- Fig. 8.34** *Few snapshots of the hydrogenated Ti_8C_{12} clusters during MD simulations at 0 K, 100 K, 150 K, 200 K, 300 K and 500 K.* **281**
- Fig. 8.35** *Flow sheet for hydrogen adsorption desorption in the Ti_8C_{12} cluster.* **282**

LIST OF TABLES

Table Number	Table Captions	Page Number
Table 1.1	<i>Different hydrogen production methods, where hydrogen is produced from water.</i>	7
Table 1.2	<i>Enthalpy of formation of hydrides in kJ/mol H₂.</i>	18
Table 3.1	<i>Lattice parameters and the total hydrogen storage capacities of Ti_{1-x}VFe_x alloys.</i>	68
Table 3.2	<i>Lattice parameters before and after hydrogenation and the maximum storage capacities of the alloys.</i>	95
Table 4.1	<i>Phases, lattice parameters before and after hydrogenation, and the maximum hydrogen storage capacities of the alloys.</i>	107
Table 4.2	<i>EDX data of the Ti₂CrV alloy.</i>	114
Table 5.1	<i>EDX data of ZrFe_{2-x}V_x (x = 0.2, 0.4, 0.6, 0.8) alloys.</i>	129
Table 5.2	<i>The lattice parameters and hydrogen storage capacities of ZrFe_{2-x}V_x alloy (x = 0.2, 0.4, 0.6, 0.8).</i>	132
Table 6.1	<i>Mnemonics used to define density functional of various families.</i>	153
Table 7.1	<i>The distortion created (in %) after doping of the substituent elements at the top layer and at the second layer. D₁₂ and D₂₃ are the distances between the first-second and second-third layer, respectively.</i>	177
Table 7.2	<i>Calculation of interaction energy of hydrogen and different activation barriers.</i>	186

Table 7.3	<i>The substitutional energies for different geometries of V-Ni composite doping on Mg(0001) surface.</i>	191
Table 7.4	<i>The average binding energies of hydrogen atom when they occupy different holes at the Mg₅₈VNi surface.</i>	195
Table 7.5	<i>The binding energies, substitutional energies and magnetic moments of Mg₅₅ cluster and Ti substituted (four different locations) Mg₅₅ cluster.</i>	205
Table 7.6	<i>Interaction energies of hydrogen with Mg₅₅ and TiMg₅₄ clusters. The numbers in the parenthesis corresponds to the same for periodic surface.</i>	208
Table 8.1	<i>Doping of charged alkali and alkaline metal atoms at different positions. In this table 1, 2, 3, 4 locations are Convex surface of central five member ring, Concave surface of central five member ring, Convex surface of side six member ring and Concave surface of side six member ring, respectively.</i>	236
Table 8.2	<i>Charge on Si, C and H atom of different SiC conformers.</i>	259
Table 8.3	<i>The average interaction energy/hydrogen molecule and the charge on the Ti atom, when the hydrogen molecule interacts one by one with Ti@SiC_{sh}.</i>	264
Table 8.4	<i>The structural parameters and energetics of Sc₈C₁₂, Ti₈C₁₂, V₈C₁₂ clusters.</i>	275

Chapter I

Introduction

Both nationally and internationally, the need for alternative energy sources is getting urgent day by day, and hence the development of renewable energy is moving fast. Various individuals and research companies are looking for new energy systems, which can meet the requirements of a renewable and CO₂-free energy. The need for CO₂ – free clean energy arises primarily due to two main reasons [1].

Firstly, in future, even though there will be a surge in demand in energy, the world will be facing a decline in production of conventional fossil fuels. According to the BP Statistical Review of World Energy 2011, oil is the world's largest primary energy source of global consumption till now. But as the demand of energy is expected to grow on an annual basis, an energy crisis is predicted in the near future. The report notes that the overall energy consumption growth is 5.6% annually. From various predictions, it is depicted that the global oil production would start declining sooner or later, and as global energy consumption rise rapidly, the oil prices will increase drastically. From Fig. 1.1 it is clear that, by the middle of the 21st Century, the demand of energy may significantly exceed the energy supplied by fossil fuel, hydrothermal and nuclear energy. The shortfall in energy becomes higher after the depletion of the fossil fuels, about 100 years in the future [2].

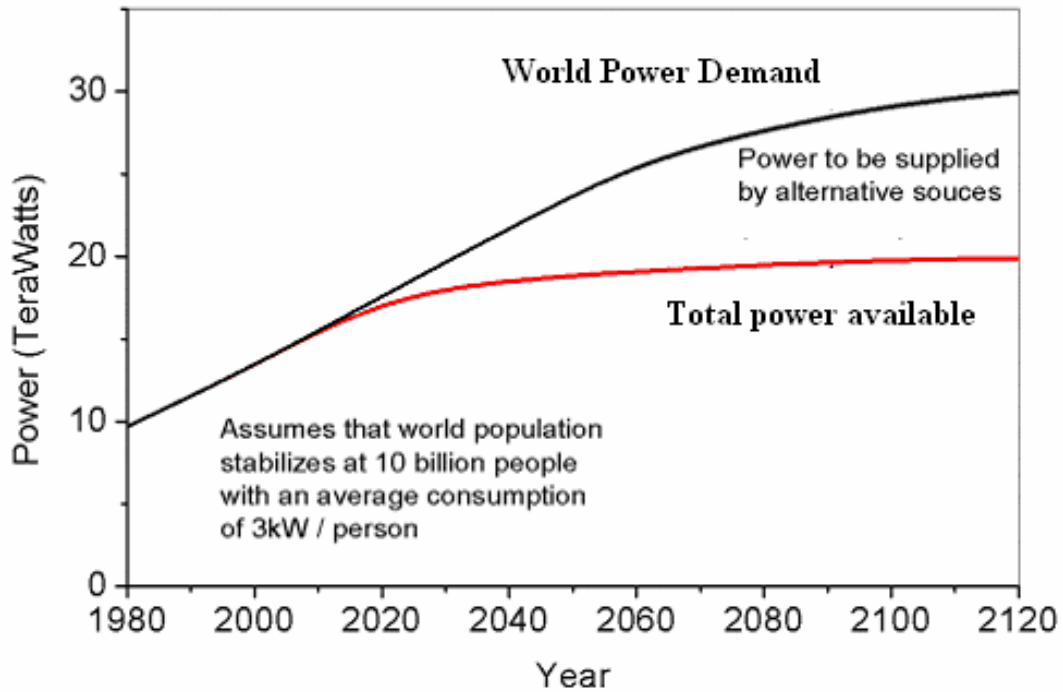


Fig. 1.1 Estimation of world energy demand and available energy form conventional sources. Adapted from <http://www.plasma.inpe.br>

The second reason behind the search of a new form of energy is that, there are serious environmental problems accompanying the combustion of the fossil fuel. Fossil fuels are hydrocarbons, containing primarily carbon and hydrogen, thus when burned, they produce water and carbon dioxide. Fossil fuel use is responsible for the majority of carbon dioxide emissions and more carbon-intensive fossil fuels produce more carbon dioxide pollution. The increase in atmospheric CO₂ has driven a rapid rise in global temperature due to green house effect [Fig. 1.2]. 72% of the totally emitted greenhouse gasses are CO₂. Recent investigations have shown that if the CO₂ concentration rises above 450 ppm, the global temperature will rise by 2°C, which will lead to inconceivable catascopic changes in the environment. Responses to these rising temperatures have already been documented in melting glaciers and ice sheets, shifting weather patterns, and changes in the timing of seasonal events.

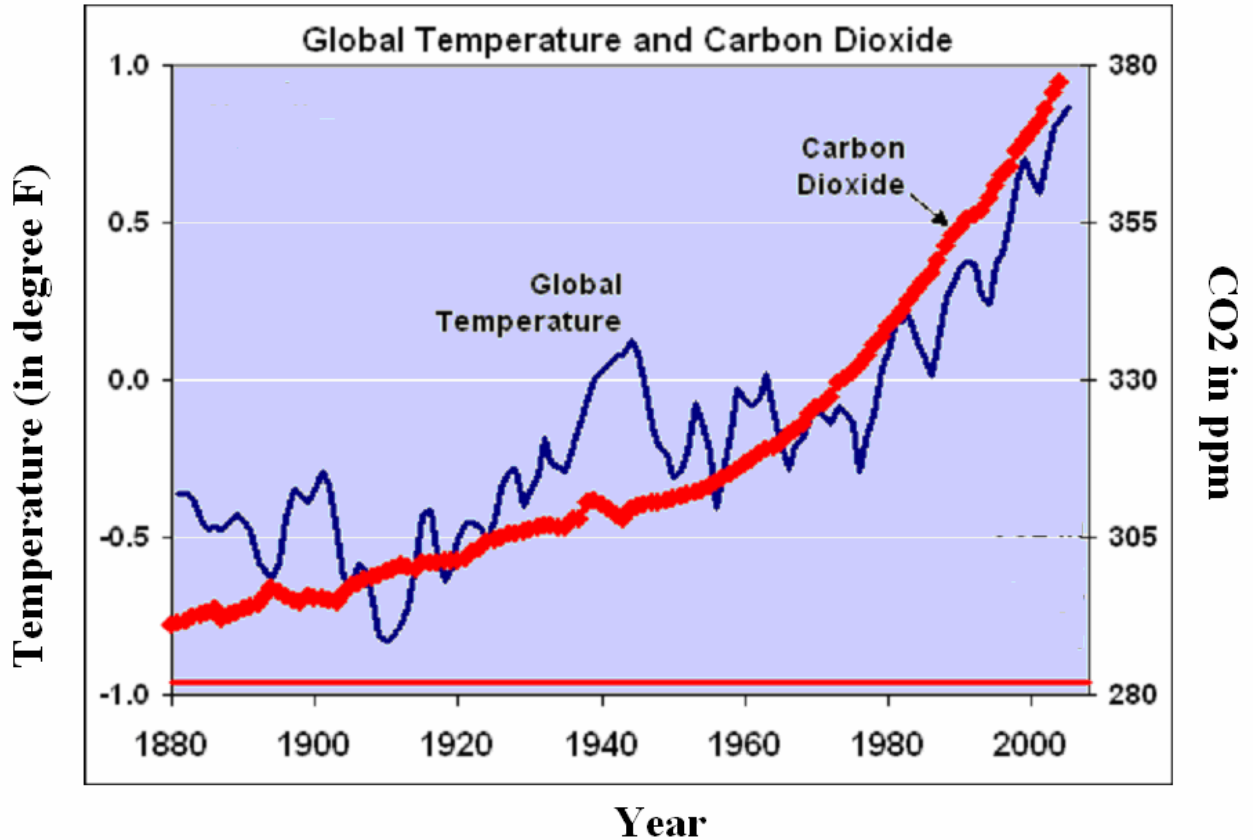


Fig. 1.2 Increase in global average temperature with increase in the CO₂ emission [Adapted from <http://www.zfact.com>]

As a consequence, investigations of alternative energy strategies have recently become important, particularly for the future world stability. The future energy systems must provide a secure, more sustainable, climate friendly and environmentally acceptable energy supply. In recent decades there has been intense international interest, discussion and agreements made, which have been directed at developing cleaner sources of energy to meet the ever-increasing energy demands without sacrificing the environment. In line with this characteristic, hydrogen economy represents such a means, with which these goals can be achieved.

1.1 Hydrogen as Energy Carrier

Hydrogen, the most common chemical element on the planet, does not exist in nature in the elemental form. The majority of it gets combined with oxygen and forms water [3]. As a result, to use hydrogen, we must first separate it from the other elements bonded to it. The hydrogen must be produced from some primary energy sources. That is why hydrogen is considered as an energy carrier, not an energy source, which transports the energy from the generation site to another location. The advantages of hydrogen as energy carrier are:

- When hydrogen is combusted or electrochemically oxidized to create heat or electricity, respectively, the only product is water. No pollutants or greenhouse gases are generated or emitted, allowing the potential of zero emission vehicles to become a reality.
- The chemical energy per mass of hydrogen (142 MJ Kg^{-1}) is almost three times higher than other liquid hydrocarbon fuels [Fig. 1.3].
- Hydrogen is highly abundant in nature.
- Hydrogen can be stored over relatively long periods of time.
- Hydrogen can be utilized in all parts of the economy (e.g., as an automobile fuel and to generate electricity via fuel cells).

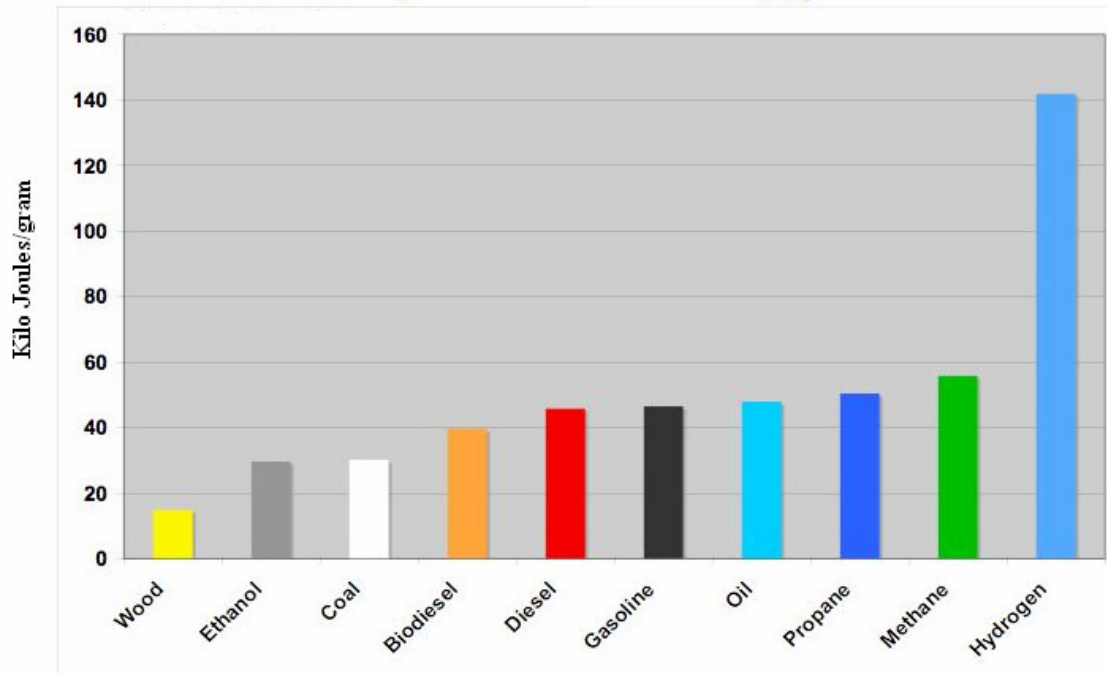


Fig. 1.3 Comparison of specific energies of different hydrocarbon fuels with that of hydrogen [Adapted from green enocometrics research].

Much research, including experimental and theoretical studies, has recently been carried out to use hydrogen energy. However, it is necessary to understand the broader aspects of hydrogen energy to make it realizable [4]. For hydrogen-fueled transportation, the four most fundamental technological and economic challenges are:

- The costs of hydrogen production from renewable energy sources, is to be reduced sharply, over a time frame of decades.
- To capture and store (“sequester”) the carbon dioxide by-product of hydrogen production from coal.
- To develop and introduce cost-effective, durable, safe, and environmentally desirable fuel cell systems and hydrogen storage systems.
- To develop the infrastructure to provide hydrogen for the light-duty-vehicle user.

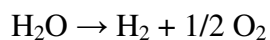
1.2 Hydrogen Production Methods

Many production processes for hydrogen exist. The hydrogen can be produced from the fossil fuels (e.g., steam reforming of natural gas or other light hydrocarbons, gasification of coal and other heavy hydrocarbons) or water (electrolysis of water, direct and indirect thermochemical decomposition, and processes driven directly by sunlight -photo catalytic route). Although having so many choices of resources sounds complicated, but indeed it is a great advantage, because no one region or country has to be dependant on one resource to produce hydrogen and which ever resources are suitable environmentally and economically can be used. In a developing country like India, by means of hydrogen economy, we can have decentralized energy, as many remote areas are not having access of direct electricity.

Presently, the commercialized hydrogen production processes are mostly fossil fuel based, like, steam methane reformation, partial oxidation of methane, auto-thermal reforming and coal gasification – the cheapest and largest being generated by steam-methane reformation. Though this processes generates CO₂, but the CO₂ generate from the reformation process is highly concentrated, therefore the recovery is much cheaper than the diluted exhaust gas of the fossil fuel. But the main advantages of hydrogen economy comes if hydrogen is extracted from water, using CO₂-free primary sources of energy such as solar energy, wind energy, or nuclear energy. The different production methods of hydrogen from water are described in the following section.

1.2.1 Hydrogen production from water

Hydrogen generation from water can be depicted by the following equation



The reaction is highly endothermic ($\Delta H = 243 \text{ KJmole}^{-1}$ at 298 K), and for direct thermolysis of water, a very high temperature is required ($>2500 \text{ }^\circ\text{C}$). The energy required to split water can be provided by a primary energy source, like, solar, wind, nuclear heat or by a secondary energy source like electricity or a combination of these sources using a chemical process. So, a large collection of diverse processes have evolved for hydrogen generation from water and some of which are listed below in Table 1.1.

None of the above except electrolysis has been commercialized and although electrolysis is an established process, cost of hydrogen production is very high. So, efforts are being taken to improve efficiency and to minimize cost of these processes to make them commercially viable. Thus, R&D on various aspects like material development, catalyst development, reactor design etc. has to be carried out.

Table 1.1 *Different hydrogen production methods, where hydrogen is produced from water*

Method	Process	Feed Stock	Energy	Emission
Thermal	Steam Reformation	Natural Gas	High temperature steam	Carbon sequestration can mitigate its small emission
	Coal Gasification	Coal, Biomass	Steam and oxygen at high temperature & pressure	Small emission. Carbon sequestration can mitigate it

	Pyrolysis	Biomass	Moderately high temperature steam	Small emission. Carbon sequestration can mitigate it
	Thermochemical Water Splitting	Water	Waste heat from high temperature nuclear reactor	No Emission
Electrochemical	Electrolysis	Water	Electricity from wind, solar, hydro, nuclear	No emission
	Photo electrochemical	Water	Electricity from direct sunlight	No emission
Biological	Photobiological	Water & Algae	Direct Sunlight	No emission
	Anaerobic	Biomass	High temperature heat	Small emission.
	Fermentative Micro organism	Biomass	High temperature heat	Small emission.

1.3 Different Hydrogen Storage Methods

Hydrogen is a potential fuel for various types of power sources, such as fuel cells, internal combustion engines, gas turbines, etc. However, a major problem is the difficulty encountered in its storage and bulk transport. Hydrogen offers tremendous gravimetric energy potential, but it has a low energy density by volume, meaning it requires a large storage container to make it practical for use in a motor vehicle. To run a standard sized car for 400 km, 24 kg of petrol or 8 kg of hydrogen is needed in a combustion engine, while 4 kg of hydrogen is needed for an electric car with a fuel cell. 4 kg of hydrogen occupies a volume of 45 m³ at ambient conditions. This volume is not practical for automobiles and requires the development of an efficient system for onboard hydrogen storage. Hydrogen in liquid form is very light with energy density of 77Kg/m³, just over one tenth that of petrol /gasoline (702

Kg/m³) but its calorific energy density (39.4 kWh/Kg) is three times that of petrol (13 kWh/Kg).

A hydrogen storage system suitable for mobile applications must meet simultaneously the following six requirements, which has been set up based on economical and environmental considerations [5]

- (i) High gravimetric (>4.5 wt. %) and volumetric (> 36g H₂/L) densities.
- (ii) Operation temperature approximately in the range 60 – 120 °C.
- (iii) Reversibility of the thermal absorption/desorption cycle.
- (iv) Low cost.
- (v) Low-toxicity.
- (vi) Safety requirements.
- (vii) Good cyclic stability.

Hydrogen can be stored in different ways, such as in gaseous and liquid forms and in solid state materials. Hydrogen stored as gaseous form in pressure vessels, pressurized to several hundred atmospheres. In liquid form hydrogen can be stored only at cryogenic temperature which is energy intensive. The main drawback in both these methods is low volume density of hydrogen [Fig. 1.4]. Solid state hydrogen storage has become an alternative method for storing hydrogen. For good hydrogen storage, the material should have greater storage capacity in terms of volume density and wt. %. The kinetics of hydrogen storage material should be very fast. In addition, the material should be lightweight, cheap and should release hydrogen under mild conditions. Refueling time of hydrogen storage materials is currently too long. There is a need to develop hydrogen storage system with refueling time less than three minutes.

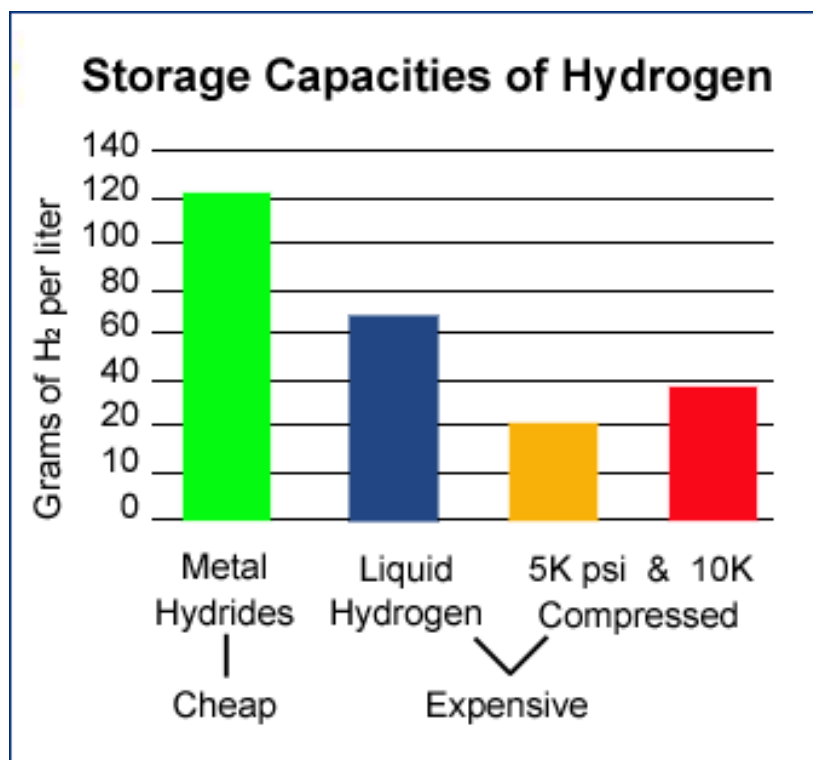


Fig. 1.4 The gravimetric storage capacities of hydrogen in different form [Adapted from www.slowmovingwater.com/hydrides2.htm]

1.3.1 Storage of hydrogen in gaseous form

Compressing a gas requires energy to power the compressor, and higher working pressures mean that more energy requirement for the compression step. Compression of hydrogen gas upto a 35 MPa consumes nearly 20 % of its total energy and the total volume of the tank comes out to be quite high. Because of this, even at a very high pressure, gaseous hydrogen is not an attractive storage medium on a volumetric basis. To store 4 kg of hydrogen in the gaseous form at 200 bar pressure, a traditional cylinder would have to have an internal volume of 220 litres, which may be suitable for buses and larger vehicles, but impractical for a modern compact car. This needs expensive containment vessels made from carbon fiber, capable of withstanding very high pressures, up to 70 MPa (about 10,000 psi). There are major designs challenges are to overcome to find suitable containers for storing hydrogen. Due to the small size of hydrogen molecule, leakage can be a potential danger at

refueling stations, as fuel tanks are refilled at very high pressures through mechanical dispensing couplings.

1.3.2 Storage in liquid form

For space travel, liquid hydrogen has been used as the fuel energy storage system since the 1960s [6]. Liquid hydrogen is light relative to other liquids, but it has a density over 800 times higher than the gaseous state and does not need the high pressure that is required for compressed gas storage, thus has less potential risks compared to gaseous storage. Cooling circuits and insulation are needed to keep it below its boiling point of 20.3°K (-252.9 °C). Considerable energy must also be expended to get and keep the temperature down. The disadvantage of this type of storage is that hydrogen has a liquefaction temperature of 20 K at 0.1 bar pressure and the energy required to liquefy hydrogen is very high, nearly 30 % of the energy content of hydrogen. This energy requirement is one of the major problems with storing hydrogen as a liquid but expenditure is compensated for as very high volumetric density of 25.9 wt. % achieved by liquid hydrogen [7]. Another problem with this method of storage is caused by the massive thermal gradient between the interior and exterior of the storage vessel requiring advanced insulation techniques in order to maintain the temperature of the liquid [3, 8]. Even so, the high thermal gradient results in hydrogen being lost due to boil-off which varies from 0.06 % per day from large static containers to 3 % per day from tanks sized for use in cars [9, 10]. For automotive applications, where space and weight limitations apply, these problems can be acute. Whether it is stored as a liquid or a gas, containment is also a problem since hydrogen molecules are very small and light; they are highly diffusive and tend to permeate through their container even at low pressures. Hydrogen boil-off, and the high cost of sophisticated insulating techniques required for maintaining the very low temperatures, coupled with the initial energy cost to create liquid

hydrogen, makes this method of hydrogen storage impractical for application in hydrogen fuel cell powered vehicles. Researchers is currently trying to find improved insulation and cooling methods. [11]

1.3.3 Solid state hydrogen storage materials

The storage of hydrogen in solid state material by absorption as chemical compounds or by adsorption on high surface area materials has definite advantages from a safety perspective [12]. In these cases some form of energy input is required to release the hydrogen for subsequent use. In solid state storage, hydrogen is bonded by either chemical forces, e.g., hydrides, imides and nitrides or by physical forces, e.g., MOF and carbon based materials. Physisorption has the advantages of higher energy efficiency and faster adsorption/desorption cycles, whereas chemisorption results in the adsorption of larger amounts of gas but in some cases it is not reversible and requires a higher temperature to release the adsorbed gas. The most well studied and practical solid state hydrogen storage material is metal hydride. In this case, hydrogen gets absorbed within the metal to form hydride, and upon heating the hydride, the hydrogen comes out. Extensive efforts have been made on solid state hydrogen storage systems, including metal hydrides, metal nitrides, metal imides, carbon based materials, metal organic frameworks (MOF), zeolites, hollow glass micro spheres and capillary arrays, doped polymers, and clathrate hydrates. Brief introductions of few of the above systems are given in the following sections.

1.3.3.1 Storage of hydrogen in the form of metallic hydride

The hydrogen storage in the metallic form is the safest method known today and it posses many advantages also. Intermetallic compounds are not only attractive as a hydrogen storage material, but also they are very well known for battery application. They can have rechargeable capacities upto 400 mAh/g. It can absorb relatively high amount of hydrogen

compared to liquid and gaseous storage (very high volumetric storage capacity) and also many other form of the solid state hydrogen storage materials. Again many of the metal hydrides show ideal thermodynamic criteria required for reversible hydrogen storage. In this section the basic properties of the metal hydrides and different well studied metal hydrogen systems has been discussed. The major challenges in the development of hydrogen storage materials for batteries and fuel cell application are improved hydrogen storage density, lower desorption temperature, good kinetics & cyclic stability, high stability against oxygen and moisture. The traditional metal hydrides are useful for solid hydrogen storage applications. They have excellent volume storage capacity, good and tunable kinetics and reversibility, but the hydrogen storage capacity is poor by weight.

1.3.3.1.1 Bonding in the metal hydrogen systems

The bonding between metal and hydrogen can be divided into three broad types [13]: (1) ionic (2) covalent and (3) metallic.

The first two groups of elements (S block) form ionic hydrides. The physical properties of the ionic hydrides are same as metallic halide. These compounds act like a salt (NaCl, KCl etc.). Thus, ionic hydrides are called saline hydrides [14]. The crystal structure of alkali metal hydride is same as sodium chloride structure, whereas, the crystal structure of alkaline earth metal hydride is similar to barium chloride structure.

Most of the metals of P block elements (Group IB through VB in periodic table) form covalent hydrides, where the bonding is predominantly covalent. Because of the weak van der Waals forces between covalent bonds, most of these hydrides have low boiling point and, therefore, they are volatile under normal conditions. These hydrides are unstable at elevated temperatures. As a matter of fact, many of them decompose below room temperature [14].

The transition metal and rare earth elements react with hydrogen forming metallic hydrides. Except some higher hydrides of rare earth metals, the metallic hydrides appear to have metallic conductivities.

Among the three types of hydrides, the metallic hydrides are found to be suitable for hydrogen storage applications. For a system to be useful for hydrogen storage, it must be capable of storing large quantity of hydrogen reversibly at room temperature. Alloys that form hydrides have generally been classified as AB, AB₂ or AB₅ systems, where A is a hydride forming element like a transition metal from group III to VI or a rare earth element and B is non hydride forming element like Fe, Co, Ni etc [13]. Most of the metal hydrides absorb and desorb below atmospheric pressure. By suitable substitution, the properties of metal hydrides can be tuned for proper application.

1.3.3.1.2 Mechanism of hydrogen absorption in the metal hydride system

Fig. 1.5 schematically shows the hydrogen absorption process on the metal surface. The hydrogen absorption process is exothermic and certain amount of heat is released during the hydrogen absorption depending upon the host material.

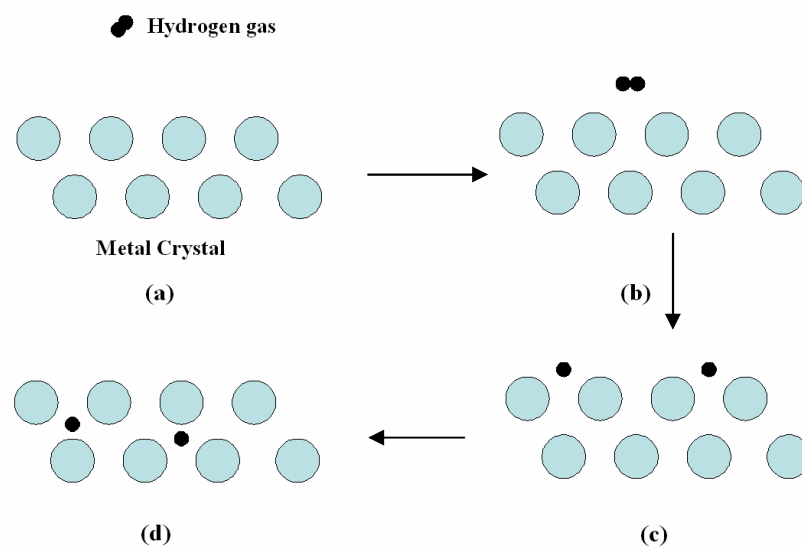


Fig. 1.5 Mechanism of metal hydride formation

Initially the hydrogen molecule approaches to the metal surface [Fig. 1.5(a)] and interacts with the surface by van der Waals force. Here the hydrogen remains in the physisorbed state [Fig. 1.5(b)], with typical binding energy of ~10 KJ/mole. In the next step, the hydrogen molecule needs to overcome the activation barrier for dissociation of the H-H bond and after that the hydrogen molecule dissociates into hydrogen atoms [Fig. 1.5(c)]. The hydrogen atoms get chemisorbed on the surface with the binding energy in the order of 50 KJ/mol-H. After the dissociative chemisorption the hydrogen atoms, they penetrate into the interior of the metal crystal to form M-H solid solution, which is known as α -phase [Fig. 1.5(d)]. In most of the cases, the hydrogen atoms occupy interstitial positions (tetrahedral or octahedral) and the cell parameter of the crystal increases. The physical arrangement of the metal atoms may also change during hydride formation. The hydrogen absorption in α -phase is governed by Sievert's law, which states that

$$C_H = kp^{1/2}$$

Where C is the concentration of hydrogen in the α -phase, p is the hydrogen pressure and k is temperature dependent constant. After increase in the concentration of hydrogen in α -phase, the metal-hydrogen phase starts precipitating and the phase is called β -phase. This process can be explained by pressure composition isotherm.

1.3.3.1.3 Pressure-composition isotherm

A plot between hydrogen pressure and hydrogen to metal ratio at a constant temperature is called pressure-composition isotherm or PCT curve [14]. In the PCT curve [Fig. 1.6], initially the hydrogen pressure increases sharply that means hydrogen diffuse into the interstices of metal or alloy forming solid solution (α -phase).

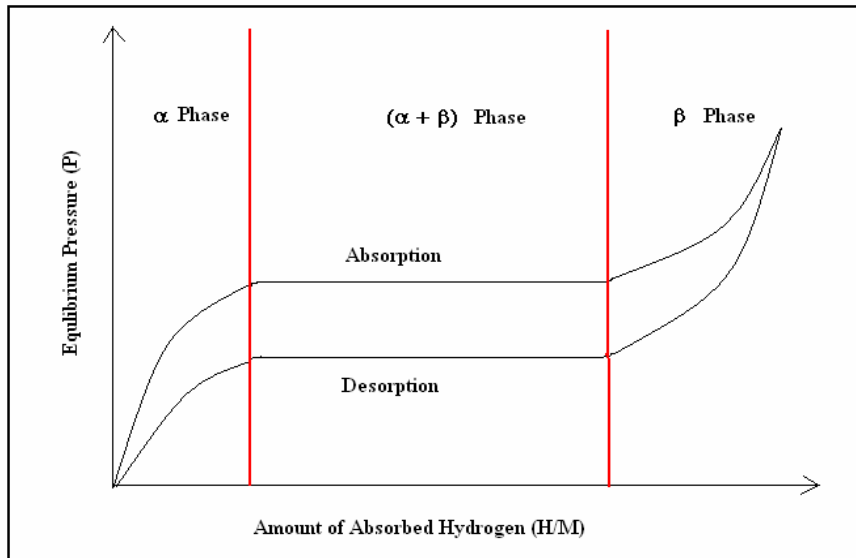


Fig. 1.6 A typical pressure composition isotherm showing the hydrogen absorption-desorption profile

As the hydrogen concentration further increases in the lattice, the hydride phase precipitates. The hydride phase is known as the β -phase. The hydride formation is indicated by the plateau of the plot. In the plateau region, the solid solution and the hydride phase coexist (α & β -phases). The length of the plateau determines how much amount of hydrogen can be stored and recovered by means of a small change in pressure. The last portion represents the hydride phase only, the hydrogen pressure increases steeply with concentration in this region.

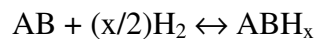
Many metal hydrides do not undergo absorption and desorption along the same path, i.e. the absorption curve & desorption curves of metal hydrides are not the same. The path difference between the absorption and desorption isotherms is known as hysteresis. In most of the cases, the desorption plateau is considered as the true plateau, as the equilibrium is reached faster during desorption. The hydride having higher desorption pressure is less stable than the lesser desorption pressure hydride.

1.3.3.1.4 Thermodynamics of hydride formation

The reaction of a metal with hydrogen to form metal hydride can be represented by the following equation:



When an intermetallic compound reacts with hydrogen the reaction can be written as follows:



Where, A & B are two elements forming the alloy.

We know from Gibbs free energy relation,

$$\Delta G = \Delta H - T\Delta S, \text{ and } \Delta G = RT \ln P_{H_2}$$

The relation between hydrogen pressure and enthalpy of hydride formation can be written as follows.

$$\ln P_{H_2} = \Delta H/RT - \Delta S/R$$

This relation is known as van't Hoff relation. ΔH and ΔS are enthalpy and entropy per mole of H_2 gas respectively. Using van't Hoff relation, the enthalpy and the entropy of the hydride can be found out by studying the pressure composition isotherm at different temperatures [Fig. 1.7]. The plateau pressure or equilibrium pressure of the PCT diagram depends on the working temperature. With increase in the temperature, the plateau pressure increases and the plateau region decreases. At a critical temperature (T_c) no plateau exists. The plot of logarithm of hydrogen pressure versus reciprocal of temperature, i.e. the graph between $\ln P_{H_2}$ and $1/T$ is known as van't Hoff plot shown in Fig. 1.7. The slope of the Hoff calculates the enthalpy of formation of a metal hydride; where as the intercept of the curve gives the entropy. The value of ΔH can be widely different for different metal atoms and alloys as it

varies from large negative to large positive value. Some of the typical hydride formation enthalpy values of different metals have been listed in Table 1.2.

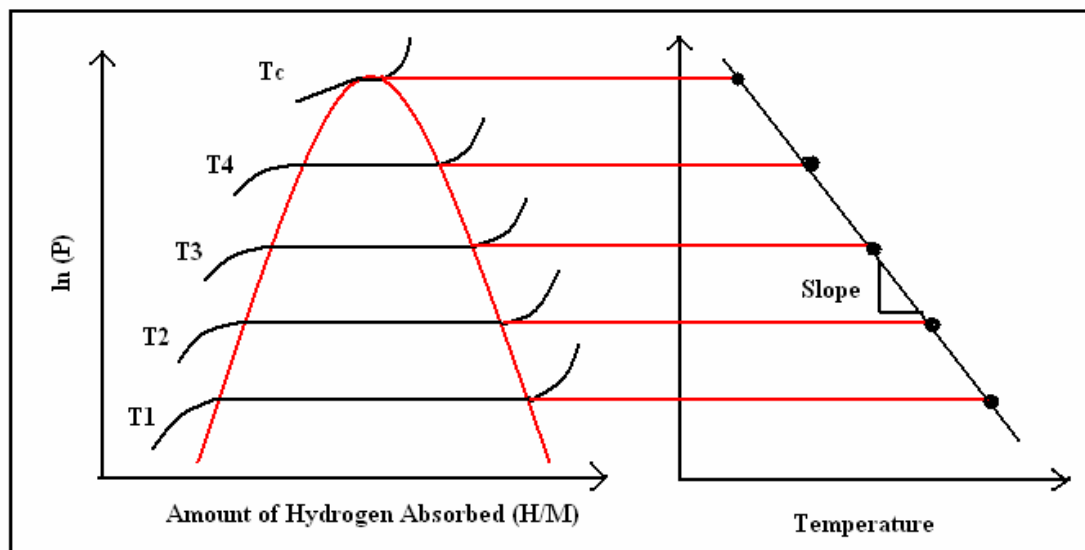


Fig. 1.7 Schematic PCT diagram at different temperature ($T_1 < T_2 < T_3 < T_4 < T_c$), and the van't Hoff plot

Table 1.2 Enthalpy of formation of transition metal hydrides in kJ/mol H_2 [13]

ScH ₂	TiH ₂	VH ₂	CrH	MnH	FeH	CoH _{0.5}	NiH _{0.5}
-200	-126	-54	-16	-9	+14	0	-6
YH ₂	ZrH ₂	NbH ₂	MoH	TcH	RuH	RhH _{0.5}	PdH _{0.5}
-225	-165	-60	-12	+36	+42	+25	-40
LaH ₂	HfH ₂	TaH _{0.5}	WH	ReH	OsH	IrH	PtH
-210	-133	-78	+16	+52	+48	+42	+26
ThH ₂	UH ₃	PuH ₂					
-146	-85	-155					

A stable hydride is the one for which the equilibrium pressure lies below 1 atmosphere at 300 K. These hydrides have enthalpy of formation more negative than -40 kJ/mole of H_2 . Several criteria have been established for the realization of a practical hydrogen storage bed [15].

- The alloy should be readily prepared, easily activated to form hydride and inexpensive.
- The enthalpy of hydride formation should be around ~40 KJ/mole.
- The hydride should have high hydrogen content per unit mass.
- The dissociation pressure of the hydride should lay in the range 0.2-2.0 MPa at near-ambient temperature.
- The system should exhibit favorable and reproducible reaction kinetics.
- The reactant bed should have high thermal conductivity.
- The system should be capable of cycling thousands of times without degradation.
- The alloy should not be poisoned by gaseous impurities.
- The system should be safe on exposure to air and should not ignite.

Binary metal hydrides do not meet the above requirements. The first report of the intermetallic hydride came in 1958 and several other intermetallic compounds are reported. Till then many interesting alloys and intermetallic compounds has been identified as hydrogen storage materials, most of which consist of one hydride forming element and one non hydride forming element. Most typical examples are LaNi₅, FeTi, AB₂ type of Laves phase systems, TiV based solid solutions, and Mg based systems.

1.3.3.1.5 LaNi₅ based system

LaNi₅ based systems are the most well studied hydrogen storage materials. LaNi₅ forms hydride with the formula unit of LaNi₅H₇ (1.5 wt. %) and easy to activate. It shows very flat plateau region with low hysteresis. But the problem with this alloy is that after a few cycle the hydrogen storage capacity decreases due to the degradation of the alloy. The thermodynamic properties of the LaNi₅ compounds vary extensively with composition. Several multi components alloys in this series, La_{1-x}RE_xNi_{5-x}M_x (RE = mishmetal, Ce, Nd & M = Fe, Co, Ni, Mn, Cu Al, Sn etc.), has been studied comprehensively [16, 17].

1.3.3.1.6 FeTi intermetallic compounds

The hydrogen storage capacity of the FeTi based intermetallic compound is 1.9 wt. % (it forms FeTiH₂), and the major advantage of this system is that the constituent elements are inexpensive. But due to the formation of TiO₂ oxide layer the activation of FeTi system is troublesome process. Different substituent elements have been studied to improve its activation and kinetics, but the most effective one found to be Pd [18, 19].

1.3.3.1.7 Zr & Ti based Laves phase compounds

The Laves phase compounds are represented by general formula AB₂. They are having mainly three types of crystal structures: cubic C15 (MgZn₂ type), hexagonal C14 (MgCu₂ type), and double hexagonal C36 (MgNi₂ type). The advantages of these types of compounds are higher hydrogen storage capacities, faster kinetics, and relatively low cost compared to LaNi₅ systems. Their thermodynamics and the electrochemical properties of the Laves phase compounds Zr_{1-x}T_xM_{2-y}N_y (T = Ti, Y, Hf, Sc, Nb & M/N = V, Cr, Mn, Fe, Co, Ni, Cu, Al, Sn, Ge) can be manipulated easily by substitution [20-25].

1.3.3.1.8 Ti-V based bcc phase alloy

The investigation of titanium-vanadium alloys for hydrogen storage dates back from 1970 with the work of Reilly and Wiswall [26]. Since then this system has been intensively studied. The series of alloys generally form two types of hydrides: a mono-hydride with a pseudo-cubic FCC structure and a di-hydride with a CaF₂ structure. Usually, the mono-hydride is too stable for practical applications; this makes the usable capacity smaller than the total capacity. If the mono-hydride could be destabilized without changing its hydrogen capacity then the bcc solid solution could be very attractive alloys for commercial applications. However, as vanadium is relatively expensive, the problem of cost should be taken into consideration. Nomura and Akiba, in their work on Ti-V-Fe alloy system, have

mentioned that ferrovanadium may be used as raw materials instead of pure vanadium [27]. Since then, use of ferrovanadium or mixture of vanadium and iron has been reported by numerous authors [27-34]. Recently, particular emphasis has been on Ti-V-Cr compositions [35]. Another system that was subject of many studies is Ti-V-Mn [36, 38].

Though transition metal hydrides provide high volumetric densities, good kinetic and thermodynamic properties and long term cyclic stability, but in most of the cases, the gravimetric storage capacities are lower for the vehicular application. It is likely however that the use of metal hydride in hydrogen storage will be confined to small applications, because of the low energy density and the cost. Due to the high volumetric densities the metallic hydrides can be used for advanced full cell driven submarines, prototype passenger ships, forklifts as well as auxiliary power unit in laptops.

1.3.3.1.9 Mg-based hydrogen storage materials

Light metal hydrides, including Li, Al and Mg, are considered to be potential in the vehicular application due to high gravimetric hydrogen storage capacities. Mg can form MgH_2 with a maximum hydrogen storage capacity of 7.6 wt. %. Furthermore, magnesium is cheap and its ore is abundantly available. It has a medium reactivity towards air and oxygen, which is an advantage over most other light-weight metal hydrides. But the major barrier towards its application as hydrogen storage material is that, it shows a quite sluggish kinetics of hydrogen absorption-desorption, which is mainly diffusion control. The high thermodynamic stability of MgH_2 results in a relatively high desorption enthalpy of 75 kJ.mol $[H_2]^{-1}$ at standard conditions, which corresponds to an equilibrium temperature of 561 K for H_2 - desorption at 1 bar H_2 . For practical use of MgH_2 as a reversible hydrogen storage material, both the hydrogen sorption rates and the desorption temperatures have to be improved.

In case of bulk Mg, the diffusion of hydrogen atom towards the bulk is very slow. Again after MgH₂ formation, the diffusion of hydrogen becomes much slower. It is documented that the diffusion of hydrogen through MgH₂ is 5000 times slower than pure Mg metal at 350 °C [39]. One of the approaches to increase the hydrogen absorption-desorption kinetics is ball milling the Mg powder or the MgH₂ powder. In many reports ball milling has been taken successfully as a mean to increase the kinetics [40-44]. By ball milling, the initial powders get heavily deformed and fractured, and slowly with time the particle size decreases. With ball milling, the diffusion path length decreases and the volume fraction inside crystallite becomes less, so the hydrogen diffusion rate increases. As a result, after ball milling both the hydrogen absorption- desorption rate increases. However, thermodynamics are not affected by such techniques, hence the desorption temperature of MgH₂ is not lowered.

Alloying or doping techniques are able to lower the desorption temperature of MgH₂ by 30-100 K, but this is accompanied by a lower hydrogen storage capacity due to the added weight [45-48]. Addition of catalytic elements like Pd, transition metal elements, Nb, can improve the kinetics of hydrogen absorption by easing the dissociation of hydrogen molecule on the Mg surface. By addition of suitable catalyst, Mg can absorb hydrogen at relatively faster rate at room temperature also. Recently, metal oxide catalysts (Nb₂O₅, V₂O₅, Mn₂O₃, Cr₂O₃, Al₂O₃, TiO₂ etc.) also have drawn much attention, as they also can improve the kinetics of hydrogen absorption in Mg based systems and the catalytic activity found to retain even up to 1000 cycles [49]. Lower desorption temperatures have also been reported for other bulk phases of magnesium hydride, such as, sputtered thin films of Mg [50-55], highly amorphous Mg [56-62], etc. Moreover, decrease in the particle size has been shown to have an effect on the hydrogen desorption temperature of metal doped magnesium hydrides [58, 59]. These results indicate that, after doping, due to the distortions of the MgH₂-lattice, there is a shift in the desorption temperature and enthalpy value [63- 67].

1.3.3.2 Hydrogen storage in carbon based material

In recent decades, many advances have been made in the preparation of microporous and nano carbonaceous materials [68]. These materials have been found to have good adsorbing properties for hydrogen gas.

1.3.3.2.1 Activated carbon

Research to evaluate the potential of carbon for hydrogen storage at low temperatures began in the 1980s. Activated carbons are bulky carbon with very porous structures and a very large surface area, some in excess of $3000 \text{ m}^2\text{g}^{-1}$. It absorbs hydrogen in macroscopic pores. Hydrogen adsorption on AX21 activated carbon, formed from chemical treatment of coke, at $-196 \text{ }^\circ\text{C}$ and room temperature has been reported [69]. The total hydrogen storage capacity is found to be 2 wt. %. The results illustrate the importance of micropore volume for the hydrogen capacity of a carbon material. Some other studies show that an activated carbon derived through a simple preparation method provides hydrogen storage values at 10 MPa close to 1 wt. %. Initially most of the hydrogen absorption studies on the activated carbon were based on the use of cryogenic systems, which are not useful from an economic point of view [70]. Recently, research has focused on the search for the ideal adsorbent that, used at room temperature, allows the storage of interesting amounts of H_2 [71]. The main problems with activated carbon are that, only some of the pores are ideal enough to catch the hydrogen atom and high pressure must be applied in order to get the hydrogen into the pore [72]. Further research is required to determine the merits and demerits of these materials.

1.3.3.2.2 Carbon nanomaterials

There are various types of carbon nanomaterials that are of interest as a candidate material for hydrogen storage. The most well studied materials are fullerene, carbon nanofibres (CNF), carbon nanotubes (CNT), carbon nano scroll, etc.

C₆₀ fullerene itself is not very promising material for hydrogen adsorption, because C₆₀ does not have real pores in its structure, which are accessible to hydrogen molecules. The tetrahedral void is too small ($d = 2.24 \text{ \AA}$) to accommodate hydrogen molecule ($d = 2.4 \text{ \AA}$), so the small hydrogen uptake of fullerene can be contributed to the octahedral void of fcc crystal ($d = 4.12 \text{ \AA}$) [73]. By modifying the fullerene molecule by means of doping and surface modification, the hydrogen storage capacities can be improved. There have been numerous research papers that associate the doping of fullerene with different metals, but they do not store hydrogen at the ambient temperature. Different metals have been reported, which can form complexes with fullerenes. Some of them are iron, titanium, niobium, rhodium, cobalt, sodium, potassium, lithium, barium, calcium, and strontium. [74-82] Hydrogen adsorption on the metal doped fullerene also has been studied by various researchers using both experimental and computational tools. Wang and Tu showed that [83], Pt-C₆₀ compound show a hydrogen uptake of 1.6 wt. % at 473 K, which was probably contributed by the hydrogenation of the basic fullerene skeleton and its metal counterparts. Simulation shows very promising results on hydrogen storage on metal doped fullerene [84]. Another theoretical calculation shows that a fullerene-like compound Li₁₂Si₆₀H₆₀ could adsorb 12.83 wt. % at 10 MPa and 77 K. Density functional theory based calculation reveals that calcium doped boron fullerene (B₈₀) is a promising hydrogen storage material [85]. Saha and Deng adopted a different approach to increase the hydrogen storage capacity of the fullerene. They have shown that the hydrogen uptake on C₆₀ fullerenes can be increased by partially truncating and opening the cage of C₆₀ [86]. It can be noted that most of the hydrogen storage studied on the metal doped fullerene was done at low temperature and high pressure, because of the very weak interaction energy between the fullerene and the material. Hydrogen sorption measurement on metal fullerides at ambient temperatures has never been reported.

CNF were first reported in the early 1970s. Due to the advancement of the microscopic technique allowed these materials to be observed [87]. In 2002, it was claimed by a team that CNF had been observed to adsorb hydrogen up to 6.5 wt. % at ambient temperatures and 120 bar [88]. They proposed that hydrogen chemisorption occurs at a rate controlled by dissociation of hydrogen at graphitic edge sites. Lueking *et. al.* has shown that pretreatment in certain environments results in the creation of catalytic sites that are favorable toward hydrogen storage. The best pretreatment resulted in a 3.8 wt. % hydrogen release after exposure at 69 bar pressure and room temperature [90]. The high hydrogen absorption value has been neither reproduced nor explained by theoretical calculations [91-92].

CNT were first prepared accidentally during the synthesis of fullerenes using the arc-discharge method in the early 1990s [93]. A nanotube is a graphene sheet rolled up in cylinder shape with diameter in the nanometer range. Carbon nanotubes can store hydrogen both by chemisorption and physisorption. Much research has been carried out to determine the potential of these systems as a hydrogen storage material. Grand Canonical Monte-Carlo simulations show that by varying tube diameter and the inter-tube spacing; the thermodynamic conditions of the tubes could be controlled and optimized for the adsorption of gases [94-95]. In 1997, Dillon *et al* has revealed experimentally that CNT might be capable of 5-10 wt. % hydrogen capacity [96]. The following year, a report claimed that more than 60 wt. % of hydrogen had been observed to adsorb on CNF at room temperature [89]. However, as yet, no group has been able to recreate these findings. In fact, against the results, a number of independent claims have done reporting the hydrogen storage capacities varying from 0-20 wt. %, for both CNF and CNT. Liu *et. al.* reported that single-walled nanotubes (SWNT) can show a reproducible hydrogen storage capacity of 4 wt. % at ambient temperature and 100 bar pressure [97]. Many theoretical studies claim that carbon nanotube can meet the United States Department of Energy target for gravimetric capacity for

hydrogen storage at cryogenic temperatures and high pressure where hydrogen gets absorbed by physisorption [98]. By chemisorption also SWNT can absorb a large amount of hydrogen and from a theoretical study using molecular simulation, a capacity of 14 wt. % was estimated for SWNT [99, 100]. The hydrogen storage properties of the pure carbon tube can be modified by doping and by creating defects. Many experiments and simulations have showed that the isolated transition metal (TM) [101] and alkali metal (AM) atoms or ions, [102] could bind a certain number of hydrogens in molecular form. After releasing hydrogen, however, the isolated transition metal atoms or ions would cluster together easily [103, 104], which is unfavorable for reversible hydrogen storage. Alkali metals doped CNT shows a great potential as hydrogen storage material and could adsorb up to 20 wt. % of hydrogen at 380 °C and 10 bar pressure [105]. However, it was later suggested that the presence of water might have influenced this result.

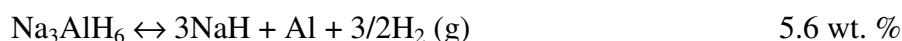
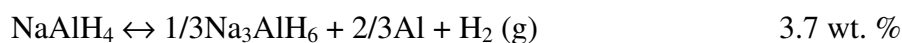
In pure carbon nanoscrolls the interlayer distance is too small to accumulate hydrogen. However, an opening of the spiral structure to approximately 7 Å followed by alkali doping can make them very promising materials for hydrogen storage application, reaching 3 wt. % at ambient temperature and pressure [106].

1.3.3.3 Other solid state hydrogen storage systems

1.3.3.3.1 Complex metal hydrides

There are few complex hydrides, which show quite high hydrogen storage capacities, but the reversibility is still not fully proven. Most of them are the ionic compound of Li, Al, B and are quite stable upto high temperature. In Al and B related chemical hydrides (alanates and borates respectively) the hydrogen atoms are located at the corner of the tetrahedron with the Al/B atom at the centre. The negative charge of $[\text{AlH}_4]^-$ or $[\text{BH}_4]^-$ tetrahedra gets compensated by the positively charged alkali or alkaline metal ion. Because of their structure,

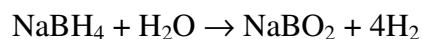
they can hold large number of hydrogen atom, and the value goes up to 18 wt. % for LiBH₄. The complex hydrides like sodium alanate (NaAlH₄), sodium boro-hydride (NaBH₄) undergo chemical reactions during absorption or desorption processes, thus restricting the kinetics and reversibility. Sodium alanate decomposes in two steps giving rise to 5.6 wt. % of hydrogen.



NaH can liberate the remaining amount of hydrogen only at the elevated temperature. Though both of the reactions are thermodynamically quite feasible, but they are kinetically limited due to the slower diffusion of the metal ions. Again, the reactions are reversible only at a temperature above the melting point of NaAlH₄ (183 °C) and at a hydrogen pressure of 10-40 MPa, which is nor practically feasible. Because of that, though the evolution of hydrogen by heating NaAlH₄ was known for many days, but it was not considered as a potential hydrogen storage material. The importance of the material revealed, only after Bogdanovic *et. al.*, in 1996, [107] showed that the charging and discharging temperature of hydrogen can be lowered by doping the hydride with addition of Ti based catalyst. Titanium catalyzed NaAlH₄ has a thermodynamic properties comparable with low temperature metallic hydrides. The first decomposition step occurs at 50-100 °C, whereas, the second step occurs at 130-180 °C. After wards many other catalysts has been tried for fast and reversible desorption of hydrogen from NaAlH₄. The hydrogen storage capacity of NaAlH₄ can be increased by partial substitution of Na by Li.

Another very important complex hydride is sodium borohydride (NaBH₄). The alkali metal borohydrides are having higher hydrogen storage capacities than the corresponding alanates, but they decompose at higher temperatures. NaBH₄ and LiBH₄ show hydrogen storage capacities of 18.5 & 10.6 wt. % respectively, and starts decomposing above 350 °C &

300 °C respectively. Researches are going on to decrease the decomposition temperature by means of addition of catalyst, morphological changes, change in particle size, etc. Another way of using NaBH₄ as a hydrogen carrier is hydrolysis [108]. The hydrolysis reaction can be represented as,



The reaction is irreversible and gives rise to 10.9 wt. % hydrogen theoretically. A mini van designed by M/s Millenium cell, USA showed that using NaBH₄ system, the van can run upto 480 km. This technology is still in very initial stage and efforts are needed to decrease the cost of transport and also reprocessing operations are needed to regenerate the NaBH₄ back from NaBO₂.

Third type of complex chemical hydride is metal amide, which can generate hydrogen by thermal decomposition [109]. Metal amide can generate hydrogen in two steps. For example in the first step, lithium amide (LiNH₂) reacts with lithium hydride (LiH) at 300 °C, to generate lithium imide (Li₂NH), and liberates 6.5 wt. % of hydrogen. In the second step Li₂NH reacts with more LiH at 430 °C to produce lithium nitride (Li₃N), which releases 5 wt. % of hydrogen. There is a need to decrease the desorption temperature of both the steps. Investigations are going on to see the effect of ball milling and addition of additives like magnesium hydride [110].

1.3.3.3.2 Chemical storage of hydrogen

Some organic chemicals, which contain a significant proportion of recoverable hydrogen, can be considered as good hydrogen carrier [111]. One such example is cyclohexane, which can catalytically yield benzene and hydrogen at high temperature. The hydrogen content is 7.1 wt. %.



The benzene can be converted to cyclohexane by the hydrogenation reaction over nickel catalyst at 150-200°C. Similarly, methyl cyclohexane (C₇H₁₄) has also been proposed, which gives rise to 6.1 wt. % of hydrogen.

In addition to the above organic chemicals, some simple inorganic compounds also have been considered as hydrogen carrier. Ammonia Borane (NH₃BH₃) is one simple example which is solid at room temperature and releases about 12 wt. % of hydrogen around 100-200 °C. After hydrogen desorption the residual polymer (NHBH)_n can be converted to NH₃BH₃ in principle and research is going on to meet the practical challenges [112].

Liquid ammonia (NH₃) and hydrazene (N₂H₄.H₂O) are also being considered as hydrogen carrier. Ammonia is decomposed catalytically at the elevated temperature to yield hydrogen and nitrogen, reaching up to 17.7 wt. % of hydrogen storage capacity [113, 114]. The difficulties lies in the fact that NH₃ is highly toxic and can generate hydrogen only at elevated temperatures under catalytic condition. One of the ways to handle toxic ammonia is conveyance of ammonia as an inert solid rather than handling in the gaseous form. Metal ammine Mg(NH₃)₆Cl₂, which is solid at room temperature and can desorb ammonia at 80-350 °C. It can hold 58 wt. % of ammonia and thus 9.1 wt. % H₂. Hydrazene hydrate contains recoverable hydrogen of 8.0 wt. %.

1.3.3.3.3 Hydrogen storage within metal organic frameworks

A recent study has highlighted a new class of hydrogen storage compound, three dimensional metal organic frameworks (MOF), with extended porous structure. MOF are crystalline solids that are assembled by the connection of metal ions or cluster through molecular bridges. An outstanding porosity and very high surface area has promoted their study as hydrogen storage material. These types of structures can adsorb up to 2 wt. % of hydrogen at 10 bar pressure and 293 K temperature, and up to 4.5 wt. % at sub-ambient

temperatures [115]. As a potential hydrogen storage material, it is still in its infancy and the work is yet to be independently confirmed. However, the initial reported results are impressive with many favorable attributes like high porosity, reproducible & facile synthesis, and scope for chemical modifications for targeting desired properties [116]. The studies have highlighted that to increase the total hydrogen storage capacity, there is need to optimize the pore size and reduce the fraction of unutilized void space.

1.3.3.3.4 Hollow glass spheres

Glass spheres are small hollow glass micro-balloons whose diameter varies from 25 micrometer to 500 micro-meters and wall thickness is about one micrometer. The hydrogen storage in glass micro sphere occurs in three steps, charging, filling and discharging [117]. The spheres are filled with hydrogen at high pressure and temperature 200-400 °C. The high temperature makes the glass wall permeable and the hydrogen is able to fill in. Once the glass is cooled down the hydrogen is trapped inside the spheres. The hydrogen can be released by heating or crushing the spheres. The storage capacity of glass spheres is about 5-6 wt. % at 200-490 bars pressure. The glass spheres can also cause accident while breaking down, if not handled properly.

1.4 Objective and Scope of the Present Thesis

In the present thesis, the main focus is to modify the hydrogen storage properties by means of varying composition and alloying modification. The kinetics and desorption temperature also has been monitored for the practical application of the metal hydrides. In certain cases the cyclic stability has been demonstrated for a few cycles to find out any degradation of the material at the experimental conditions.

In chapter II of the thesis, the experimental methodologies have been discussed. Apart from the different instrumental techniques used for characterization, emphasis has been given to the measurement procedure of hydrogen storage capacity, pressure composition isotherm, kinetics of hydrogen absorption, thermodynamics of metal hydrogen system and the desorption profile.

In Chapter III, Chapter IV & Chapter V, we have discussed different transition metal based systems for their hydrogen storage properties. Ti-V-based BCC phase alloys have attractive prospects for use as hydrogen storage media and cathode materials for Ni-MH batteries, because they have higher room temperature hydrogen capacities than the materials currently used. Modifications have been done in the Ti-V based alloy and the effect of substitution on the structure and hydrogen storage properties have been reported. The effect of V on the hydrogen storage properties of $ZrFe_2$ type Laves phase alloy also has been studied in detail. Our work aims to enhance the hydrogen storage capacities of the alloys in a gas-solid reaction and improve their hydrogen storage properties mainly through partial substitution of elements and optimizing the composition. The objectives of the study are:

- Investigation of a variety of transition metal based alloys, known to store hydrogen, to determine the limit of performance and improvement upon them.
- Report the hydrogen storage behavior of certain material as a function of temperature and pressure.
- Understand the effect of doping on the structure, activation, hydrogen storage properties and kinetics of certain materials.

In Chapter VI, we have discussed the theoretical methodology adapted for the First Principle based calculation. In Chapter VII & VIII, magnesium and carbon systems have been studied

theoretically to see the effect of substitution, cluster size and geometry on the hydrogen storage properties. The objective of the study is to

- Fundamental understanding of the mechanism of hydrogen storage in Mg and C based materials
- Theoretical calculation to see the effect of doping elements and finite size on magnesium system to underscore their hydrogen absorption desorption behavior.
- Theoretical efforts are performed to design new carbon based materials that meets the requirements of a good hydrogen storage material.

Chapter II

Instrumentation & Experimental Methods

This chapter deals with the various experimental techniques employed for the synthesis, characterization and evaluation of hydrogen storage properties of the alloys/intermetallic compounds. All the samples under investigation were prepared by melting the high purity constituent elements, with stoichiometric ratio, in DC arc melting furnace, in a water cooled copper (Cu) hearth. The melting was done in argon (Ar) atmosphere and buttons were remelted several times to ensure homogeneity. The basic principle of arc melting is discussed later in this chapter. Conventional Sievert's type volumetric hydrogen storage setup, which had been developed in our laboratory, was used for the synthesis for the corresponding hydride. The actual activation methods used during the hydride formation, the procedure to measure the pressure-composition isotherm and hydrogen absorption kinetics in the Sievert's type setup are discussed in detail. Various characterization techniques were used for the characterization of the alloys, as well as the hydrides. They are as follows: X-Ray Diffraction (XRD), Scanning Electron Microscopy (SEM), Energy Dispersive X-ray (EDX), Mössbauer Spectroscopy, Electron Probe Micro-analyzer (EPMA), Thermo Gravimetric Analyser (TGA), Differential Thermal Analyser (DTA), Differential Scanning Calorimetry (DSC) and Temperature Programmed Desorption (TPD). Brief descriptions of the general principles of these techniques are presented.

2.1 Arc Melting Setup

An arc melting furnace [118] is a furnace that transfers electrical energy to thermal energy in the form of an electric arc to melt the raw materials held by the furnace. The arc is established between an electrode and the melting bath, and is characterized by a low voltage and high current.

Fig. 2.1 shows the direct current (DC) arc melting setup used in our laboratory. The arc melting furnace used for the present work can melt a few grams of samples and the temperature can go up to 3000 °C. The melting of the raw materials is done in the chamber by means of a non-consumable tungsten electrode (cathode) on a water cooled Cu hearth (anode). Cu anode is one of the best materials due to its high melting point and very high conductivity. Before melting the raw materials, Zr metal is kept inside the chamber, and it is purged with argon (Ar) gas for at least 20 minutes. Zr metal acts as the oxygen getter, and removes the dissolved oxygen from the Cu hearth, thus greatly reduces the oxygen impurity. After the melting of the Zr metal, the raw materials are generally melted several times (2-4 times) to ensure homogeneity and during melting continuous Ar flow is maintained. The arc zone volume depends on several factors. The zone volume increases as Ar pressure decreases and increases with the increase in current. The arc zone volume also depends on the nature of the inert gas. As the ionization potential of the gas increases the zone volume increases. After melting, the sample is kept under Ar atmosphere, for proper cooling under the inert gas supply for 20 minutes, before taking out.



Fig. 2.1 *The chamber of the arc furnace used during the study*

2.2 Sievert's Type Setup

In the present work, the hydrides have been prepared using a standard Sievert's type of volumetric set up developed in our laboratory. The principle of Sievert setup is based on the measurement of the change in pressure at constant volume and temperature [119].

The schematic diagram of Sievert's type set up is given in Fig. 2.2. The apparatus consists of a high-pressure manifold connected to the pressure transducer, vacuum line, high-pressure cylinder and hydriding reactor. The setup is made of SS316 to resist high temperature and pressure. The reactor is a cylindrical one with ~24 mm inner diameter, ~37 mm outer diameter and ~210 mm height. The sample holder of 20 mm dia and 39 mm height is placed inside the reactor along with spacer rod to reduce the excess volume. The reactor is connected with the manifold with a screw connection and Viton "O" ring is placed at the connection to avoid any possible gas leakage. The Viton "O" ring is cooled externally by

passing water through the Cu coil to prevent its damage at high temperature. In the connection line between the reactor and manifold, a filter is put with 200 mesh size to prevent the entering of fine hydride particles into the system. An on-off valve (V_5) is put in between the reactor and manifold which is used to expose the sample in the hydrogen atmosphere. During the course of the experiment, for the high temperature activation of samples and high temperature hydrogen absorption-desorption study, the reactor is inserted into a tubular furnace. Chromel-alumel thermocouple is used for measuring the temperature of the reactor. The manifold is connected with the rotary and diffusion vacuum through the valve V_4 . The set-up has been tested in high vacuum (10^{-6} mbar) and high pressure (60 atm.). The volume of different parts of the setup has been calibrated accurately using gas law.

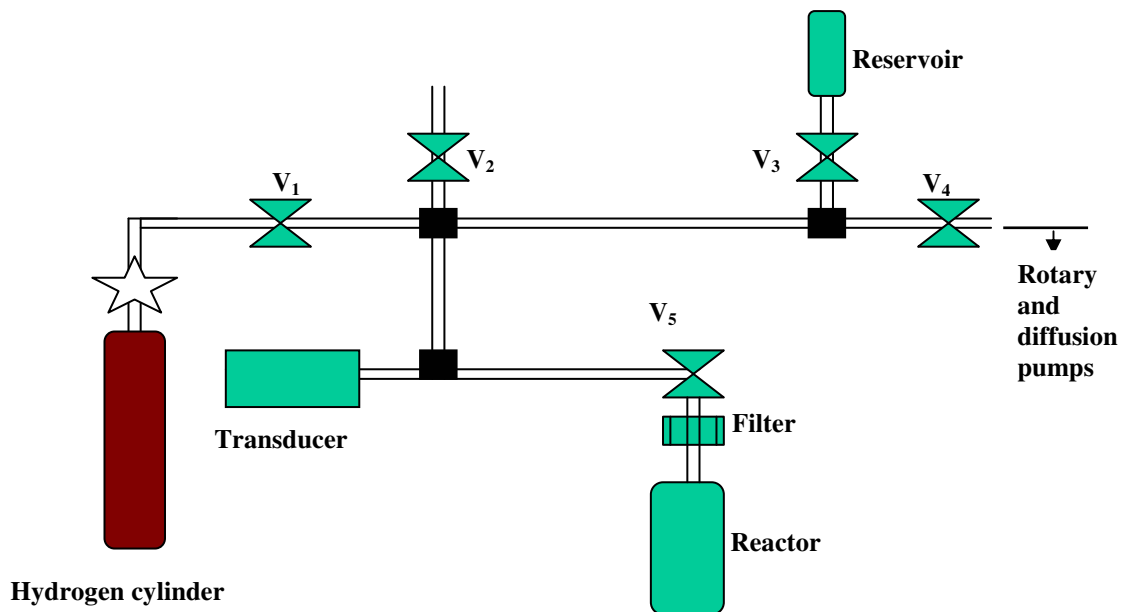


Fig. 2.2 Sievert's type hydriding setup

Before starting the experiment the whole setup is evacuated under diffusion vacuum. In our study most of the activation procedure involved heating the sample under diffusion vacuum (10^{-6} mbar) for 2 hours at 673 K. Some of the samples studied in this thesis absorb hydrogen without prior heat treatment, which will be discussed in the respective chapters.

After activation the sample is cooled to the working temperature under vacuum. Before starting the hydrogen absorption experiment, the manifold is purged with little amount of hydrogen repeatedly and after that evacuated completely. For the pressure-composition isotherm measurements, at the experimental temperature, certain pressure of hydrogen is put in manifold opening the valve V_1 , keeping the reactor isolated by putting off the V_5 valve. After that the valve V_5 is opened to equilibrate hydrogen gas between reactor and manifold. As the volume of the reactor, manifold and the total volume is calibrated, so from the final pressure (equilibrium pressure) of the system, the amount of the absorbed hydrogen gas in the sample can be calculated. During hydrogen absorption, initially the sample forms solid solution with the hydrogen (α -phase) and the equilibrium pressure increases steadily with introduction of hydrogen. After a certain pressure, the hydride formation (β -phase) takes place and the equilibrium pressure remains almost constant. This is plateau region where the α - and β -phase coexist together and the alloy can absorb and desorbs hydrogen reversibly. After that again the equilibrium pressure increases as it can't take more hydrogen. During the desorption study the reverse procedure is followed. Small amount of hydrogen is taken out from the manifold using rotary pump opening the valve V_4 , and keeping the valve V_5 closed. After that opening the valve V_5 the sample reactor is allowed to equilibrate. From the increase in the equilibrium pressure the amount of the desorbed hydrogen can be calculated. When the equilibrium pressure is plotted against the amount of hydrogen absorbed/desorbed then we get the pressure-composition isotherm. For most of the cases the pressure-composition isotherms were studied in the temperature range 298-473 K and up to hydrogen pressure of 25 atm., using freshly crushed samples. For the kinetic study the alloy is kept at a certain pressure and temperature, and the amount of hydrogen absorbed with respect to time is monitored. The surface poisoning of the hydride samples were done by air exposure at liquid nitrogen temperature.

The limitations of the instrument are as follows. In this instrument the transducer can not measure pressure below 0.02 atm. Again the instrument has not been tested above 60 atm. pressure.

2.3 Hydrogen Estimation Setup

After preparing the hydride, it is very essential to estimate the hydrogen content of the hydride independently. The most common method for analyzing the hydrogen content in hydrides is the vacuum fusion technique, in which the material is heated in vacuum and the amount of hydrogen gas released is measured.

The experimental set-up used in the present study, for the estimation of hydrogen content of metal hydride systems, was assembled in our laboratory. The principle is based on the measurement of pressure change, when a known amount of the hydrogenated sample is heated in a standard volume. The schematic diagram of apparatus is given in Fig. 2.3.

The apparatus mainly consist of glass manifold with a mercury manometer for pressure measurement. One end of manifold connected to a vacuum system and the other end to a quartz tube, which serve as sample holder. There is a provision for heating the sample up to 1473 K using an induction heater.

Any apparatus of this type needs to be calibrated for its volume. In present case, we have calibrated our set-up by decomposition of calcium carbonate (CaCO_3) inside the set-up. Known amount of calcium carbonate is heated at high temperature, which evolves known amount of CO_2 gas. Now by observing the pressure change in the mercury level, the volume of the cell and manifold can be calibrated. A known amount of the hydride sample normally in the range of 20-30 mg is introduced into the sample holder and heated to 1473 K using an induction heater. This temperature is found to be sufficient to decompose completely all the

hydride studied in this work. From the fall in mercury level the volume of H₂ released could be calculated.

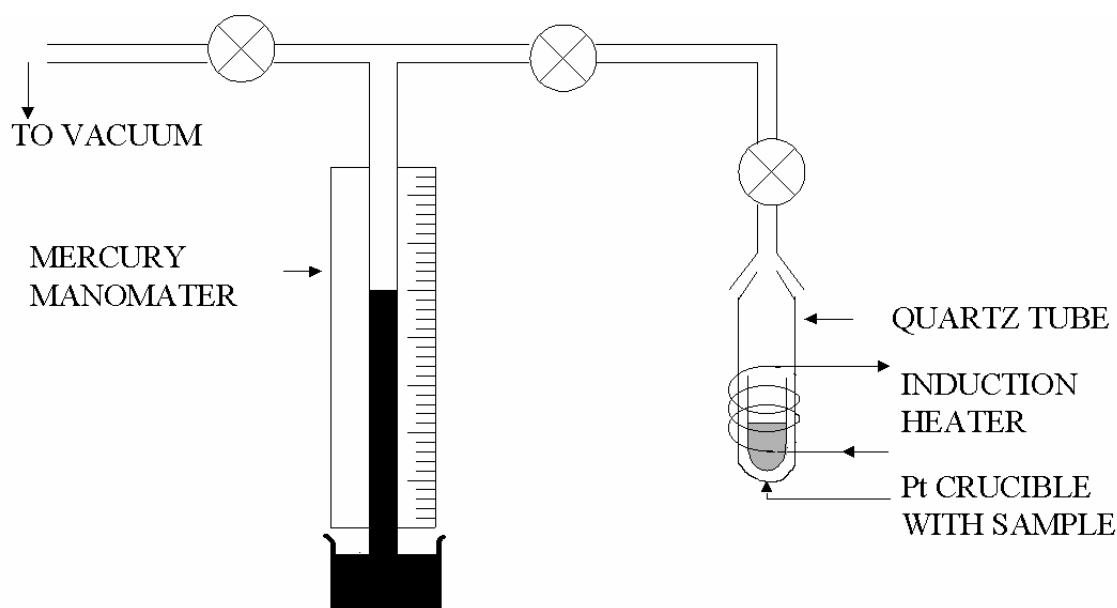


Fig. 2.3 *The schematic diagram of the estimation set up used during the study*

2.4 X-Ray Diffraction (XRD)

X-ray diffraction (XRD) is the most extensively used technique to identify the crystalline phases and to determine the crystal structures. In our present study we have used the technique to identify the phase structure of the entire alloys and their corresponding hydrides. X-rays are electromagnetic radiation with typical photon energies in the range of 100 eV - 100 keV. For the diffraction applications, only short wavelength X-rays (hard X-rays) in the range of a few angstroms to 0.1 angstrom (1 keV - 120 keV) are used. As the wavelength of X-rays is comparable to the size of atoms, they are ideally suited for probing the structural arrangement of atoms and molecules in a wide range of materials. The energetic X-rays can penetrate deep into the materials and provide information about the bulk structures.

The principle of XRD technique is based on scattering of X-rays by a crystal consisting of well-defined array of atoms, ions and molecules. Since the crystal lattice consists of parallel arrays of atoms equivalent to the parallel lines of the diffraction grating, the inter-planar spacing could be successfully determined, from the separations of bright fringes of the diffraction pattern. Interaction of X-rays reflected by a set of parallel planes satisfying Bragg's condition lead to constructive interference only at a particular angle. The peaks positions in a X-ray diffraction pattern are directly related to the atomic distances. The Bragg condition for the occurrence of such diffraction can be written as:

$$n\lambda = 2d \sin \theta$$

Where, λ is wavelength of X-rays, θ is the glancing angle (called as Bragg's angle), d is inter-planar separations, and n is the order of diffraction.

A typical classical powder X-ray diffractometer consists of a source of X-rays and a detector for the detection of diffracted X-rays. Common diffractometer geometries are based on the Bragg-Brentano geometry. A block diagram of the typical powder diffractometer is shown in the Fig. 2.4.

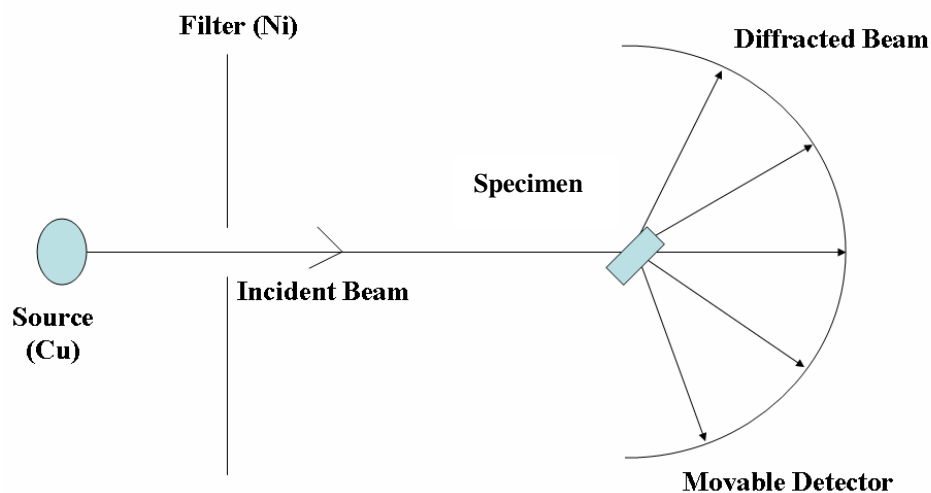


Fig. 2.4 A simplified diagram of the X-Ray diffractometer

There are several kinds of sources for X-rays are available, but the most common laboratory diffractometer uses a sealed tube X-ray source. Bombarding high-speed electrons on a metal target produces the X-rays. A part of the electron energy is used in producing X-ray beam, which is a combination of a continuous radiation with wavelength ranging from a particular shortest value (λ_{cut}) onwards and several intense spikes, which are characteristic of the target elements (called characteristic radiation). The typical X-ray spectrum of elemental Cu is given in Fig. 2.5.

The intense continuous radiations or the monochromatic wavelength radiations are to be used for the diffraction experiments. The latter is used in the most common diffraction instruments (angle dispersive) [120, 121]. Though the X-rays are produced in all the directions, it is allowed to escape from a particular direction (commonly using a beryllium window) for experiments. The background and β -radiations are filtered using β -filters. The beam of X-rays is passed through the divergence slits and then allowed to fall on the sample.

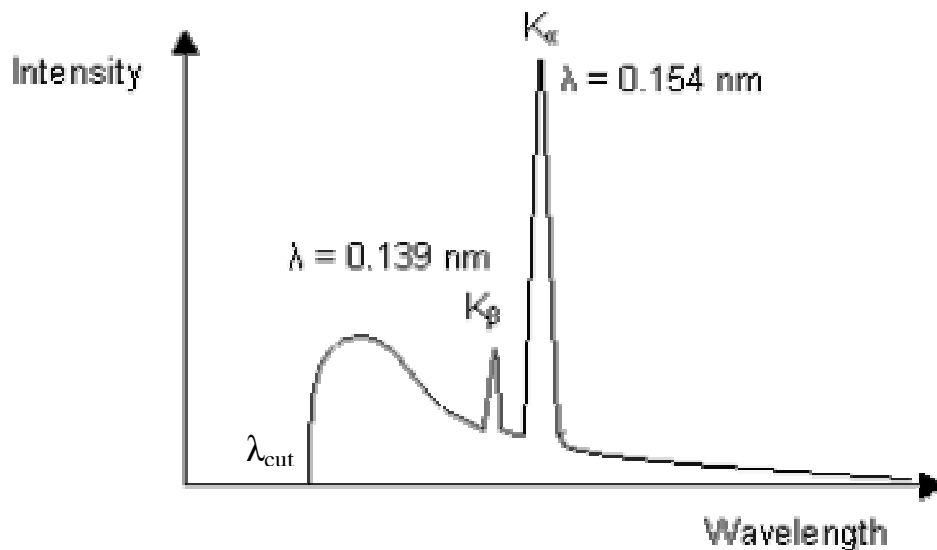


Fig. 2.5 Characteristic X-ray of metallic Cu

In case of powder diffraction, the fine grains of sample are generally spread uniformly over a rectangular area of a glass slide, so that all the orientations get exposure. The sample is

usually adhered to a glass slide either using binders like collodion or grease or wax. The amounts of the sample exposed generally depend on the scattering power of the elements, absorption coefficient, X-ray source intensity and of course on availability of the sample. The crystalline sample usually shows good scattering and sharp diffraction lines. The X-rays diffracted from the powder samples are collected either by a film or movable counters. In the diffractometer, the diffracted beams are passed through the Soller slits and divergence and receiving slits. Then it is usually allowed to fall on a monochromator before detection.

For the detection of X-ray, the gas filled tube or scintillation counters are commonly used. These tubes can either be the proportional counter or Geiger-Muller counter. This particular tube is usually filled with a gas, which gets ionized by the impact of the radiation. Applying a potential difference between the two electrodes, the ions are collected. The typical current obtained is proportional to the number of photons reaching to the detector. The diffracted rays are scanned by sweeping the detector from one angle to another. The angle where the Bragg's law is satisfied for a particular plane, a constructive interference among the diffracted X-rays from that plane takes place, giving a sharp rise in the intensity (peak). Thus, the counts or count rates of the X-ray photon are measured at different angles. The output is obtained as plot of the intensity of diffracted X-rays (Y-axis) vs angle (X-axis).

The peaks (also called as reflections) in the plot correspond to a set of parallel planes with inter-planar spacing d_{hkl} . The d-values are calculated from the position of the peaks. Thus, for a particular sample a set of d-values giving constructive interference is observed. The peak positions (d values) are related with the unit cell parameters of the lattice. Hence they can be used for identification of the materials and they generally act as the fingerprint for the crystalline materials. The intensity distribution of the reflections is governed by the nature and kind of distribution of atoms in the unit cell.

In the present work, a Philips 1710 diffractometer was mostly used for the characterization process. Philips-1710 diffractometer is based on the Bragg-Brentano reflection geometry. The Cu K α emissions from sealed tube are used as the incident beam. The Philips (PW-1710) diffractometer has a proportional counter (Argon filled) for the detection of X-rays. The X-ray tube rating was maintained at 30 kV and 20 mA in the Philips unit.

The data collection protocols often depend on the specific purpose of the data collections. In general a short time scan in the two-theta (2θ) range of 10 to 80° is sufficient for the identification of a well crystalline inorganic material. However, low symmetry samples and samples with not good X-ray scattering power may need a slow scan. The scan time was optimized for getting good intensity peaks. Prior to data collections, the goniometer needs to be properly aligned for correct zero position. After the proper alignment, the instrument has to be calibrated with standard known materials for the accurate peak position. Usually silicon is used for calibration. The silicon peak positions are adjusted by the correct angle and set angle command or by applying the zero settings to the diffractometer. After the data collection, the observed d-values were fitted to standard patterns and the unit cell parameters were refined with respect to the standard values. By comparing the observed diffraction pattern with JCPDS (Joint Committee on Powder Diffraction Standards, 1974) files available for reported crystalline samples, fingerprinting of sample materials is normally done. The refinements are usually done by a least square method. The computer software used for this purpose was “Powder-X” [122]. The unit cell parameters are made free to adjust in the best way to fit the observed experimental data. The use and interpretation of the powder diffraction patterns are explained in several books [120-122]

The approximate crystalline size and the stain can be estimated from broadening of the X-ray peak by the Scherrer’s formula. The line broadening is measured as

$$\beta^2 = \beta_M^2 - \beta_s^2$$

where, β_M is the measured peak width in radians at half peak height and β_s is the measured peak width of a peak of a standard material, mixed in the sample, having a diffraction peak near to the relevant peak of the sample [123]. Line broadening β can be written as

$$\beta = \varepsilon \tan \theta + \frac{0.9\lambda}{B \cos \theta}$$

Where ε is the parameter defining approximate strain, λ the X-ray wavelength measured in angstrom (\AA) or nanometer (nm) units and θ the Bragg angle and B is the parameter defining approximate crystallite size. Now, the equation can be rearranged as

$$\beta \cos \theta = \varepsilon \sin \theta + \frac{0.9\lambda}{B}$$

So if we plot $\cos\theta$ vs $\sin\theta$, then from the slope we can calculate the strain and from the intercept we can calculate the approximate crystalline size. The actual sizes in a number of crystalline samples and their hydrides were actually investigated by means of SEM, as explained in another section.

2.5 Scanning Electron Microscope (SEM) and Energy Dispersive X-ray (EDX)

The scanning electron microscope technique is used to study the microstructure evolution (grain size, porosity, etc.) of the samples and their hydrides. The instrument used were a SEM SERON INC, South Korea made, Model number ATS 2100. EDX instrument is made by Oxford Instrumentation, UK, Model Number INCAE350.

The Scanning Electron Microscope is discussed briefly in the paragraph below. When a finely focused electron beam interacts with the matter (specimen) there are three major

phenomena occur: (i) emission of secondary electrons (SE) (ii) back-scattering electrons (BSE) and (iii) transmission of electrons. These three phenomena and some other important phenomena are depicted in Fig. 2.6.

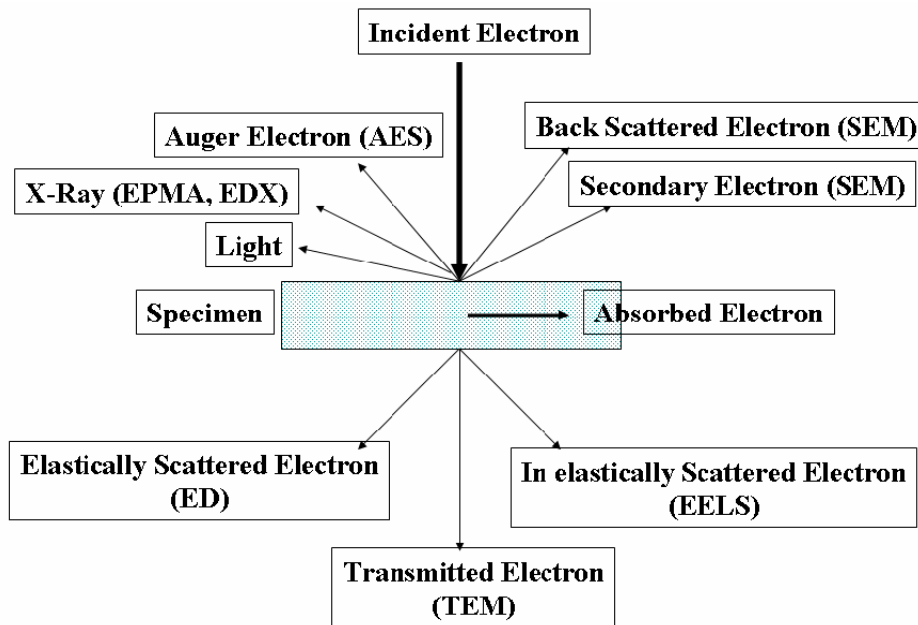


Fig. 2.6 Depiction of different phenomena occurring on interaction of electron beam with specimen

In Scanning Electron Microscopy, the signals generated from the surface by secondary and back-scattered electrons are detected and are fed to a synchronously scanned CRT as an intensity-modulating signal and thus displays a specimen image on the CRT screen [124]. The CRT raster width divided by the electron probe scanning width determines the image magnification. Scanning microscope is composed of (i) electron optical system, (ii) specimen stage, (iii) display and recording system and (iv) vacuum system.

In SEM technique [124], the electrons from a finely focused beam and get restored across the surface of the sample. Electrons are reflected by the surface of the sample and emitted secondary electrons are detected to give a map of the surface topography of the sample. It is useful for looking at particle size, crystal morphology, magnetic domains, surface defects, etc. A wide range of magnification can be used, the best achievable

resolution being about 2 nm. An electron beam incident on a metal gives rise to the emission of characteristic X-rays from the metal. In electron microscopy, the elements present in the sample also emit characteristic X-rays. These are separated by a silicon-lithium detector, and each signal collected, amplified and corrected for absorption and other effects, to give both qualitative and quantitative analysis of the elements present (for elements of atomic number greater than 11) in the irradiated particle, a technique known as energy dispersive analysis of X-rays (EDAX or EDX). In the present study we have used SEM as a tool to determine the particle size and to see the surface morphology. Again from the EDX analysis the qualitative and quantitative analysis of the elements present in the sample was done to confirm their composition.

2.6 Electron Probe Micro Analyser (EPMA)

The principle electron probe forming and emerging components of the EPMA are similar to SEM. They include an electron optical column to produce a finely focused electron beam, a scanning system, one or more electron detectors and a cathode ray tube (CRT) display system. Differences arise from the fact that in the EPMA emphasis is placed on micro chemical analysis while the main use of SEM is microscopic imaging [125]. Micro chemical analysis in EPMA is based on the measurement of X-rays generated by the focused electron beam. The ability to perform chemical analysis in an EPMA is a result of existence of a relationship between the wavelength λ of the characteristic X-ray emitted from an element and its atomic number Z (for K radiation) which can be given as

$$Z \propto \lambda^{-1/2}$$

When an electron incident on the sample having sufficient energy to exceed the excitation potential E_c (the bonding energy of the core electron), then core electron is ejected from atom leaving a vacancy, which is then filled by the electron from higher energy state by

the electronic relaxation by simultaneous release of a discrete energy corresponding to the difference between the orbital energy levels. This energy may be either in the form of X-rays or Auger electron. The probability of the ejection of core electron of an atom by the incident electron is one out of ten thousand.

These X-rays are detected and characterized either by means of an energy-dispersive spectrometer (EDS) or a crystal diffraction spectrometer (CDS, also known as wavelength-dispersive spectrometer WDS). The basic operating principles of the instrument are illustrated in Fig.2.7.

Electron Probe Micro-Analyzer

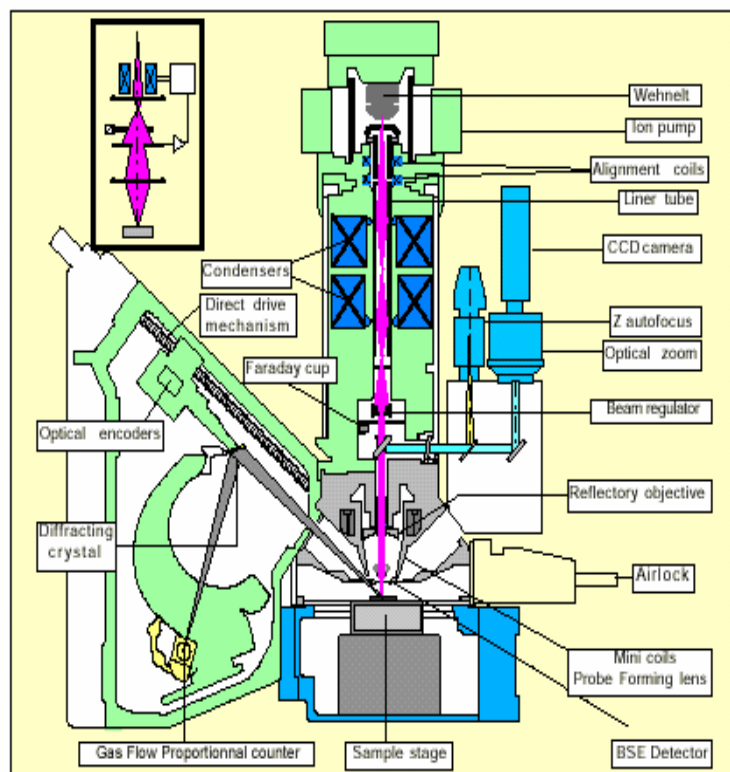


Fig. 2.7 Operating principle of EPMA

An electron optical column containing an electron gun, magnetic lens, a specimen chamber and various detectors are maintained at vacuum of at least 10^{-5} mm Hg. A directly heated filament provides a source of electron for the electron gun. The filament is held at a

negative potential, 5 to 30 kV relative to the gun anode, which is grounded. A grid placed between the filament and the anode is biased at a potential slightly less than that of the filament. Thus electrons are attracted from the filament to the anode focused by the field of the grid cap. The electron gun acts as a lens, forming an image of the filament which is then demagnified by two or more magnetic lenses to form the final probe. The probe size is in the range of 0.1 to 1 μ m with corresponding probe currents in the range of about 10-1000 nA. When the focused electron beam strike the sample a variety of signals are generated, including backscattered electrons, secondary electrons and X-rays. Although the backscattered electron signal varies with atomic number but mainly it is the X-rays that provides a unique way of performing both quantitative and qualitative analysis which can be detected by either WDS or EDS systems. By using wavelength dispersive spectra better resolution in the composition analysis can be found in EPMA than the energy dispersive SEM analysis. In this thesis we have used WDS-EPMA to confirm any phase segregation and also to find the composition of the different existing phases.

2.7 Mössbauer Spectroscopy

The phenomenon of recoilless emission and resonance absorption of γ -rays by identical nuclei bound in solid is known as Mössbauer effect [126, 127]. Rudolph Mössbauer first observed “Mössbauer Effect” [Fig. 2.8] in 1957 in ^{191}Ir and received the Nobel Prize in Physics in 1961 for his work. He discovered that, when the atoms are within a solid matrix, the effective mass of the nucleus is very much high. The recoiling mass is effectively the mass of the whole system, so if the gamma-ray energy is small enough, the recoil of the nucleus is too low to be transmitted as a phonon (vibration in the crystal lattice) making the recoil energy practically zero (recoil-free event). The relative number of recoil-free events (and hence the strength of the signal) is strongly dependent upon the gamma-ray energy and

so the Mössbauer effect is only detected in isotopes with very low lying excited states. Similarly the resolution is dependent upon the lifetime of the excited state. These two factors limit the number of isotopes that can be used successfully for Mössbauer spectroscopy. ^{57}Fe is the most commonly used isotope for Mössbauer spectroscopy, which has both a very low energy gamma-ray and long-lived excited state, matching both requirements well.

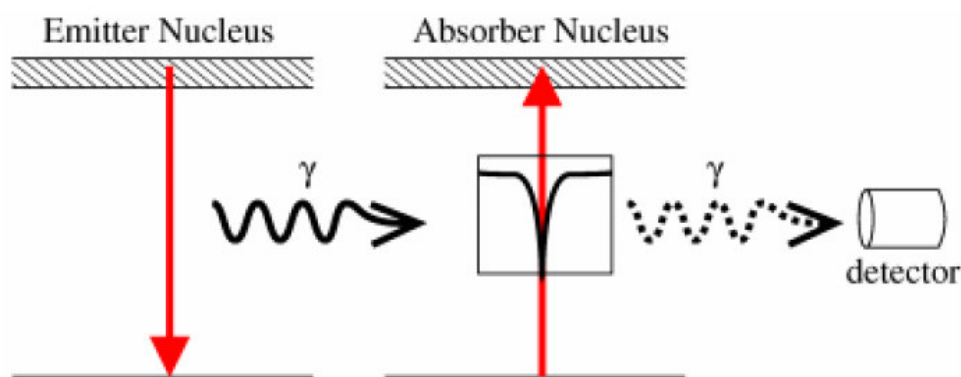


Fig. 2.8 Simple Mössbauer spectrum from identical source and absorber.

In the present thesis, ^{57}Co source embedded in the Rh matrix is used as a monochromatic source of γ -ray. Room temperature ^{57}Fe Mössbauer spectra were recorded using the 14.4 keV gamma ray energy, emitted from ^{57}Fe (produced from ^{57}Co by electron capture process), which is modulated by Doppler motion provided by constant acceleration mode. The spectrometer was calibrated with α -Fe and the isomer shift values given in this work are with respect to α -Fe. The experimental data were fitted by least square curve-fitting program.

2.7.1 Isomer shift

Basically, the isomer shift arises due to the difference in chemical environments of the emitting and absorbing nuclei. The isomer shift arises because of the non-zero volume of the nucleus, and the electron charge density of the s-electrons within it. This leads to a monopole (Coulomb) interaction, altering the nuclear energy levels. Thus any difference in the s-

electron environment between the source and absorber produces a shift in the resonance energy of the transition. The shift of the whole spectrum becomes positive or negative depending upon the s-electron density, and sets the centroid of the spectrum. As the shift cannot be measured directly it is quoted relative to a known absorber. For example, ^{57}Fe Mössbauer spectra will often be quoted relative to α -iron at room temperature. The isomer shift value is defined by the following equation:

$$IS = \delta = \frac{4\pi}{5} Ze^2 R^2 \frac{\Delta R}{R} \left[|\Psi(0)|_{abs}^2 - |\Psi(0)|_{sou}^2 \right]$$

Here Ze is the positive charge of the nucleus, the term $\Delta R/R$ is the fractional change in the nuclear charge radius on the excitation and ΔR is the difference in the radii of the nuclear excited and ground states.

The isomer shift is useful for determining valence states, ligand bonding states, electron shielding and the electron drawing power of electronegative groups. For example, the electron configurations for Fe^{2+} and Fe^{3+} are $(3d)^6$ and $(3d)^5$ respectively. The ferrous ions have less s-electron at the nucleus due to the greater screening of the d-electrons. Thus ferrous ions have larger positive isomer shifts than ferric ions. Intermetallic compounds, on hydriding, show an increased isomer shift. Even equivalent sites with different number of hydrogen neighbors and geometrical arrangements could be distinguished by their different IS values.

2.7.2 Quadrupole splitting

Nuclei in states with an angular momentum quantum number $I > 1/2$ have a non-spherical charge distribution. This produces a nuclear quadrupole moment. In the presence of an asymmetrical electric field (produced by an asymmetric electronic charge distribution or

ligand arrangement) the nuclear energy levels split. The charge distribution is characterised by a single quantity called the Electric Field Gradient (EFG).

In the case of an isotope with $I = 3/2$ excited state, such as ^{57}Fe or ^{119}Sn , the excited state is split into two substates $m_I = \pm 1/2$ and $m_I = \pm 3/2$. This is shown in Fig. 2.9, giving a two lines spectrum or 'doublet'. The extent of the splitting depends on the electron charge asymmetry. For ^{57}Fe the magnitude of the quadrupole splitting is given by

$$QS = \frac{1}{2}(e^2q_{zz}Q)(1 + \eta^2/3)^{\frac{1}{2}}$$

where q_{zz} is the principal component of the electric field gradient, η is asymmetry parameter $= (q_{zz} - q_{yy})/q_{zz}$. QS is highly sensitive function of charge state (high spin and low spin) as well as the nearest neighbor environment of the probe atom.

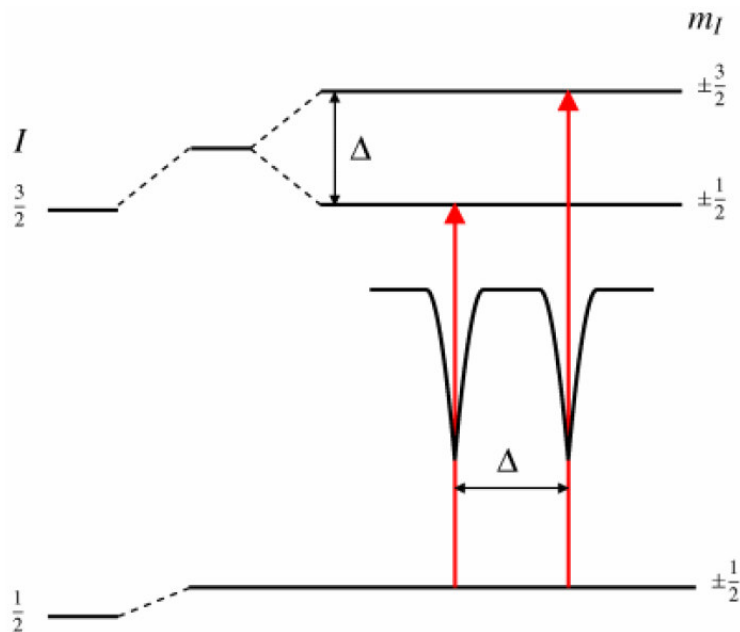


Fig. 2.9 *Quadrupole splitting for a 3/2 to 1/2 transition.*

2.7.3 Magnetic hyperfine interaction

In the presence of a magnetic field the nuclear spin moment experiences a dipolar interaction with the magnetic field which is called as Zeeman splitting. There are many sources of magnetic fields that can be experienced by the nucleus. The total effective magnetic field at the nucleus, H_{eff} is given by:

$$H_{\text{eff}} = (H_{\text{contact}} + H_{\text{orbital}} + H_{\text{dipolar}}) + B_{\text{applied}}$$

The first three terms are due to the atom's own partially filled electron shells. H_{contact} is due to the spin on those electrons polarising the spin density at the nucleus, H_{orbital} is due to the orbital moment on those electrons, and H_{dipolar} is the dipolar field due to the spin of those electrons.

This magnetic field removes the nuclear degeneracy and splits nuclear levels with a spin of I into $(2I+1)$ substates, so that the m_I levels have energies given by

$$E_{m_I} = -g_n \beta_n m_I H_{\text{eff}}$$

Where g_n is the electronic g factor or gyromagnetic ratio, β_n is the nuclear Bohr magneton and m_I is the component of nuclear spin I . Transitions between the excited state and ground state can only occur where m_I changes by 0 or 1. This gives six possible transitions for a $3/2$ to $1/2$ transition, giving a sextet as illustrated in Fig. 2.10, with the line spacing being proportional to H_{eff} .

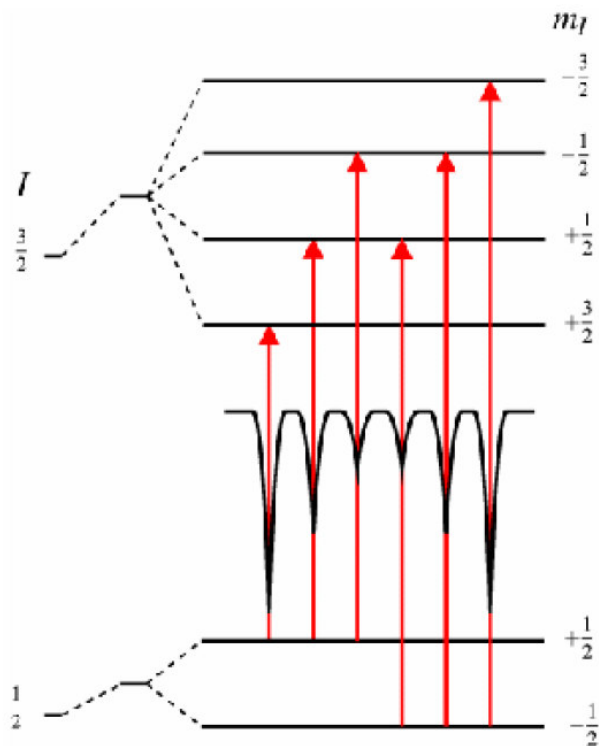


Fig. 2.10 *Magnetic splitting of the nuclear energy levels*

The line positions are related to the splitting of the energy levels, but the line intensities are related to the angle between the Mössbauer gamma-ray and the nuclear spin moment. Thus a purely polycrystalline Fe-metal gives a symmetric six line spectrum (sextet), with intensities in the ratio 3:2:1:1:2:3 and the line separation gives a measure of hyperfine field at the nucleus.

These interactions, Isomer Shift, Quadrupole Splitting and Magnetic Splitting, alone or in combination are the primary characteristics of many Mössbauer spectra.

2.8 Thermo Gravimetric Analyser (TGA)

In thermo gravimetric analysis the sample is heated at a constant heating rate and the sample weight is measured as function of temperature [128]. In this technique the heating can be done under air (oxidative) or nitrogen/argon (inert) atmosphere. This technique is quite

effective in hydrogen storage study as the desorption of hydrogen leads to the mass change which can be monitored during the temperature ramp, and from the temperature of the mass loss, the hydrogen desorption temperature can be estimated. In a properly calibrated instrument, the hydrogen storage capacity also can be estimated roughly by the amount of mass loss. Fig. 2.11 shows a simplified diagram of the thermogravimetric analyzer.

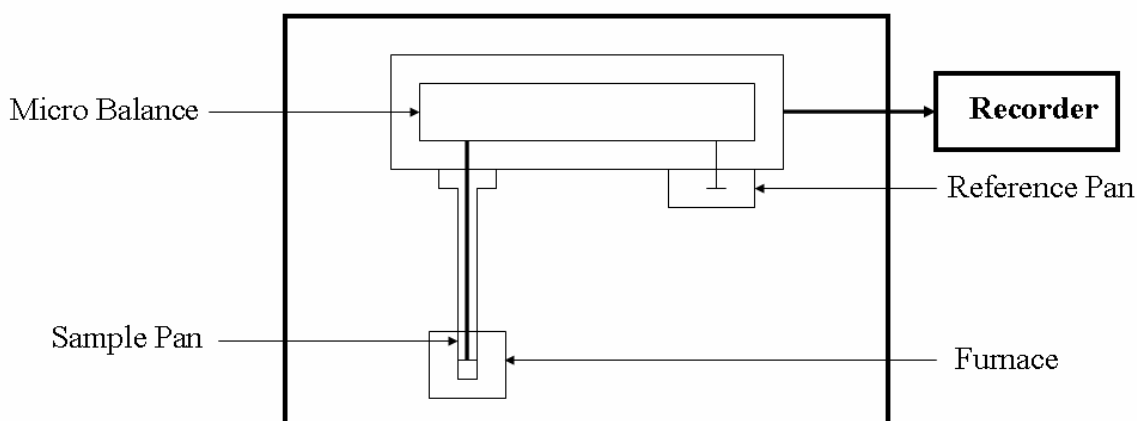


Fig. 2.11 *The simplified diagram of a TG apparatus*

The heart of the instrument is the micro-balance. During the measurement, the change in sample mass affects the equilibrium of the balance. This imbalance is fed back to a force coil, which generates additional electromagnetic force to recover equilibrium. The amount of additional electromagnetic force is proportional to the mass change. During the heating process the temperature may go as high as 1500 °C inside the furnace depending upon the configuration of the instrument.

2.9 Differential Thermal Analyser (DTA)

Differential Thermal Analysis measures the temperature difference between a sample and a reference material as a function of temperature, when they are heated or cooled at a constant heating rate [129]. Reaction or transition temperatures are then measured as a

function of the temperature difference between the sample and the reference. Any transition occurring in sample, which are associated with heat change can be monitored by this analysis. It provides vital information of the materials regarding their endothermic and exothermic behavior at high temperatures. As most of the hydrogen storage materials the hydrogen desorption reactions are highly endothermic in nature, so the desorption temperature can be determined from the DTA peak. The technique finds most of its applications in analyzing and characterising clay materials, ceramic, ores, etc.

2.10 Differential Scanning Calorimeter (DSC)

Differential scanning calorimetric technique is quite similar to DTA, except that, it is an isothermal measurement. It means that, during the measurement the sample and reference material are simultaneously heated or cooled at a constant rate just like DTA [129]. But here the amount of heat absorbed or released by a sample, to keep both the sample and reference at the same temperature is measured. In case of any exothermic/endothermic transition, the amount of heat flow from the system varies in order to keep both the sample and the reference at same temperature. The difference in temperature between them is proportional to the difference in heat flow (from the heating source i.e. furnace), between the two materials. This technique is applied to most of the polymers in evaluating the curing process of the thermoset materials as well as in determining the heat of melting and melting point of thermoplastic polymers, glass transition temperature (T_g), endothermic & exothermic behaviour. As desorption of hydrogen occurs with absorption of heat, so it can detected for the endothermic peak of DSC. The instrumentation of DSC [Fig. 2.12] is exactly similar to that of DTA, except for the difference in obtaining the result.

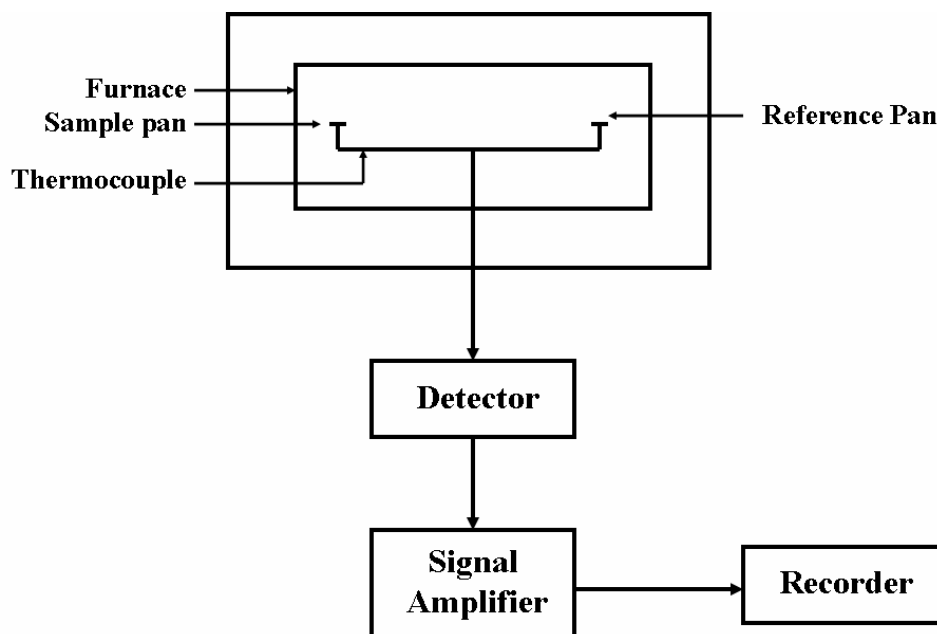


Fig. 2.12 *The schematic diagram of DTA/DSC*

2.11 Temperature Programmed Desorption (TPD)

When the hydride is heated at a constant heating rate, and the amount of hydrogen desorbed measured with respect to temperature, then it can be found that, the hydrogen desorption takes place at definite well defined temperature, depending on the site in which the hydrogen atoms are trapped. This particular method is known as Temperature Programmed Desorption (TPD) and is widely used for determining the H site occupancy [130]

The instrument used for TPD/TPR/TPO studies was TPDRO – 1100 of Thermoquest (Italy) make. Fig. 2.13 depicts a typical block diagram of the instrument used. This instrument is based on the in-flow method where analysis is carried at atmospheric pressure using continuous flow of inert or reactive gases. In a typical TPD experiment the sample is placed in a quartz reactor system that constitutes of two concentric tubes as shown in Fig. 2.13.

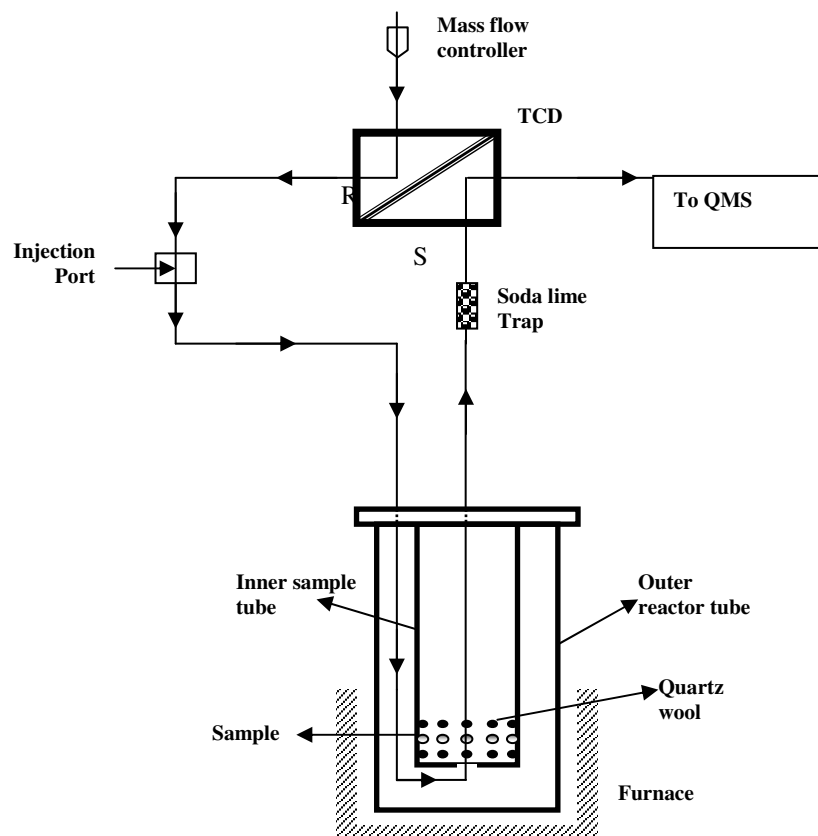


Fig. 2.13 Schematic for the TPDRO – 1100 instrument

Before start of actual analysis, the hydride sample is first preconditioned under argon flow, at room temperature for 40 minutes. The desorption profile is thereafter recorded by heating the sample at a fixed rate under the controlled flow of Argon. A thermal conductivity detector is employed to monitor the change in hydrogen concentration with time. Initially, as temperature is low for desorption to occur, a steady baseline is obtained. As the desorption process starts, the hydrogen concentration in effluent stream increases and this change is recorded by TCD. Any water vapor present in the system is removed from the flowing gas with the help of a soda lime trap placed just before the detector. Hence the signal obtained is primarily due to change in thermal conductivity of the hydrogen produced in the desorption process. As the desorption rate increases with increasing temperature the signal intensity also increases. Later on with the decrease in concentration of hydrogen the rate of desorption

decreases and so does the signal intensity. After completion of desorption of hydrogen from a particular site of the hydride the signal comes back to baseline despite of the high sample temperature. The sample is cooled after completion of the analysis. This dehydrided sample can be analysed by subsequent XRD analysis, in order to identify product. From this we can also ensure that after the hydrogen removal the alloy comes back to its original structure.

Effect of Substitution on Hydrogen Storage Properties of Ti-V-Fe System

Ti-V based alloys are considered as promising third generation hydrogen storage materials, as they have a great potential to replace the AB₅ alloys in the hydrogen compressor systems [25-38, 131]. V can form both monohydride (VH₋₁) and dihydride (VH₋₂). Though thermodynamical parameters for the conversion of the monohydride to dihydride are appropriate for room temperature hydrogen storage, but the stability of the monohydride is higher for the practical fuel cell application. As a result the reversible hydrogen storage capacity of V remains well below the theoretical value. Again the activation of the pure body centered cubic (bcc) V phase remains a problem. So by alloying with suitable materials, the bcc phase solid solution can be designed as an appropriate material for hydrogen storage. The most effective alloying element is found to be Ti, as both Ti & V can absorb large amount of hydrogen. The maximum hydrogen content of Ti and V are found to be 3.78 and 3.54 wt. % respectively. Though Ti has an hcp structure at room temperature, it can form bcc structure by the addition of small amount of bcc forming elements, such as, V, Fe or Mn. Ti and V can form solid solutions at all proportions. The physical factors for formation of substitutional solid solution are guided by Hume –Rothery rule [132]. According to that, the atomic size of

the two elements should not differ more than 15 % and they should have similar crystal structure. Their electro negativity difference should not be very high, because it is likely that in such cases they prefer to form a stable structure than continuous solid solution. The most advantageous factor of V based solid solution is that in almost all the cases the solid solutions react with hydrogen without disproportionation [27] and after reaction with hydrogen they form single phase face centered cubic (fcc) lattice structure.

The different hydrogen absorption sites of bcc phase solid solutions can be explained from the crystal structure. When hydrogen interacts, then three types of hydrides, with three different structures, can be formed. When the H/M ratio is less than 0.5 then the hydride shows bcc structure with slightly extended lattice parameter than the parent alloy. But with increase in the amount of hydrogen the structure of the hydride changes. The mono hydrides form pseudo face centered cubic (fcc) lattice, where the metal atoms occupy the fcc sites and the hydrogen atoms occupy the octahedral holes. The saturated dihydride shows a fluorite type of structure, where the metal atoms occupy the fcc sites and the hydrogen atoms occupy the tetrahedral holes. Fig. 3.1 shows the crystal structures of the mono hydride and the dihydride indicating different tetrahedral and octahedral holes.

The transformation of the bcc alloy towards the fcc hydride [Fig. 3.2] can be explained assuming that the arrangement of metals does not changed during hydrogenation even though anisotropic volume expansion there. As shown in the figure the direction of $[100]$ in bcc crystal corresponds to the direction $[\bar{1}10]$ of the fcc crystal.

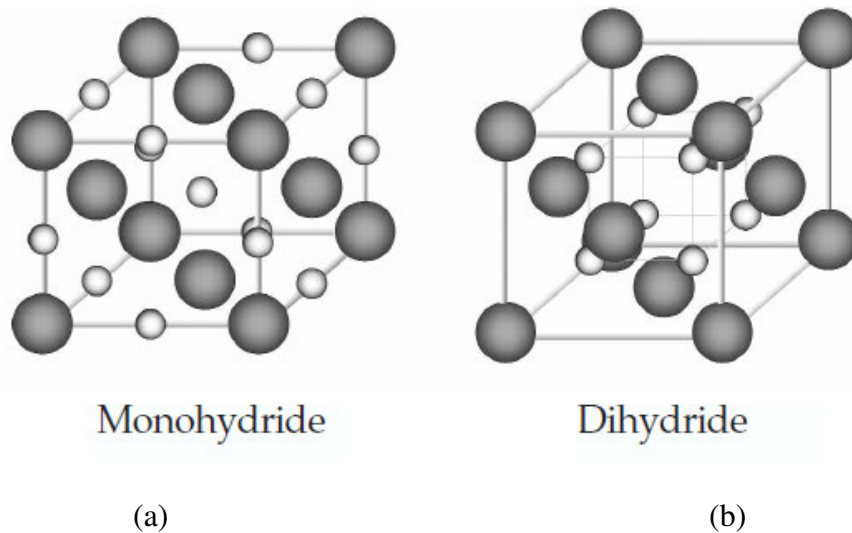


Fig. 3.1 The structure of (a) the monohydride (hydrogen atoms occupying the octahedral sites) and (b) the dihydride (hydrogen atoms occupying the tetrahedral sites). The larger spheres represent the metal atoms and the smaller spheres represent the hydrogen atom.

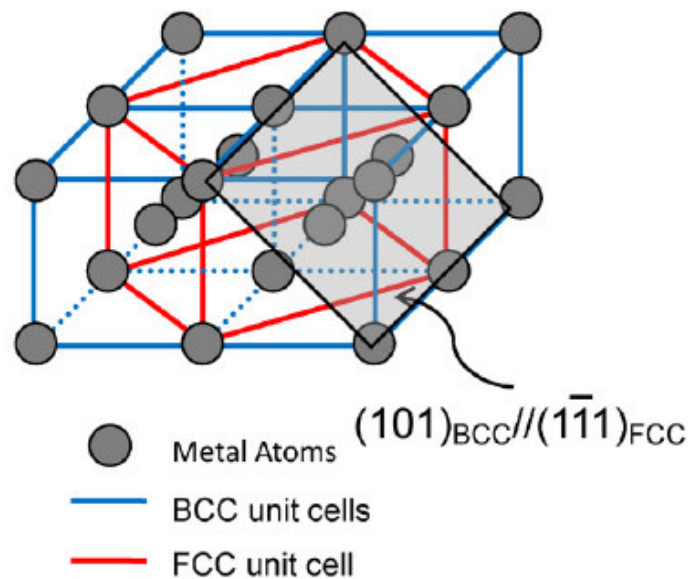


Fig. 3.2 Transformation of the bcc alloy structure towards the fcc hydride structure.

Due to large number of available interstitial sites, the hydrogen absorption capacity of the bcc phase alloys are usually better than the conventional AB_2 types of Laves phase alloy. Though they show quite high hydrogen absorption capacities, but Ti-V based bcc solid solution suffer from certain disadvantages towards practical application. The alloys need rigorous activation prior to hydrogen absorption, the kinetics of hydrogen absorption is not

satisfactory, and they need high desorption temperature for the complete desorption of the stored hydrogen. As both the Ti and V hydrides are quite stable, the enthalpy of dihydride formation has relatively high values compared to those of LaNi₅ hydrides. As a result, the alloys have flexibility in the choice of their thermodynamic properties through modification of the alloy composition. Substitution of a small amount of a transition element like Fe, Co, Ni, Mn or Cr changes the hydrogen absorption characteristics of Ti-V system very drastically [25-38, 131-151]. Nomura *et. al.* has reported the hydrogen absorbing properties of the Ti-V-Fe system, and found that a bcc alloy with a composition of Ti_{0.435}V_{0.490}Fe_{0.075} absorbed a large amount of hydrogen (3.9 wt. % at 252 K) indicating that that proper amount of Fe substitution for part of Ti can improve the hydrogen storage properties and the kinetics of hydrogen absorption [27]. One of the highest value of the hydrogen storage capacity reported so far at room temperature is 4.2 wt. % in the bcc single phase Ti-40V-10Cr-10Mn alloy [137]. The hydrogen storage capacity of Ti-V-Cr was found to improve with the substitution of Ti by Zr, though it increases the slope of the P-C isotherm [135]. From the hydrogen absorption studies in Ti-V-M (M = Fe, Mn, Co, Cr, Ni) alloys it was found that Laves phase related bcc solid solutions show a flat plateau, fast kinetics and easiness in activation [5]. Ti_{0.70}V_{0.30}-10 at. %M (M = Fe, Mn, Co, Cr, Ni) alloys react with hydrogen at room temperature without any heat treatment can absorb hydrogen just after evacuation in the apparatus consisting of glass components [148]. The results from the studies gives a new way to find a novel hydrogen absorbing phase by studying the constituent phases in multiphase alloys which desorbs hydrogen under ambient conditions. In general, substitution leads to an easy activation of the material, while the hydrogen storage capacity is reduced. Substitution of Ti or V with elements like Zr, Cr, Fe or Mn often results in the formation of a secondary phase, which is identified to be a C14 Laves phase and the coexistence of Laves phase makes the activation procedure easier as compared to pure bcc phase [138]. Zr substitution is

reported to improve the hydrogen absorption properties of Ti-V alloys by improving the grain boundary network of C14 Laves phase [131]. Hang *et. al.* [34] has found for $Ti_{10}V_{84-x}Fe_6Zr_x$ ($x = \frac{1}{4} 1, 2, 4, 6, 8$) alloys, the ratio of the secondary phase (C14 laves phase) increases with increasing Zr content. They also found that, as the Zr content in the alloy increases, the activation behavior is improved, but the hydrogen absorption and desorption capacities decrease gradually.

In the present chapter we report our systematic approach towards the improvement of hydrogen storage properties of Ti-V solid solution. In the first section we will discuss the experimental parameters for the preparation of alloys, hydrides and the characterizations. The hydrogenation and dehydrogenation conditions also will be discussed for the particular experiments. In the next section we will give the interesting results we got during our present study and will discuss our results accordingly. In the last section of the chapter we will conclude our experimental findings.

3.1 Experimental Details

The alloys were prepared by arc melting the high purity elements (99.9%) in a water-cooled copper hearth under argon atmosphere. The buttons were remelted several times to ensure homogeneity. The crystal structures of the alloys were examined by X-ray diffraction (XRD) using monochromatic CuK_{α} radiation.

X-ray Microanalyses of the representative alloys were done using Electron Probe Micro-Analyser (EPMA, CAMECA SX-100 model). For analysis, the alloys were mounted in resin, ground with different grades of emery paper and polished on lapping wheel with diamond paste of 0.25 μm grain size. An acceleration voltage of 20 kV and stabilized beam current of 4 nA and 20 nA were used for ‘back scattered electron (BSE)’ and quantitative/qualitative analysis, respectively. The beam size was kept at $< 1 \mu m$ to reduce

the convolution effect so as to arrive at good compositional estimates. Raw intensity data were corrected for atomic numbers, absorption and fluorescence using the PAP (Pouchou and Pichoir) procedure [152].

Hydriding was carried out using a standard Sieverts type set up discussed in Chapter II. The activation procedure involved heating the sample under diffusion vacuum (10^{-6} mbar) for 2 hours at 673 K. After activation, the sample was cooled to the working temperature under vacuum, followed by introduction of hydrogen gas into the reaction chamber. Pressure-composition isotherms were studied in the temperature range 298-523 K and up to a hydrogen pressure of 2 MPa, using freshly crushed samples. The surface poisoning of the hydride samples were done by air exposure at liquid nitrogen temperature. The deuterides of selected alloys were prepared following the same procedure as described above.

Some of the compositions were hydrogenated without any activation treatment. This procedure involved degassing of the freshly crushed alloy particles under high vacuum (10^{-6} mbar) for 1 hour followed by introduction of hydrogen gas into the chamber.

The kinetic study was done at room temperature and a hydrogen pressure of 20 atm. after one absorption-desorption cycle.

^{57}Fe Mössbauer spectra were recorded using $^{57}\text{Co}(\text{Rh})$ source in a conventional spectrometer working in constant acceleration mode. The spectrometer was calibrated with α -Fe and the isomer shift values given in this work are with respect to α -Fe. The experimental data were fitted by least square curve-fitting program.

The amount of total hydrogen/deuterium in the hydrides was estimated by monitoring the change in the hydrogen/deuterium pressure during the absorption process. The saturation composition was also determined by complete decomposition of a small amount of the hydride sample in an evacuated and calibrated chamber as discussed in Chapter II.

The temperature programmed desorption (TPD) measurements were done using an automated TPD instrument up to 1073 K, at a constant heating rate of 10 K/min. High purity argon was used as the carrier gas.

Electrochemical measurements were carried out using Potentiostat/galvanostat (PGSTAT20, Echochemie, Netherlands) attached with frequency response analyzer (FRA). The alloy button cut into plate shape was used as working electrode, Ag/AgCl as the reference electrode and platinum wire mesh as the counter electrode. 6 M KOH solution was used as electrolyte. Impedance measurements were carried out using a sinusoidal *ac* excitation signal with peak to peak amplitude of 10 mV and frequency in the range 0.1 Hz to 100 kHz.

3.2 Results and Discussion

The section deals with the results & discussion part of the Ti-V-Fe alloys which has been studied during the present thesis. Based on the alloys composition this section has been divided in three parts and discussed separately. This part of the work is organized as follows. In the first part the findings on $\text{Ti}_{1-x}\text{VFe}_x$ ($x = 0.1, 0.15, 0.2, 0.4$) and Ti-V-Fe-Cr alloys are discussed. Here the effect of different amounts of Fe substitution on Ti-V alloy is depicted. The effect of Cr substitution on selected Ti-V-Fe alloys is presented also. In the second part the hydrogen storage characteristics of Zr Substituted $\text{Ti}_{0.85}\text{VFe}_{0.15}$ alloy is discussed and the effect of Zr on the structural and hydrogen storage properties has been reported. In the third part of the effect of Ce substitution on the hydrogen storage and electrochemical properties of the $\text{Ti}_{0.85}\text{VFe}_{0.15}$ alloy has been presented. In the remaining portion of the section will be discussed separately with the exact work plan.

3.2.1 Hydrogen storage properties of $\text{Ti}_{1-x}\text{VFe}_x$ ($x = 0.1, 0.15, 0.2, 0.4$) and Ti-V-Fe-Cr alloys

In this part of the work, we report the hydrogen absorption properties of Ti-V alloys with 10, 15, 20 and 40 at. % of Fe substitution for Ti. The alloys have been characterized for the crystal structure and the pressure composition isotherm, kinetics of hydrogen absorption, hydrogen storage properties and the hydrogen desorption are studied in detail. Again, the expensive vanadium metal is partially substituted with less expensive Cr metal, in order to study the effect of Cr substitution on the hydrogen absorption properties and the activation treatment. The following two compositions, $\text{Ti}_{0.85}\text{VFe}_{0.15}$ and $\text{Ti}_{0.8}\text{VFe}_{0.2}$ have been substituted with Cr (60 at. %) in place of V forming two new compositions, $\text{Ti}_{0.85}\text{V}_{0.4}\text{Fe}_{0.15}\text{Cr}_{0.6}$ and $\text{Ti}_{0.8}\text{V}_{0.4}\text{Fe}_{0.2}\text{Cr}_{0.6}$ respectively.

3.2.1.1 The structural aspects of the alloys and the hydrides

3.2.1.1.1 X-ray diffraction

The XRD patterns of the compositions $\text{Ti}_{0.9}\text{VFe}_{0.1}$ and $\text{Ti}_{0.85}\text{VFe}_{0.15}$ and their corresponding hydrides are shown in Fig 3.3. From the XRD data we found that, except $\text{Ti}_{0.85}\text{VFe}_{0.15}$, all the other Ti-V-Fe compositions show a mixed structure composed of a body centered cubic (bcc) phase and a secondary C14 Laves phase, with bcc as the major phase. The nature of the secondary phase has been examined by the earlier researchers also using XRD and scanning electron microscope techniques [138, 139]. The lattice parameters of the secondary phase for $\text{Ti}_{0.9}\text{VFe}_{0.1}$ alloy in the present study are found to be $a = 5.10 \text{ \AA}$ and $c = 7.78 \text{ \AA}$. The composition, $\text{Ti}_{0.85}\text{VFe}_{0.15}$ contains mainly the bcc phase. The X-ray diffraction studies have been done on $\text{Ti}_{0.85}\text{V}_{0.4}\text{Fe}_{0.15}\text{Cr}_{0.6}$ and $\text{Ti}_{0.8}\text{V}_{0.4}\text{Fe}_{0.2}\text{Cr}_{0.6}$ shows the presence of a secondary C14 hexagonal Laves phase along with the bcc phase. The secondary phase is indexed on the basis of C14 Laves phase for $\text{Ti}_{0.85}\text{V}_{0.4}\text{Fe}_{0.15}\text{Cr}_{0.6}$ alloy and the corresponding

lattice parameters are found to be $a = 6.850 \text{ \AA}$ and $c = 7.616 \text{ \AA}$. To see the effect on annealing on the secondary phase we have annealed $\text{Ti}_{0.9}\text{VFe}_{0.1}$ alloy for 9 days at 900C in vacuum sealed quartz tube. It has been observed that after annealing the bcc phase increases for $\text{Ti}_{0.9}\text{VFe}_{0.1}$ alloy. Though in case of Cr containing samples, there is not much effect of annealing on the secondary phase. The lattice parameters for the various $\text{Ti}_{1-x}\text{VFe}_x$ alloys are listed in Table 3.1.

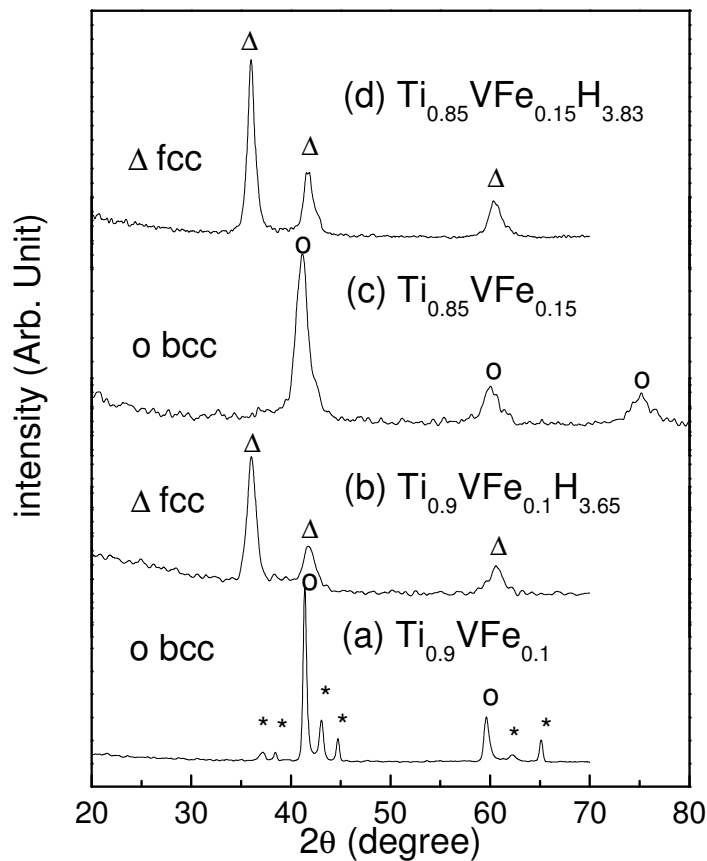


Fig. 3.3 X-ray diffraction patterns for (a) $\text{Ti}_{0.9}\text{VFe}_{0.1}$ (b) $\text{Ti}_{0.9}\text{VFe}_{0.1}\text{H}_{3.65}$ (c) $\text{Ti}_{0.85}\text{VFe}_{0.15}$ and (d) $\text{Ti}_{0.85}\text{VFe}_{0.15}\text{H}_{3.83}$ (The lines corresponding to the secondary phase are marked by ‘*’.)

Table 3.1 Lattice parameters and the total hydrogen storage capacities of $Ti_{1-x}VFe_x$ alloys

Alloy composition	Bcc phase lattice parameter (Å)	Hydrogen/Formula unit	Total hydrogen storage capacity (wt. %)
TiV	3.12	2.92	2.86
Ti_{0.9}VFe_{0.1}	3.10	3.65	3.53
Ti_{0.85}VFe_{0.15}	3.09	3.83	3.7
Ti_{0.8}VFe_{0.2}	3.01	2.5	2.42
Ti_{0.6}VFe_{0.4}	3.00	2.26	2.01

From the table it can be stated that the lattice parameter of the bcc phase decreases with increasing Fe content. This due to the smaller atomic radius of Fe as compared to that of Ti and V (Ti: 1.47 Å, V: 1.34 Å, Fe: 1.26 Å). Similar trend has been observed by other experimentalists also [27, 28]. In the present case, the lattice parameter decreases from 3.098 Å to 3.086 Å as the Fe content increases from 10 at. % to 15 at. %. This change is in accordance with the Vegard's law which states that for substitutional solid solution the change in unit cell dimension is be linear with the change in composition. The structure of the corresponding hydrides are found to be face centered cubic (fcc) and the lines corresponding to the secondary phase are not seen in the X-ray diffraction patterns of the hydrides. After the hydrogenation all the metals go in the powder form due to fact that bcc structure of the alloy transforms into a new fcc structure with an increase in the internal stress. As the hydriding takes place at room temperature so it can not reveal the internal stress so crack formation occurs and eventually with cycling the hydride goes into powder form.

3.2.1.1.2 Electron probe micro analysis

Fig. 3.4 shows the electron probe X-ray micrographs of $Ti_{0.9}VFe_{0.1}$, $Ti_{0.85}VFe_{0.15}$, $Ti_{0.8}VFe_{0.2}$ and $Ti_{0.6}VFe_{0.4}$ alloys. $Ti_{0.85}VFe_{0.15}$ alloy shows a single phase bcc structure in the

EPMA analysis. For all the other alloys the X-ray micrographs clearly indicate a mixed phase structure and the proportion of the secondary phase varies with the alloy composition.

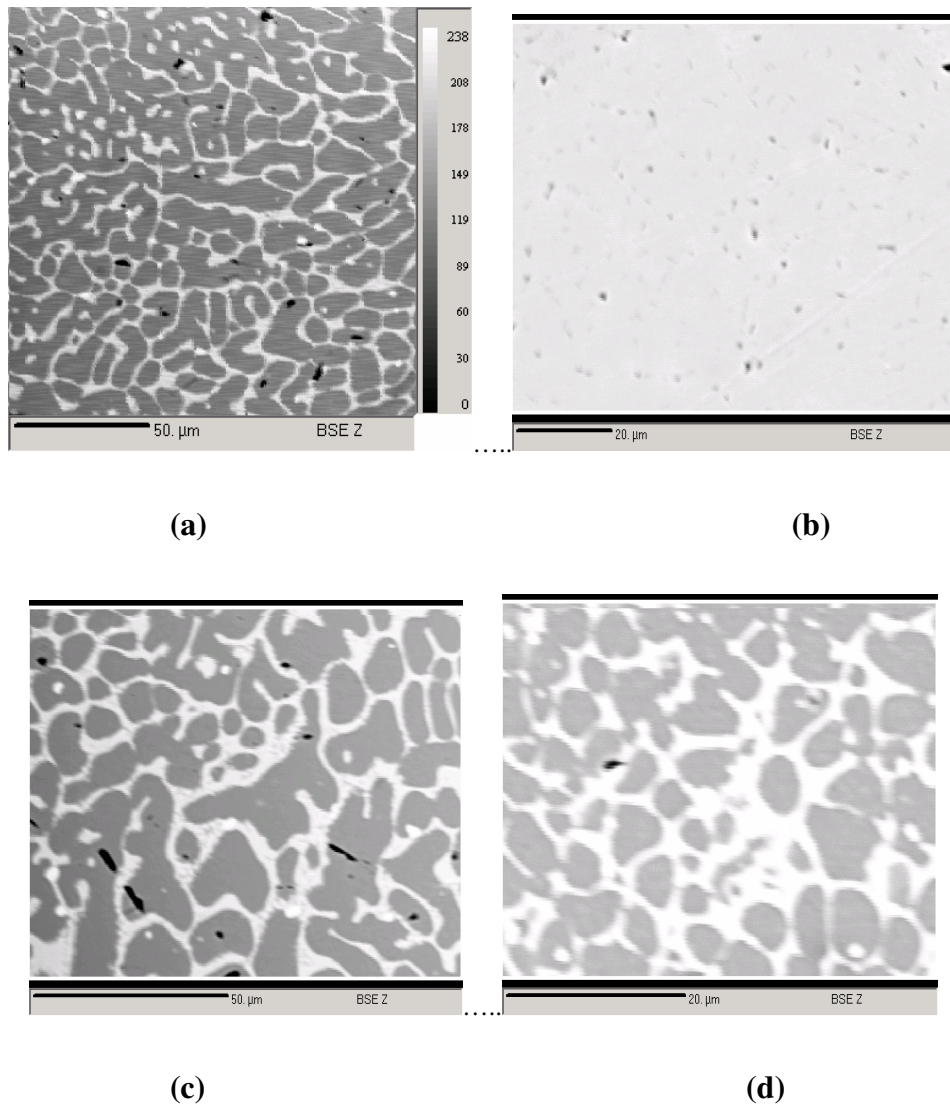
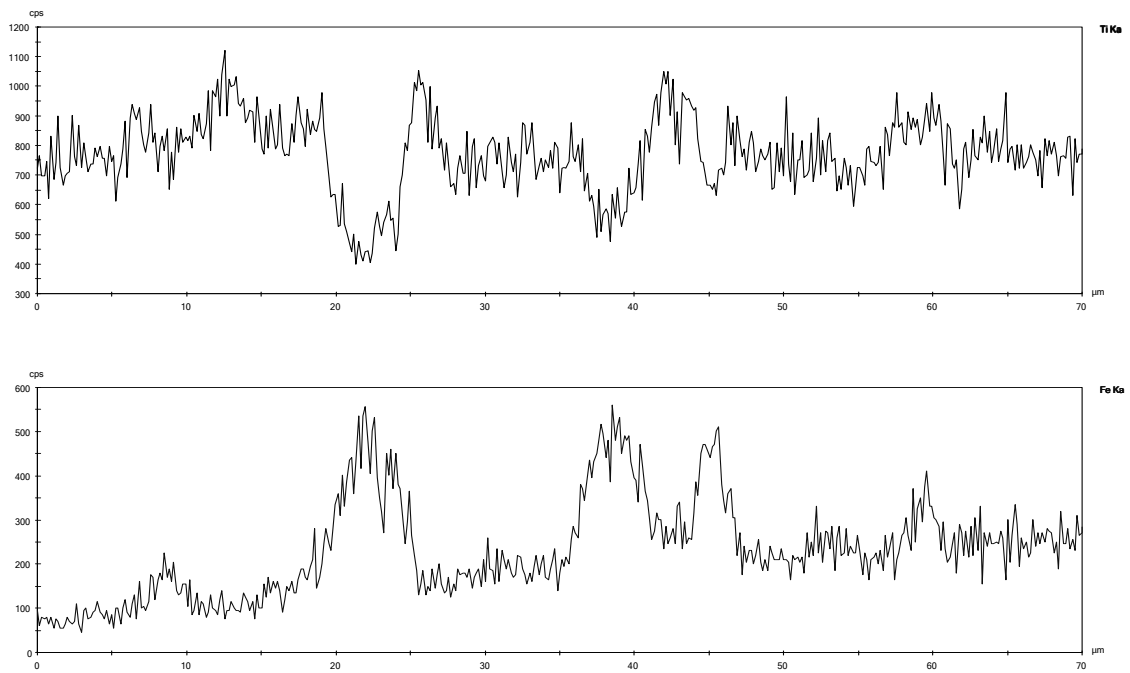


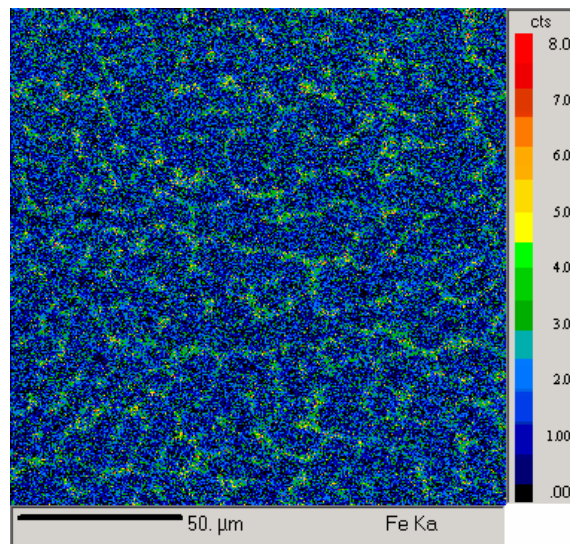
Fig. 3.4 Electron micrographs for (a) $Ti_{0.9}VFe_{0.1}$ and (b) $Ti_{0.85}VFe_{0.15}$ (c) $Ti_{0.8}VFe_{0.2}$ and (d) $Ti_{0.6}VFe_{0.4}$ alloys

The composition of two phases analyzed by EPMA shows that the Fe substitutes some of the Ti atoms forming the Fe substituted Ti-V alloys. This becomes apparent from the Ti $K\alpha$ and Fe $K\alpha$ X-ray line profiles [Fig. 3.5]. Wave-length dispersed X-ray line spectra obtained from each of the phases indicate that both the bright phase and light phases are essentially constituted of Ti, V and Fe where as the Fe content of the secondary phase is

larger than that of the bcc phase. This can also be confirmed by the micro elemental analysis of $Ti_{0.9}VFe_{0.1}$ alloy which clearly shows larger concentration of Fe in the secondary phase.



(a)



(b)

Fig. 3.5 (a) *Ti Kα* and *Fe Kα* X-ray line profiles of $Ti_{0.9}VFe_{0.1}$ alloys (b) Electron micrographs for $Ti_{0.9}VFe_{0.1}$ alloys showing the relative concentrations of Fe metal in the bcc and secondary phase.

3.2.1.2 The hydrogen absorption behavior of Ti-V-Fe alloys

Hydrogen absorption desorption behavior of any alloy is characterized by the pressure composition isotherm (PCT) diagram. The pressure-composition absorption curves for $Ti_{1-x}VFe_x$ ($x = 0.0, 0.1, 0.15, 0.20$ and 0.40) alloys at room temperature are shown in Fig. 3.6.

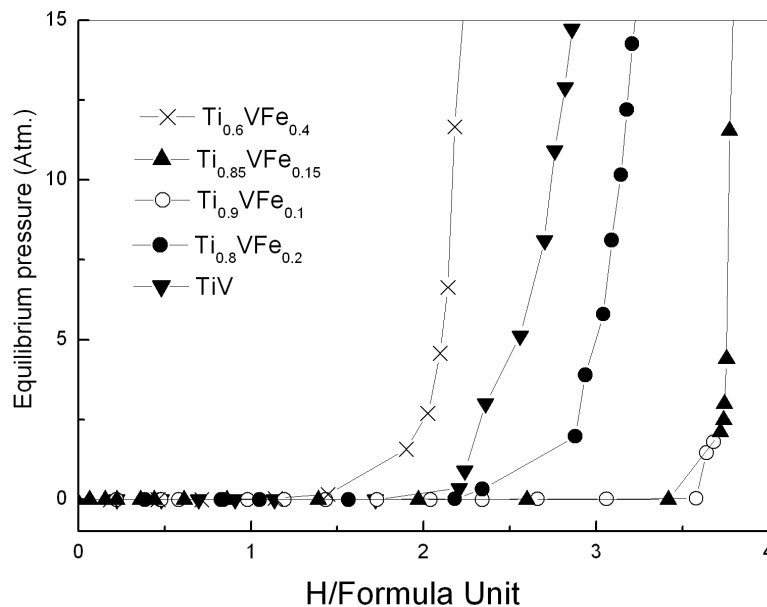


Fig. 3.6 Pressure-composition absorption curves for $Ti_{1-x}VFe_x$ ($x = 0, 0.1, 0.15, 0.2$ and 0.4) alloys at room temperature

For all the above compositions, the plateau regions are found to be flat with a plateau pressure <0.02 atm., which is the lowest detection limit in our set up. The two-plateau regions observed in some earlier studies on Ti-V-Cr-Mn systems [138, 139], are not observed for any of our systems within the pressure ranges studied. The pressure composition isotherms of all the alloys have been studied at different temperature as shown in Fig. 3.7. With increase in temperature, the plateau region decreases for all the alloys, but the increase in the absorption plateau pressure is still lower than the detection limit of our instrument.

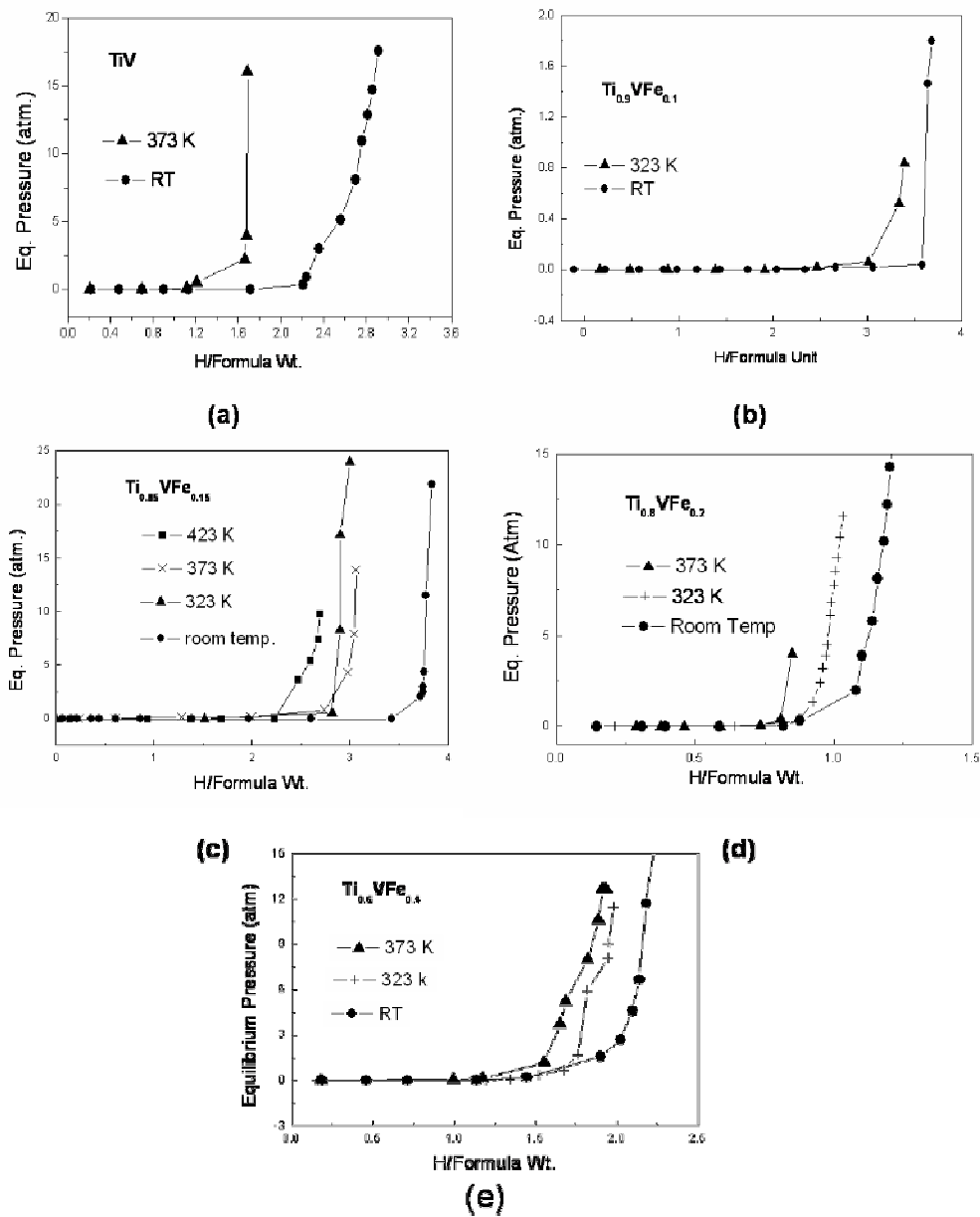


Fig. 3.7 Pressure-composition absorption curves for $Ti_{1-x}VFe_x$ ($x = 0, 0.1, 0.15, 0.2$ and 0.4) alloys at different temperatures.

It may be seen from the figure that with increase in temperature, the plateau region decreases and the absorption/desorption plateau pressure is quite low even at 523 K. The hydrogen absorption kinetics of all the alloys was studied at room temperature and 20 atm. hydrogen pressure after one hydrogen absorption desorption cycle. It has been found that the

kinetics of hydrogen absorption is quite fast and the equilibrium is reached within 5 minutes in each step.

The hydrogen storage capacities of $Ti_{1-x}VFe_x$ alloys as a function of Fe content, x , are plotted in Fig. 3.8.

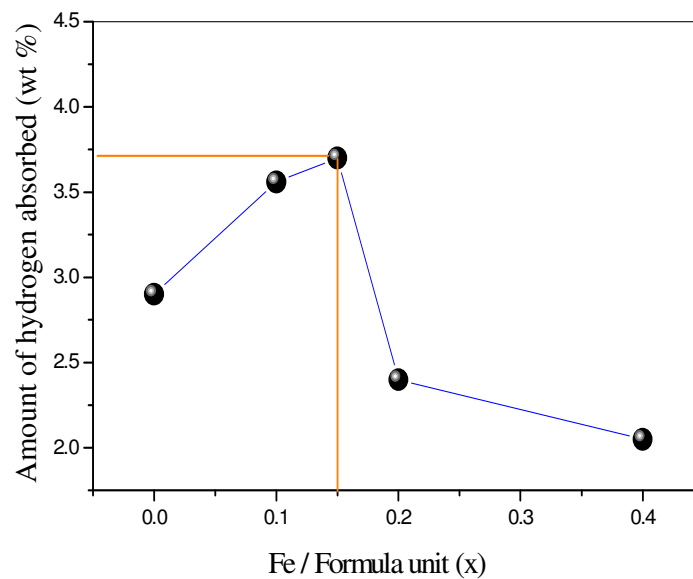


Fig. 3.8 Variation of hydrogen absorption capacity with respect to the Fe content in $Ti_{1-x}VFe_x$ alloys ($x = 0.0, 0.1, 0.15, 0.2$ and 0.4).

From the figure it can be found that the hydrogen storage capacity of $Ti_{1-x}VFe_x$ increases steadily with Fe content up to $x = 0.15$. Further increase in the Fe content brings down the hydrogen storage capacity drastically. The hydrogen storage capacity of the Ti-V-Fe series under investigation can be strongly correlated with the structures of the parent alloys. At higher Fe concentrations, the bcc phase is found to coexist with the secondary phase. The bcc phase in Ti-V system is reported to absorb more hydrogen than the secondary phase [12] due to less packing density of bcc phase. The composition $Ti_{0.85}VFe_{0.15}$ is found to have only the bcc structure for the as cast alloy, and it has the maximum storage capacity of 3.7 wt. % among the various Ti-V-Fe compositions studied in this work.

It is interesting to note that with increasing Fe content the process of activation becomes easier. The alloys $Ti_{0.8}VFe_{0.2}$ and $Ti_{0.6}VFe_{0.4}$ absorb hydrogen without any high temperature activation treatment, involving the heating of the samples at 673 K for 2 hours under high vacuum. It may be noted at this point that, due to the presence of secondary phase the crack formation at the surface becomes easier. As a result, before hydrogen absorption these samples require lesser activation. The bcc phase alloys are much harder and more hardly pulverized than the C14 Laves phase alloys. In Laves phase alloys, the cracking occurs easily resulting in the exposure of new fresh surface in the hydrogen atmosphere. As a result more hydrogen can penetrate into the alloy through the newly formed alloy surface and the lattice expansion due to hydrogenation of the alloy enhances further cracking. In this way the alloys get activate quite easily. However, in our case for $Ti_{0.8}VFe_{0.2}$ and $Ti_{0.6}VFe_{0.4}$ alloys the absorption requires the application of a higher H_2 pressure ~ 0.8 MPa and an incubation time of 1 hour is observed. Their storage capacities are found to be 2.42 wt. % and 2.01 wt. %, respectively. We also found that the annealed samples have a relatively slow hydrogen pick up as compared to the as cast material, which directly prove the positive effect of secondary phase on the activation treatment of the alloy before hydrogen absorption. Various works in the literature also have shown that the presence of a secondary phase makes hydriding of this system easier [34].

We have substituted less expensive Cr in place of V for $Ti_{0.8}VFe_{0.2}$ and $Ti_{0.6}VFe_{0.4}$ and established its effect on the hydrogen absorption capacities and the activation treatment. The hydrogen storage capacities for $Ti_{0.85}V_{0.4}Fe_{0.15}Cr_{0.6}$ and $Ti_{0.8}V_{0.4}Fe_{0.2}Cr_{0.6}$ are found to be 2.01 wt. % and 1.51 wt. %, respectively. The pressure composition diagrams are shown in Fig. 3.9.

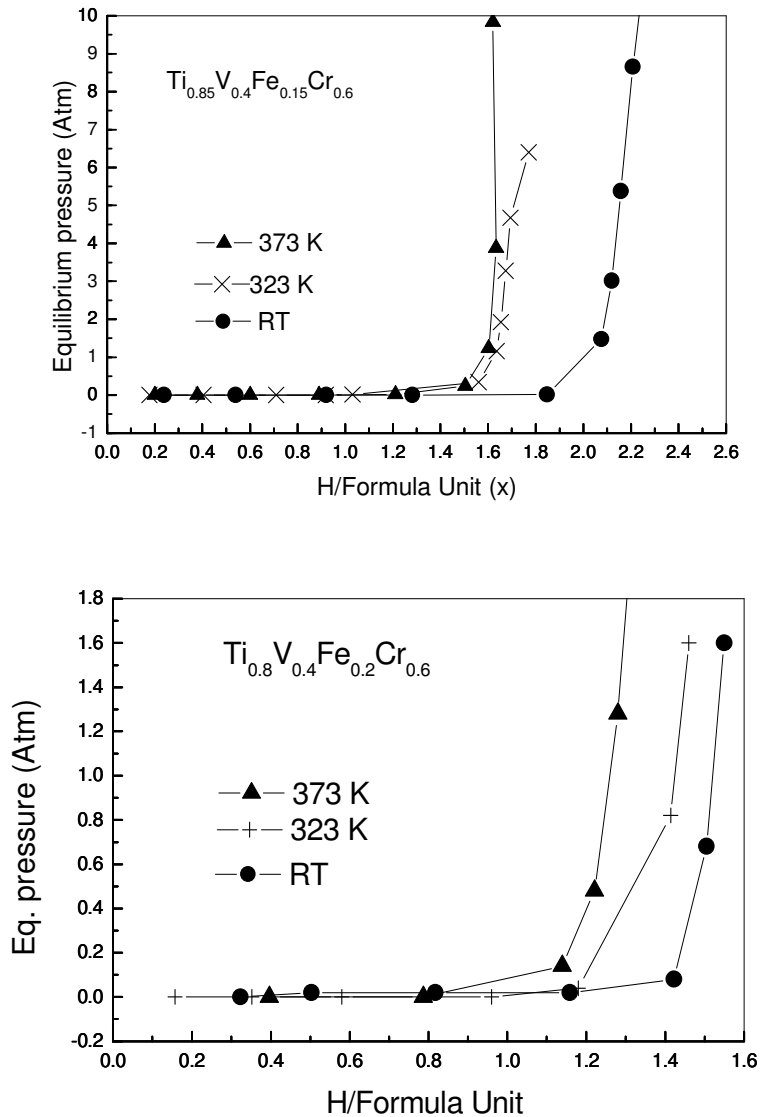


Fig. 3.9 Pressure-composition diagram of $Ti_{0.85}V_{0.4}Fe_{0.15}Cr_{0.6}$ and $Ti_{0.8}V_{0.4}Fe_{0.2}Cr_{0.6}$ alloy at room temperature, 323 K and 373 K.

We find that the storage capacity decreases with increasing Cr concentration but there is no observable change in the absorption plateau pressure up to 423 K. Among the two compositions, $Ti_{0.8}V_{0.4}Fe_{0.2}Cr_{0.6}$ is found to absorb hydrogen without any prior activation. In this case, the freshly crushed coarse alloy powder is degassed for one hour to remove the adsorbed gases and then hydrogen is introduced into the reaction chamber. The absorption of

hydrogen without activation takes place at a hydrogen pressure as low as 0.02 MPa, unlike the Cr free composition $Ti_{0.8}VFe_{0.2}$, which requires the application of a higher hydrogen pressure of 0.8 MPa. The initial absorption is quite fast for Cr substituted sample and within one hour it reaches its maximum hydrogen storage capacity of 1.51 wt. %.

3.2.1.3 Desorption characteristics of the alloys

To compare the stabilities of different hydride temperature programmed desorption profile has been studied in an automated TPD instrument. The experiments were carried out with the air poisoned hydride because of the limitations of the home made Sievert's setup. Though the air poisoned hydrides show some what higher desorption temperature due to the oxide layer on the surface, still it gives quite good comparison about the stability of the hydrides from the desorption peak temperature. In temperature programmed desorption more than one peak can be obtained due to different reasons. If the alloy shows multiphase structure, then depending upon the relative stabilities of the different hydride phases, hydrogen can desorb at different temperatures. Again in a single phase alloys also, the absorbed hydrogen atoms can occupy different interstitial sites with different potential energies, which again results in the multiple peak in the TPD profile. It can be mentioned at this point that, with increase in the heating rate the peak position shifts. Subsequently always it is more fundamental to compare between the desorption onset temperatures than the peak temperatures for different hydrides. But in the present case the heating rate is kept constant, so we can compare between the desorption peak temperature of different hydrides. As an example, a comparison between the TPD profiles of $Ti_{0.9}VFe_{0.1}H_{3.65}$ and $Ti_{0.8}VFe_{0.2}H_{2.5}$ reveal that, with increasing Fe concentration, the hydrogen desorption temperature decreases as shown in Fig. 3.10, which in turns reflects the relative stabilities of the hydrides. This may be attributed to the fact that with increasing Fe concentration the relative stability of the hydride decreases and hence the hydrogen desorption takes place at a lower temperature. As Fe is

more electronegative element than the Ti and V so it forms much unstable hydrides and as a result with the doping of Fe in the Ti-V system the relative stability of the hydride decreases. It may be recalled that FeTi is a reversible hydride at room temperature.

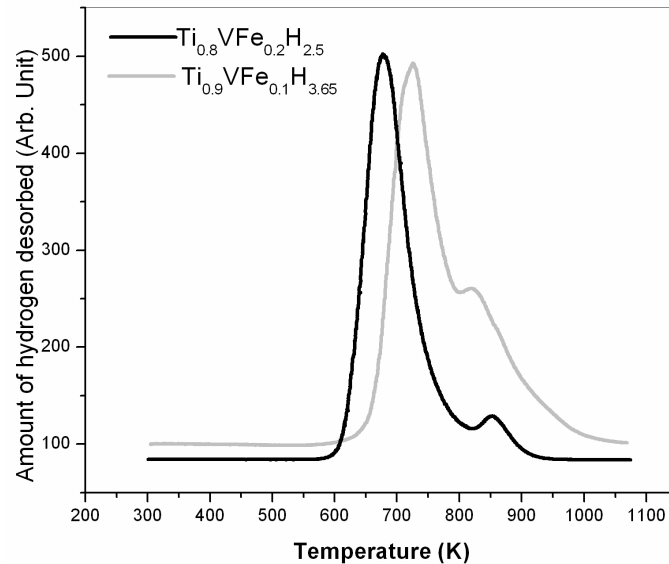


Fig. 3.10 Thermal desorption profiles of (a) $Ti_{0.8}VFe_{0.2}H_{2.5}$ (b) $Ti_{0.9}VFe_{0.1}H_{3.65}$.

Most of the metal hydride systems exhibit normal *isotope effect* at room temperature, where the protide is more stable than their corresponding deuteride. As a rule, at sufficiently low temperatures, a deuteride will be more stable than the corresponding hydride [13, 153]. After a certain cross over temperature, the hydride becomes more stable. If for a certain alloy, the cross over temperature is higher than the room temperature then at the room temperature it shows inverse isotope effect. In the case of commercial V metal, the crossover point is calculated to be 410 K [153] and because of this fact many of the Vanadium based alloys are reported to exhibit inverse isotope effect at lower temperature [153], where the deuteride and tritide form more stable compound (i.e. compound having lower dissociation pressure at room temperature) than the corresponding hydride. In general, the isotopic effect is indicated by the ratio of the dissociation pressure of the deuteride to that of the hydride. In the present work, in order to compare the stability of the hydride vis-à-vis. the deuteride, TPD studies

have been carried out on the hydride as well as the deuteride of $\text{Ti}_{0.9}\text{VFe}_{0.1}$ alloy. The TPD profiles for $\text{Ti}_{0.9}\text{VFe}_{0.1}\text{H}_{3.65}$ and the corresponding deuteride $\text{Ti}_{0.9}\text{VFe}_{0.1}\text{D}_{3.65}$ are shown in Fig. 3.11.

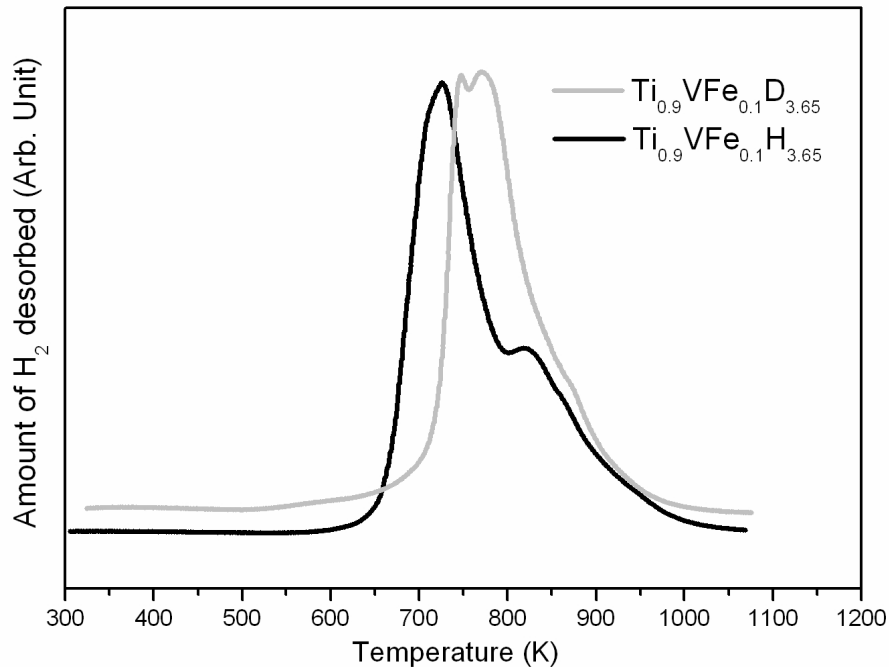


Fig. 3.11 Thermal desorption profiles of (a) $\text{Ti}_{0.9}\text{VFe}_{0.1}\text{H}_{3.65}$ (b) $\text{Ti}_{0.9}\text{VFe}_{0.1}\text{D}_{3.65}$.

The desorption profiles show two peaks for the hydride as well as the deuteride. From the TPD data it can be seen that the desorption onset temperature shifts to higher temperature for the deuteride as compared to that of the hydride. The onset of desorption is seen at 660 K and the peak temperatures of the deuteride are 763 K and 863 K, respectively. The desorption onset temperature of the hydride is 629 K and the peak temperatures are 724 K and 822 K, respectively. Thus, from this observation we conclude that the deuteride is more stable than the corresponding hydride of $\text{Ti}_{0.9}\text{VFe}_{0.1}$ alloy, which means that the system shows reverse isotope effect. This type of reverse isotope effect has been reported earlier also for the Ti-V based solid solution. Cho *et. al.* [150] has reported lower plateau pressure for deuterium in $\text{Ti}_{1.0}\text{Cr}_{1.5}\text{V}_{1.7}$ alloy indicating higher stability of the deuteride which can be explained by the

differences between the standard enthalpy and entropy of formation for the deuteride and the hydride.

TPD profiles are recorded for the Cr free $Ti_{0.8}VFe_{0.2}$ hydride and Cr containing $Ti_{0.8}V_{0.4}Fe_{0.2}Cr_{0.6}$ hydride and are shown in Fig. 3.12. From the TPD data of $Ti_{0.8}V_{0.4}Fe_{0.2}Cr_{0.6}H_{1.55}$ it can be seen that desorption starts at 570 K and the peak temperature is 685 K. The desorption profile for the Cr substituted sample $Ti_{0.8}V_{0.4}Fe_{0.2}Cr_{0.6}H_{1.55}$ is less broad as compared to the Cr free system though the peak temperature is almost the same. This implies that all the stored hydrogen can be desorbed over a narrower temperature range, starting from 560 K up to 800 K as compared to the Cr-free sample.

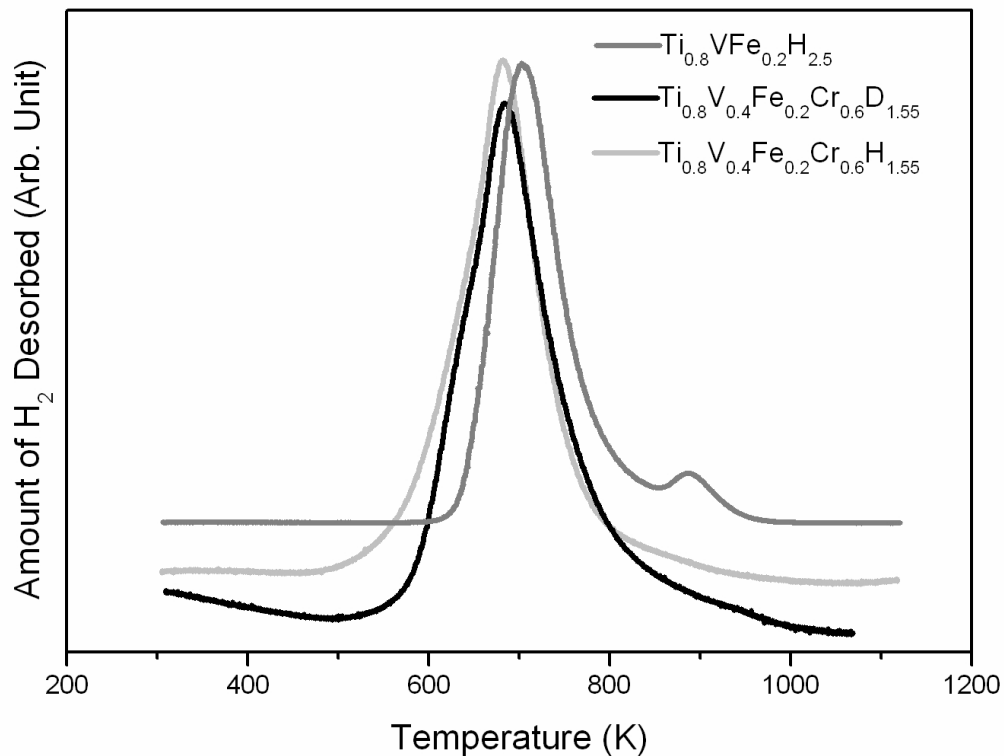


Fig. 3.12 Thermal desorption profiles of $Ti_{0.8}V_{0.4}Fe_{0.2}Cr_{0.6}H_{1.55}$, $Ti_{0.8}V_{0.4}Fe_{0.2}Cr_{0.6}D_{1.55}$ and $Ti_{0.8}VFe_{0.2}H_{2.5}$.

Fig. 3.12 also shows the TPD of the hydride as well as the deuteride of $Ti_{0.8}V_{0.4}Fe_{0.2}Cr_{0.6}$. The onset temperature for desorption of the deuteride is slightly higher

than that of the hydride showing a small signature of inverse isotope effect. The desorption peak temperature is almost the same for both the hydride and the deuteride. Since the Cr substituted $Ti_{0.8}V_{0.4}Fe_{0.2}Cr_{0.6}$ absorbs hydrogen without any prior activation and hydrogen can be recovered at a reasonable temperature range, this system can be a good getter material for hydrogen and its isotopes, as compared to the conventional material like U which is radioactive and highly pyrophoric in nature.

3.2.1.4 Summary

In this work, the effect of Fe substitution on the hydrogen absorption properties and activation treatment of Ti-V system have been investigated. The activation of the alloy Ti-V for hydrogenation is facilitated by Fe substitution. The hydrogen storage capacity increases with Fe content up to 15 at. % and decrease drastically on further increase in the Fe content. A maximum storage capacity of 3.7 wt. % is obtained for the composition $Ti_{0.85}VFe_{0.15}$. From the desorption temperatures of the hydride and the deuteride of $Ti_{0.9}VFe_{0.1}$, it is seen that the deuteride is more stable than the corresponding hydride. Again with increase in the Fe substitution the desorption temperature increase due to the destabilization of the hydride. The ease of activation of Ti-V-Fe system is improved further by Cr substitution (60 at. %) in place of V. The composition $Ti_{0.8}V_{0.4}Fe_{0.2}Cr_{0.6}$ absorbs hydrogen without any prior activation or any heat treatment. The total hydrogen content of the hydride is reduced on Cr substitution. Thermal desorption studies show a sharper desorption profile for the Cr containing hydride as compared to the Cr-free hydride.

3.2.2 Hydrogen absorption characteristics of Zr substituted $\text{Ti}_{0.85}\text{VFe}_{0.15}$ alloy

In the previous work on Ti-V-Fe system, we studied Fe substitution to improve the activation treatment of TiV alloy. As the Fe content increases, the maximum hydrogen absorption capacity improves slightly up to 15 at. % Fe substitution at Ti site and thereafter, it decreases. $\text{Ti}_{0.85}\text{VFe}_{0.15}$ alloy exhibited the maximum hydrogen storage capacity (3.7 wt. % at room temperature) within the studied $\text{Ti}_{1-x}\text{VFe}_x$ series. However, this alloy needed rigorous activation before hydrogen absorption. In the present study, $\text{Ti}_{0.85}\text{VFe}_{0.15}$ alloy is modified by 5 at. % Zr substitution in place of vanadium, to explore the possibility of improving the hydrogen absorbing properties without any significant reduction in the hydrogen storage capacity.

3.2.2.1 Crystal structure

The powder X-ray diffraction (XRD) patterns of $\text{Ti}_{0.85}\text{VFe}_{0.15}$ and the corresponding hydride $\text{Ti}_{0.85}\text{VFe}_{0.15}\text{H}_{3.83}$ are given in Fig. 3.13. From the XRD pattern it can be seen that $\text{Ti}_{0.85}\text{VFe}_{0.15}$ alloy shows bcc structure and the lattice parameter is found to be 3.08 Å. The structure changes to fcc on complete hydrogenation, which is in agreement with the earlier studies on Ti-V-Fe based systems [30]. The XRD pattern of the hydride $\text{Ti}_{0.85}\text{VFe}_{0.15}\text{H}_{3.83}$ could be indexed on the basis of fcc structure with a lattice parameter 4.29 Å.

Fig. 3.14 shows the XRD patterns of $\text{Ti}_{0.85}\text{V}_{0.95}\text{Fe}_{0.15}\text{Zr}_{0.05}$ and its hydrides with compositions $\text{Ti}_{0.85}\text{V}_{0.95}\text{Fe}_{0.15}\text{Zr}_{0.05}\text{H}_2$ and $\text{Ti}_{0.85}\text{V}_{0.95}\text{Fe}_{0.15}\text{Zr}_{0.05}\text{H}_{3.74}$, respectively. It is observed from the XRD pattern that 5 at. % Zr substitution in place of vanadium results in a multi phase structure consisting mainly C15 Laves phase along with some V based bcc solid solution [Fig. 3.14]. In some earlier works [131, 139], Zr substitution is reported to result in a secondary Laves phase formation. It may be noted that the C15 Laves phase structure

remains unchanged on hydrogenation of $Ti_{0.85}V_{0.95}Fe_{0.15}Zr_{0.05}$ alloy though there is appreciable shift in the peak positions to lower 2-theta values indicating volume expansion due to hydrogenation. The lattice parameter of the alloy is 7.36 \AA , where as that of the saturated hydride is 7.85 \AA .

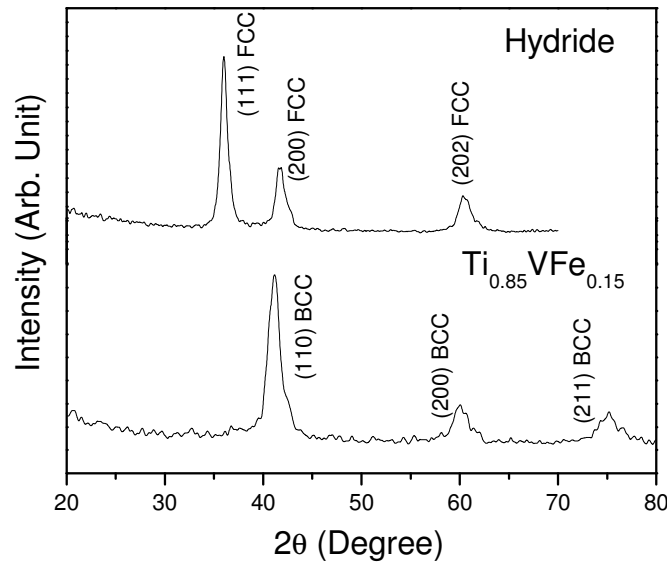


Fig. 3.13 XRD patterns of $Ti_{0.85}VFe_{0.15}$ alloy and the hydride $Ti_{0.85}VFe_{0.15}H_{3.83}$.

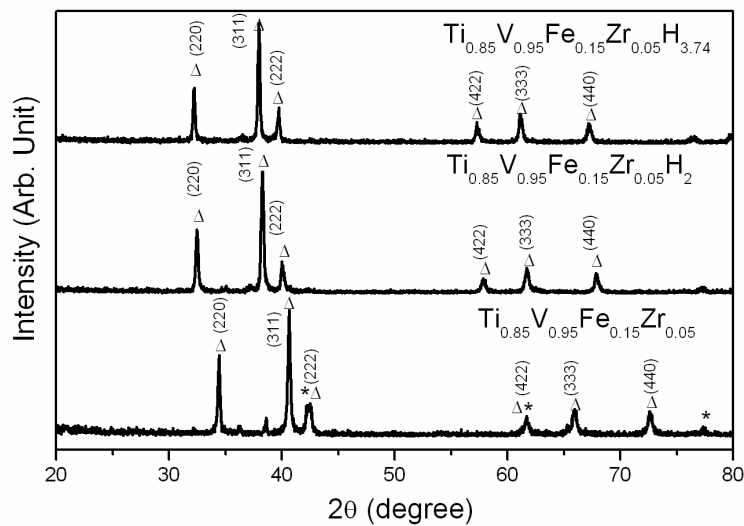


Fig. 3.14 XRD patterns of $Ti_{0.85}V_{0.95}Fe_{0.15}Zr_{0.05}$, $Ti_{0.85}V_{0.95}Fe_{0.15}Zr_{0.05}H_2$ and $Ti_{0.85}V_{0.95}Fe_{0.15}Zr_{0.05}H_{3.74}$ (Δ C15 Laves phases, * V based bcc solid solution)

For comparison purpose, the XRD pattern of the intermediate hydride composition $\text{Ti}_{0.85}\text{V}_{0.95}\text{Fe}_{0.15}\text{Zr}_{0.05}\text{H}_2$ is shown along with that of the saturated hydride. The intermediate hydride has been prepared by exposing the activated alloy under calculated amount of hydrogen. The composition has been rechecked in the hydrogen estimation setup. The intermediate dihydride ($\text{Ti}_{0.85}\text{V}_{0.95}\text{Fe}_{0.15}\text{Zr}_{0.05}\text{H}_2$) and is found have the same structure as that of the saturated hydride ($\text{Ti}_{0.85}\text{V}_{0.95}\text{Fe}_{0.15}\text{Zr}_{0.05}\text{H}_{3.74}$), with smaller lattice parameter (7.73 Å).

3.2.2.2 Hydrogen absorption properties

The alloy $\text{Ti}_{0.85}\text{VFe}_{0.15}$ is found to absorb a maximum of 3.83 H atoms/formula unit (3.7 wt. %) to form a saturated hydride with a composition $\text{Ti}_{0.85}\text{VFe}_{0.15}\text{H}_{3.83}$ while $\text{Ti}_{0.85}\text{V}_{0.95}\text{Fe}_{0.15}\text{Zr}_{0.05}$ forms a saturated hydride with a composition $\text{Ti}_{0.85}\text{V}_{0.95}\text{Fe}_{0.15}\text{Zr}_{0.05}\text{H}_{3.74}$ (3.5 wt. %), at room temperature.

The maximum hydrogen absorption capacities of $\text{Ti}_{0.85}\text{VFe}_{0.15}$ and $\text{Ti}_{0.85}\text{V}_{0.95}\text{Fe}_{0.15}\text{Zr}_{0.05}$ alloys are found to be 3.7 wt. % (H/M = 3.83) and 3.5 wt. % (H/M = 3.74), respectively. This implies that the total hydrogen storage capacity of Ti-V-Fe alloy does not change appreciably by Zr substitution. While $\text{Ti}_{0.85}\text{VFe}_{0.15}$ requires activation treatment at 673 K for 2 hours prior to hydrogen absorption, Zr substituted alloy could absorb hydrogen without any prior activation treatment. Zr substituted system is found to absorb hydrogen without any heat treatment with an incubation time of 5 hours at a hydrogen pressure of 10 atm. Thus, by substituting a small amount of Zr, the activation of the alloy prior to hydrogen absorption becomes easier. This could be due to the fact that with Zr substitution, the C15 Laves phase increases and crack formation at the surface becomes easier, so that hydrogen can easily diffuse through the cracks. The rate of hydrogen absorption for both the alloy systems as a function of time after one absorption-desorption cycle is shown in

Fig. 3.15. It can be seen that the hydrogen absorption rate is quite fast and both the alloys reach the saturation composition in about 200 seconds.

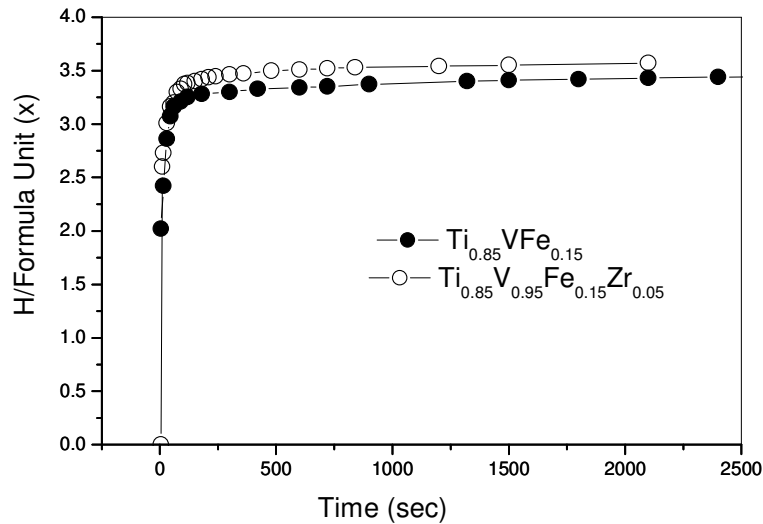


Fig. 3.15 Kinetic study of $Ti_{0.85}VFe_{0.15}$ and $Ti_{0.85}V_{0.95}Fe_{0.15}Zr_{0.05}$ alloys at room temperature and 20 atm. hydrogen pressure (Recorded after one absorption desorption cycle).

The pressure composition isotherms (PCT) for the two alloys $Ti_{0.85}VFe_{0.15}$ and $Ti_{0.85}V_{0.95}Fe_{0.15}Zr_{0.05}$ are shown in Fig. 3.16 and Fig. 3.17, respectively. The pressure composition isotherms have been studied at room temperature and 373 K. It can be seen from the figures that the plateau region is flat for both the alloys at room temperature and the plateau pressure is less than 0.02 atm.

For the Ti-V-Fe system within the pressure range of 0.02 to 20 atm., we have not observed two distinct plateau regions as reported in the earlier studies on Ti-V-Mn systems [37]. They studied the hydriding properties of Mn substituted $Ti_{0.9}Zr_{0.1}V_xMn_y$ alloys which are similar in composition to our Ti-V-Fe-Zr system and reported that the first plateau pressure is very close to zero atmosphere. With increasing temperature the length of the plateau region is found to decrease as expected, though the increase in the plateau pressure is beyond the detection limit of our set-up.

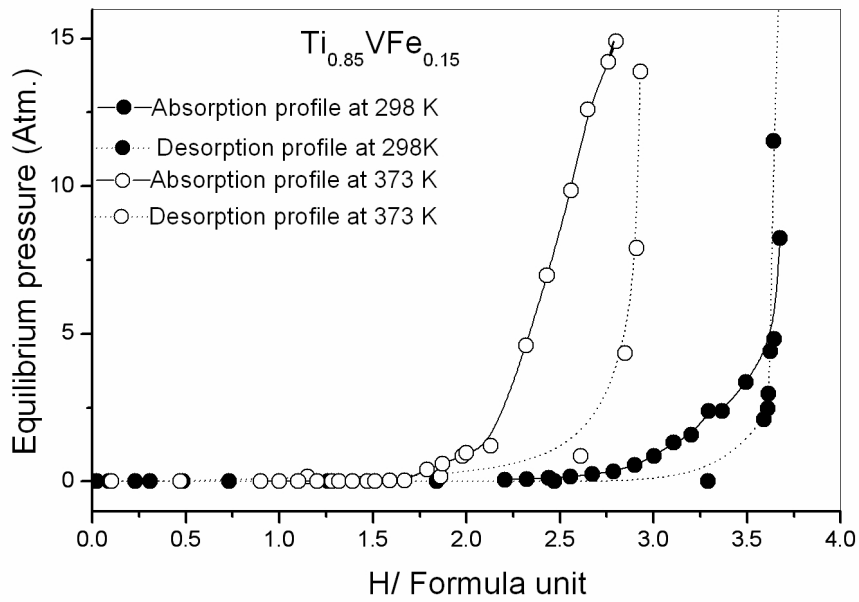


Fig. 3.16 PCT curves of $Ti_{0.85}VFe_{0.15}$ at room temperature and 373 K

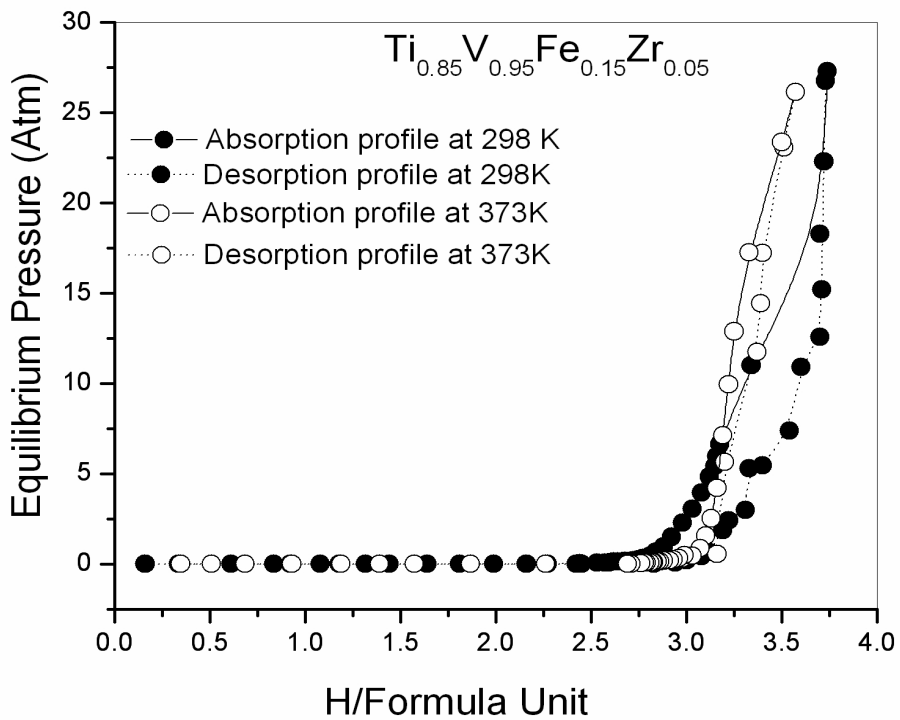


Fig. 3.17 PCT curves of $Ti_{0.85}V_{0.95}Fe_{0.15}Zr_{0.05}$ at room temperature and 373 K.

For the Ti-V-Fe-Zr system, in order to check the presence of a second plateau, a hydride with a lower hydrogen content having the composition $Ti_{0.85}V_{0.95}Fe_{0.15}Zr_{0.05}H_2$ is

prepared. However, from the X-ray diffraction studies mentioned above, this dihydride is found to have the same structure as that of the saturated hydride. By comparing the pressure composition isotherms of $\text{Ti}_{0.85}\text{VFe}_{0.15}$ and $\text{Ti}_{0.85}\text{V}_{0.95}\text{Fe}_{0.15}\text{Zr}_{0.05}$ alloys, it can be seen that the Zr substituted system shows an improved PCT profile with low hysteresis loss and a flat desorption plateau which are very important for long cyclic stability.

We have observed that the effective hydrogen storage capacity of the Zr-substituted system is slightly higher than that of the unsubstituted Ti-V-Fe system. In the present study, we define the effective hydrogen storage capacity as the amount of hydrogen desorbed from the alloy at 373 K under rotary vacuum (10^{-3} mbar) in one hour. The temperature 373 K has been chosen for the experiment due to the fact that, according to Japanese WE-NET project, 373 K is the ideal operating temperature of the hydrogen absorbing alloys for the vehicular applications [35]. It has been found that the effective hydrogen storage capacity of $\text{Ti}_{0.85}\text{VFe}_{0.15}$ is 1.8 wt. % where as that of $\text{Ti}_{0.85}\text{V}_{0.95}\text{Fe}_{0.15}\text{Zr}_{0.05}$ alloy is 2.1 wt. %. It could be due to the fact that the removal of hydrogen from bcc phase is relatively difficult than from Laves phase, which is present as a secondary phase in the Zr substituted system.

3.2.2.3 Mössbauer study

Fig. 3.18 and 3.19 show the Mössbauer spectra of $\text{Ti}_{0.85}\text{VFe}_{0.15}$ and $\text{Ti}_{0.85}\text{V}_{0.95}\text{Fe}_{0.15}\text{Zr}_{0.05}$ alloys and the corresponding saturated hydrides recorded at room temperature.

The alloy $\text{Ti}_{0.85}\text{VFe}_{0.15}$ shows a singlet with an isomer shift value of -0.120 mm/s. Upon hydrogenation, two not very well separated peaks are observed in the Mössbauer spectrum having isomer shift values of 0.010 and 0.567 mm/s and with relative areas of 1.000 and 0.200, respectively indicating the presence of two different Fe sites.

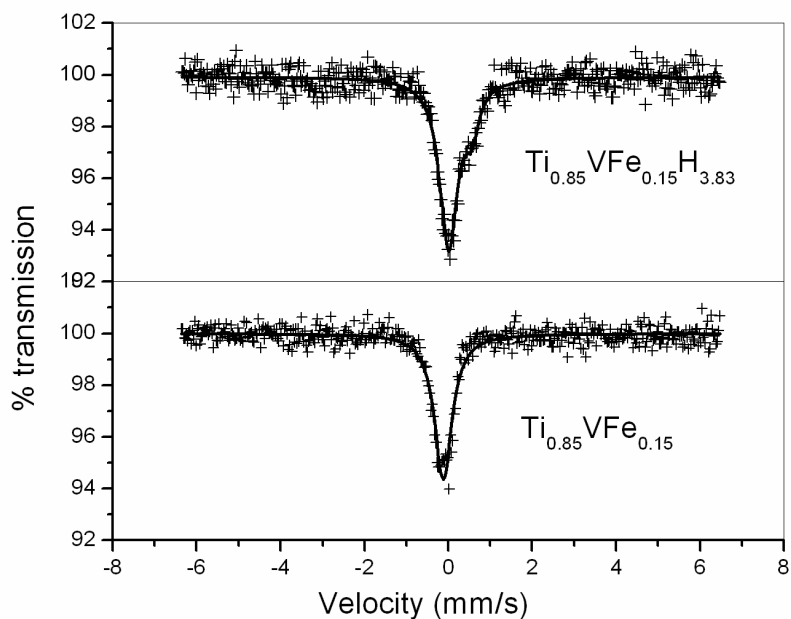


Fig. 3.18 Room temperature Mössbauer spectra of $Ti_{0.85}VFe_{0.15}$ and $Ti_{0.85}VFe_{0.15}H_{3.83}$.

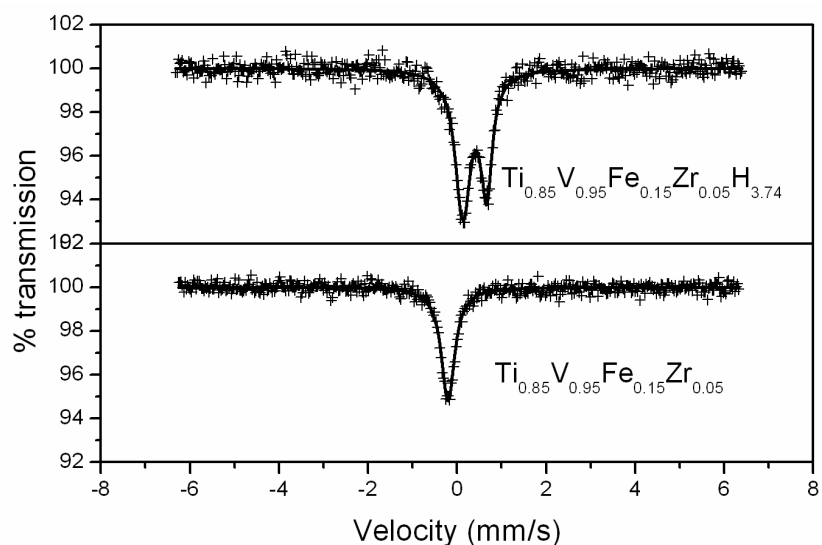


Fig. 3.19 Room temperature Mössbauer spectra of $Ti_{0.85}V_{0.95}Fe_{0.15}Zr_{0.05}$ and $Ti_{0.85}V_{0.95}Fe_{0.15}Zr_{0.05}H_{3.74}$.

In the case of $Ti_{0.85}V_{0.95}Fe_{0.15}Zr_{0.05}$ alloy, Mössbauer spectrum shows a single peak with a negative isomer shift value of -0.208 mm/s. However, the hydride $Ti_{0.85}V_{0.95}Fe_{0.15}Zr_{0.05}H_{3.74}$ shows two distinct peaks with isomer shift values of 0.132 and 0.661 mm/s, respectively. The relative areas of the two peaks are found to be 1.000 and 0.598 , respectively. The origin of the two peaks for the hydride can be attributed to the fact that

there are at least two nonequivalent hydrogen-absorbing sites with different isomer shift values. The large change in the isomer shift value observed for one of the peaks in the hydride samples suggests a possible interaction between the metal and hydrogen atoms.

3.2.2.4 Temperature programmed desorption study

Temperature programmed desorption (TPD) profiles of $\text{Ti}_{0.85}\text{VFe}_{0.15}\text{H}_{3.83}$ and $\text{Ti}_{0.85}\text{V}_{0.95}\text{Fe}_{0.15}\text{Zr}_{0.05}\text{H}_{3.74}$ are shown in Fig. 3.20. It can be seen from the figure that there are at least two hydrogen-desorbing sites for $\text{Ti}_{0.85}\text{VFe}_{0.15}\text{H}_{3.83}$ and three hydrogen desorbing sites for $\text{Ti}_{0.85}\text{V}_{0.95}\text{Fe}_{0.15}\text{Zr}_{0.05}\text{H}_{3.74}$. The hydride $\text{Ti}_{0.85}\text{VFe}_{0.15}\text{H}_{3.83}$ shows two peaks, at 723 and 935 K, respectively and the lower temperature peak is the major peak indicating the desorption of most of the hydrogen around this temperature.

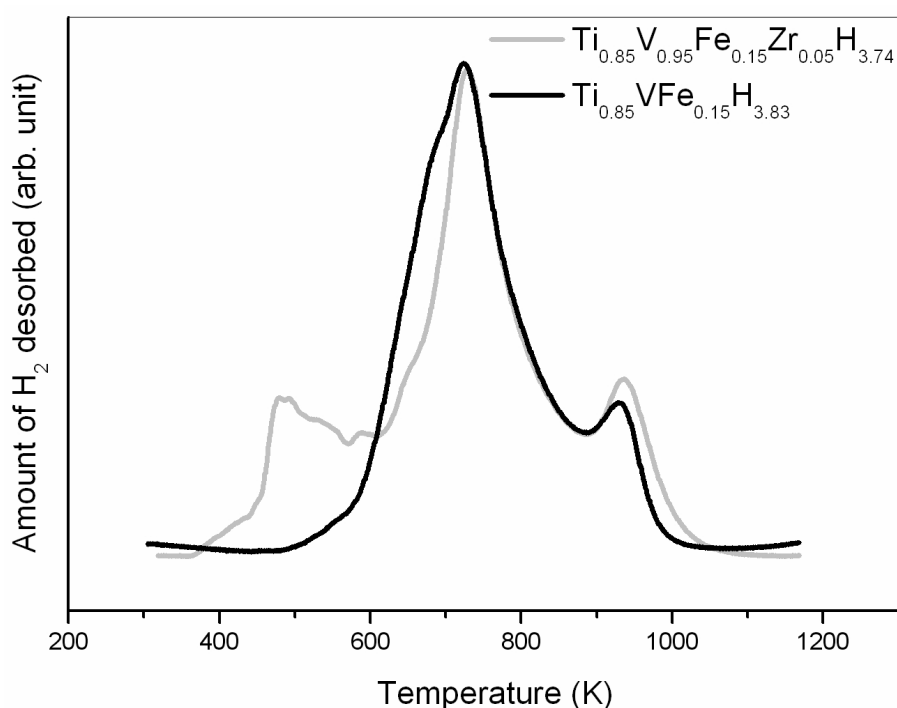


Fig. 3.20 TPD profiles of the hydrides $\text{Ti}_{0.85}\text{VFe}_{0.15}\text{H}_{3.83}$ and $\text{Ti}_{0.85}\text{V}_{0.95}\text{Fe}_{0.15}\text{Zr}_{0.05}\text{H}_{3.74}$

For the Zr-substituted hydride $\text{Ti}_{0.85}\text{V}_{0.95}\text{Fe}_{0.15}\text{Zr}_{0.05}\text{H}_{3.74}$, these two peaks are observed around 723 and 935 K and an additional peak is observed at 473 K indicating the onset of hydrogen desorption at a lower temperature. Thus, in the case of the Zr Substituted hydride,

appreciable amount of hydrogen desorption takes place at low temperatures. This observation support the fact that the reversible (effective) hydrogen storage capacity of the Zr substituted alloy is higher than that of the non-substituted alloy though their maximum hydrogen storage capacities are comparable.

3.2.2.5 Summary

The hydrogen absorption and desorption characteristics of $\text{Ti}_{0.85}\text{VFe}_{0.15}$ alloy is modified by substitution of 5 at. % Zr in place of V. The maximum hydrogen absorption capacities of $\text{Ti}_{0.85}\text{VFe}_{0.15}$ and $\text{Ti}_{0.85}\text{V}_{0.95}\text{Fe}_{0.15}\text{Zr}_{0.05}$ alloys are found to be 3.7 and 3.5 wt. %, respectively. Zr substitution results in the formation of a mixed phase structure and the activation of this material for hydrogen absorption is easier as compared to the unsubstituted Ti-V-Fe system. Zr substitution improves the hydrogen absorption-desorption characteristics of $\text{Ti}_{0.85}\text{VFe}_{0.15}$ alloy by decreasing the hysteresis loss without affecting the maximum hydrogen storage capacity considerably. The effective hydrogen storage capacity is found to improve by 5 at. % Zr substitution in place of V. The increase in the effective hydrogen storage capacity can be attributed to the fact that Zr substituted alloy has an additional site, which desorbs hydrogen at a lower temperature as compared to Ti-V-Fe system.

3.2.3 Hydrogen absorption studies on Ce substituted $\text{Ti}_{0.85}\text{VFe}_{0.15}$

In this study, we attempted to improve the hydrogen absorption characteristics of the bcc $\text{Ti}_{0.85}\text{VFe}_{0.15}$ alloy by substituting a small amount of Ce (2 and 5 at. %) for Ti. Since rare earths have strong affinity towards oxygen, they preferentially react with oxygen, thereby improving the homogeneity of the bcc phase [18-22]. The alloys $\text{Ti}_{0.85-x}\text{Ce}_x\text{VFe}_{0.15}$ ($x = 0$ and 0.02 and 0.05) have been characterized by pressure-composition isotherms studies. The microstructures of the alloys have been characterized by electron probe microanalysis

(EPMA) technique. Further, the electrochemical performance of Ce-free and Ce-substituted alloys has been studied.

3.2.3.1 Structural characterization

Fig. 3.21 shows the XRD patterns of $Ti_{0.85-x}Ce_xVFe_{0.15}$ ($x = 0, 0.02$ and 0.05) alloys.

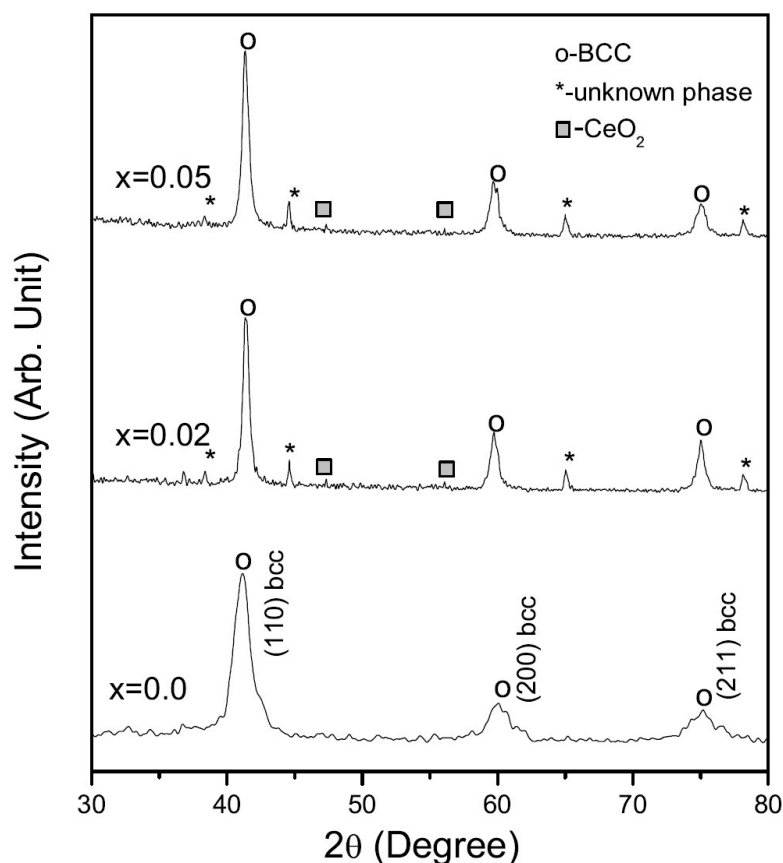


Fig. 3.21 X-ray diffraction patterns of $Ti_{0.85-x}Ce_xVFe_{0.15}$ alloys with $x = 0, 0.02$ and 0.05

The XRD pattern indicates that $Ti_{0.85}VFe_{0.15}$ alloy crystallizes in bcc structure with a lattice parameter of 3.086 \AA . It is observed from the XRD patterns that Ce substitution for Ti results in a small amount of CeO_2 phase along with the main bcc phase. This observation is in agreement with the earlier works [140-143], wherein a small amount of Ce substitution in $V_{55}Ti_{22.5}Cr_{16.1}Fe_{6.4}$ is reported to result in a secondary CeO_2 phase formation. Since most of the Ce is getting converted into CeO_2 , the change in lattice parameter is very small. For example, the lattice parameter changes from 3.086 \AA for the Ce-free alloy to 3.095 \AA for the

2 at. % Ce substituted alloy to 3.097 Å for the 5 at% Ce substituted alloy. We also find peaks due to an additional phase in the Ce substituted alloys, although the exact composition is not known. This phase is not matching with any of the reported phases such as Ti_2FeO_x , $CeTiO_x$ or Ce-Ti alloys. Yan et al [141] made similar observations in Ce substituted $V_{55}Ti_{22.5}Cr_{16.1}Fe_{6.4}$ wherein these peaks are attributed to unknown phase. Since the composition of our parent alloy $Ti_{0.85}VFe_{0.15}$ is different from the alloy $V_{55}Ti_{22.5}Cr_{16.1}Fe_{6.4}$ studied by Yan et al [140], the intensity of the X-ray peaks corresponding to unknown phase is at variance.

Fig. 3.22 shows the XRD patterns of the representative alloy $Ti_{0.83}Ce_{0.02}VFe_{0.15}$ and its hydride, $Ti_{0.83}Ce_{0.02}VFe_{0.15}H_{4.26}$, respectively.

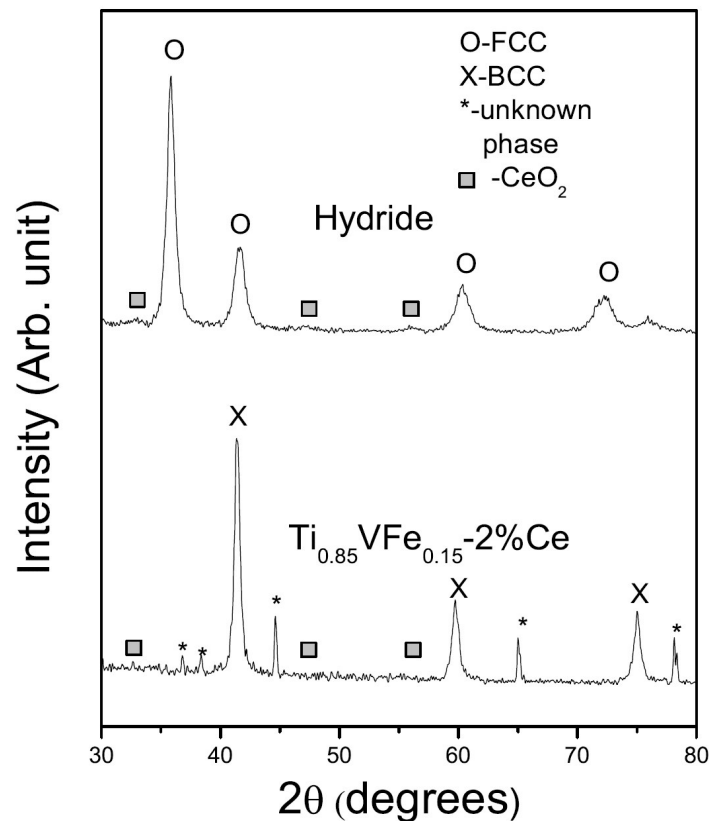


Fig. 3.22 X-ray diffraction patterns of 2 at. % Ce substituted alloy $Ti_{0.83}Ce_{0.02}VFe_{0.15}$ and its hydride $Ti_{0.83}Ce_{0.02}VFe_{0.15}H_{4.26}$.

The structure changes from bcc to fcc on hydrogenation. The peaks corresponding to the unknown phase are not prominent in the XRD pattern of the hydride except the one at higher angle, 76.25° . This may be due to the partial overlapping of some of the peaks of the hydride of the unknown phase (shifted to the lower 2-theta value upon hydrogen absorption) with the peaks of the main fcc hydride phase. The XRD pattern of the hydride $\text{Ti}_{0.83}\text{Ce}_{0.02}\text{VFe}_{0.15}\text{H}_{4.26}$ could be indexed on the basis of fcc structure with lattice parameter 4.350 \AA . Similarly, the hydrides $\text{Ti}_{0.85}\text{VFe}_{0.15}\text{H}_{3.83}$ and $\text{Ti}_{0.80}\text{Ce}_{0.05}\text{VFe}_{0.15}\text{H}_{4.27}$ are found to have fcc structure with lattice constants 4.292 and 4.350 \AA , respectively.

3.2.3.2 Micro chemical analysis using EPMA

Detailed microchemical analyses of the alloys have been carried out using EPMA technique. The $\text{Ti}_{0.85}\text{VFe}_{0.15}$ alloy shows a single phase microstructure (Fig. 3.23(a)) whereas Ce-substituted $\text{Ti}_{0.83}\text{Ce}_{0.02}\text{VFe}_{0.15}$ and $\text{Ti}_{0.80}\text{Ce}_{0.05}\text{VFe}_{0.15}$ alloys exhibit three phase microstructure. Representative back scattered electron image for $\text{Ti}_{0.83}\text{Ce}_{0.02}\text{VFe}_{0.15}$ alloy is shown in Fig. 3.23(b).

It is apparent from the image that there are (i) large bright (roughly 10-15 micron size) and (ii) small bright (roughly 2-5 micron size) phases distributed within single phase matrix. It is noted that the large bright phases have a tendency to cluster at the triple point junctions and grain boundaries whereas small bright phases are more random in nature. Wave-length dispersed X-ray line spectra obtained from each of these different phases indicate that the large bright phase is essentially constituted of Ce and O whereas small bright phase contains significant amount of Ce together with Ti and V. This becomes apparent from the Ce La-, Ti Ka- and V Ka X-ray line profiles (3.24 (a)-(c)).

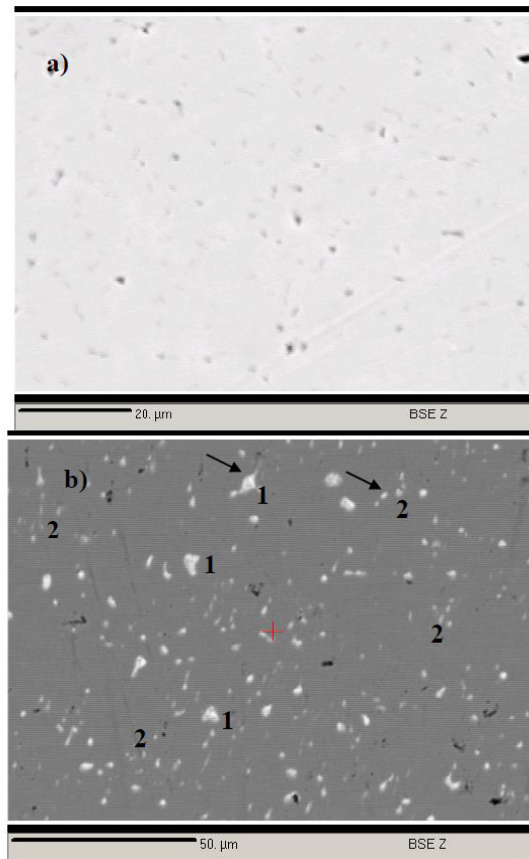


Fig. 3.23 Electron micrographs of (a) $Ti_{0.85}VFe_{0.15}$ and (b) $Ti_{0.83}Ce_{0.02}VFe_{0.15}$, respectively. Back scattered electron image is showing occurrence of large and small Ce precipitates within the matrix of $Ti_{0.83}Ce_{0.02}VFe_{0.15}$ alloy. Note that the **bright big** areas (marked as 1) are mostly occurring at the triple point junction (marked by black arrows) and **less bright small** areas (marked as 2) are defining the grain boundaries.

A comparative study of EPMA results with those obtained from XRD analysis show good correlation. Additionally, EPMA data identifies the third unidentified phase of XRD spectra as the one having significant amount of Ce, Ti and V. This may be the same in case of Yan et al [140] and Wu et al [141].

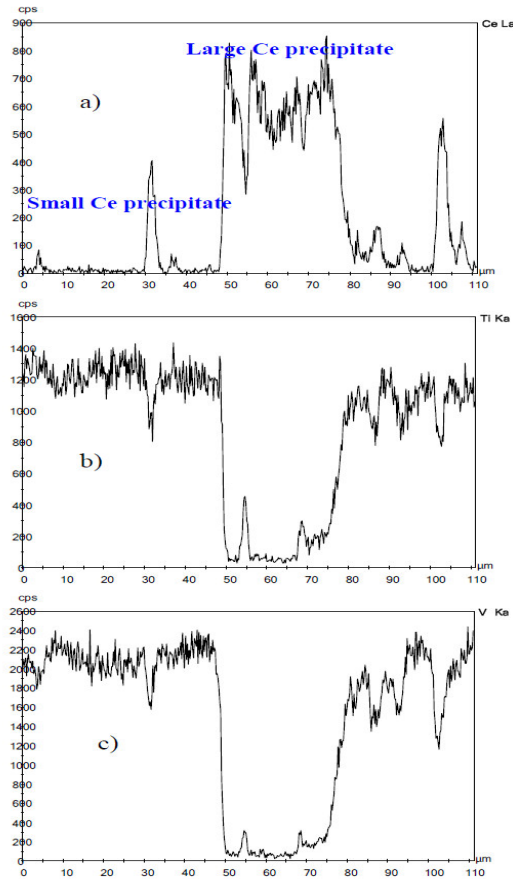


Fig. 3.24 (a) Ce La, (b) Ti Ka and (c) V Ka X-ray line scans showing compositional variations among different phases of $Ti_{0.83}Ce_{0.02}VFe_{0.15}$ alloy.

3.2.3.3 Hydrogen absorption characteristics

The alloys $Ti_{0.95}VFe_{0.15}$, $Ti_{0.83}Ce_{0.02}VFe_{0.15}$ and $Ti_{0.80}Ce_{0.05}VFe_{0.15}$ are found to have maximum hydrogen absorption capacities of 3.7 wt. % (H/M = 3.83), 4.02 (H/M = 4.26) and 3.92 wt. % (H/M = 4.27), respectively. The hydrogen storage capacities of $Ti_{0.85-x}Ce_xVFe_{0.15}$ alloys as a function of Ce content, x, are given in Table 3.2.

The activation of Ce containing alloys is found to be easier as compared to Ce-free alloy. This could be due to the fact that the Ce-containing alloys have a secondary phase with crack formation at the surface so that hydrogen can easily diffuse through the cracks. The rate of hydrogen absorption for all the alloys as a function of time after one absorption-desorption cycle is shown in Fig. 3.25.

Table 3.2 Lattice parameters before and after hydrogenation and the maximum storage capacities of the alloys

Alloy	Lattice parameter of BCC phase (Å)	Hydride Composition	Lattice parameter of FCC phase (Å)	Capacity (Wt. %)
Ti _{0.85} VFe _{0.15}	3.086	Ti _{0.85} VFe _{0.15} H _{3.83}	4.292	3.7
Ti _{0.83} Ce _{0.02} VFe _{0.15}	3.095	Ti _{0.83} Ce _{0.02} VFe _{0.15} H _{4.26}	4.350	4.02
Ti _{0.80} Ce _{0.05} VFe _{0.15}	3.097	Ti _{0.80} Ce _{0.05} VFe _{0.15} H _{4.27}	4.350	3.92

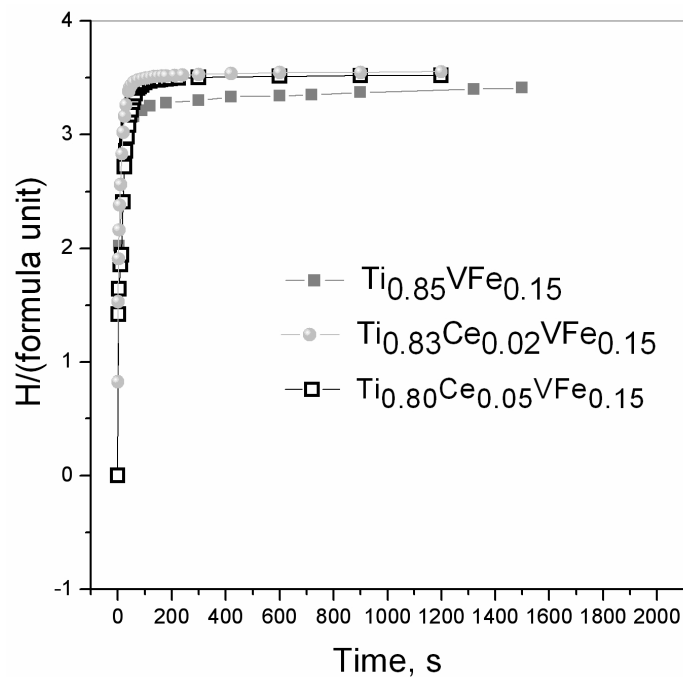


Fig. 3.25 Kinetic study on Ti_{0.85}VFe_{0.15}, Ti_{0.83}Ce_{0.02}VFe_{0.15} and Ti_{0.80}Ce_{0.05}VFe_{0.15} alloys.

It may be noted that the hydrogen absorption rate is quite fast and the hydrides reach near saturation value in about 120 seconds. Kinetic studies show that the hydrogen absorption is quite fast for all the three alloys. Fig. 3.26 shows the pressure-composition isotherms of Ti_{0.85-x}Ce_xVFe_{0.15} (x = 0.0, 0.02 and 0.05) alloys at room temperature.

For all compositions, the plateau region is found to be <0.02 atm., which is the lowest detection limit of our set up. In general, V based bcc alloys form monohydride and dihydride phases, exhibiting two plateau regions in the P-C isotherms [131, 134, 146]. The plateau corresponding to monohydride exists in the region of low pressure of the order of 10^{-2} mbar, at room temperature. The two plateau region was not observed in the pressure range of this study, as resolving the two plateau region needs pressure measurements in the low pressure region [131, 134, 146]. As can be seen from the pressure-composition isotherm study, the length of the plateau region increases for the Ce substituted alloys as compared to that of Ce-free alloy, $\text{Ti}_{0.85}\text{VFe}_{0.15}$. The hydrogen storage capacity of $\text{Ti}_{0.85-x}\text{Ce}_x\text{VFe}_{0.15}$ increases with the increase in Ce content up to $x = 0.02$. Further increase in the Ce content to $x = 0.05$, reduces the hydrogen storage capacity of the alloy marginally.

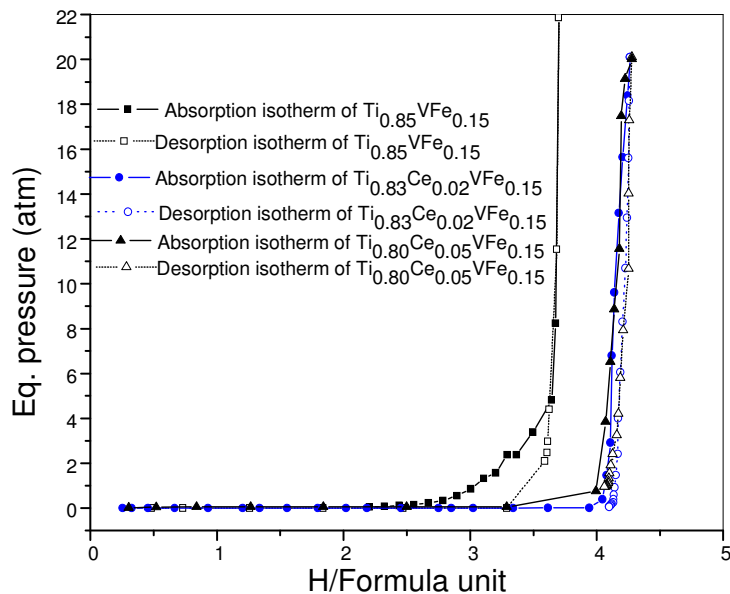


Fig. 3.26 Pressure-composition isotherms of $\text{Ti}_{0.85-x}\text{Ce}_x\text{VFe}_{0.15}$ ($x = 0, 0.02$ and 0.05) alloys at room temperature.

As seen from EPMA studies, the formation of CeO_2 phase in the bcc phase plays a crucial role in improving the hydrogen storage capacity of Ce substituted alloys. Due to the

strong affinity of Ce to oxygen, Ce preferentially reacts with trace oxygen during melting, thereby, reducing the reaction of Ti with oxygen. This is likely to lead to improved homogeneity of the bcc phase with higher Ti content as mentioned in ref. [140-144].

3.2.3.4 Electrochemical characterization

Electrochemical characterization of the two representative alloys $\text{Ti}_{0.85}\text{VFe}_{0.15}$ and $\text{Ti}_{0.83}\text{Ce}_{0.02}\text{VFe}_{0.15}$ are presented in this section. From the polarization measurements carried out at small over-potentials (-6 to +4 mV vs. ref. electrode) at a scan rate of 1.5 mV/s for $\text{Ti}_{0.85}\text{VFe}_{0.15}$ and $\text{Ti}_{0.83}\text{Ce}_{0.02}\text{VFe}_{0.15}$ alloys, the estimated polarization resistance values are 264 and 253 m Ω , respectively. Corresponding exchange current densities calculated are 98 and 108.52 mA/g. The increased exchange current density of Ce doped alloy indicates improved electrocatalytic activity for the hydrogen electrode reactions. The exchange current density is dependent both on the construction of MH electrode plate and the additives in the electrode plate. An increase in the exchange current density for a battery electrode leads to an increase in the high-rate discharge capability [146].

Fig. 3.27 shows the current density versus time of $\text{Ti}_{0.85}\text{VFe}_{0.15}$ and $\text{Ti}_{0.83}\text{Ce}_{0.02}\text{VFe}_{0.15}$ alloys (un-charged) measured in KOH electrolyte at a DC voltage of 0.25 V.

The initial current density obtained is 538 and 783 mA/g for $\text{Ti}_{0.85}\text{VFe}_{0.15}$ and $\text{Ti}_{0.83}\text{Ce}_{0.02}\text{VFe}_{0.15}$ alloys studied with a broad and stable plateau region of ~175-100 mA/g for both the alloys. It may be noted that the Ce-containing alloy has higher initial current density as compared to that of Ce-free alloy.

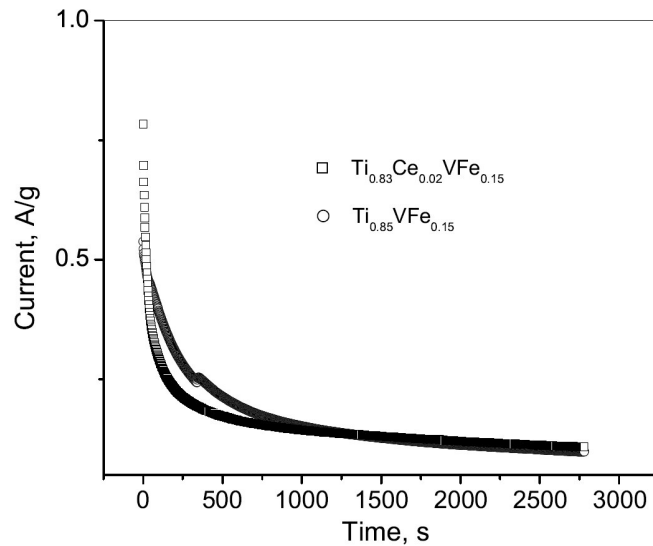


Fig. 3.27 Current versus time characteristics of $Ti_{0.85}VFe_{0.15}$ and $Ti_{0.83}Ce_{0.02}VFe_{0.15}$ alloys.

Fig. 3.28 shows the impedance spectra of $Ti_{0.85}VFe_{0.15}$ and $Ti_{0.83}Ce_{0.02}VFe_{0.15}$ (un-charged).

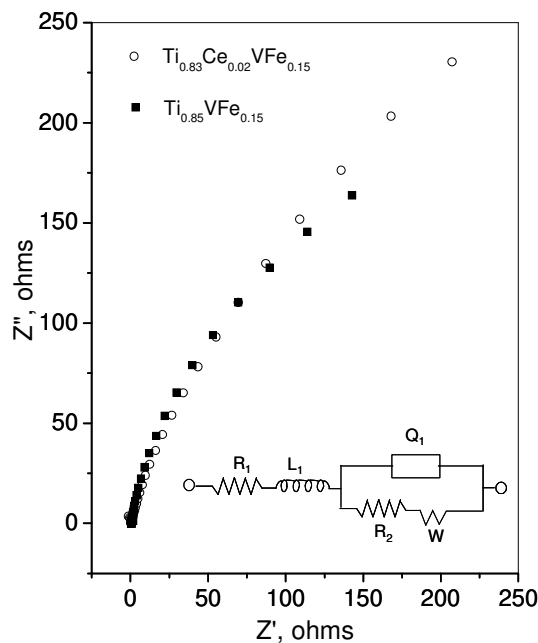


Fig. 3.28 Measured impedance data plots of $Ti_{0.85}VFe_{0.15}$ and $Ti_{0.83}Ce_{0.02}VFe_{0.15}$ alloys. Inset shows the equivalent circuit used for fitting the data. R_1 is the contact resistance, L_1 is the inductance, $R_2//Q_1$ represent the charge transfer resistance at the electrode electrolyte interface.

The impedance spectra were recorded for $\text{Ti}_{0.85}\text{VFe}_{0.15}$ and $\text{Ti}_{0.83}\text{Ce}_{0.02}\text{VFe}_{0.15}$ in the frequency range of 0.1 Hz to 100 kHz. Impedance data fitted using a complex non linear least square program shows that contributions for electrode reactions are both from the charge transfer resistance and the diffusion resistance (W). $(R_2||Q_1)$ represents the charge transfer resistance at the electrode/electrolyte interface. R_1 accounts for the contact resistance. The equivalent circuit used for fitting the data is shown in the inset of Fig. 3.28. Both the samples studied required an inductance element (L_1) for an optimized fit. Diffusion resistance was higher for $\text{Ti}_{0.83}\text{Ce}_{0.02}\text{VFe}_{0.15}$ compared to that of $\text{Ti}_{0.85}\text{VFe}_{0.15}$. The anodic oxidation peaks of hydrogen in the cyclic voltammograms were observed at -0.59 V and -0.55 V vs. Ag/AgCl reference electrode respectively, for $\text{Ti}_{0.83}\text{Ce}_{0.02}\text{VFe}_{0.15}$ and $\text{Ti}_{0.85}\text{VFe}_{0.15}$. The shift of anodic peak potential results from the change of hydrogen diffusivity [147]. The diffusion resistance values of the fitted impedance data also agree with the negative anodic peak shift of the Ce doped sample.

3.2.3.5 Summary

In this work, the effect of Ce substitution on the microstructure, hydrogen absorption properties, peak current of hydrogen absorption and electrochemical behaviour of $\text{Ti}_{0.85}\text{VFe}_{0.15}$ system have been investigated. Substitution of Ce (2 and 5 at. %) for Ti is found to improve the hydrogen absorption capacity of $\text{Ti}_{0.85}\text{VFe}_{0.15}$ alloy. The maximum storage capacity of $\text{Ti}_{0.85}\text{VFe}_{0.15}$, $\text{Ti}_{0.83}\text{Ce}_{0.02}\text{VFe}_{0.15}$ and $\text{Ti}_{0.80}\text{Ce}_{0.05}\text{VFe}_{0.15}$ alloys are found to be 3.7, 4.02 and 3.92 wt. %, respectively. The plateau pressure is found to be <0.02 atm. for all compositions. The ease of activation of Ti-V-Fe system is found to improve by Ce substitution. EPMA studies showed the presence of CeO_2 phase in Ce-substituted alloys along with a third phase. Electrochemical studies showed increased exchange current density for Ce doped alloy indicating improved electrocatalytic activity for the hydrogen electrode reactions.

3.4 Conclusion

From the hydrogen storage studies on $Ti_{1-x}VFe_x$ series we could conclude that, by varying the concentration of Fe, the hydrogen storage properties of the alloys can be modified drastically. $Ti_{0.85}VFe_{0.15}$ shows the maximum hydrogen storage capacity of 3.7 wt. % within this series. Cr substitution in place of V does not increase the hydrogen storage capacity but improves the activation properties. Both Zr and Ce substitutions in $Ti_{0.85}VFe_{0.15}$ alloy provide positive effect on the hydrogen absorption properties. Zr substitution improves the hydrogen absorption-desorption characteristics of $Ti_{0.85}VFe_{0.15}$ alloy by decreasing the hysteresis loss without affecting the maximum hydrogen storage capacity considerably. The hydrogen storage capacity and the ease of activation of Ti-V-Fe system are found to improve by small amount of Ce substitution.

Chapter IV

Hydrogen Storage Studies on Ti-V-Cr Based Systems

It has been discussed already in the last chapter that Ti-V based solid solutions with body centered cubic (bcc) structure are considered as promising third generation hydrogen storage materials, due to their high hydrogen storage capacity of ~ 3 wt. %. In the last chapter we have conferred our findings on the hydrogen storage properties of Ti-V-Fe and substituted Ti-V-Fe systems. This chapter depicts the hydrogen storage properties of Ti-V-Cr and substituted Ti-V-Cr systems.

Ti-V-Cr alloy with the bcc structure has been regarded as one of the promising candidate for the hydrogen storage application [33-35, 135-138, 154-171]. These alloys exhibit a bcc solid solution structure and their hydrogen storage capacity is larger than that of the conventional AB_2 types of alloys. Ti-Cr-V alloys are known to absorb about 3.8 mass % of protium (hydrogen atom), but desorbs about 2.4 mass % [156]. However, their rechargeable hydrogen capacity is limited due to their stable nature and higher desorption temperature. The poorer activation characteristics and higher cost are other two critical drawbacks limiting their successful practical applications. In order to resolve these problems, much work has been done to improve the activation characteristics and decrease the cost. The hydrogen storage properties such as reversibility, desorption capacity, hydrogen storage

capacity, and desorption temperature of the alloys are significantly influenced by melting methods, heat-treating conditions, chemical compositions and additional elements. It is reported that the activation of bcc phase alloys would be easier if the alloys contain some Laves phase [163]. However, the presence of Laves phase in bcc phase alloys would decrease the hydrogen storage capacity. In many of the studies, the bcc phase TiVCr alloy has been chosen as the parent system, which is reported to exhibit good hydrogen absorption capacity [156, 161-163]. There are reports on the improvement of the hydrogen absorption desorption characteristics of the Ti-V-Cr alloy by Fe, Al and Mn substitution [154, 160, 164, 165, 169]. Ti-20Cr-12Mn-24V-5Fe alloy shows a maximum capacity of 3.3 wt. % and an effective capacity of 2.2 wt. % for the quenched alloy, which is of great importance to the practicality of bcc phase alloy for hydrogen storage a system [154]. The phase structures analysis of Ti-25V-xCr-(35-x)Mn alloys shows that the increase of Cr content in the alloys is effective for obtaining a single bcc-phase structure, which results in an increasing hydrogen capacity. The maximum and effective hydrogen storage capacities among studied alloys are 3.99 and 2.44 wt. %, respectively [155]. Ti_{0.32}Cr_{0.43}V_{0.25} alloys shows the maximum and effective hydrogen storage capacities of 3.7 and 2 wt. % respectively and the cyclic study shows that the after 1000 cycles also the effective hydrogen storage capacity remains constant. The storage capacity could be recovered nearly to the original level by reactivating the specimen during the cyclic test [162]. With increase of V content in Ti-V-Cr-Mn alloys, two-phase structure of bcc and C14 Laves transforms into a single bcc phase [138]. However in some of the studies, the hydrogenation of TiVCr is reported to result in phase separation into TiH₂ and TiCr_{1.8}H_{5.3} when subjected to cyclic hydrogenation-dehydrogenation process [161]. The hydrogen storage properties and the phase stability of some of the alloys of Ti-V-Cr series are found to improve with the substitution of Zr for Ti, though it increases the slope of the P-C isotherm [135]. As an example, the heat-treated Ti_{0.16}Zr_{0.05}Cr_{0.22}V_{0.57} alloy showed maximum

hydrogen storage capacity and effective hydrogen storage capacities of 3.55 and 2.14 wt. % respectively, without any phase separation.

Here, we report the hydrogen absorption-desorption properties, crystal structure and kinetics of $\text{Ti}_{1-x}\text{Zr}_x\text{VCr}$ ($x = 0, 0.05, 0.1$ and 1.0) alloys to determine the effect of Zr substitution on the phase separation and the hydrogen storage capacity. The hydrogen absorption-desorption properties of Ti_2VCr also has been reported in this chapter, which shows quite high gravimetric hydrogen absorption capacity. The material has been characterized for the phase structure and morphology. The hydrogen storage properties such as pressure-composition isotherms, hydrogen storage capacity, hydrogen absorption kinetics and the desorption temperature has been studied in detail. The research has emphasized the cyclic hydrogen absorption and desorption of the alloy. The cyclic hydrogen absorption-desorption properties of Ti_2VCr alloy is systematically investigated upto 10th cycle. We believe that the present study can provide a good support towards the search for potential hydrogen storage material with optimal performance.

4.1 Experimental Details

All the alloys were prepared by arc melting of high purity constituent elements (> 99.9 %) in a water-cooled copper hearth under Ar atmosphere. The ingots were turned over and remelted 4-5 times to ensure homogeneity. Phase purity of the alloys was checked by powder X-ray diffraction (XRD) technique using CuK_α radiation. The SEM micrographs of Ti_2VCr alloy and hydride have been taken by SEM SERON INC., South Korea, (Model No. ATS 2100). The compositional measurement has been done by using EDX made from Oxford instrumentation UK (model No. INCAE350).

The hydrogen absorption-desorption characteristics were measured using a Sievert's type set up described in chapter II. The alloys were activated by heating under diffusion

vacuum (10^{-6} mbar) for 2 hours at 673 K. After activation, the sample was cooled to the working temperature under vacuum, followed by introduction of hydrogen into the reaction chamber. The pressure composition isotherm (PCT) was studied in the pressure range of 0.02-25 atm. H_2 at ambient temperature. After each cycle, the sample was dehydrogenated by heating at 673 K under diffusion vacuum. The kinetic study was done at room temperature and a hydrogen pressure of 20 atm. after one absorption desorption cycle. The hydride sample was surface poisoned with air at liquid nitrogen temperature, before being taken out.

The total hydrogen storage capacity was estimated by heating a small amount of the hydride sample, in an evacuated and calibrated quartz chamber. The temperature programmed desorption (TPD) measurement was done on TiVCr hydride and Zr substituted TiVCr hydrides using an automated TPD instrument up to 1173 K, at a constant heating rate of 10 K/min using argon as carrier gas.

The amount of hydrogen desorption at different temperature has been studied in-situ for Ti_2VCr alloy by heating the sample at 373, 473 and 473 K under vacuum in Sievert's type set up. The hydride sample was surface poisoned before being taken out.

To compare between the desorption temperature of the cycled and uncycled hydride, desorption studies were carried out on the surface poisoned hydride of Ti_2VCr alloy using TG, DTA and DSC measurements. Thermo-gravimetry (TG) and differential thermal analysis (DTA) were done by SETARAM SETSYS Evolution-1750 model with temperature increasing rate of 10K/min under argon flow for uncycled hydride. The DSC measurement was done by using DSC823^e Mettler-Toledo instrument under argon flow with temperature ramping rate of 10K/min for both samples uncycled and cycled Ti_2VCr hydrides. As these studies has been done with the surface poisoned hydride in a different instrument so the desorption profiles can not give the exact desorption temperature, but for comparison purpose these results are quite important.

4.2 Results & Discussion

4.2.1 Hydrogen storage properties of Zr doped TiVCr alloys

In this study we report the structure and hydrogen absorption/desorption properties of TiVCr and Zr substituted TiVCr alloys. 0.05, 0.1 and 1 at. % of Zr has been substituted for Ti atom to modify its hydrogen absorption properties and to see its effect on the cyclic stability.

4.2.1.1 Crystal structure of the alloys

The X-ray diffraction patterns of $Ti_{1-x}Zr_xVCr$ alloys with $x = 0, 0.05, 0.1$ and 1.0 and their hydrides are shown in Fig. 4.1 & Fig. 4.2 respectively. The XRD pattern indicates that TiVCr exists as single phase bcc structure with a lattice parameter 3.051 \AA which is in agreement with the values reported earlier for the TiVCr alloy [162, 164]. When Zr is substituted for Ti, secondary phase formation takes place. The XRD pattern of $Ti_{0.95}Zr_{0.05}VCr$ alloy consists of a small fraction of a secondary phase besides the main bcc phase with a lattice parameter $a = 3.067 \text{ \AA}$.

The earlier studies on Ti-Zr-Cr-V systems [135] reported the secondary phase as C15 cubic Laves phase compound $ZrCr_2$. In our study also, the additional lines in the XRD patterns of $Ti_{0.95}Zr_{0.05}VCr$ and $Ti_{0.9}Zr_{0.1}VCr$ match with those of $ZrCr_2$ phase. As the Zr content increases, the intensity of the peaks corresponding to the secondary phase increases. When Zr is completely substituted for Ti, single phase $ZrVCr$ is formed with C15 cubic Laves phase structure having lattice parameter $a = 7.283 \text{ \AA}$. The lattice parameters of the alloys are listed in Table 4.1.

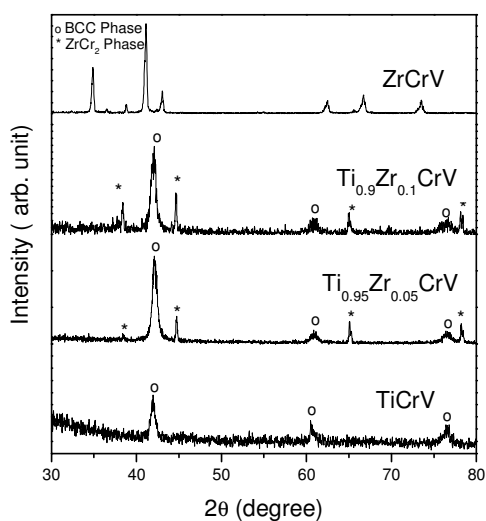


Fig. 4.1 X-ray diffraction patterns of $Ti_{1-x}Zr_xVCr$ alloys ($x = 0.0, 0.05, 0.1$ and 1.0)

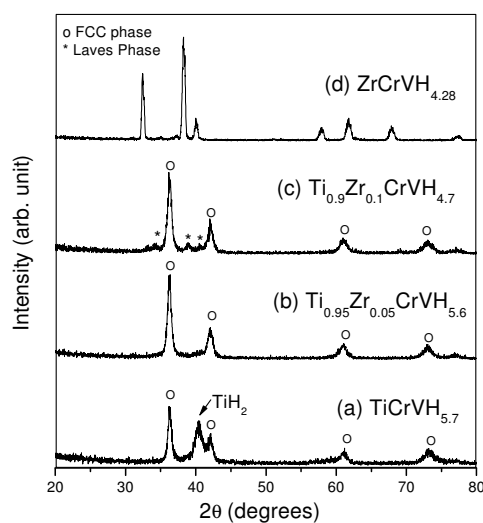


Fig. 4.2 X-ray diffraction patterns of the hydrides: (a) $TiCrH_{5.7}$, (b) $Ti_{0.95}Zr_{0.05}VCrH_{5.6}$, (c) $Ti_{0.9}Zr_{0.1}VCrH_{4.7}$ and (d) $ZrVCrH_{4.28}$.

4.2.1.2 Hydrogen absorption studies on different compositions

The compound $TiVCr$ absorbs a maximum of 5.7 H atoms / formula unit (3.64 wt. %) forming a hydride with a composition, $TiVCrH_{5.7}$ at room temperature. This maximum absorption capacity is observed at a hydrogen pressure of 20 atm.

For $x = 0.05$, $Ti_{0.95}Zr_{0.05}VCr$ is found to absorb a maximum 5.6 H atoms/formula unit forming a hydride with a composition $Ti_{0.95}Zr_{0.05}VCrH_{5.6}$ at room temperature. This implies that the maximum hydrogen absorption capacity of $TiVCr$ alloy does not decrease appreciably for $x = 0.05$. However, further increase in the Zr content reduces the hydrogen absorption capacity. $Ti_{0.9}Zr_{0.1}VCr$ absorbs a maximum of 4.7 H atoms/formula unit forming a hydride with composition $Ti_{0.9}Zr_{0.1}VCrH_{4.7}$. The hydrogen storage capacities are listed in the tabular form in Table 4.1.

Table 4.1 Phases, lattice parameters before and after hydrogenation, and the maximum hydrogen storage capacities of the alloys.

Alloy	Phases	Lattice Parameter (Å)	Hydride Composition	Hydride Phases	Lattice Parameter (Å)	Capacity (wt. %)
TiCrV	Bcc	3.051	TiCrVH _{5.7}	fcc	4.292	3.64
Ti_{0.95}Zr_{0.05}CrV	bcc	3.067	Ti _{0.95} Zr _{0.05} CrVH _{5.6}	fcc	4.280	3.53
	C15	7.280		C15	-	
Ti_{0.9}Zr_{0.1}CrV	bcc	3.071	Ti _{0.9} Zr _{0.1} CrVH _{4.7}	fcc	4.260	2.93
	C15	7.280		C15	7.800	
ZrCrV	C15	7.283	ZrCrVH _{4.28}	C15	7.817	2.16

With increase in Zr content to 10 % ($x = 0.1$), the peaks corresponding to ZrCr₂ phase are seen in the X-ray diffraction pattern. This cubic phase is found to absorb lower hydrogen content as compared to pure bcc phase of TiVCr. The compound ZrVCr absorbs only 4.28 H atoms /formula unit forming a hydride with composition ZrVCrH_{4.28} at room temperature and a hydrogen pressure of 20 atm. The maximum hydrogen absorption capacities of different compositions are listed in Table 4.1. The pressure composition (P-C) isotherms of TiVCr, Ti_{0.95}Zr_{0.05}VCr, Ti_{0.9}Zr_{0.1}VCr and ZrVCr are shown in Fig. 4.3 (a-d), respectively.

The plateau pressure is found to be less than 0.02 atm., which is the lowest detection limit of our set up. The bcc alloys generally exhibit two plateaus in the pressure-composition isotherms [134, 163]. The two plateaus observed in the earlier studies on Ti-V-Cr systems [[134, 163]] needs resolution of pressure readings in the range of 10⁻³ bar which could not be achieved in our set up. The Zr substituted Ti_{0.95}Zr_{0.05}VCr system shows improved P-C isotherm with low hysteresis loss and relatively flat desorption plateau which are very important for long term cyclic stability.

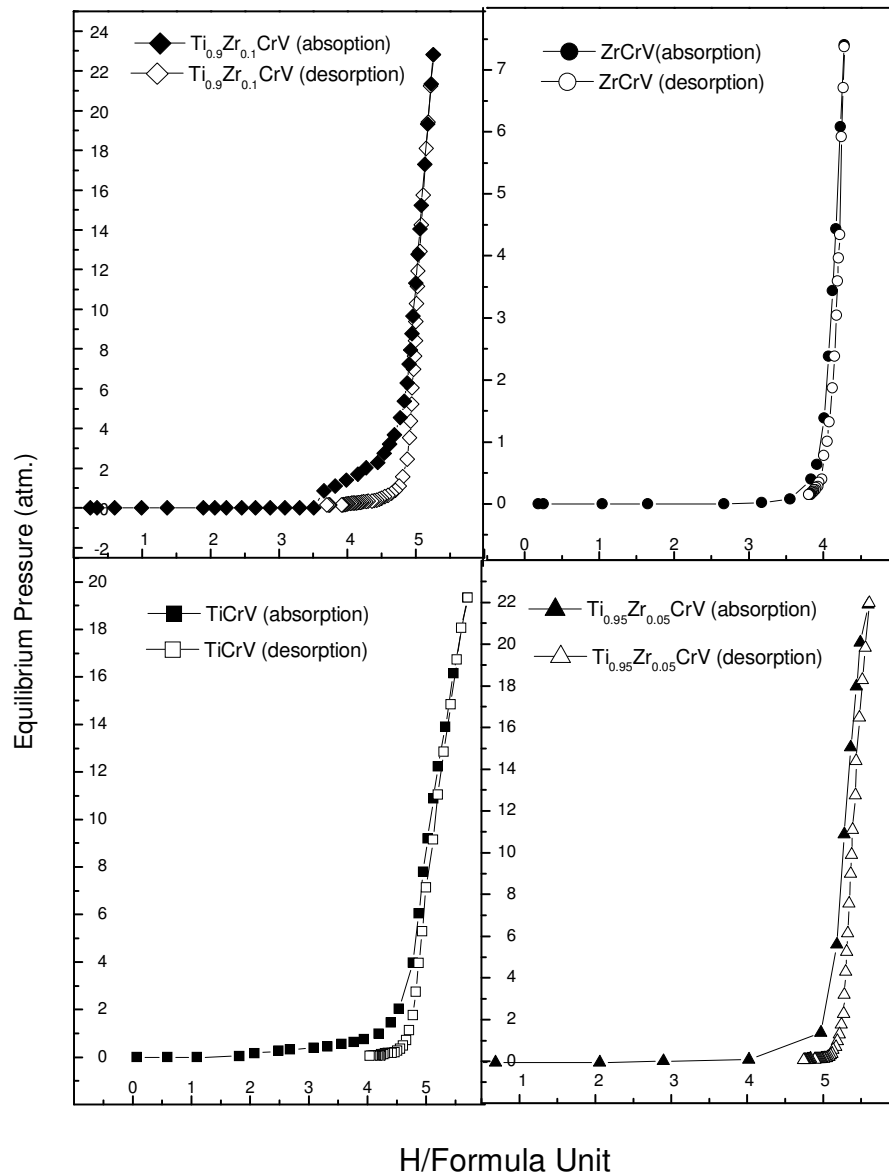


Fig. 4.3 *P-C isotherms for $Ti_{1-x}Zr_xVCr$ alloys ($x = 0.0, 0.05, 0.1$ and 1.0) at room temperature.*

The rate of hydrogen absorption for $TiVCr$, $Ti_{0.95}Zr_{0.05}VCr$ and $Ti_{0.9}Zr_{0.1}VCr$ after one absorption-desorption cycle at room temperature is shown in Fig. 4.4. All the compositions were dehydrogenated at 673 K under vacuum before carrying out the kinetic study. It can be seen from Fig. 4.4 that for all the three alloys, the hydrogen absorption rate is quite fast and the hydrides reach near saturation values in about 80-200 seconds.

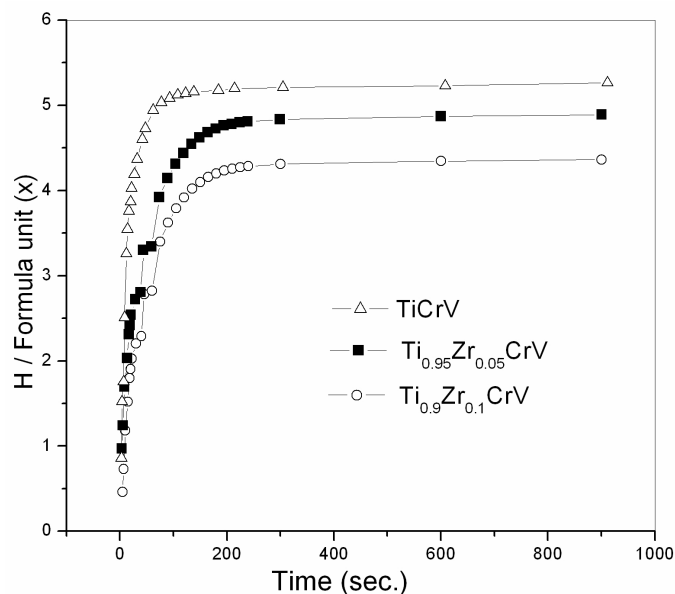


Fig. 4.4 Kinetic study of the alloys at room temperature and 20 atm. hydrogen pressure. (Recorded after one absorption-desorption cycle.)

4.2.1.3 Crystal structure of the hydrides

The XRD patterns of the hydrides with saturated compositions are shown in Fig. 4.2. The hydride $\text{TiVCrH}_{5.7}$ is having face centered cubic (fcc) structure. Ti-V-Cr and Ti-V-Fe based bcc alloys generally form monohydride with distorted bcc structure which subsequently transforms into fcc structure upon further hydrogen changing [134, 163, 164]. The lattice parameter of fcc structured $\text{TiVCrH}_{5.7}$ is found to be $a = 4.292 \text{ \AA}$ [Table 4.1]. Lin et al [161] reported the appearance of $\text{TiCr}_{1.8}\text{H}_{5.3}$ hydride with fcc structure, when TiVCr is hydrogenated with a hydrogen content of 1.5 wt. %. They also observed that further increase in hydrogen content to saturation value of 3.55 wt. %, led to TiH_2 phase formation in addition to $\text{TiCr}_{1.8}\text{H}_{5.3}$ phase. Wang et al [165] also reported a decrease in the hydrogen absorption capacity of TiVCr alloy due to phase separation into TiH_2 and $\text{TiCrH}_{5.3}$ upon cycling. In our opinion, the phase coexisting with TiH_2 should have been Ti-deficient. Unlike in ref. 161 and 165 wherein TiH_2 formation is reported on hydrogenation, we find the formation of fcc hydride, $\text{TiVCrH}_{5.7}$, with lattice parameter $a = 4.292 \text{ \AA}$ as shown in Fig. 4.5(a).

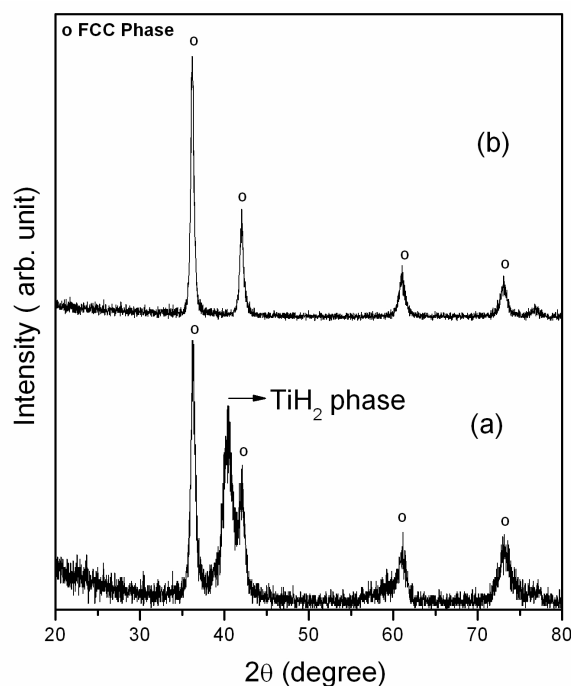


Fig. 4.5 X-ray diffraction pattern of TiVCr hydride (prepared by dehydrogenation at 673 K followed by hydrogenation at room temperature) showing TiH_2 phase and the fcc $TiVCrH_{5.7}$ without TiH_2 phase separation.

There are no peaks corresponding to TiH_2 in the XRD pattern of the saturated hydride. The fcc hydride $TiVCrH_{5.7}$ shown in Fig. 4.5(a) is formed by exposing the activated TiVCr to hydrogen at 298 K and the hydride is not subjected to cycling. However, on dehydrogenation of $TiVCrH_{5.7}$ at 673 K followed by second cycle of hydrogen absorption, the peaks corresponding to TiH_2 appear in the XRD pattern along with the main fcc hydride phase (Fig. 4.5(b)). It is quite likely that the main fcc phase seen in Fig. 4.5(b) is Ti-deficient as compared to stoichiometric TiVCr after the TiH_2 phase separation.

For $x = 0.05$, the hydride $Ti_{0.95}Zr_{0.05}VCrH_{5.6}$ is found to have fcc structure with lattice parameter $a = 4.280 \text{ \AA}$. There is no TiH_2 or ZrH_2 phase separation seen in the XRD pattern of this hydride even after five hydrogenation-dehydrogenation cycles. Thus, 5 at. % Zr substituted sample is expected to exhibit better cyclic hydrogen absorption capacity than TiVCr. The lattice parameter of $Ti_{0.9}Zr_{0.1}VCrH_{4.7}$ is found to be 4.260 \AA . This hydride

contains a small amount of $ZrCr_2$ hydride phase. The alloy $ZrVCr$ retains the C15 cubic Laves phase structure upon hydrogenation and the lattice parameter increases due to hydrogen absorption which can be seen from the decrease in the 2θ values of the peaks in the XRD pattern. The lattice parameter for $ZrVCrH_{4.28}$ is found to be 7.807 \AA .

4.2.1.4 Temperature programmed desorption study

In order to study the relative stability and the number of hydrogen desorbing sites, temperature programmed desorption (TPD) measurements have been carried out on the hydride samples. The TPD profiles for $TiVCrH_{5.7}$, $Ti_{0.95}Zr_{0.05}VCrH_{5.6}$, $Ti_{0.9}Zr_{0.1}VCrH_{4.70}$ and $ZrVCrH_{4.28}$ are shown in Fig. 4.6(a-d).

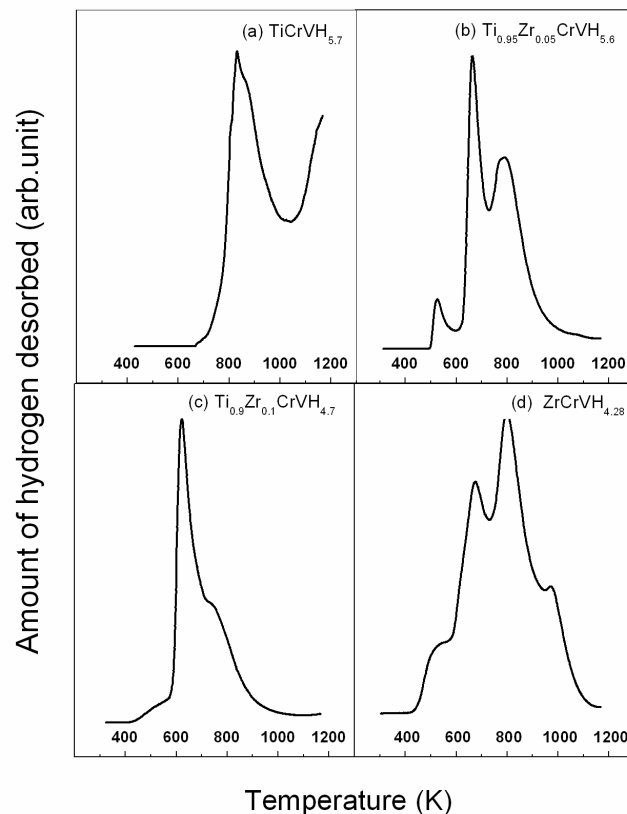


Fig. 4.6 Temperature programmed desorption profiles of the hydrides: (a) $TiVCrH_{5.7}$, (b) $Ti_{0.95}Zr_{0.05}VCrH_{5.6}$, (c) $Ti_{0.9}Zr_{0.1}VCrH_{4.7}$ and (d) $ZrVCrH_{4.28}$

It can be seen from the TPD profiles that the desorption of $TiVCr$ hydride is incomplete up to 1180 K. The hydride shows two sites, one at 830 K and another at higher

temperature around 1173 K. The higher temperature peak could be ascribed to the decomposition of the binary hydride, TiH_2 . In the process of heating to higher temperature, $\text{TiVCrH}_{5.7}$ undergoes phase separation to form the binary hydride, TiH_2 . The hydride $\text{Ti}_{0.95}\text{Zr}_{0.05}\text{VCrH}_{5.6}$ shows an additional peak at lower temperature, around 527 K as compared to $\text{TiVCrH}_{5.7}$. Similarly, the 10 at. % Zr substituted hydride $\text{Ti}_{0.9}\text{Zr}_{0.1}\text{VCrH}_{4.7}$ shows a change of slope at lower temperature in the TPD profile. The number of interstitial sites available in the substituted systems are larger than in unsubstituted systems. Hence additional peaks are expected in the Zr substituted samples. It is clear from the TPD profiles that the Zr containing samples have additional hydrogen desorbing sites at lower temperatures. Based on our earlier work on Zr substituted Ti-V-Fe system [166], we expect that the Zr substituted samples would desorb appreciable amount of hydrogen at lower temperatures as compared to pure TiVCr , implying higher effective hydrogen storage capacity. It is known that the removal of hydrogen from bcc phase is relatively difficult than from Laves phase, which is present as a secondary phase in the Zr substituted systems [167].

For $x = 1.0$, the cubic Laves phase hydride $\text{ZrVCrH}_{4.28}$ shows a broad TPD profile with four peaks over a wide range of temperatures from 439 K to 1083 K. At least three different sites are reported for cubic Laves phase hydrides based on the observance of three peaks in the TPD profiles [167]. The peak at higher temperature of ~ 980 K is due to the desorption of hydrogen from binary ZrH_2 which is formed during the heating of $\text{ZrVCrH}_{4.28}$.

4.2.1.5 Summary

In the present study, the hydrogen absorption and desorption characteristics of $\text{Ti}_{1-x}\text{Zr}_x\text{VCr}$ with $x = 0, 0.05, 0.10$ and 1.0 have been investigated. The maximum storage capacities of these alloys are found to be 3.64, 3.53, 2.93 and 2.16 wt. %, respectively. While TiVCr is formed in bcc structure, ZrVCr is a C15 cubic Laves phase compound and the

intermediate compositions with $x = 0.05$ and 0.1 show the presence of a small amount of $ZrCr_2$ along with the main bcc phase. A small amount of Zr substitution (5 at. %) for Ti decreases the storage capacity of TiVCr alloy marginally, but TiH_2 phase separation is suppressed, possibly, leading to better cyclic hydrogen absorption capacity. Hysteresis is found to be less for Zr substituted systems. Further increase in the Zr concentration decreases the hydrogen storage capacity considerably due to the formation of the secondary Laves phase in addition to the bcc phase. Temperature programmed desorption studies have shown the presence of an additional desorption site at lower temperature for Zr substituted hydrides as compared to TiVCr hydride, indicating higher effective capacity for Zr substituted systems.

4.2.2 Hydrogen storage characteristics and cyclic study of Ti_2VCr alloy

The section deals with the hydrogen absorption desorption properties of the Ti_2VCr alloy with a special emphasis on the hydrogen desorption behavior and the cyclic hydrogen absorption desorption study.

4.2.2.1 Crystal structure

The XRD patterns of Ti_2VCr alloy before and after hydrogen absorption are shown in Fig.4.7. The Ti_2VCr alloy crystallizes in pure body centered cubic (bcc) structure with lattice parameter of 3.10 \AA . After hydrogenation the alloy reacts with hydrogen to form a hydride with composition $Ti_2VCrH_{0.05}$. The saturated hydride shows face centered cubic (fcc) structure with a lattice parameter of 4.35 \AA . In contrary to the TiVCr alloy [168], on cycling the hydride of Ti_2VCr does not show any TiH_2 phase separation upto 10^{th} cycle indicating good cyclic stability of the hydride.

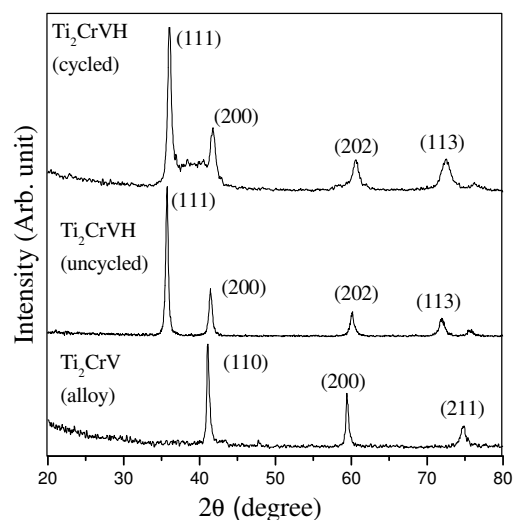


Fig. 4.7 X-ray diffraction patterns of Ti_2VCr alloys and $Ti_2VCr H_{9.5}$.

To ensure the homogeneity of the alloy, compositional study has been done by EDX at different positions of the alloy. The average composition is given in Table 4.2 and the EDX graph for the alloy is shown in Fig. 4.8. It shows that the composition is close to the expected ratio of Ti, Cr and V which is 2:1:1.

Table 4.2 EDX data of the Ti_2CrV alloy

Element	Weight %	Atom %
TiK	50.96	52.75
VK	24.74	24.08
CrK	24.30	23.17
Total	100	

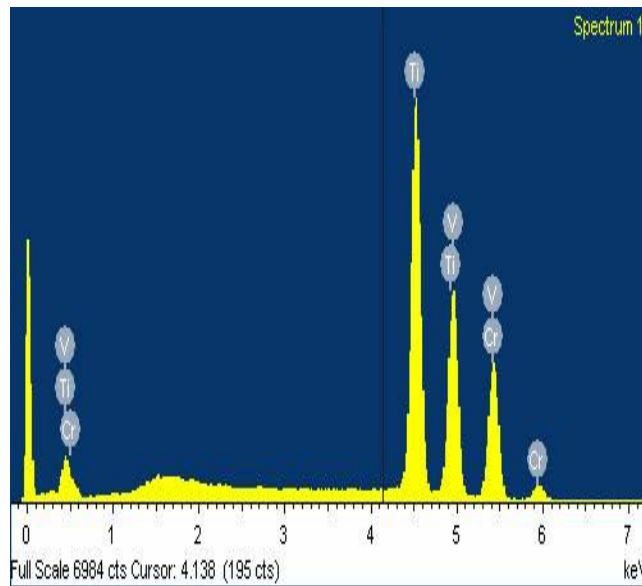


Fig. 4.8 EDX mapping of Ti_2VCr alloy.

4.2.2.2 Hydrogen absorption study

The hydrogen absorption and desorption properties have been studied using a Sievert's type set up. Fig. 4.9(a) shows the pressure-composition isotherms of Ti_2VCr alloy at room temperature and 373 K. The absorption isotherm measured at room temperature shows that the plateau pressure is less than 0.02 atm. The plateau region is found to be very flat and the hysteresis is very less.

The maximum storage capacity is calculated from the PCT diagram by taking into account the molecular weight of the hydride and the hydrogen concentration per formula unit. It has been calculated that, at room temperature and 25 atm. hydrogen pressures, Ti_2VCr alloy forms a hydride with composition $Ti_2VCrH_{9.05}$, which is having a maximum hydrogen storage capacity of 4.37 wt. %. As expected, with increase in temperature the the plateau region decreases. At 373 K the alloy found to absorb 2.05 wt. % of hydrogen. The rate of hydrogen absorption, after one hydrogen absorption-desorption cycle, as a function of time is shown in Fig. 4.10 (b).

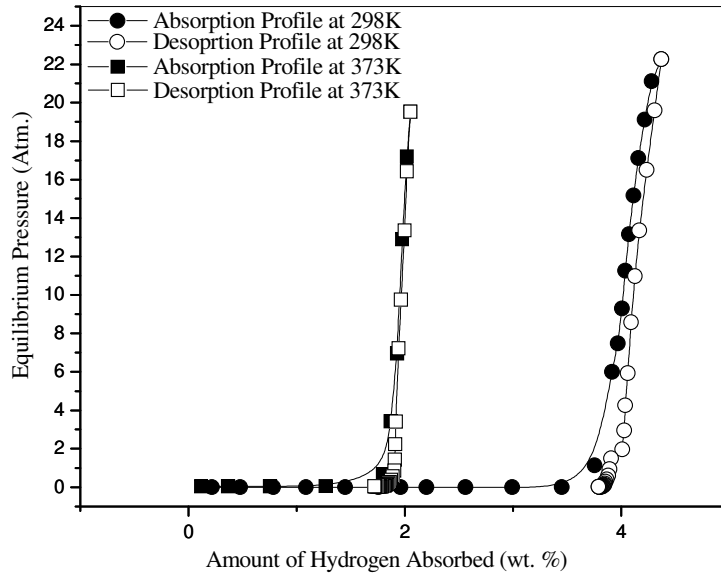


Fig. 4.9 *P-C isotherms of Ti_2VCr alloy at 298 K and 373 K.*

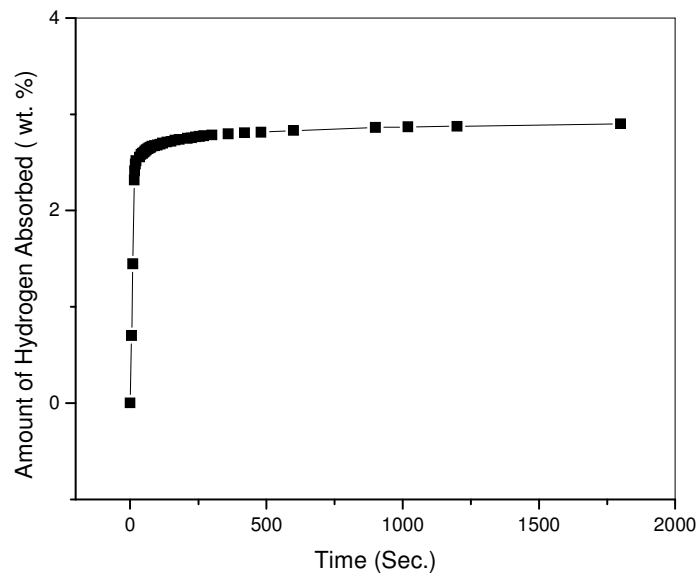


Fig. 4.10 *Kinetic study of Ti_2VCr at room temperature and 20 atm. hydrogen pressure. (Recorded after one absorption-desorption cycle.)*

The kinetics of hydrogen absorption is found to be quite fast for the Ti_2VCr alloy. It can be seen from Fig. 4.10, Ti_2VCr alloy absorbs hydrogen without any incubation time and it reaches 2/3 of the saturation value within 5 minutes.

4.2.2.3 Cyclic hydrogen absorption–desorption characteristics of Ti_2VCr

Fig. 4.11 shows the cyclic hydrogen capacities of the Ti_2VCr alloy. The alloy is subjected to cyclic hydrogen–absorption-desorption at 298 K, and after each absorption-desorption experiment the alloy is heated at 673 K under diffusion vacuum and prepared for the next cycle. It is found that there is a 20 % decrease in the hydrogen absorption capacity after the third cycle, which remains almost constant for the successive cycles.

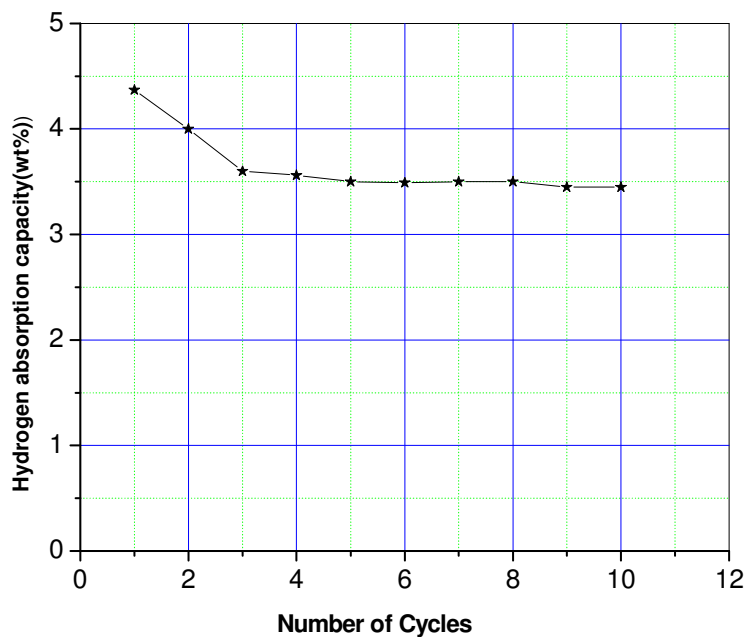
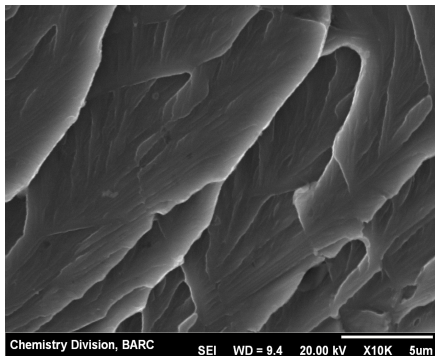


Fig. 4.11 Cyclic hydrogen absorption capacity of Ti_2VCr alloy at room temperature upto 10th cycle.

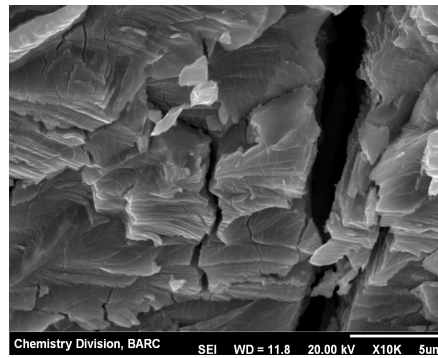
The hydrogen storage capacity is measured up to 10 cycles, and a stable absorption capacity of 3.5 wt. % is found. The decline in hydrogen absorption ability can be related to the formation of irreversible stable hydride. Many researchers have found similar cyclic absorption capacity trend in the Ti-V-Cr based alloys [161, 169].

4.2.2.4 Morphology

Fig. 4.12 shows the morphology of Ti_2VCr alloy before and after hydrogenation. Fig. 4.12(a) shows the surface of the as cast Ti_2VCr alloy. The fracture observed in Fig. 4.12(b) is caused by volume expansion due to the hydride formation.



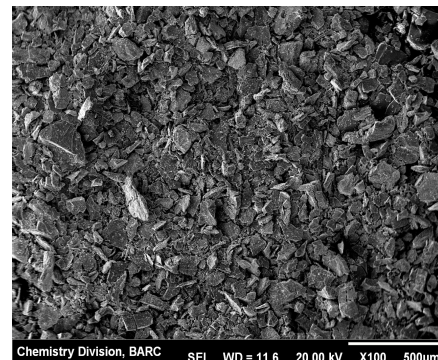
(a)



(b)



(c)



(d)

Fig. 4.12 SEM micrographs of (a) The Ti_2VCr alloy (b) after initial hydrogen absorption (c) hydride after one cycle and (d) hydride after 10th cycle.

When the alloy starts absorbing hydrogen, lattice expands forming cracks at the surface. The hydrogen absorption process also leads to finer particles, referred to as pulverization [170]. Fig. 4.12(c) and 4.12(d) show the SEM images of Ti_2VCr hydride without cycling and after 10 cycles of hydrogen absorption–desorption, respectively. From the SEM micrograph it can be seen that the multi-cycled hydride has smaller particles than

the uncycled hydride. The particle sizes of the hydride have reduced from 50–250 to 10-150 micrometer after 10 cycles. Yang *et. al.* [171] has also found the similar results in their study.

4.2.2.5 Hydrogen desorption study

In order to understand the hydrogen desorption behavior of Ti_2VCr hydride, the hydride was heated in-situ at different temperatures in the Sievert's type set up and the amount of hydrogen desorbed were found out. In Fig. 4.13 the amount of hydrogen desorbed has been plotted with respect to temperature. It has been found from the figure that at room temperature and 373 K the amount of hydrogen desorbed is 0.95 and 2.2 wt. %. If we heat the sample at higher temperature the desorption capacity increases. At 473 K and 573 K the desorption capacity is found to be 2.77 and 3.15 wt. % respectively. At 673 K Ti_2VCr alloy desorbs 3.5 wt. % of hydrogen which is equal to its cyclic hydrogen absorption capacity.

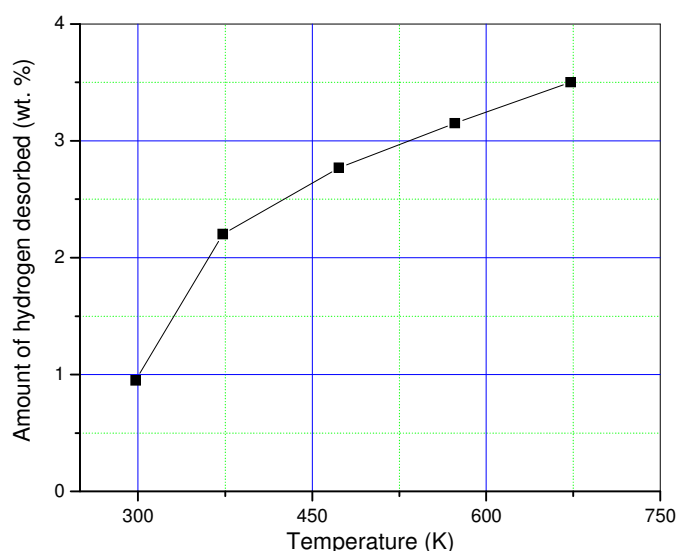


Fig. 4.13 Amount of hydrogen desorbed (wt. %) of Ti_2VCr at different temperature.

To compare between the hydrogen desorption of the uncycled hydride and multi cycled hydride, high temperature TG-DTA and DSC measurements were done on the surface poisoned saturated hydride, $Ti_2VCrH_{9.05}$. The measurements were performed under argon

atmosphere with temperature ramping rate 10K/min for all samples. The TG and DTA curve of uncycled Ti_2VCr hydride is shown in Fig. 4.14. In the DTA curve two endothermic peaks can be seen indicating two different hydrogen desorption sites. The uncycled hydride shows maximum weight loss in the temperature range of 650 to 720 K with a peak temperature of 675 K. The other small peak is at 640 K. The TG curve shows 2.5% wt. loss indicating the release of hydrogen at the temperature range of 650 to 720 K.

Fig. 4.15 shows the DSC curve of uncycled and multi-cycled hydride.

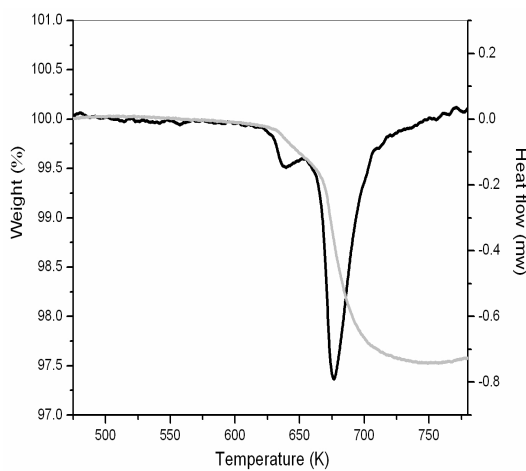


Fig. 4.14 TG-DTA curve of Ti_2VCr uncycled hydride.

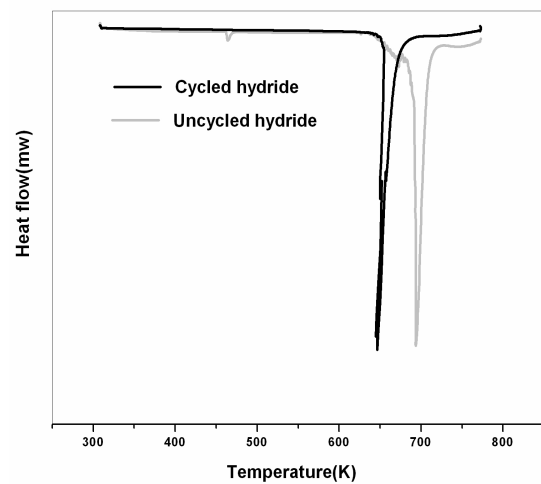


Fig. 4.15 DSC graph of Ti_2VCr of (a) uncycled hydride and (b) multi-cycled hydride (after 10^{th} cycle)

From the figure it can be seen that both hydride of the uncycled and multi-cycled hydride show endothermic peak. The main dehydrogenation peaks for multi-cycle hydride and hydride after one hydrogen absorption desorption cycle, are found at 650 and 695 K, respectively. It has been found that the multi-cycled hydride releases hydrogen at slightly lower temperature as compared to uncycled Ti_2VCr hydride. The decrease in peak temperature seems to be due the decrease in the particle size which has been confirmed by microstructure analysis.

4.2.2.6 Summary

The hydrogen absorption-desorption properties of Ti_2VCr alloy have been studied in detail. This alloy is found to have a maximum storage capacity of 4.37 wt. %. The plateau pressure is found to be less than 0.02 atm. at room temperature, indicating that this alloy forms a stable hydride at room temperature. The cyclic hydrogen absorbing ability decreased progressively during the first few cycles and after that it remains almost constant. The alloy shows a maximum 3.5 wt. % hydrogen absorption capacity after a few cycles. The kinetics of hydrogen absorption is found to be fast for Ti_2VCr alloy without any incubation time. The desorption capacity of Ti_2VCr hydride was measured by heating the sample at different temperatures. It has been found that the hydrogen desorption capacity at room temperature is 1 wt. % only, which increases with an increase in temperature. From the DSC analysis, the multi-cycled hydride shows hydrogen desorption at a lower temperature as compared to the uncycled hydride of Ti_2VCr . Due to the high storage capacity, the studied alloy can be used in Ni-MH batteries, though the desorption temperature is quite high for practical application. Further study has been done by substituting Co and Ni in place of Ti in the Ti_2VCr alloy, which shows an appreciable decrease in the desorption temperature with a marginal decrease in the storage capacity.

4.3 Conclusion

The effect of Zr substitution for Ti on the hydrogen absorption/desorption characteristics of $\text{Ti}_{1-x}\text{Zr}_x\text{VCr}$ alloys ($x = 0, 0.05, 0.1$ and 1.0) has been reported in this chapter. While TiVCr shows separation of TiH_2 phase on cycling, a small amount of Zr substitution for Ti is found to have advantageous effects on the hydrogen absorption properties of TiVCr as it suppresses TiH_2 phase separation and decreases hysteresis. It is

found that the hydrogen absorption capacity of $Ti_{1-x}Zr_xVCr$ decreases as the Zr content increases, due to the increased fraction of Laves phase. The Ti_2VCr alloy in Ti-V-Cr series shows a hydrogen storage capacity of 4.37 wt. % at room temperature. From the cyclic hydrogen absorption study of Ti_2VCr alloy it has been found that the hydrogen storage capacity decreased progressively with cycling initially, but the alloy can maintain steady cyclic hydrogen absorption capacity 3.5 wt. % after 5th cycle.

Chapter V

Vanadium Substituted $ZrFe_2$ as Laves Phase Hydrogen Storage Material

AB_2 type of Laves phase alloys are one of the promising hydrogen storage materials, because of their potentially high hydrogen storage capacity and fast hydrogen absorption/desorption kinetics. Many of the Laves phase compounds show a suitable range of equilibrium plateau pressure around 1 atm. at room temperature [20-24, 172-176]. Laves phases form the largest group of intermetallics, with currently more than 1400 known representatives [177-179]. They belong to the family of the Frank-Kasper phases [180, 181]. The general building principle has been revealed by F. Laves and J.B. Friedel [182-184]. All the Laves phases are binary or pseudo binary compounds with the general formula of AB_2 , where the atomic radius of A is larger than that of B. In these compounds, the A element is a rare earth (R) or R-like element and the B atom is mostly Mn, Fe, Co, Rh or Ru. In ideal case, for the formation of Laves phase, the atomic radius of A should be about 1.225 times larger than the atomic radius of B. This enables a close packing of the atoms with a space filling of

71%. Though there are infinite number of prototype Laves phase compounds, but the three most prominent are C14 (MgZn₂-type), C36 (MgNi₂-type) and C15 (MgCu₂-type) modification. The different forms can transfer from one to the other during heating and cooling (typically C14 at high temperatures and C15 at low temperatures). The C15 structure is a fcc-based structure containing six atoms (two formula units) in the primitive unit cell, while the C14 and C36 structures are hexagonal structures containing 12 and 24 atoms in the primitive unit cell, respectively [Fig. 5.1].

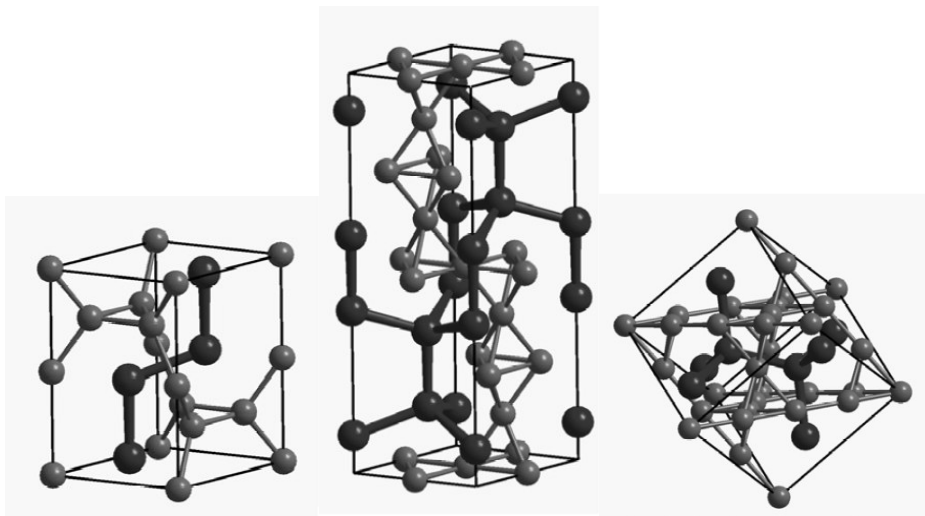


Fig. 5.1 Structure models of the (a) C14, (b) C36 and (c) C15 polytypic crystal structures of Laves phases. Black: A atoms, grey: B atoms

In AB₂ types of Laves phase A and B must not necessarily symbolize only one type of atoms, the corresponding sites in the crystal structure can also be occupied by different atoms resulting in the pseudo binary Laves phases. In case of the transition metal atoms this type of pseudo-binary Laves phases are more probable, because in this case the atomic radii within a series do not vary much, and as a result a considerable homogeneity range is achieved. In case of pseudo binary Laves phase a deviation from the ideal situation is expected due to the occurrence of constitutional point defects. Though the chemical bonding in Laves phases is

predominately of metallic character, but the ionic bond also contributes to different extent depending on the constituting atoms.

It is well known that many of the pseudo binary compounds like AB_2 , can be considered as potential hydrogen storage materials. Many of the AB_2 type pseudo binary compounds show excellent hydrogen absorption-desorption properties and can absorb three hydrogen atoms per molecule [185-187]. Many of the AB_2 compounds has been explored for their different properties such as crystal structure, phase composition, hydrogen absorption-desorption characteristics in the gas phase and charge/discharge characteristics as a cathode material in Ni/MH batteries. The behavior of the AB_2 Laves phase compound changes when both A and B are substituted systematically by other elements.

If we look for the hydrogen absorption sites in the AB_2 types of compounds, we find that, there are different definite hydrogen absorption sites [187, 188]. The interstitial sites are classified according to the types of atom (A or B) surrounding it. For the C14 and C15 Laves phase compounds the absorbed hydrogen may occupy total three types of tetrahedral interstitial site namely A2B2, AB3, and B4 type. There are a total of 17 such interstices per AB_2 formula unit in both the cubic and hexagonal structures (C14 and C15). They are 12 numbers of A2B2, 4 numbers of AB3 and 1 number of B4 sites respectively. The 2A2B site has the largest interstitial hole size and the 4B site has the smallest. Though there are large number of interstitial sites, but all of them do not get occupied because of the geometrical and electrostatic effect. Combining these two effects the maximum sorption of hydrogen is found to be a maximum of about 6 H atoms per AB_2 formula unit. The interstitial sites formed by A and/or B atoms, a ball-stick model of the face centered cubic (fcc) C15 structure is given in Fig. 5.2 (a & b). The interstices, i.e. A2B2-, AB3- and B4-type, are further classified depending on the tetrahedron faces shared. In case of C15 structure, A or B atoms within

each type of sites (2A2B, 1A3B, and 4B) are locally equivalent. This is not the case for the C14 structure. In general, in these ZrB_2 [B = Sc, Ti, V, Cr, Mn, Fe, Co, Ni] compounds, the absolute value of the hydrogen binding energy decreases as the atomic number of B increases; eventually, the atomic hydrogen atoms become unstable in $ZrNi_2$.

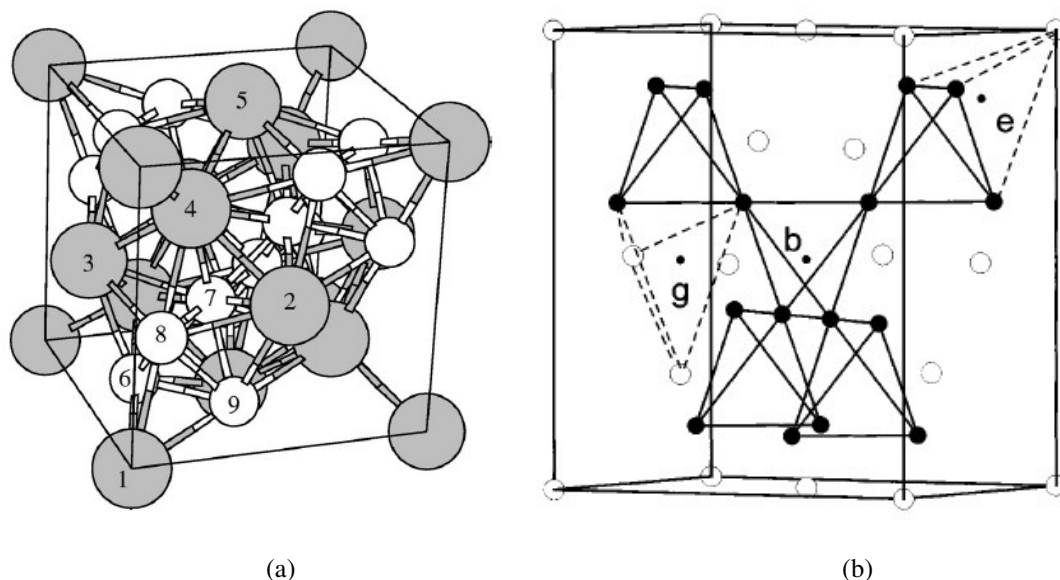


Fig. 5.2 (a) The C15 Laves phase structure, where the larger and smaller balls represent A and B atoms, respectively. Here, for example, 2A2B site is formed by the atoms labeled 2, 4, 7, and 8; a 1A3B site by atoms 1, 6, 8, and 9; and 4B site by atoms 6, 7, 8, and 9. (b) Simplified representation of C15 Laves phase structure, where the white and the black balls represent A and B atoms, respectively. The 2A2B, 1A3B and 4B interstitial sites are represented by g, e and b respectively.

Among the AB_2 series, $ZrFe_2$ intermetallic compound is having C15 Laves phase structure (MgCu₂ type) with lattice parameter of 7.064 Å. At ambient conditions, it can absorb only a small amount of hydrogen to form a solid solution with a composition of $ZrFe_2H_{0.16}$. Jain *et. al.* [190-193] has reported several combinations by substituting Zr and Fe in the $ZrFe_2$ by suitable substitution elements, and found the effect of substituting elements in the Laves phase compounds. The dependence of enthalpy and entropy of dissolved hydrogen in $ZrFe_{2-x}Ni_xH$ ($x = 0.2, 0.4, 0.6, 0.8$) with Ni content is shown. With the increase in Ni

content, enthalpy of the system decreases, this indicates the reduction in the stability of hydride. In $\text{ZrFe}_{2-x}\text{Mn}_x$ alloys, the enthalpies of hydride formation, derived from temperature variation of equilibrium pressure for $x = 0.2, 0.4, 0.6, 0.8$ show the increase of hydride stability with increase in the Mn content. In the hydrogen absorption of $\text{Zr}_{1-x}\text{Cr}_x\text{Fe}_2$ ($x = 0.2, 0.3, 0.4, 0.5$) alloys, the enthalpy of the alloys was found decreasing with the increase in Cr content, so Cr substitution in this system makes these alloys to form less stable hydrides, which is good for practical applications. When Zr is substituted with Co, with increasing Co addition, the unit cell volume decreases. P - C - T curves were measured in the pressure and temperature range of $0.5 \leq P \leq 60$ bar and $303 \leq T \leq 373$ K using a Sievert's type apparatus. The results indicate that with increasing Co content in the samples, the plateau pressure increases whereas hydrogen storage capacity and stability decreases.

In the present work, we have substituted different amount of V for Fe in ZrFe_2 Laves phase alloy, and demonstrated its effect on phase formation, hydrogen absorption desorption properties, hydrogen absorption capacity and thermodynamic stability. As we have discussed earlier that ZrB_2 compounds, the absolute value of the hydrogen binding energy decreases as the atomic number of B increases, so we can stabilize the hydride of ZrFe_2 compound by substituting Fe with V. As V is a good hydride forming element so it can increase the stability of the hydride for the practical application of the metal hydride batteries at room temperature. The samples studied in this work are (a) $\text{ZrFe}_{1.8}\text{V}_{0.2}$ (b) $\text{ZrFe}_{1.6}\text{V}_{0.4}$ (c) $\text{ZrFe}_{1.4}\text{V}_{0.6}$ and (d) $\text{ZrFe}_{1.2}\text{V}_{0.8}$. This chapter is divided into three sections.

5.1 Experimental Details

5.2 Results and discussion

5.3 Conclusion

5.1 Experimental Details

ZrFe_{2-x}V_x (x = 0.2, 0.4, 0.6, 0.8) alloys were prepared by arc melting the appropriate ratio of the constituent metals, of purity better than 99.8 %, in a water cooled Cu hearth under an argon atmosphere. The alloy ingot was arc melted several times to ensure homogeneity. The crystal structures of the alloys were examined by X-ray diffraction (XRD) using monochromatic CuK_α radiation. Hydrogen absorption-desorption studies and kinetics were carried out using a standard Sievert's type set up. The activation procedure involved heating the sample under diffusion vacuum (10⁻⁶ mbar) for 2 hours at 673 K. After activation, the sample was cooled to the working temperature under vacuum, followed by introduction of hydrogen gas into the reaction chamber. Pressure-composition isotherms were studied in the temperature range 298-523 K and up to a hydrogen pressure of 2 MPa, using freshly crushed samples. The surface poisoning of the hydride samples were done by air exposure at liquid nitrogen temperature.

The amount of total hydrogen in the hydrides was estimated by monitoring the change in the hydrogen pressure during the absorption process. The saturation composition was also determined by complete decomposition of a small amount of the hydride sample in an evacuated and calibrated chamber.

The temperature programmed desorption (TPD) measurements were done using an automated TPD instrument up to 1073 K, at a constant heating rate of 10 K/min. High purity argon was used as the carrier gas.

5.2 Results and Discussion

5.2.1 Compositional studies

The weight of the constituent elements before melting of the alloy and after melting is found to be same indicating that there may be no oxidation during the melting. To ensure the homogeneity of the alloy, compositional study has been done by EDX at different positions of the alloy. The EDX graphs for the alloys are shown in Fig 5.3. The EDX data has been listed in Table 5.1.

Table 5.1 EDX data of $ZrFe_{2-x}V_x$ ($x = 0.2, 0.4, 0.6, 0.8$) alloys.

Composition	Element	Weight %	Atom %
ZrFe_{1.8}V_{0.2}	V K	5.00	6.45
	Fe K	54.98	64.71
	Z L	40.02	28.84
ZrFe_{1.6}V_{0.4}	V K	10.50	13.62
	Fe K	47.02	55.62
	Z L	42.48	30.76
ZrFe_{1.4}V_{0.6}	V K	16.05	20.60
	Fe K	42.40	49.63
	Z L	41.55	29.77
ZrFe_{1.2}V_{0.8}	V K	20.06	26.36
	Fe K	32.25	38.65
	Z L	47.69	34.99

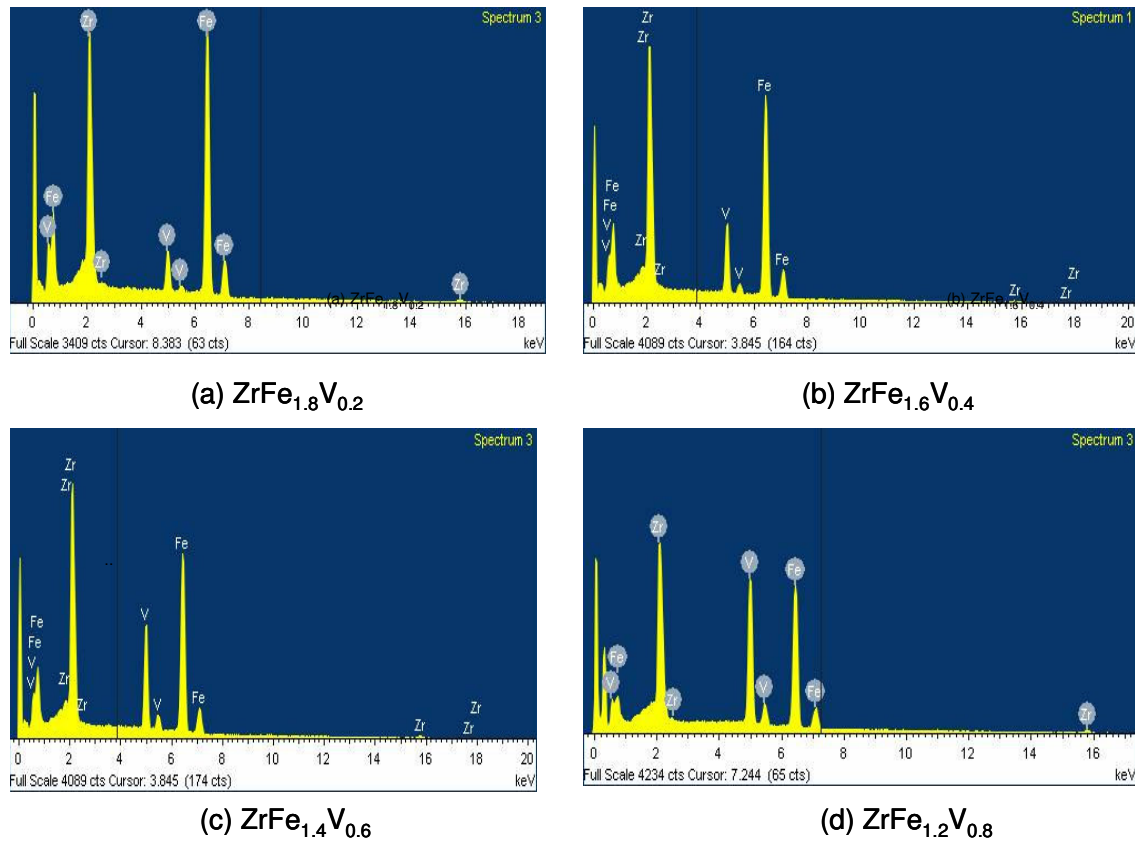


Fig. 5.3 The EDX mapping of $\text{ZrFe}_{2-x}\text{V}_x$ ($x = 0.2, 0.4, 0.6, 0.8$) alloys

5.2.2 Crystal structure of the alloys and their corresponding hydrides

Let us first discuss the structures of the $\text{ZrFe}_{2-x}\text{V}_x$ alloys. The XRD patterns of the compositions ZrFe_2 , $\text{ZrFe}_{1.8}\text{V}_{0.2}$, $\text{ZrFe}_{1.6}\text{V}_{0.4}$ and $\text{ZrFe}_{1.4}\text{V}_{0.6}$ and $\text{ZrFe}_{1.2}\text{V}_{0.8}$ shown in Fig 5.4. It has been found that ZrFe_2 shows pure C15 Laves phase structure (MgCu_2 type) with lattice parameter of 7.064 \AA . In case of V substituted alloys, we observe that small amount of V substitution (upto $x = 0.2$) does not lead to any change in the lattice structure but only the lattice parameter changes.

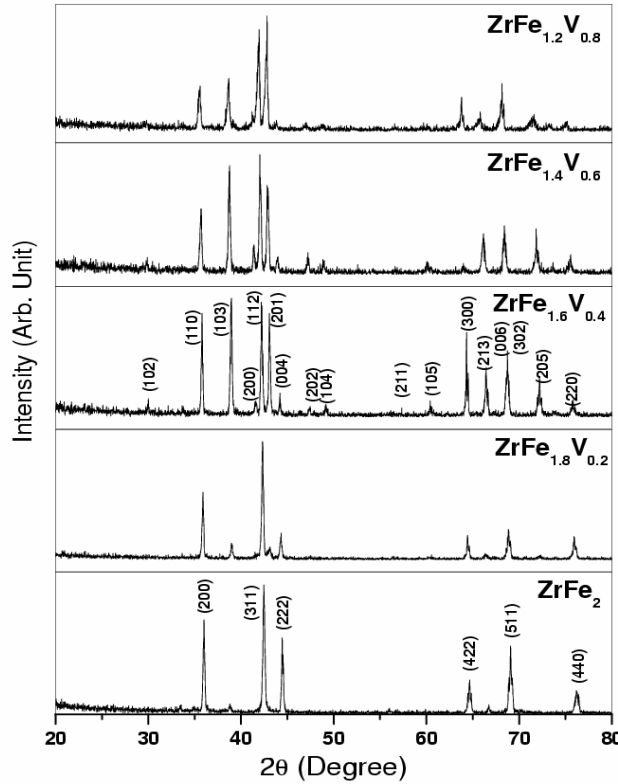


Fig: 5.4 The X-Ray diffraction profile of alloys. The numbers in the parenthesis represent the respective lattice planes.

As the atomic radius of the V atom (1.92 Å) is more than that of the Fe atom (1.72 Å), so with the vanadium substitution, the lattice parameter increases slightly and the peaks shift towards lower 2θ values. As an example, $\text{ZrFe}_{1.8}\text{V}_{0.2}$ shows a C15 cubic Laves phase structure with lattice parameter of 7.085 Å, slightly higher than that of the ZrFe_2 . If the V content is increased further ($x \geq 0.4$), the C15 cubic structure transforms into C14 hexagonal structure (MgZn_2 type). In the present study the alloys with compositions $\text{ZrFe}_{1.6}\text{V}_{0.4}$ and $\text{ZrFe}_{1.4}\text{V}_{0.6}$ and $\text{ZrFe}_{1.4}\text{V}_{0.8}$ show C14 Laves phase structure and as expected in this case also, the lattice parameter increases with increase in the V. The lattice parameters of $\text{ZrFe}_{1.6}\text{V}_{0.4}$ are $a = 5.02$ Å and $c = 8.192$ Å.

Table 5.2 The lattice parameters and hydrogen storage capacities of $ZrFe_{2-x}V_x$ alloy ($x = 0.2, 0.4, 0.6, 0.8$)

Composition	Lattice Structure	Lattice Parameter (Å)	Composition of the hydride	Hydrogen Storage Capacity	Enthalpy of formation of the hydrides (KJ/mole)
$ZrFe_2$	C15	7.064	$ZrFe_2H_{0.16}$		
$ZrFe_{1.8}V_{0.2}$	C15	7.085	$ZrFe_{1.8}V_{0.2}H_{2.52}$	1.3	25.1
$ZrFe_{1.6}V_{0.4}$	C14	a = 5.02, b = 8.19	$ZrFe_{1.6}V_{0.4}H_{3.26}$	1.6	29.5
$ZrFe_{1.4}V_{0.6}$	C14	a = 5.04, b = 8.22	$ZrFe_{1.4}V_{0.6}H_{3.61}$	1.77	35.9
$ZrFe_{1.4}V_{0.8}$	C14	a = 5.05, b = 8.24	$ZrFe_{1.4}V_{0.8}H_{3.78}$	1.85	41.8

We have plotted the variation of cell volume as a function of V concentration in the studied alloys in Fig. 5.5 and found that there is a systematic increase in the cell volume with the increase in the V concentration as the atomic radius of V is more than that of the Fe atom. The higher affinity of the V atom towards hydrogen compared to the Fe atom, and the higher atomic radius of V atom compared to that of the Fe atom, influence the hydrogen storage properties of this type of alloy profoundly, which can be seen in their hydrogen storage properties.

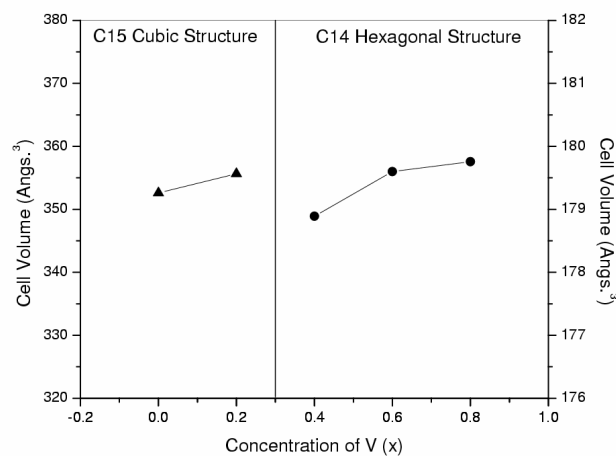


Fig. 5.5 Variation of lattice volume with the V substitution. The variation in volume both for the C14 and C15 structures are shown separately.

The XRD patterns of the hydrides have been shown in Fig. 5.6. We have not plotted the hydride of $ZrFe_2$ as in the ambient condition as it can absorb only a small amount of hydrogen to form a solid solution with composition $ZrFe_2H_{0.16}$. All the hydrides show similar structures as of their parent alloys, with an increased lattice parameter. It can be noted that during the hydride formation all the alloys go into powder form due to the expansion of cell. From the volume expansion and the number of hydrogen atom absorbed it has been calculated that the volume expansion due to hydrogenation is around 2.9 \AA^3 per hydrogen atom. No evidence of ZrH_2 phase separation is found in any of the alloy.

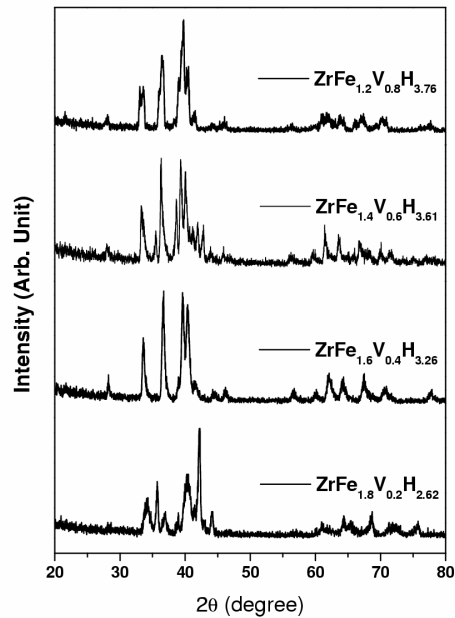
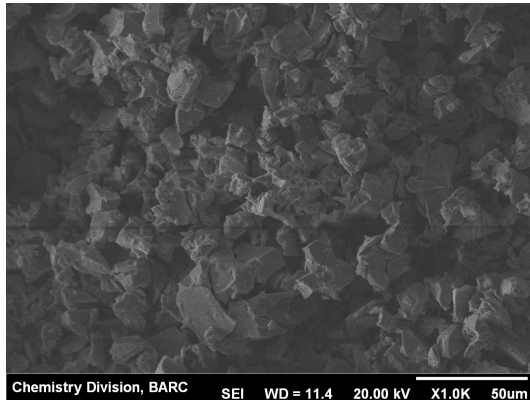
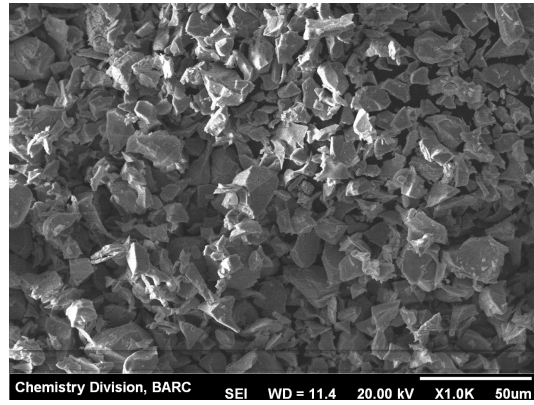


Fig. 5.6 The X-Ray diffraction profile of the saturated hydrides of the alloys

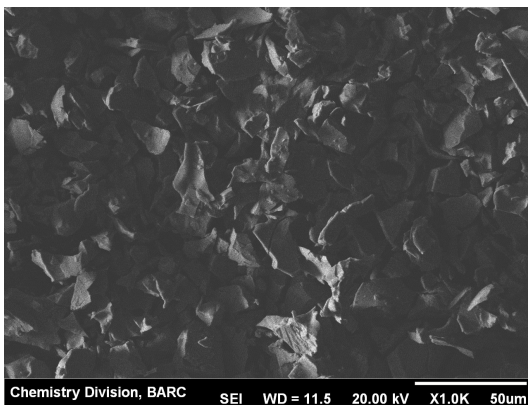
Fig. 5.7 (a-d) shows the SEM pictures of the hydrides of the alloys after four absorption desorption cycle. From the SEM picture we can explain the broadening of peak of the XRD of the hydrides also.



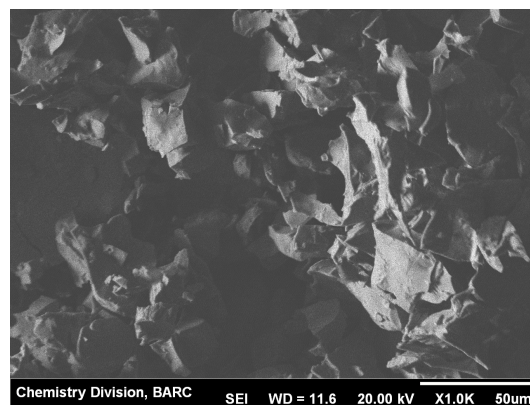
(a)



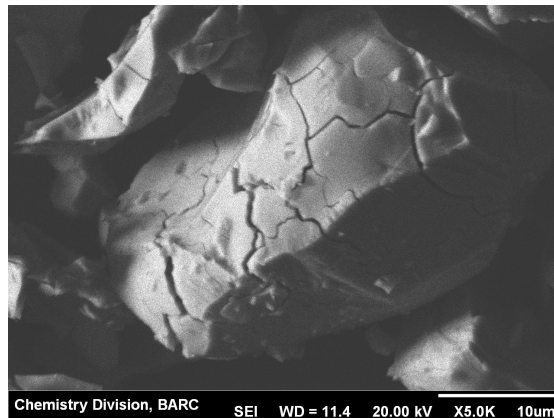
(b)



(c)



(d)



(e)

Fig. 5.7 The SEM pictures of the hydrides after four absorption-desorption cycle (a-d). (a) $ZrFe_{1.8}V_{0.2}H_{2.52}$ (b) $ZrFe_{1.6}V_{0.4}H_{3.26}$ (c) $ZrFe_{1.4}V_{0.6}H_{3.61}$ (d) $ZrFe_{1.4}V_{0.8}H_{3.78}$ (e) The cracks formed on $ZrFe_{1.8}V_{0.2}$ surface during interaction with hydrogen.

In the SEM picture Fig. 5.7 (e), we observed a lot of cracks on the particles during hydride formation. Initially when the alloy starts absorbing hydrogen, then crack formation occurs at the surface of the alloy and more and more hydrogen penetrate through the crack. By this way the alloy goes into the powder form and the particle size decreases. During that process lots of strain created in the particle which is resulted in the XRD peak broadening. Alloys with higher V content to get pulverized better due to the higher H content. Along with the strain, the size of the particle also decreases with cycling, that results in the peak broadening in the XRD patterns.

5.2.3 Hydrogen absorption studies of different compositions

It has been stated earlier that the compound ZrFe_2 absorbs a maximum of 0.16 H atoms/formula unit forming a hydride with a composition, $\text{ZrFe}_2\text{H}_{0.16}$ at room temperature. This hydrogen absorption capacity is observed at a hydrogen pressure of 20 atm. As the hydrogen absorption capacity is very low the potentiality of ZrFe_2 as a hydrogen storage element is nil.

Now we describe the change in the hydrogen storage capacity of ZrFe_2 , if V is substituted in place of Fe. The maximum hydrogen absorption capacities of alloys with the compositions $\text{ZrFe}_{1.8}\text{V}_{0.2}$, $\text{ZrFe}_{1.6}\text{V}_{0.4}$, $\text{ZrFe}_{1.4}\text{V}_{0.6}$, and $\text{ZrFe}_{1.2}\text{V}_{0.8}$ are listed in Table 5.2. $\text{ZrFe}_{1.8}\text{V}_{0.2}$ alloy absorbs 2.52 H/formula unit. The result shows that, with V substitution in place of Fe in ZrFe_2 , the alloy transforms into a good hydrogen absorbing material. The alloys $\text{ZrFe}_{1.6}\text{V}_{0.4}$, $\text{ZrFe}_{1.4}\text{V}_{0.6}$ and $\text{ZrFe}_{1.2}\text{V}_{0.8}$ absorb 3.26, 3.61 and 3.78 H/formula unit respectively. The alloy with highest concentration of V, $\text{ZrFe}_{1.2}\text{V}_{0.8}$ has been found to absorb maximum amount of hydrogen within the studied series to form $\text{ZrFe}_{1.2}\text{V}_{0.8}\text{H}_{3.78}$ at around 20 atm. pressures. So with increase in the V concentration the hydrogen storage capacity

increases systematically. As when we replace Fe atom with V atom, there is a decrease in the 3d occupation number in the transition elements which leads to the better hydrogen storing capacity. So basically here two factors play major role for the increase in the hydrogen storage capacity. First, as V is better hydride forming element than Fe, so in this case the substitution of Fe atom with V atom leads to the higher hydrogen storage capacity. Secondly, the size of the V atom is more than that of the Fe atom, so as the cell volume increases with V substitution, as a result the volume of the interstitial positions increases and it leads to more hydrogen storage capacity.

Now let us discuss the hydrogen absorption-desorption behavior of different compositions at different temperatures. In the present case the hydrogen absorption-desorption studies have been done at four different temperatures (300 K, 323 K, 350 K, and 373 K). The isotherms at 298 K and 373 K have been shown in Fig. 5.8 for all the alloys. It has been found from Fig. 5.8, that $\text{ZrFe}_{1.8}\text{V}_{0.2}$ shows a high absorption-desorption plateau at room temperature. The plateau region is not absolutely flat and significant slope is found to be in that region. The desorption plateau pressure decreases significantly with the increase in the V concentration and also the flatness of the plateau increases. For all the cases with increase in the temperature the plateau pressure increases and the plateau region decreases which is the characteristics of the PCT diagram. It has been found from the PCT diagrams that with increase in the V concentration the hysteresis increases slightly, whereas $\text{ZrFe}_{1.8}\text{V}_{0.2}$ alloy does not show any hysteresis at higher temperature.

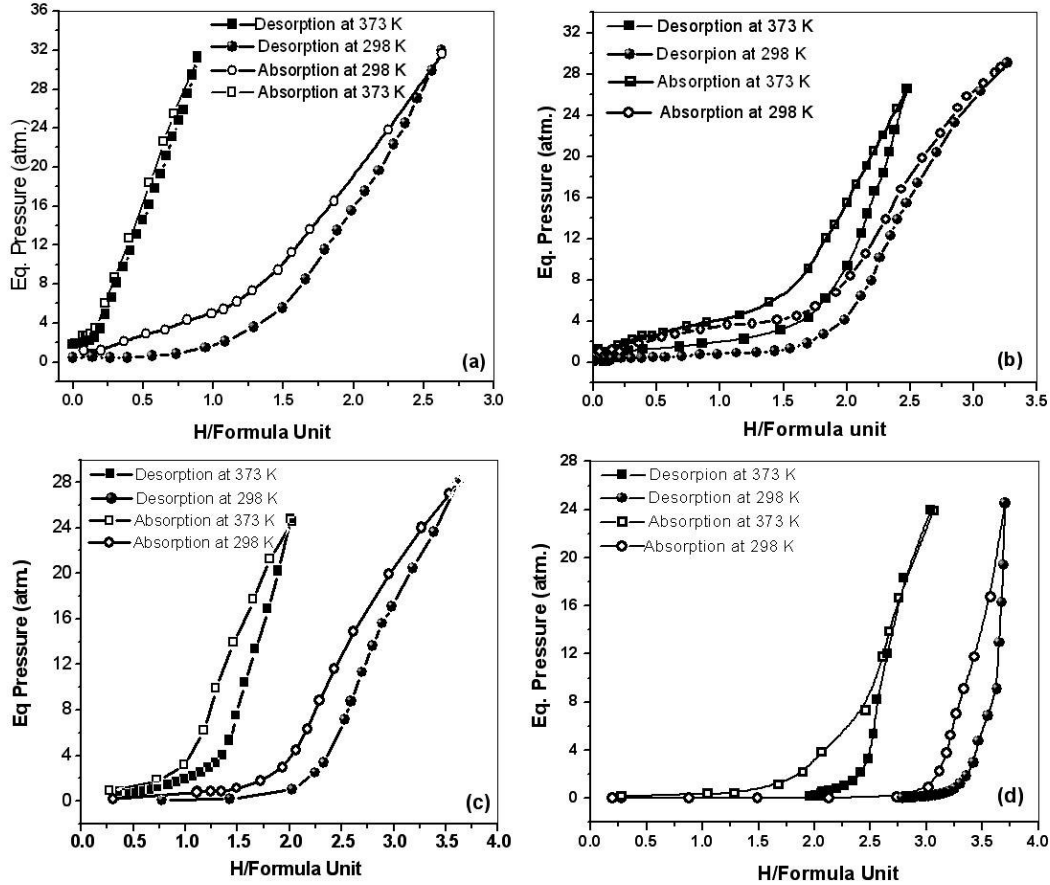


Fig. 5.8 The pressure composition isotherm of (a) $ZrFe_{1.8}V_{0.2}$ (b) $ZrFe_{1.6}V_{0.4}$ (c) $ZrFe_{1.4}V_{0.6}$ and (d) $ZrFe_{1.2}V_{0.8}$ at 298 and 373 K.

By determining the desorption plateau pressures at different temperatures, for a certain composition, we could find out the enthalpy value of formation of the corresponding hydrides. As the hydrides are forming a sloping plateau so the plateau pressure has been taken at the middle of plateau region (P).

According to the vant' Hoff equation,

$$\frac{1}{2}(\ln P) = \frac{\Delta H}{RT} - \frac{\Delta S}{R},$$

where R is the real gas constant: 8.314 J/mol K, T the thermodynamic temperature. So the enthalpy and entropy of hydride formation can be calculated from the van't Hoff plot of $\frac{1}{2}(\ln P_{1/2})$ versus $1/T$. The enthalpy (ΔH) and entropy (ΔS) of hydride formation have been

derived by utilizing the least square technique from the slope and from the intercept respectively of the Van't Hoff plot shown in Fig. 5.9.

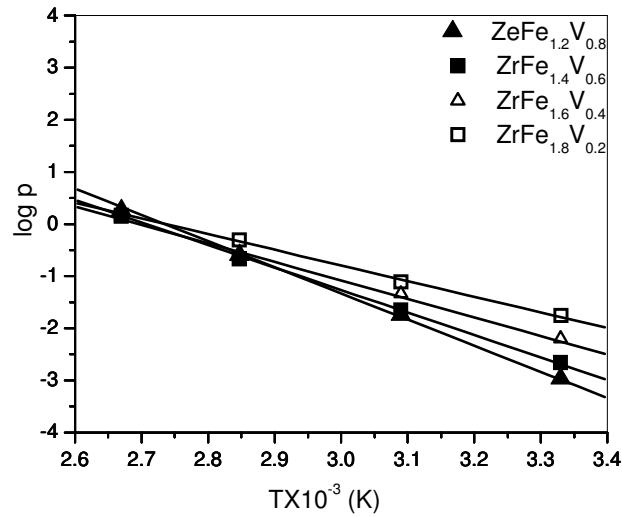


Fig. 5.9 Van't Hoff plots for $ZrFe_{2-x}V_x$

The variation of enthalpy of hydrogen absorption with the increase of V concentration, obtained by van't Hoff plots are depicted in Fig. 5.10. It as been found from the figure that, with increase in the V concentration, the slope of the fitted straight line increases, which indicates the increase in the absorption enthalpies of the hydrides.

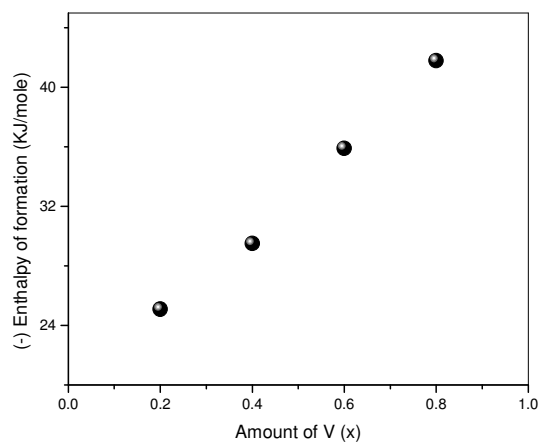


Fig. 5.10 The variation of enthalpy of formation of $ZrFe_{2-x}V_x$ ($x = 0.2, 0.4, 0.6, 0.8$)

The practical significance of enthalpy of formation (ΔH) is that, it is an index of the thermochemical stability of the metal hydride. High value of $(-\Delta H)$ represents low dissociation pressure and the requirement of moderately higher temperature to decompose it to liberate the hydrogen from the hydride. From the above studies it can be concluded that $ZrFe_{2-x}V_x$ pseudo binary compounds can be tailored to make suitable hydrogen absorbing material. The enthalpy of formation values of different hydrides has been tabulated in table 5.2.

5.2.4 Temperature programmed desorption

Temperature Programmed Desorption Profiles are shown in Fig. 5.11 for different V doped $ZrFe_2$ hydrides to compare between desorption temperatures and number of sites for desorption of hydrogen. Though the TPD profile is not corresponding to the exact desorption temperature for a certain alloy, as the hydride was poisoned with oxygen before taking out in the atmosphere, but certainly the profile can give good comparison between the desorption temperature of different hydrides. From the TPD data of $ZrFe_{1.8}V_{0.2}H_{2.62}$ it can be seen that desorption of hydrogen starts at 140 °C and the peak temperature is 195 °C.

The desorption profile for the hydride is very sharp compared to the other V substituted samples due to the fact that it consist of only C15 cubic Laves phase structure where as the other hydrides consist of two phase structure. So due to the presence of more than one desorption sites the desorption peaks become broad in case of $ZrFe_{1.6}V_{0.4}$, $ZrFe_{1.4}V_{0.6}$, and $ZrFe_{1.2}V_{0.8}$ hydrides. The comparison between the desorption temperatures of $ZrFe_{1.6}V_{0.4}$, $ZrFe_{1.4}V_{0.6}$, and $ZrFe_{1.2}V_{0.8}$ hydrides also have been shown in Fig 5.11. $ZrFe_{1.6}V_{0.4}H_{3.26}$ shows two desorption peaks at temperatures of 240 °C and 310 °C respectively. In case of $ZrFe_{1.4}V_{0.6}H_{3.61}$ the desorption peaks come at 235 °C and 341 °C. $ZrFe_{1.2}V_{0.8}H_{3.78}$ shows still higher desorption temperature and it shows two desorption peaks

at 360 °C and 450 °C respectively. So from desorption peak temperatures it reveals that with increasing V concentration, the hydrogen desorption temperature increases. This may be attributed to the fact that with increasing V concentration the relative stability of the hydride increases and hence the hydrogen desorption takes place at a higher temperature.

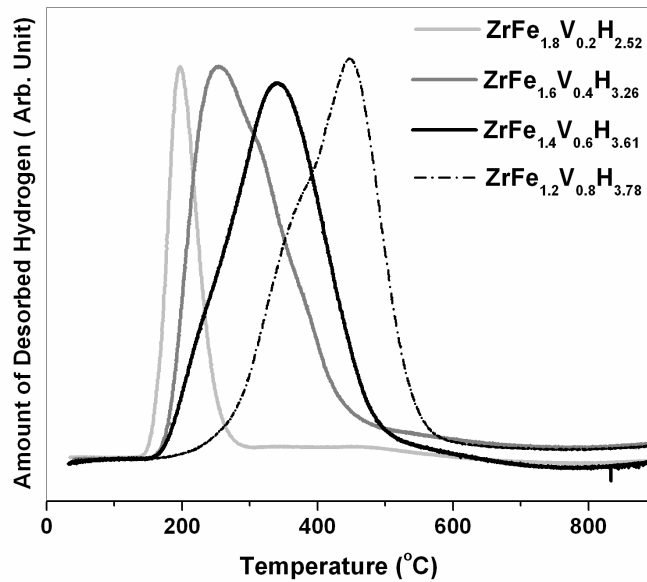


Fig. 5.11 Temperature programmed desorption profile of the air exposed hydrides of $ZrFe_{1.8}V_{0.2}$, $ZrFe_{1.6}V_{0.4}$, $ZrFe_{1.4}V_{0.6}$ and $ZrFe_{1.2}V_{0.8}$ hydrides

5.3 Conclusion

In this chapter the systematic improvements of the hydrogen storage capacity of $ZrFe_2$ Laves phase compound by V substitution is described. It has been found from the above study that, with increase in the V substitution, the cell parameter increases and the lattice gets transform from the C15 structure towards the C14 structure. Where as $ZrFe_2$ forms unstable hydride, with the increase in the V concentration, the stability of the hydrides increases. Due to the higher stability of the hydride, the plateau pressure decreases in the pressure composition isotherm. This phenomenon gets reflected in the van't Hoff diagram also and it has been found that the hydrogen absorption enthalpy increases with increase in the V

concentration. The formation enthalpy of the hydride of $\text{ZrFe}_{1.2}\text{V}_{0.8}$ is found to be -41.8 KJ/mol, which is close to the enthalpy value required for the room temperature absorption-desorption of hydrogen.

Chapter VI

Theoretical Methodology

Quantum mechanics predicts the behavior of a particle, using a set of principles, with known elementary properties such as rest masses and charges. The equation which represents the quantum aspect of a material is the Schrödinger equation. The exact solution of the Schrödinger equation is possible in principle, and from that solution one can access all the properties of a material of any size. Quantum mechanical calculations, including both non-empirical and semi-empirical methods, are used extensively for the calculation of the interaction energy of hydrogen with different hydrogen storage systems and their feasibility for practical applications [194-202]. For the non-empirical methods, especially Hartree Fock plus the correlation energy, needs a very high computational time as it use a larger basis set. This is due to the fact that in the wave functional based calculation, a wave function of N electron system contains $3N$ coordinates. So for larger systems, where the numbers of electrons are high, the wave function based methods are not desirable and the problem becomes practically unsolvable. In the Hartree Fork approach the correlation energy has not been taken into consideration. To take account of the dynamic correlation term, correlation methods has to be used, which needs multi-determinant wave function and their scales are of the fifth or greater power with the size of the system. The best method to avoid this type of complexity, which enables us to describe larger systems, is the Density Functional Theory.

The chapter starts with a short introduction of the Schrödinger equation, Born Oppenheimer Approximation and wave function based methods. Density Functional Theory (DFT), which we have used extensively for the electronic structure calculations of many body cluster and periodic systems, is discussed next, followed by the exchange correlation schemes, basis sets and the pseudo potential approaches. The technical details for the modeling of a periodic system also have been discussed briefly in this chapter. At last we have discussed the details of calculations of some physical properties. So the chapter is divided into eight sections.

6.1 The Schrödinger Equation

6.2 Born Oppenheimer Approximation

6.3 Wave Functional Based Calculation

6.4 Density Functional Based Calculation

6.5 Exchange Correlation Function

6.6 Basis Set

6.7 Pseudo Potential

6.8 Modeling of a Periodic System

6.9 Calculation of Physical Properties

6.1 The Schrödinger Equation

In 1926, Erwin Schrödinger described the quantum aspect of matter by a fundamental equation known as Schrödinger equation. If M nuclei and N electrons interact with each other then the time independent Schrödinger equation is

$$\hat{H} \Psi_i(r_1, r_2, \dots, r_N, R_1, R_2, \dots, R_M) = E_i \Psi_i(r_1, r_2, \dots, r_N, R_1, R_2, \dots, R_M)$$

where, \hat{H} denoted the Hamiltonian, Ψ_i is the wave function or set of solutions, which depends on all the electronic (r) and nuclear coordinates (R) and E is the Eigen value corresponding to the state.

In principle the above equation can be applied to any system regardless of the size, and can be solved exactly. But in practical situation, since the number of variables to deal with is determined by 3(M+N) degrees of freedom, it makes the exact solution of the Schrödinger equation computationally unaffordable for larger systems and some sensible approximations are used to solve it. So, at this point it is needed to apply some approximations, which practically affords the solution of the Schrödinger equation.

6.2 Born-Oppenheimer Approximation

The Born-Oppenheimer (B-O) approximation [203] implies the separation of nuclear and electronic wave functions.

$$\Psi(r, R) = \Psi_{\text{electronic}}(r, R) \times \Psi_{\text{nuclear}}(R)$$

The motivation behind this approximation is the significant mass differences between the nuclei and the electrons. The nuclei are much heavier than the electrons so move much slowly, or in other words, electrons are so much lighter than the nuclei and their motion can easily follow the nuclear motion.

In the first step of B-O Approximation, the nuclear positions are freezed at the origin (nuclear kinetic energy is zero in the electronic Hamiltonian) and the electronic Schrödinger equation, which depends only on the electronic coordinate, is solved. However, it is important to remember that the electronic energy is not the total energy of a system. Within the Born-Oppenheimer approximation, we estimate the total energy by adding the nuclear-

nuclear repulsion energy and the nuclear kinetic energy to the total electronic energy of equation.

6.3 Wave Function Based Calculations

The heart of the wave function based calculation is the central field approximation, which states that an electron moves in its own orbital in a potential created by all other electrons and the nucleus. The many electron wave functions can be written as the simple product of one electron wave function.

$$\Psi = \Psi_1(r)\Psi_2(r)\Psi_3(r)\dots\dots\Psi_N(r)$$

The product is called the Hartree product.

A many particle wave function describing electrons is forced to obey the Pauli Exclusion Principle, i.e., no electrons in the same system are allowed to have the same set of quantum numbers, or the wave function needs to be antisymmetric. One such wave function is Slater determinant [204].

By varying the spatial part of the Slater determinant, i.e., the molecular orbital, the total energy can be minimized. The value of the energy that is obtained is an upper bound of the exact solution according to the variational principle [205]. This is known as the Hartree-Fock approximation [206-208]. The solution is an approximation, as the Coulomb interaction between electrons can not be separated, thus, the exact solution can not be a product of one-particle wave functions. The Hartree-Fock approximation was made more practical for numerical solutions by Roothaan in 1951 [209], who introduced the concept of basis sets. The molecular orbital are represented as a linear combination of prescribed three-dimensional one-electron wave functions.

Energies calculated by the HF method are typically in error by 0.5 % to 1% of the total energy [206]. Though an absolute basis this is not too much, but it is of the order of the chemical bond energy. So, to study the clusters having weak interaction, one needs to improve on the HF energy. The motions of electrons are correlated with each other and this is called electron correlation. The electron correlation energy is the difference between the exact non-relativistic energy and HF energy of the systems (clusters). The wave function in HF method is single determinant, not capable of considering the correlation of the electron motion. To include the electron correlation energy several *ab-initio* post HF multi-determinant methods are constructed, namely, second order Moller-Plesset perturbation theory (MP2), Configuration interaction (CI), Coupled cluster (CC) etc. It is well known that all these methods are costly ones and some time it is impossible to calculate the geometry of a larger system by applying these methods. Density functional theory (DFT) is developed to improve the time requirement over the *ab-initio* correlated methods like MP2, CC, etc.

6.4 Density Functional Theory

The definite characteristics of DFT are that it considers the ground state electron density distribution (n_0) of a system, instead of many body wave functions itself. Since real space is only three dimensional, regardless of the number of electrons in the system, the required minimization is with respect to only 3 variables and not $3N$ variables. In practice if the system is having a net magnetic moment, one may need to perform spin-density functional theory calculations which is a function of six variables.

The density functional theory states that the ground state energy is completely determined by the diagonal elements of the first order density matrix – the charge density. The density functional theory is stands on the two theorems by Hohenberg and Kohn [210].

The first theorem states that “The total energy in the ground state in an external potential ‘v’ is a unique functional of electron density $n(r)$ ”

$$-E_v[n] \equiv F[n] + \int v(r)n(r)dr$$

$F[n]$ is a universal function and valid for any number of particles and any external potential. The Hamiltonian operator is specified by the external potential and the total number of electrons N . The external potential (v) which can be computed from electron density, and it is unique functional of electron density. Since in turn the external potential fixes the Hamiltonian, so the extension of the theorem is that the Hamiltonian operator can be uniquely determined by the electronic density and thus ψ and all other material properties can be computed.

The second theorem established a variational principle:

“For any positive definite trial density n_t , such that $\int n_t(r)dr = N$, then $E[n_t] \geq E_0$ ”

The theorem restricts density functional theory to study the ground state.

6.4.1 The Energy Functional

The energy functional contains three terms, the kinetic energy ($T[n]$), energy due to external potential ($V[n]$) and the electron - electron interaction energy ($U[n]$).

$$E_v[n] = T[n] + V[n] + U[n]$$

$$E_v[n] = F[n] + V[n]$$

The energy due to external potential is known and can be found out exactly by the following equation:

$$V [n] = \int v(r)n(r)dr$$

The long range classical Columbic repulsion energy (Hartree Energy – known exactly) can be separated out from the $F[n]$ conveniently.

$$F[n] = \frac{1}{2} \iint \frac{n(r)n(r')}{|r-r'|} drdr' + G[n],$$

where $G[n]$ is another universal functional of the density.

To find out an approximation of $G[n]$, Kohn and Sham [211] have proposed a scheme which contains a major part of the effects of exchange and correlation. So $G[n]$ can be written as

$$G[n] \equiv T_{KS}[n] + E_{xc}[n]$$

$T_{KS}[n]$ kinetic energy of a fictitious system of N non interacting electrons with density $n[r]$.

The electrons can be described by a single determinant wave function in N “orbitals” ϕ_i and the exact kinetic energy and electronic wave function can be calculated by the following equation:

$$T_{KS}[n] = -\frac{1}{2} \sum_i^N \langle \phi_i | \nabla^2 | \phi_i \rangle$$

and the true ground state density of the non interacting electrons is $n(r) = \sum_i^N |\phi_i|^2$

$E_{xc}[n]$ is the exchange correlation functional of a system of interacting electrons with density $n(r)$, and it contains all part of the energy that cannot be handled properly. Though it is called exchange correlation functional, but it includes the errors made in using the non interacting kinetic energy, and the error made (exchange and correlation energy) in treating electron – electron interaction energy classically. The electron exchange arises because a many body wave function must be anti-symmetric under the exchange of any two electrons as the electrons are Fermions. This anti symmetry of the wave function, which simply a general expression of the Pauli Exclusion Principle, reduces the coulomb Energy of the electron

system by increasing the spatial separation between electrons of like spin. Like wise the electron correlation further reduces the Coulomb energy between electrons of unlike spin because the motion of each individual electron is correlated with the motion of all others, also to keep electrons of unlike spin spatially separated. Putting the expressions for the non interacting system and the interaction due to the external potential in the equation of the energy functional we get:

$$E[n] = T_{KS} + \int v(r)n(r)dr + \frac{1}{2} \iint \frac{n(r)n(r')}{|r-r'|} drdr' + E_{xc}[n]$$

For an arbitrary $n(r)$ there is no exact expression for $E_{xc}[n]$. However if $n(r)$ is sufficiently slow varying then

$$E_{xc}[n] = \int n(r)\epsilon_{xc}(n(r))dr,$$

where, ϵ_{xc} is the exchange and correlation energy per electron of a uniform electron gas [212, 213].of density n and the corresponding Schrödinger equation is

$$\left[-\frac{1}{2}\nabla^2 + v(r) + \int \frac{n(r)n(r')}{|r-r'|} drdr' + \epsilon_{xc}(r) \right] \phi_i(r) = \epsilon_i \phi_i(r)$$

From the above discussion it can be stated that the utility of the density functional theory rests on the approximation used for the exchange correlation effect of the system under consideration, as the other form of the functional are known exactly.

6.4.2 Limitations of DFT

1. Density functional theory calculations do not give the exact solution due to the approximations used in the exchange correlation part. Careful comparison should be done with available experimental results before choosing correct exchange correlation function.
2. Hohenberg Kohn Sham theorem applied to ground state only.

3. Density functional theory under estimates band-gap.
4. DFT cannot deal van der Waals interaction accurately as the van der Waals interactions are a direct results of long range electron correlation.

6.5 Exchange Correlation Functions

There are two types of approximations are mostly used for $E_{xc}[n]$ namely Local Density Approximation (LDA) and Generalized Gradient Approximation (GGA).

6.5.1 Local density approximation (LDA)

The Local Density Approximation [214, 215] may be considered as the zeroth order approximation to the semi classical expansion of the density matrix in terms of the density and its derivative. The Local Density Approximation the inhomogeneous electronic system are considered to be locally homogeneous, and then the exchange correlation hole corresponding to the homogeneous electron gas is used, for which there are very good approximations are available. The local exchange correlation energy per electron might be approximated as a simple function of the local charge density ($\epsilon_{xc}(\rho)$). This is an approximation in the form

$$E_{xc}[n] \approx \int n(r)\epsilon_{xc}(n(r))dr$$

As within LDA $\epsilon_{xc}(\rho)$ is only function of local value of density so it can be separated into exchange and correlation contributions.

$$\epsilon_{xc}(n) = \epsilon_x(n) + \epsilon_c(n)$$

The accurate value of the exchange correlation function can be obtained using Direc form

$$\epsilon_x(n) = -\frac{3}{4} \left[\frac{3}{\pi} n \right]^{1/3}$$

The functional form of $\epsilon_c(\rho)$ is unknown and for homogenous electron gas it can be simulated by different approaches and mostly done by using numerical quantum Monte Carlo calculations. In LDA approximation the exchange energy is generally under estimated where as the correlation energy is over estimated, but due to the cancellation error the approximation is quite successful in many of the bulk materials as there the valance electron density varies quite slowly. The LDA approximation is fruitful in case of certain property calculation such as structures, vibrational frequencies, elastic moduli and phase stability. But the binding energy and energy barrier calculation of certain systems may have significant error.

6.5.2 Generalized gradient approximation

In Generalized gradient approximation to take account for the inhomogeneity of the electron density, a first order gradient term in the expansion is included; as a result the energy function depends both on the density and its gradient. The use of the GGA is mandatory for calculating adsorption energies, but the choice of the correct GGA is important.

The typical form of the GGA functional is

$$E_{xc}[n] \approx \int n(r) \epsilon_{xc}(n, \Delta n) dr$$

GGA improves significantly over the LDA approximation for the binding energy calculation (LDA leads to bond energies and cohesive energies too large) and it makes the approximation very popular and widely accepted. Many other functional are being developed based on different approximations called Meta-GGA functionals, Hybrid exchange functionals and development of more accurate functional is an ongoing process [Table 6.1]. Here we have listed some of the popular exchange correlation functional [216-218].

Table 6.1 Mnemonics used to define density functional of various families

Mnemonic	Family
LDA	Local
BLYP [219, 220]	GGA
PBE Perdew, Burke, Ernzerhof, [217]	GGA
HCTH	GGA
VS98	Meta-GGA
PKZB	Meta-GGA
Hybrid	Hybrid-exchange

6.6 Basis Set

The purpose of a basis set [221-224] is to express any unknown arbitrary function ψ as a sum of known basis function

$$\Psi = \sum_i^M C_i \phi_i$$

The basis set is said to be complete if M is infinity and ψ is represented accurately. But in practical no one use complete (infinite) basis set as the cost of the calculation is very high. In practice, M is finite and the representation of basis set is approximate. The error due to the incompleteness of basis set is called the basis set truncation error. A key computational consideration therefore is to keep the number of basis function low, but to choose them cleverly so that the basis set truncation error is small.

An unknown molecular orbital can be expanded in terms of known atomic orbitals using similar mathematical expression. The basis functions $\phi_1 \phi_2 \dots \phi_n$ should be chosen such that ψ should be single valued, finite, continuous and quadratically integrable. The most widely used three basis sets are:

1. Slater Orbital
2. Gaussian orbital
3. Plane Wave Basis Set

We will discuss them one by one in the following portion.

6.6.1 Slater type orbital (STO)

The Slater type of orbitals can be used for the most accurate calculations on atoms and small molecules and it depends upon basic quantum numbers n, l, m and exponent zeta, ζ . It is having mathematical form:

$$\Psi_i = \sum_i^P C_{\mu_i} e^{-\zeta r}$$

The expanded form of Slater type orbital is

$$\Psi_{\zeta,n,l,m}(r, \theta, \phi) = N Y_{l,m}(\theta, \phi) r^{n-1} e^{-\zeta r}$$

$Y_{l,m}(\theta, \phi)$ is Spherical Harmonics and N is the normalization factor.

Advantages of Slater type orbital (STO)

From the mathematical expression of STO it can be seen that dependence of exponent part on distance from the nucleus is very close to the real hydrogen orbital. So this type of orbital gives the most accurate results.

Disadvantages of Slater type orbital (STO)

1. For many electron larger molecules many centers two electron integrals are rather difficult and require very extensive numerical integration techniques, thus very time consuming.

2. STO contains no radial node, though radial nodes can be introduced by making linear combination of STOs.
3. The optimal orbital of many electrons atom in the single determinant approximation do not have precisely the same shape as hydrogen orbital, and in many cases they are quantitatively different.

6.6.2 Gaussian-type orbital (GTO)

S. F. Boys [225] introduced Gaussian type orbital which made the *ab-initio* calculations computationally more feasible. The Gaussian type orbital is quite flexible and very useful for the electronic structure calculation of poly atomic systems. The GTO's depends upon basic quantum numbers n, l, m and exponent zeta, ζ . It is having mathematical form

$$\Psi_i = \sum_i^P C_{\mu_i} e^{-\zeta r^2}$$

The expanded form in the polar coordinate can be written as:

$$\Psi_{\zeta,n,l,m}(r, \theta, \phi) = N Y_{l,m}(\theta, \phi) r^{2n-2-l} e^{-\zeta r^2}$$

Advantages of GTO

1. As the product of two GTO's is another GTO so by using linear combination of Gaussian functions, many centers two electron integrals can be represented into much simpler form.
2. For electronic structural calculation it is very useful.

Disadvantages of GTO

1. A 1S hydrogenic orbital has a cusp at the atomic nucleus; an n = 1 STO also has a cusp there but a GTO does not. At the nucleus GTO is having zero slopes; hence the behavior

near the nucleus is poorly represented. So a larger basis must be used to achieve an accuracy that is comparable to that obtained from STO's.

2. GTO diminish too rapidly with distance thus the tail behavior is poorly represented.

In fact for these types of calculations large number of functions are to be added to provide flexibility and accuracy, which increases the computational time enormously. To alleviate the problem several GTO's are group together to form contracted Gaussian function. Each contracted Gaussian is taken to be a fixed linear combination of the original or primate Gaussian function, g , centered on the same atomic nuclei.

$$\chi_j = \sum_i d_{ji} g_i$$

with the contraction coefficient d_{ji} and the parameter characterizing g held fixed during the calculation. The special orbital then in terms of the contracted Gaussian:

$$\psi_i = \sum_j c_{ji} \chi_j$$

The use of contracted rather than the primitive Gaussian reduces the number of unknown coefficients c_{ji} to be determined in the HF calculation. These decrease in number of coefficients leads to the potentially large savings in the computational time with little loss of accuracy if the contracted Gaussians are well-choosen.

The simplest type of basis set is minimal basis set. Minimal basis set is represented by one basis function on each atomic orbital, which means it has only as many orbital as are needed to accommodate the electrons to the neutral atom and retain spherical symmetry. In minimal basis set the coefficient of the Gaussian functions are adjusted to give as good a fit as possible to the Slater orbital. e.g. STO-3G, which represents Slater types orbital simulated by 3 Gaussian added together. 1 basis function is required per hydrogen. 5 basis functions are needed per atom from Li to Ne (1s, 2s, 2p_x, 2p_y, 2p_z). 9 basis functions are needed for second

row elements Na-Ar (1s, 2s, 2p_x, 2p_y, 2p_z, 3s, 3p_x, 3p_y, 3p_z). As only one best fit for a Slater type of orbital is possible for a given number of Gaussian function so all STO-3G basis set for any row of the periodic table are same except for the exponents of the Gaussian functions. The STO-G and other minimal basis set work reasonably well at reproducing geometries of the simple molecules but as minimal basis set is mimicking the atomic orbital so they do not give best result in the molecular environment. Mainly they overestimate the π acceptor character of electropositive elements, energy calculation not good and fail badly for carbocation and carboanion and the energies are not very close to the H-F limit. In fact calculations using STO-3G types of basis sets are no longer acceptable for publication and accurate calculation needs more extensive basis sets.

Double zeta (DZ) basis set is having two basis functions on each atomic orbital (both core and valance). In triple zeta (TZ) basis set three basis functions are needed to represent each atomic orbital encountered in elementary valence theory.

A Split Valance Basis Set is compromise between the inadequacy of a minimal basis set and computational demands for the DZ and TZ basis set. Here each valance orbital is represented by two basis functions where as the each inner shell atomic orbital is represented by two basis function. In Split Valance Basis Set, each minimal basis set orbital (or each valance atomic orbital) is replaced by two orbital of different sizes. For example hydrogen has two 1s functions namely 1s and 1s' and they represent inner and outer functions. The inner function '1s' is having larger exponent so it is less diffuse where as the outer function '1s'' is having smaller exponent so it is more diffuse in nature.

The coefficients of these two kinds of orbitals can be varied independently during the course of construction of molecular orbital. Split valance Basis set modify the valance orbital in this way. Similarly, when both the valance and core orbital are taken care of by splitting

then the basis set is called Double Zeta (DZ). By this way the flexibility increases and the resulting orbital fits more in the molecular environment and yields a better description of charge distribution.

Extended basis set is formed by adding polarization and diffuse function in the basis set. Though the basis set is isotropic around the nucleus, bonding introduces anisotropy and the atomic orbitals are distorted (polarized) by adjacent atoms. To take care of that the polarization function is added. The distortion can be taken into account by including basis functions representation orbitals with higher l values. For example, the inclusion of 'p' type basis function work reasonably well for the distort ion of a s-orbital, and a d-type function are used to describe the distortion in p-orbital. For modeling small rings and compound with second row element polarization is needed.

Again for dealing with lone pairs, anions, & excited states electrons can move far from the nucleus which means the electron density is more diffuse on the molecule. To take care of that the diffuse function is added. For the accurate description of anion, hydrogen bonded systems, and systems with significant electron density, requires the addition of diffuse function. In dipole moment and polarizability calculations also addition of diffuse function is quite helpful.

The most popular nomenclature of the extended basis set is done by Pople group. They represent the basis set as $n_1-n_2n_3n_4++G^{**}$. '-' indicates split valence, '+' indicates the diffuse function and '*' represents the polarization function. 'n1' gives the number of Gaussian primitive functions used in linear combination to approximate the core shell Slater-type orbital. For example 6-31G indicates that there are six Gaussian primitive functions in the core orbital. Two sizes of basis functions represent the valence state. One basis function is represented by 3 primitive Gaussian functions and other by only one Gaussian function. Now

including polarization function the nomenclature changes to 6-31G** (also can be represented as 6-31G(d,p)) the first star (or d) indicates the d functions on heavier atoms. 'd' function induces the polarization of p-orbital. The second star (or p) indicates the p function on H atom. It induces a polarization of s-orbital. The '+' sign before G denotes the diffuse function. Thus 6-311++G (2df, 2pd) indicates triplet split valance; augmented with sp-on heavy atoms and diffuse s on H's. Polarization function 2d & 1f on heavy atoms: 2p & 1d on H's. The total nomenclature for the calculation can be represented as "model/basis set//model/basis set". The model term represents type of ψ namely RHF, MP2, CCSD, B3LYP. Basis set indicates the constructed set of MO. '/' separates the higher level single point energy (usually to recover correlation energy) from the level at which the geometry is optimized.

e.g MP2/6-311G(2df,2pd)//RHF/6-31G(d,p) denotes the geometry of the molecule was first optimized with the restricted HF employing 6-31G basis set with one set of 'd' polarization function with heavy atoms and one set of 'p' polarization function with H's. Then the correlation energy was computed with MP2 method & a more extended basis set. The valance triple zeta 6-311G basis set plus the polarization function on heavy atoms (two sets of 'd' and one sets of 'f' function) and hydrogen (two sets of 'p' and one sets of 'd' function).

6.6.3 Plane wave basis set

It works extremely well for the calculation of the atomic & electronic structure of a crystallite solid where the periodicity concept is employed. The mathematical form of the plane wave basis set is

$$\Psi_i = \sum_i^P C_{\mu i} \sin(2\pi i k r) = \sum_i^P C_{\mu i} e^{i k r}$$

Advantages of plane wave basis set

1. There are very efficient algorithms for performing Fourier transform allowing calculations to be performed in the most efficient space-real space or reciprocal space.
2. Convergence of physical properties is controlled by single parameter, the cut off energy, and can be tested.
3. They provide the same accuracy in all the points in space.
4. The simplicity of plane waves makes it easy to add little functionality to code & to try alternative algorithm.

Disadvantages of plane wave basis set

1. Needs lots of them
2. It always use periodic unit cells
3. Provide same accuracy at all points in space, even if there is no electron density.

6.7 Pseudo-potential Approximation

Pseudo potential (PP) is an effective screen electrostatic potential, which valance electrons feel from nuclei and from the core electrons [Fig. 6.1]. Pseudo potential formalism is based on the fact that chemical bonds between the atoms are formed by sharing or transferring the valance electrons and the core electrons do not take part in bonding [226]. Pseudo potential can reduce the size of the basis set considerably, thus reduce the computational time with out compromising much on accuracy. Before using a pseudo potential for a particular system, it should be tested in a well known similar chemical environment. The results obtained by pseudopotential calculation should give results close to the results of all electrons in similar chemical environment.

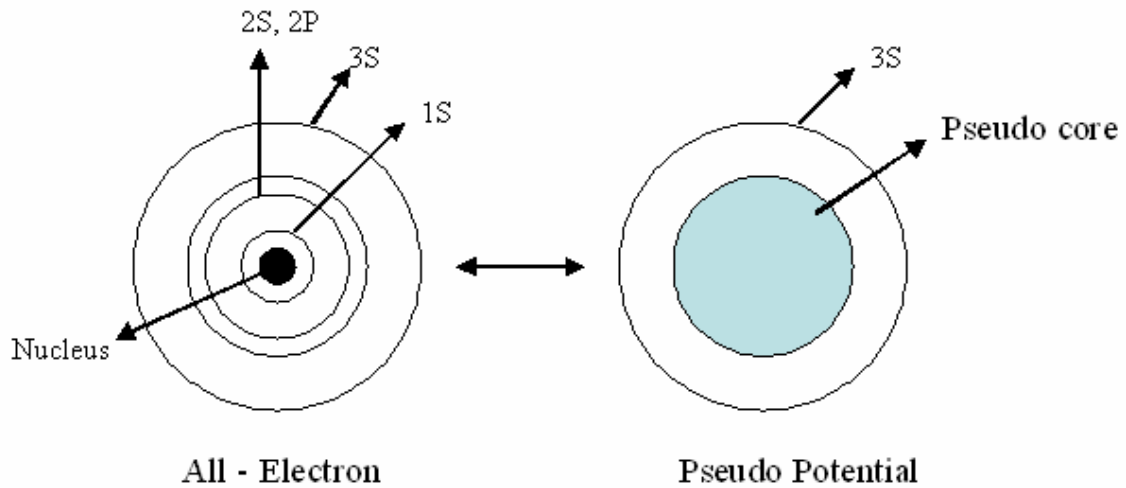


Fig. 6.1 *The pseudo potential concept*

The constructed pseudo potential [227] must satisfy some general norms [Fig. 6.2].

1. Due to the electrostatic screening of the core electrons, the Pauli repulsion and exchange correlation effect, the PP is weaker than the original nuclear potential in the vicinity of the core. This is the so-called Phillips-Kleinman Cancellation Theorem [228].
2. Pseudo potential should be smooth and not oscillate within the core region. The pseudo valance wave function (ψ_{ps}) contains no radial nodes.
3. ψ_{ps} and the valance all electron wave function (ψ_{ae}) corresponds to the same Eigen value ϵ_i .
4. ψ_{ae} and ψ_{ps} agrees beyond a chosen cut off radius r_c i.e. pseudo potential and true potential are same beyond a cutoff radius r_c .
5. The logarithmic derivatives of ψ_{ae} and ψ_{ps} agree at r_c , i.e. normalized PP and the true orbital are equal outside the core region ($V_{ae} = V_{ps}$).
6. The integrated charge inside r_c for each wave function agrees i.e. conservation of charge in the core region. This is called norm conservation [229] (later discussed in detail).

- The first energy derivative of the logarithmic derivatives of all electron ψ_{ae} and ψ_{ps} agrees at r_c . ($\epsilon_{ae} = \epsilon_{ps}$)

The Pseudo-Hamiltonian form can be represented below:

$$-\frac{1}{2}\nabla^2 + v_{eff}^{(ps)}\psi_j^{(ps)} = \epsilon_j\psi_j^{(ps)}$$

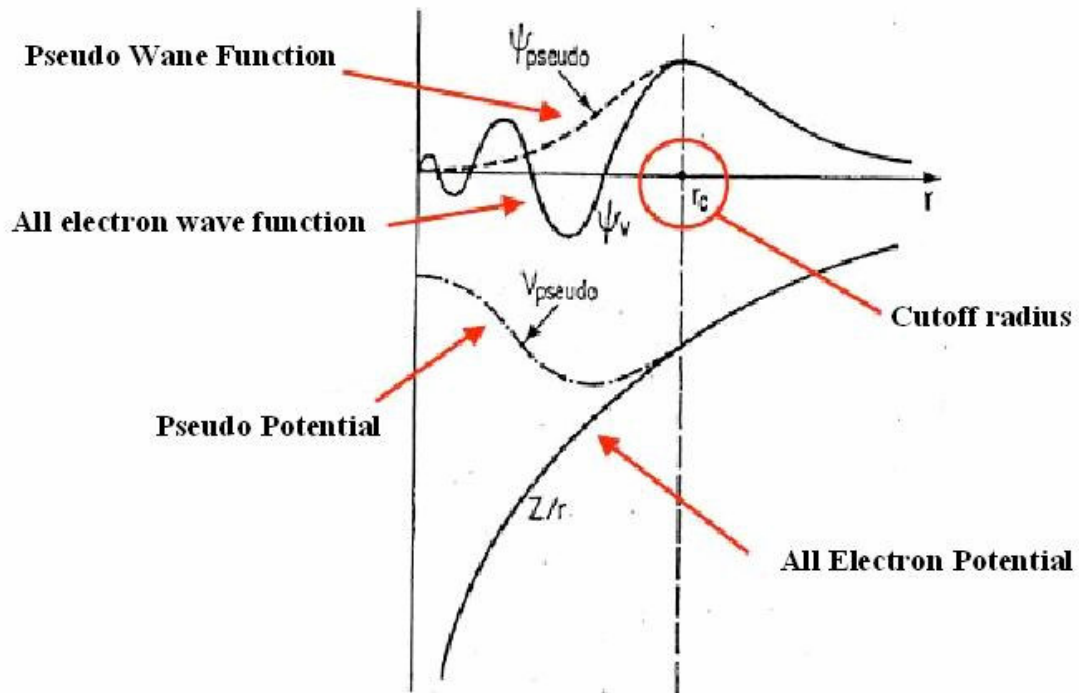


Fig. 6.2 Pseudo potential wave functions

Advantages of Pseudo Potential

- Saves enormous amount of computational times.
- The PP form factor can be determined by direct comparison with the energy gaps (known as empirical pseudo potential) from *ab-initio* calculations.
- Pseudo potential for specific ions is portable.
- It is easy to improve.
- Free softwares available like SIESTA, ABINIT.

Disadvantages of Pseudo potential

1. The Pseudo potential is not unique. So it should be tested before using.
2. Some pseudo potentials can be generated easily but does not work properly and gives rise to the ghost state.
3. Using pseudopotential, some properties which have significant contribution from the core region cannot be described properly (eg. nuclear magnetic resonance).

Types of Pseudo Potential

At present there are three types of PP's are available namely Norm Conserving Pseudo Potential (NCP), Ultra Soft Pseudo Potential (USPP) [230-232] and Projector Augmented Wave (PAW) Pseudo Potential [231, 233, 234]. Norm-conserving PP's can be very accurate, but they are usually not very smooth. The pseudo wave functions are somewhat bumpy due to norm conservation. Ultra Soft Pseudo Potential takes some different approach. Here the norm-conservation condition is relaxed, which means that the core auxiliary functions are not orthogonal and do not conserve the charge. The main disadvantage of the techniques based on energy-independent PP calculations is that, it is not possible to restore the actual wave function. Alternative scenario can be found in the Projector-Augmented plane-Wave (PAW) method. The PAW method, developed by Blöchl [231] is a very powerful tool for performing pseudo potential electronic structure calculations within DFT. While retaining information about the correct nodal behavior of the valence electron wave functions, it has the ability to include upper core states in addition to valence states in the self consistent iterations, without significant additional computational time. Similar to the ultra-soft PP method, it introduces projectors and auxiliary functions. The method also defines a functional for the total energy, which also involves auxiliary functions by keeping the full all electron wave function. Here the whole wave function for each electron is

calculated (as opposed to only valence pseudo-wave functions in the techniques based on PPs). All integrals are evaluated as a combination of integrals of smooth functions extending through space plus localized contributions evaluated over muffin-tin spheres, as in the augmented plane wave (APW) approach. The main idea behind the PAW approach is that here the full valence electron function is split into three parts. If we arrange them with respect to the accuracy then we find that $\text{NCPP} < \text{USPP} < \text{PAW}$. In several cases where the core effect is significant, the NCPP & USPP do not give accurate results. In fact where the effect of core and d orbital are extremely important to predict the structure and magnetic properties PAW pseudo potential approach is a mild way to take care of the core, as well as the computational time.

6.8 Modeling of Periodic System

If a system obeys a set of periodic boundary conditions, this enables to model a large system using only a small part of it that is far from its edge. Crystalline bulk materials with no surfaces present are perfect examples of systems with periodicity. Such systems can be studied using unit cells to reduce the computational effort. In mathematical terms, for the potential of a periodic system operating on an electron we have:

$$V(\mathbf{r}+\mathbf{R}) = V(\mathbf{r})$$

for all Bravais lattice vectors \mathbf{R} .

Bloch's Theorem

In a condensed system the number of electrons can be assumed as infinite, which makes the solution of the Schrödinger equation very complicated. Felix Bloch, in year 1928, developed a theorem that enables the consideration of only the electrons within the unit cell

to solve the Schrödinger equation [235, 236]. The theorem states that the wave function of an electron within a perfectly periodic potential can be written as

$$\Psi_{nk}(r) = u_{nk}(r)e^{iK \cdot r}$$

where k is the wave vector analogous to that of the wave vector in the theory of free electrons, r is a position vector, and $u_{nk}(r)$ is a periodic function that satisfies the boundary condition, $u_{nk}(r) = u_{nk}(r+R)$. The corresponding energy Eigen value is

$$\varepsilon_n(K) = \varepsilon_n(k + K)$$

where K is a reciprocal lattice vector, $\varepsilon_n(k)$ is a continuous function, and since the energies associated with the index, n , vary with wave vector, k , all distinct values of $\varepsilon_n(k)$ are represented by k values within the first Brillouin zone of the reciprocal lattice.

In general, structures with high symmetry can be sampled with a reduced k -point set, since it is sufficient to consider the k -points only within the irreducible part of the Brillouin zone. Metallic systems require dense set of k -points for a more accurate determination of Fermi level. There exist several methods to generate suitable k -point sets and corresponding weights. Using these k -point sets generated by such methods, an accurate approximation of the electronic potential and total energy can be possible at a reduced computational cost. The magnitude of the errors in the calculated results decreases by making use of denser k -point sets.

6.9 Calculation of Physical Properties

6.9.1 Density of states

The number of states at each energy level, which are available to be occupied, is called the density of states (DOS). A zero DOS of an energy level means that no states can be

occupied. On contrary, a high DOS for an energy level represents that many states are available for occupation. DOS delivers invaluable information about the bonding within solid and in classification of materials as metallic, semiconductor or insulator. Metals and semi-metals have non-localized electrons and no gap (separation between the valance band and conduction band). Materials with large gap (≥ 4 eV) is called insulators, where as a system with smaller gap is categorized with semiconductor. In the representation of DOS, specific relation between ϵ and k must be known to convert between the energy and wave vector [235, 236]. In case of a parabolic relation, such as applied to free electrons, or to the electron in solid with an isotropic parabolic band structure, the energy is related to the wave vector as $\epsilon = \frac{\hbar^2}{2m} k^2$. Accordingly, the density of state in the three dimensions are given by,

$$D(\epsilon) = \frac{1}{2\pi^2} \left(\frac{2m}{\hbar^2} \right)^{3/2} \epsilon^{1/2}$$

Although DFT seems to systematically underestimate the band gap in insulator and semiconductors by about 30-40 %, it is successful in reporting the shape of the DOS.

6.9.2 Charge analysis

In order to make a quantitative conclusion, the identification of the amount of electrons on a particular atom is useful. However, there is no unique way to extract the number of electrons that are associated with a particular atom in a molecule, or in a solid. Many different schemes have been proposed, some are based on population analysis of wave functions (Mulliken population analysis, Coulson's charges), and some others are based on partitioning of electron density distributions (Bader analysis, Hirshfeld analysis) [237-240]. The charge density analyses of the materials discussed in this thesis are performed via the Bader analysis [241, 242]. In this approach, molecules or solids are partitioned into atomic

volumes, such that the flux of the gradient of the electron density vanishes at every point on the surfaces. That is for every point r_s on the surface $S(r_s)$,

$$\nabla_n(r_s) \cdot U(r_s) = 0$$

where $u(r_s)$ is the unit vector normal to the surface at r_s . The charge density reaches a minimum between atoms, which defines a natural location to separate the atoms from each other. The electron density used in a Bader analysis is obtained via self consistent static DFT calculations based on the equilibrium structure.

Hydrogen Storage in Magnesium Based Systems

Introduction

Magnesium based systems are considered as one of the promising hydrogen storage material because of its low cost and high hydrogen storage capacity [1, 45, 109, 115, 243]. Ideally, it can absorb 7.66 wt. % of hydrogen, which is sufficiently high for on board hydrogen storage. But the problems with magnesium are its slow kinetics of hydrogen absorption and desorption and high thermal stability of the magnesium hydride [45, 244]. On reaction with hydrogen at extreme conditions, Mg forms MgH_2 and the heat of formation is estimated to be -39 KJ/mole [245-247]. Due to such higher stability of the MgH_2 , the hydrogen desorption occurs at a temperature around 360 °C, which is very high for practical on-board applications.

The chemical reaction between Mg and hydrogen to form MgH_2 is accompanied by a large change in the crystal structure of Mg. A representative crystal structure of Mg and MgH_2 is shown in Fig. 7.1. The bulk Mg forms hexagonal structure and upon charging with hydrogen, the metallic Mg atoms trade their hexagonal environment and forms rutile (TiO_2) type MgH_2 . Moreover, during hydriding process, the Mg atom losses electronic charge to hydrogen and become cationic, leading to shrinkage of its atomic radius. This yields enough

space for the large hydrogen atoms (anions) to be inserted, creating the rutile-like MgH_2 . The increase in the molar volume during this transformation is around 30 %.

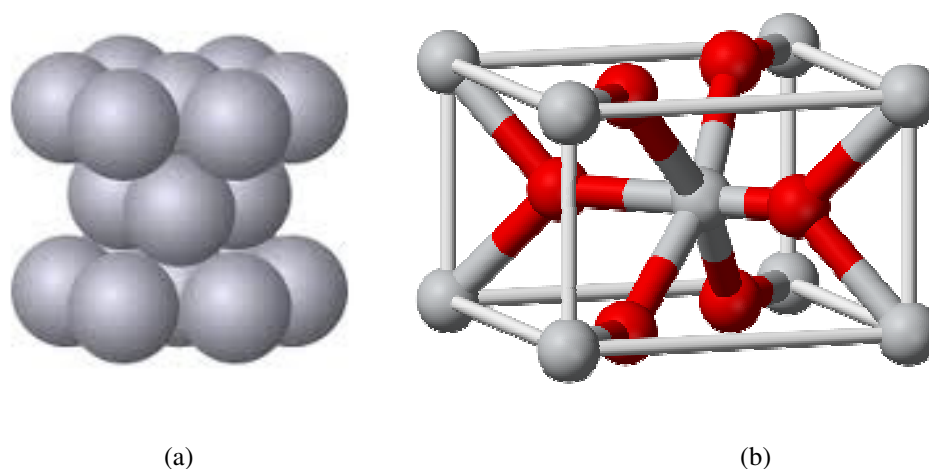


Fig. 7.1 Structures of (a) unit cell of bulk Mg, (b) unit cell of bulk $\beta\text{-MgH}_2$

Many experimental and theoretical works were carried out to improve the hydrogen absorption efficiency of Mg metal, to meet the criteria for hydrogen storage application [45, 244-273]. It was found that transition metal elements acts as a catalyst for the absorption of hydrogen on the Mg surface, thus improves the kinetics of hydrogen absorption [244-263]. It so happens because of the interaction between the 1s orbital of hydrogen and 3d orbital of transition metal elements, but very little is known about the detail mechanism of their catalytic action. It has also been reported that ball milling of Mg can improve the hydrogen absorption-desorption kinetics by a factor of 10. By ball milling, it is possible to get particle size as low as 20 nm, so that the diffusion path length decreases and the kinetics for hydrogen dissociation and absorption increase. Here, an attempt to provide such an understanding is made by carrying out first-principles calculations to investigate the structure and stability of Mg(0001) surface doped with M atoms ($M = \text{Ti}, \text{V}, \text{and Ni}$), and their interaction with hydrogen molecule. Subsequently, the effect of double substitution on the Mg surface by doping V and Ni simultaneously on the Mg surface was evaluated. Finally the effect of finite

size and doping was underscored for the hydrogen absorption-desorption properties of magnesium using Mg_{55} and smaller clusters.

The remaining of the chapter is consisting of three different sections:

7.1 Hydrogen adsorption and diffusion properties of transition metal doped Mg(0001) surface

7.2. Hydrogen adsorption and desorption properties of Ti doped Mg cluster.

7.3. Conclusion

7.1 Hydrogen Adsorption and Diffusion Properties of the Transition Metal Doped Mg(0001) Surface

From previous reports [45, 244-273], it is known that the incorporation of transition metal atoms in the Mg host would lead to an improvement of its kinetics towards the absorption and desorption of hydrogen. Few theoretical results are available in this direction, where Ti, Ni, and Pd were used as dopants [262-264]. It is found that the catalytic activity of the transition element varies by the nature of its interaction with the host as well as with hydrogen molecules. Most of these studies were carried out by substitution one of the Mg atoms from the top layer. The substitutional doping is justified as by ball milling it is possible to create a vacancy, where the impurity atom can be placed easily. However, in the earlier reports, the stability of the doped elements was not verified so as to know whether they prefer to replace the Mg atoms from the surface layer or from the bulk. For obvious reasons, in these two cases, the impurity atom will interact differently with incoming hydrogen molecules.

Here in the present thesis, first-principles calculations were carried out to investigate the structure and stability of Mg(0001) surface doped with M atoms ($M = Ti, V, \text{ and } Ni$) and their interaction with hydrogen molecule. First we have calculated the stability of the M

atoms on the Mg surface. Subsequently the effect of double substitution on the hydrogen dissociation and diffusion were evaluated, by doping V and Ni simultaneously on the Mg(0001) surface. For this purpose, first the stability of the doubly doped Mg surface was calculated by placing the dopants at different layers. In the second step the interaction of a hydrogen molecule with the clean and doped Mg surfaces were studied. Further, the energy barriers for the dissociation of M-H bonds and the diffusion of hydrogen atoms were calculated. For the double substituted system also, the dissociative chemisorptions of hydrogen molecules followed by diffusion of hydrogen atoms on the doubly doped Mg surfaces were investigated and these results were compared with that of the single doped Mg surface. Finally, these results were analyzed in terms of stability, dissociation of H₂ molecule on the surface, and the diffusion of H atoms on the surface to understand the role of doping towards designing magnesium based alloys for hydrogen storage applications.

7.1.1 Computational details

All calculations were performed with density functional theory (DFT) [210, 211], within the plane-wave pseudo potential approach as implemented in the Vienna *ab-initio* Simulation Package (VASP) [275]. The Perdew-Burke-Ernzerhof (PBE) functional was used for the calculation of the exchange-correlation energy. The electron-ion interactions are described with projector augmented wave (PAW) method [234], expanded up to a plane-wave cutoff energy of 210 eV. The PAW method is an all-electron frozen core method, which combines the features of both the ultra-soft pseudopotentials and augmented plane wave methods. For the geometry optimization, the forces were minimized up to 0.05 eV/Å.

In order to establish the accuracy of the present method, few test calculations of bulk Mg and the clean surface were performed. In particular the lattice parameters and cohesive energy for the bulk and interlayer relaxation and surface energy for the clean surface were

examined. The total energy convergence with respect to the k-point sampling of the first Brillouin zone was performed with a (11X11X11) and (15X15X15) Monkhorst-Pack grid [276]. From the calculations, the lattice parameters were found to be $a = 3.19 \text{ \AA}$ and $c = 5.18 \text{ \AA}$, which are close to the experimental values (3.21 \AA and 5.21 \AA) [277], with an error less than 1 %. The slight difference from the experimental values can be due to room temperature thermal expansion in the experimental values, which are not being considered in the theoretical calculations. The corrected cohesive energy was estimated to be 1.50 eV/atom, which is in excellent agreement with the experimental value of 1.51 eV/atom [236].

The Mg(0001) surface was modeled by five layer slab (each layer consists of (i) 2 Mg atoms, (ii) 12 Mg atoms, and (iii) 30 Mg atoms) separated by large vacuum distances of 20 \AA as shown in Fig. 7.2. For the surface energy, a 2 atoms/layer slab, were used and the total energy were calculated using 11X11X1 and 15X15X1 k-points mesh. The energy was found to be converged within 1 meV and the surface energy calculated (0.31 eV/atom) [278] was found to be in good agreement with previous reports from theoretical and experimental studies [262-264].

In the super cell calculations, two types of super cells was constructed; (i) with 12 atoms/ atomic layers and (ii) 30 atoms/atomic layer. For the 12 atoms/layer slab, the k-point sampling of the first Brillouin zone is performed with a (5X5X1) Monkhorst-Pack grid and the surface energy is calculated to be 0.30 eV/atom. For the second case, where 30 atoms per atomic layers were considered, a (3X3X1) k-points mesh was used. In this case the surface energy was estimated to be 0.31 eV/atom. On the basis of these results, further surface calculations that are reported in this work were done with 12 Mg atoms/layer and the first Brillouin zone was integrated using a (5X5X1) Monkhorst-Pack grid.

The nudged elastic band (NEB) method was employed to find out the minimum energy path (MEP) and the corresponding energy barrier for the dissociation and diffusion of hydrogen molecules on the clean and doped Mg surface. The method involves the optimization of chain of images, obtained by linear interpolation, between the initial and final state. In most of the cases, the total number of images used was equal to 10, which is sufficient to map the minimum energy path (MEP) accurately. Each image was allowed to move in the direction perpendicular to the hyper tangent. Hence the energy is minimized in all direction except the direction of reaction path.

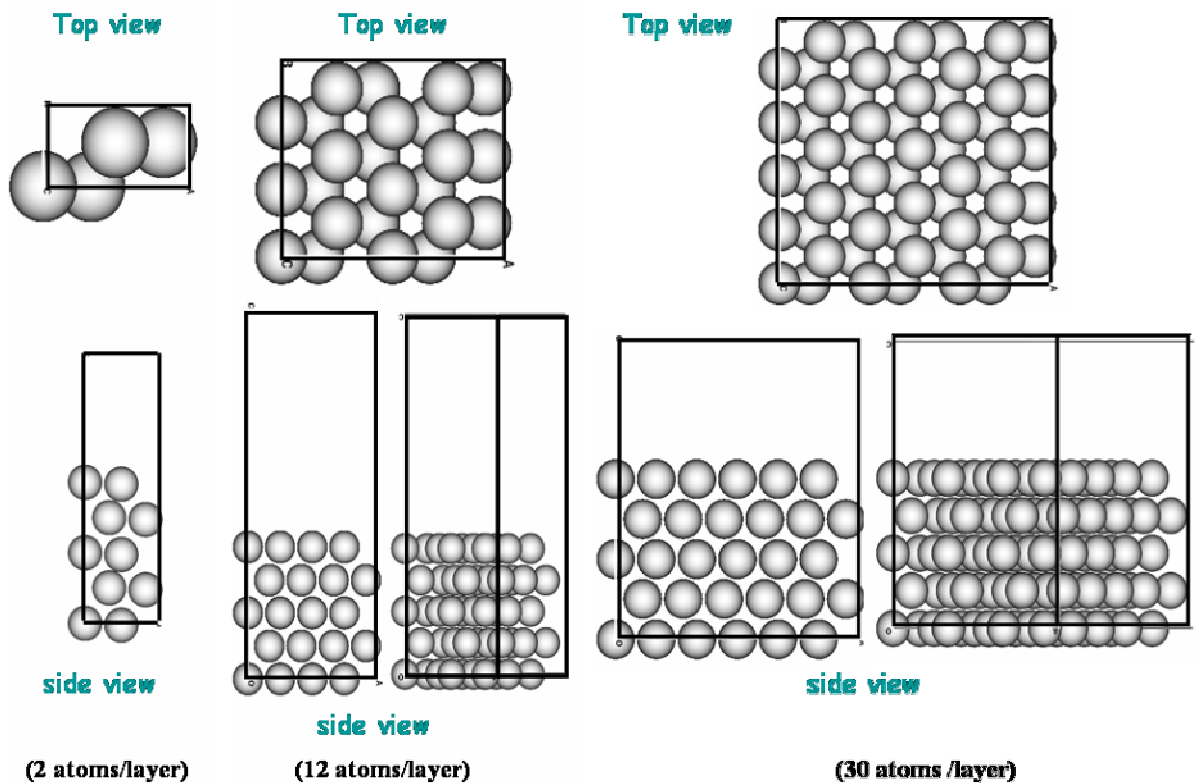


Fig 7.2 Surface calculation with five layers of surface atoms using different super cells

7.1.2 Results & discussion

7.1.2.1 Thermodynamic and kinetic stability of M atoms (Ti, V and Ni) on the Mg(0001) surface

After the test calculations for bulk and clean Mg surfaces, which showed an excellent agreement between present work and previous studies, the stability of Mg surface doped with M (Ti, V and Ni) elements were calculated. In order to obtain the most preferred location of the M elements on the surface, one of the Mg atoms from the first and second layers were substituted as shown in Fig. 7.3.

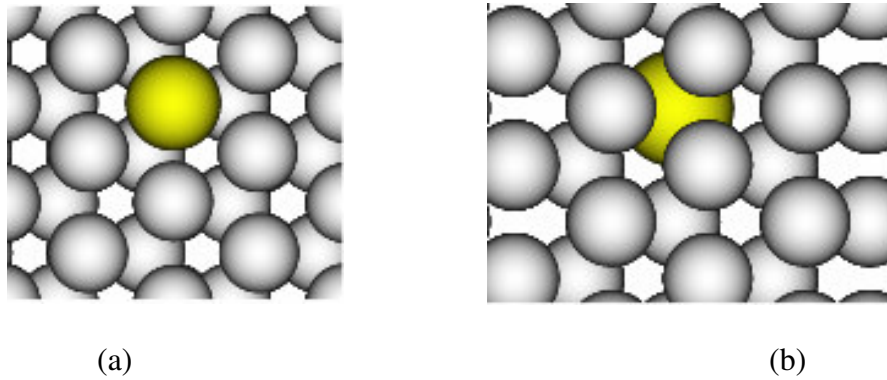


Fig 7.3 Transition metal doped Mg surface. (a) The M is doped at the top layer of the surface (b) the M doped at the second layer of the surface.

A calculation was also performed on the M doped Mg surface by placing the Ti atom at the interstitial position. After optimization, the structure was distorted significantly, causing instability in the overall arrangement of the Mg atoms. The reason for such behavior has been attributed to the unavailability of space in the interstitial positions of bulk Mg to accommodate the transition metal atoms. The energy gain by the substitution of M atoms (E) in the Mg surface is calculated as follows:

$$E = E_{\text{Mg/M}(0001)} + E_{\text{Mg(atom)}} - E_{\text{M}} - E_{\text{Mg}(0001)}$$

Where, $E_{Mg/M(0001)}$ is the energy of M metal substituted Mg(0001) surface, $E_{Mg(atom)}$ is the energy of one bulk Mg atom, E_M is the energy of M atom in the free state and $E_{Mg(0001)}$ is the energy of clean Mg surface. The substitutional energies estimated from the above equation were plotted for different M atoms when they are placed at first and second layer as shown in Fig. 7.4.

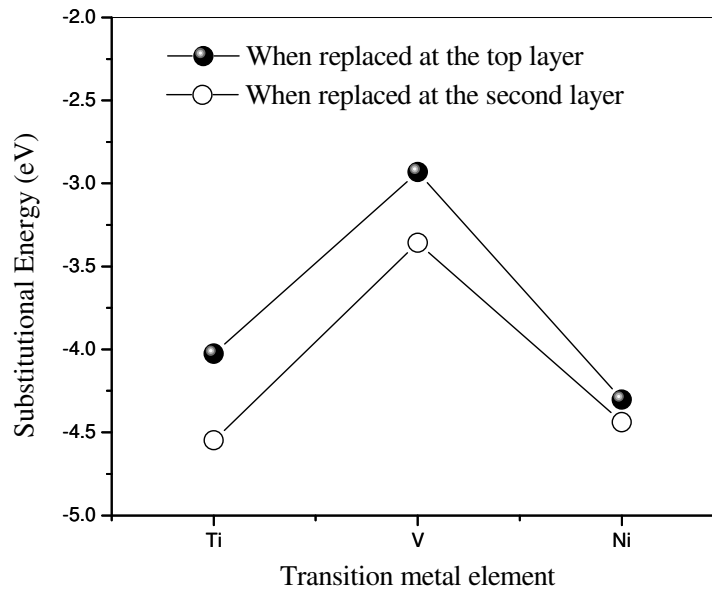


Fig 7.4 Substitution for different M atoms when they are placed at first and second layer

It may be noted that all substitutional energies are negative, indicating that M atom doping is thermodynamically favorable. More importantly, it is clearly seen that all the M atoms prefer to substitute one of the Mg atoms from the second layer than that from the first/surface layer. But the amount of stability differs for different transition metal elements. For Ti and V the difference in energy is almost 0.52 and 0.425 eV respectively and in case of Ni it is 0.13 eV only. However, in both cases (either in the first or second layer substitution), it was found that the substitutional energy decreases in the order of Ti~Ni>V. It is also important to look at the geometrical changes that occur by the presence of M atoms in the Mg

surface. In general it is found that the substitution of M atoms on the surface layer introduces local structural distortions. For example, when M atoms replace one of the Mg atoms from the surface layer, then due to the stronger interaction between M atom with Mg (shorter M-Mg bond), there is a small dip in the top layer at the M atom site. However, the extent of dip depends on the nature of the M elements. The order of distortion created by the transition metal atom in the Mg surface increases in the order Ti<V<Ni as found in the Table 7.1.

Table 7.1 The distortion created (in %) after doping of the substituent elements at the top layer and at the second layer. D_{12} and D_{23} are the distances between the first-second and second-third layer, respectively.

M atom	M atom at the top layer			M atom at the second layer		
		Distances (Å)	Distortion (%)		Distances (Å)	Distortion (%)
Clean	D_{12}	2.636	1.38	-	-	
	D_{23}	2.60651		-	-	
	Mg-Mg	3.21		-	-	
Ti	Substitutional Energy	-4.0265 (eV)		Substitutional Energy	-4.5479 (eV)	
	D_{12} (near M atom)	2.352	9.53	D_{12} (near M atom)	2.46	5.38
	D_{23} (near M atom)	2.65	+1.92	D_{23} (near M atom)	2.56	1.54
	D_{12} (other site)	2.616		D_{12} (other site)	2.63	
	D_{23} (other site)	2.60		D_{23} (other site)	2.59	
	Mg-M distance	2.97		Mg-M distance	3.13	
	Substitutional Energy	-2.931 (eV)		Substitutional Energy	-3.356 (eV)	
V	Substitutional Energy	-2.931 (eV)		Substitutional Energy	-3.356 (eV)	

	D ₁₂ (near M atom)	2.23	14.23	D ₁₂ (near M atom)	2.3943	7.91
	D ₂₃ (near M tom)	2.6714	+2.69	D ₂₃ (near M atom)	2.523	2.96
	D ₁₂ (other site)	2.62		D ₁₂ (other site)	2.618	
	D ₂₃ (other site)	2.6115		D ₂₃ (other site)	2.58	
	Mg-M distance	3.21		Mg-M distance	3.199	
Ni	Substitutional Energy	-4.3032 (eV)		Substitutional Energy	-4.4386 (eV)	
	D ₁₂ (near M atom)	1.977	23.96	D ₁₂ (near M atom)	2.5567	1.665
	D ₂₃ (near M atom)	2.674	+2.84	D ₂₃ (near M atom)	2.344	9.84
	D ₁₂ (other site)	2.614		D ₁₂ (other site)	2.626	
	D ₂₃ (other site)	2.616		D ₂₃ (other site)	2.595	
	Mg-M distance	3.21		Mg-M distance	3.106	

After establishing of the stability of M atom at the sub-surface layer, the energy barrier for diffusion of M atom from the surface layer to the second layer were calculated. Though it is known that during high energy ball milling the constituent M atom can stabilize itself by the process of diffusion but for the fundamental understanding it is important to find out the activation barrier for the diffusion process. For this purpose NEB method was used to map the minimum energy diffusion path. The calculations were carried out using six images, including the initial and final one. The activation barrier for the diffusion of Ti atom from the

first layer towards the second layer was estimated to be 1.2 eV, whereas that of V was 1.02 eV. Ni showed the least activation barrier of 0.7 eV for its diffusion from the top surface to the second layer. It was found that the activation barrier for the diffusion of M atom decreases in the order of $Ti > V > Ni$ which shows a consistent trend with the atomic sizes of M elements ($Ti = 2.00\text{\AA}$, $V = 1.92\text{\AA}$ and $Ni = 1.62\text{\AA}$). So it can be concluded that kinetically the M atom with lower atomic radius will diffuse more easily towards the second layer.

7.1.2.2 Interaction of hydrogen with clean Mg surface and M (M = Ti, V and Ni) doped Mg surface (*dopants are at the surface layer*)

First, the activation barrier of the dissociation and diffusion of hydrogen molecule on the clean Mg surface was investigated. To start with, the hydrogen molecule was placed on the Mg surface at 3\AA above as shown in Fig. 7.5.

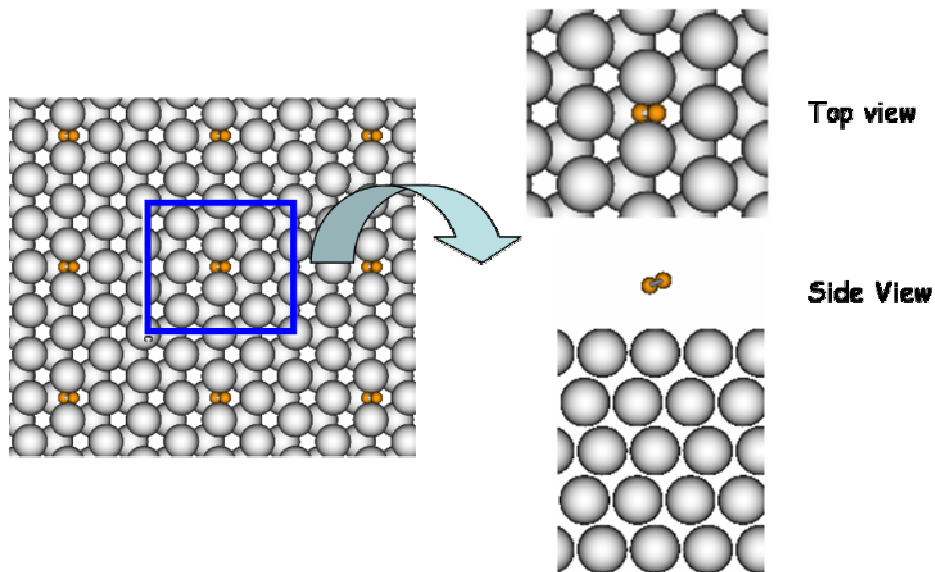


Fig. 7.5 Interaction of hydrogen with the clean Mg surface

After dissociation of the hydrogen molecule, the nascent hydrogen atoms can move towards several positions. To find out the most stable location, the adsorption energy of hydrogen on the Mg(0001) surface were determined at low coverage in four possible sites:

top, bridge, hollow fcc, and hollow hcp sites. The binding energy of hydrogen atom was calculated from the following equation:

$$E = (E_{\text{total surface}+2\text{H}} - E_{\text{total surface}} - E_{\text{H}_2})/2$$

where, $E_{\text{total surface}+2\text{H}}$ is the total energy of the system after hydrogen absorption, $E_{\text{total surface}}$ is the total energy of the surface and E_{H_2} is the energy of hydrogen molecule. It was found that, the hydrogen molecule preferably dissociates over a bridged site than the top site on the clean Mg surface, and after dissociation the hydrogen atoms preferably occupy the face center cubic (fcc) and hexagonal closed packed (hcp) holes [Fig. 7.6]. The results correspond well with the earlier study [264, 269].

From the NEB calculation it was found that the activation barrier for the dissociation of hydrogen molecule on the clean Mg(0001) surface is 0.97 eV [Fig. 7.7], which is in good agreement with previously reported values [263-265]. The barrier height for the diffusion of hydrogen atoms towards the adjacent hollow sites is estimated to be 0.26 eV. The smaller energy barrier for diffusion (0.26 eV) of hydrogen atoms in comparison to their dissociation energy (0.97 eV) suggest that in case of clean Mg surface, the dissociation of hydrogen will govern the rate limiting step.

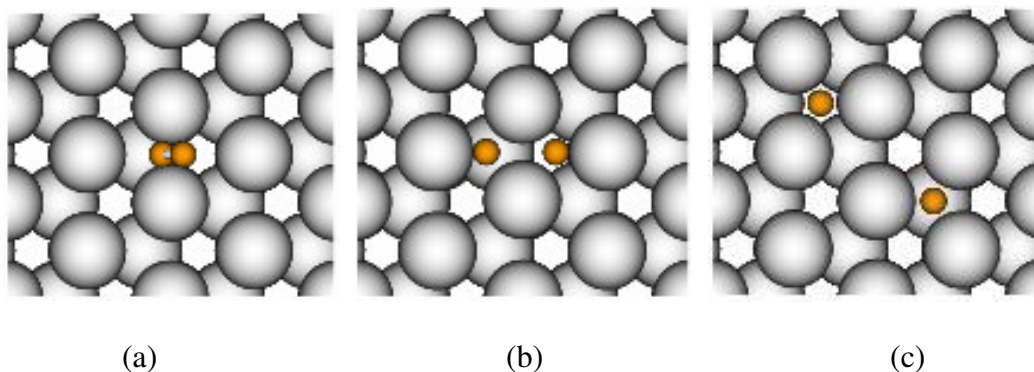


Fig. 7.6 Hydrogen dissociation and diffusion on the pure Mg surface as viewed from the top. (a) initial state, (b) after dissociation of hydrogen molecule and (c) after diffusion of hydrogen atom.

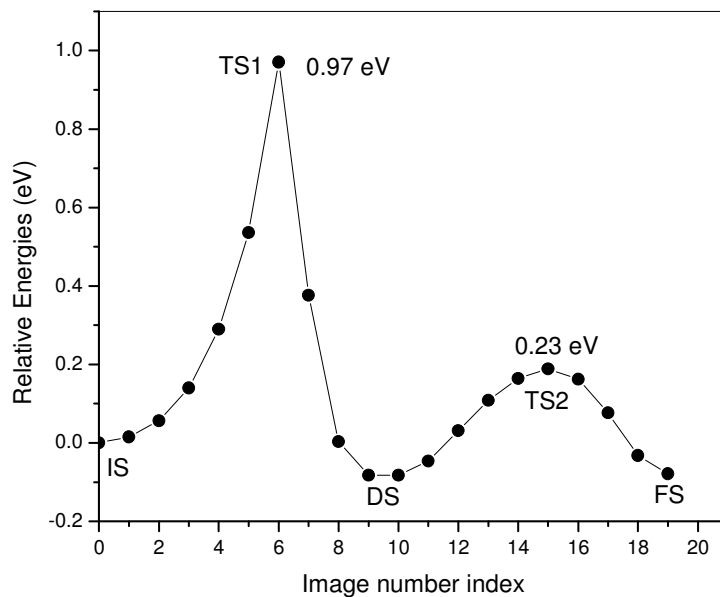


Fig. 7.7 The minimum energy path for hydrogen dissociation and diffusion on pure Mg surface. IS = Initial State, DS = After dissociation of hydrogen, FS = Final state after diffusion of hydrogen, TS1 = First transition state, TS2 = Second transition state

For the M substituted Mg surface, the interaction of hydrogen molecule by placing the M atoms on the surface layer [Fig. 7.8] was calculated. It is obvious from the figure that the hydrogen molecules gets dissociated on the catalytic site on the Ti, V and Ni doped Mg surface and after the dissociation the hydrogen atom goes towards different positions depending upon the nature of the substituent atom [Fig. 7.8]. So all four possible sites for H adsorption after dissociation were tested and it was found that the atomic hydrogen prefers to adsorb into two of the possible three hollow fcc sites around the Ti and V atoms for the Ti and V substituted Mg surface, where as, in case of Ni substitution the dissociated hydrogen atoms go towards the hollow hcp hole around the Ni atom as shown in the Fig. 7.8.

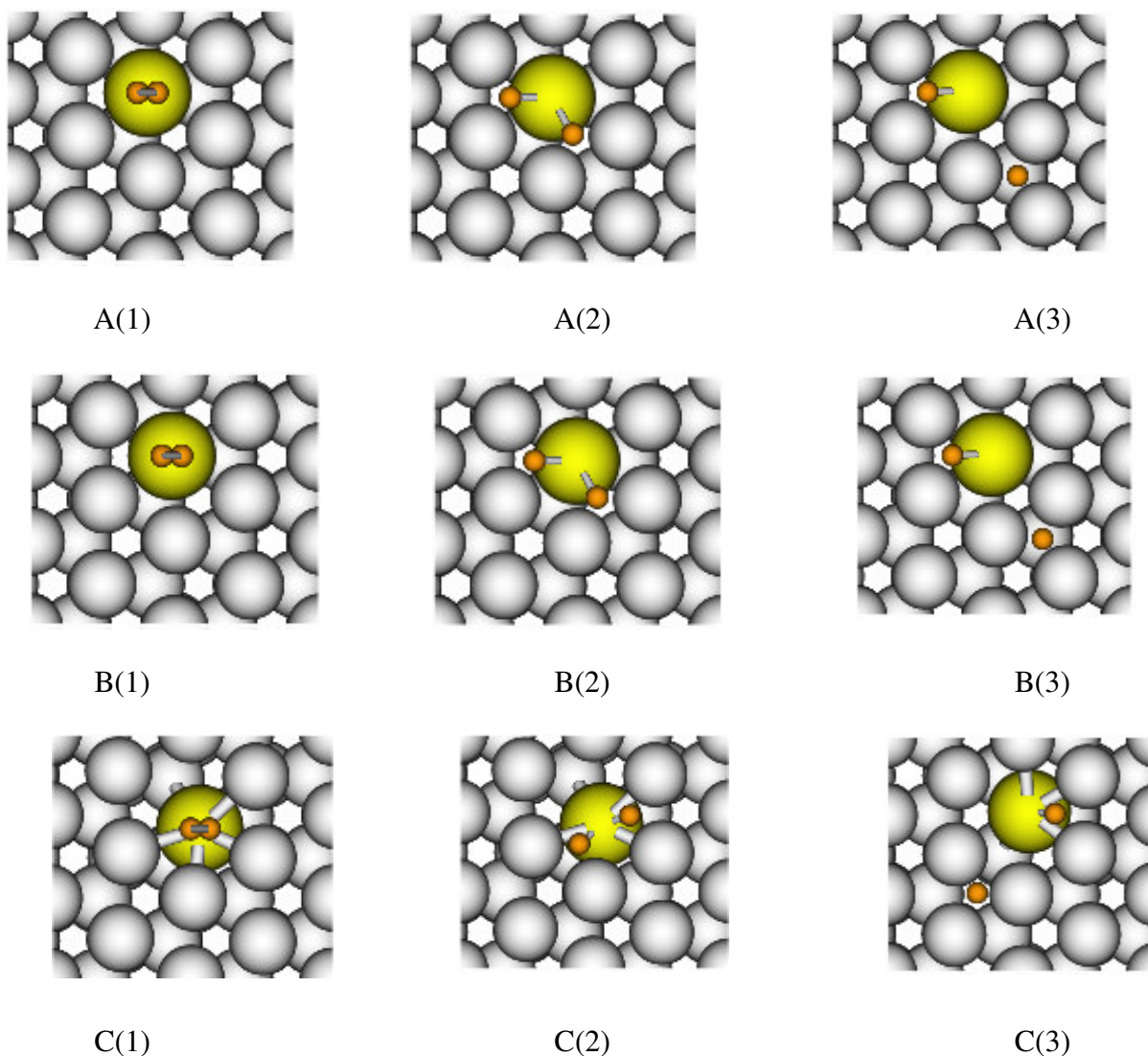


Fig 7.8 *Hydrogen dissociation and diffusion (A) Ti, (B) V and (C) Ni doped Mg surface when the substituent elements remains in the top layer as viewed from the top. 1) Initial State, (2) After dissociation of hydrogen, and (3) After diffusion of hydrogen.*

The NEB profile for the dissociation and diffusion of hydrogen on the clean and doped Mg surface was shown in Fig. 7.9. For the dissociation of hydrogen molecule towards hydrogen atom, it was found that hydrogen molecule interacts spontaneously with Ti and V doped Mg surface which means they can dissociate on the catalytic site without any activation barrier. However, for Ni doped surface, unlike the other two systems (Ti and V),

the dissociation of hydrogen molecule requires small activation energy. The activation barrier for dissociation is found to be 0.1 eV.

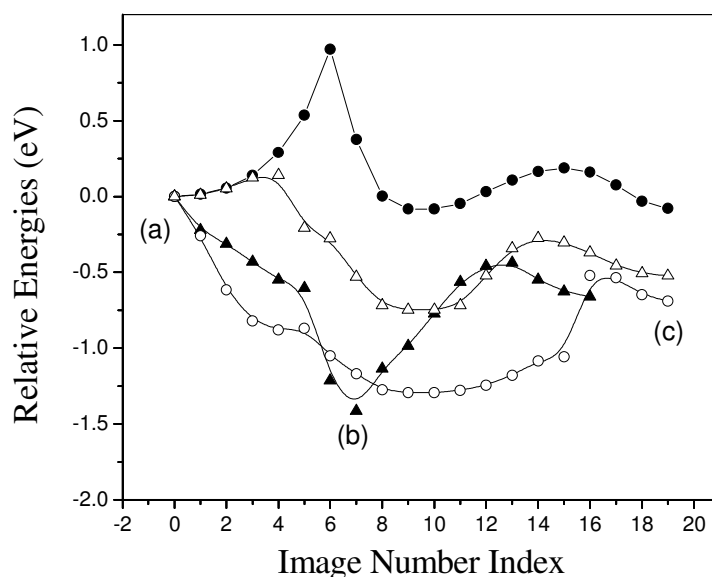


Fig. 7.9 NEB profiles for the dissociation and diffusion of hydrogen on the clean and doped Mg surface when M (Ti, V, and Ni) atoms are on the surface layer. The symbols “solid circle”, “solid triangle”, “hollow circle” and “hollow triangle” represent the clean, and Ti, V, and Ni doped Mg surface, respectively. The relative energies of the initial state, after dissociation of hydrogen molecule on the surface, and after diffusion of hydrogen atoms on the surface are marked by (a), (b) and (c), respectively.

After estimation of the dissociation activation barrier, the diffusion behavior of hydrogen atoms on the doped Mg surface was calculated using the NEB method. The diffusion barrier was calculated for the diffusion of the atomic hydrogen towards the adjacent hollow site on the surface. The diffusion barrier of hydrogen atom from the adsorption site to the next hollow site is estimated to be 0.96 eV, 0.73 eV, and 0.45 eV, for Ti, V, and Ni, respectively. The difference in the barrier energy is consistent to the M-H bond energy. Moreover, the lower diffusion barrier for Ni doped Mg surface suggest its better catalytic performance than Ti and V doped surfaces.

7.1.2.3 Interaction of hydrogen with M (M = Ti, V and Ni) doped Mg surface (*dopants are at the second layer*)

As it is seen that M is more stable in the second layer so it is quite necessary to see the effect of transition metal elements when they are placed at the second surface. For this purpose all previous calculations were repeated by keeping the M atom in the second layer. In this case we have done the calculations in three steps as shown in the Fig 7.10.

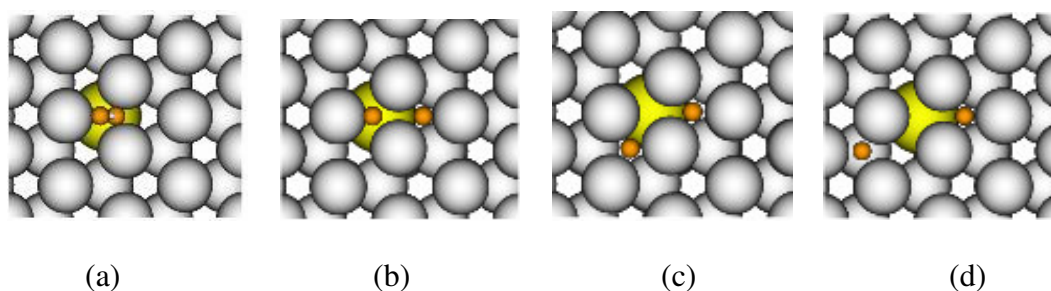


Fig 7.10 *Geometry of hydrogen dissociation and diffusion on the Ti doped Mg surface when Ti is in the second layer as represented by initial State (a), after dissociation of hydrogen (b) and (c) and after diffusion of hydrogen (d).*

1) Dissociation of hydrogen. 2) Diffusion of hydrogen atom towards more stable fcc position and 3) Diffusion of one hydrogen atom from fcc to hcp position. To start the geometry optimization, the hydrogen molecule was placed at 3 Å above the plane of the Mg surface.

For the first case i.e.; when the Ti atom is doped in the second layer, in order to obtain the activation energy for the molecular dissociation, the elastic band calculations were performed. Fig. 7.11 shows the energy variations as a function of 10 images that are generated between initial state and dissociated state. It could be seen from the NEB calculation that when Ti remains in the second layer it shows an activation barrier of 0.8 eV/hydrogen atom, which is less than the clean Mg surface.

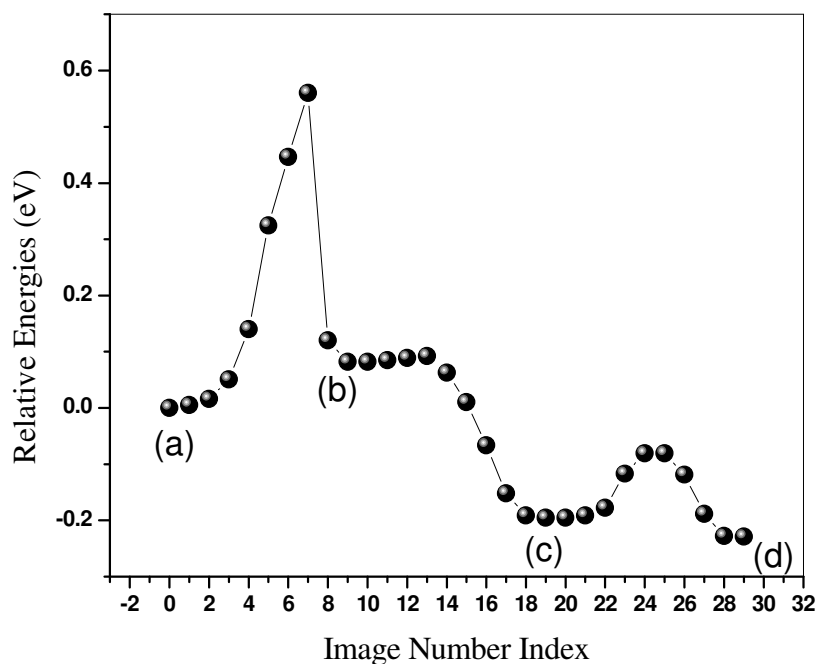


Fig. 7.11 NEB profile for hydrogen dissociation and diffusion on the Ti doped Mg surface when Ti is in the second layer as represented by initial state (a), after dissociation of hydrogen (b) and (c) and after diffusion of hydrogen (d).

The binding energy of hydrogen atom is -0.157 eV in the Ti site on Mg surface. Once it gets dissociated the hydrogen atoms can go toward the more stable fcc position with an activation barrier of 0.01 eV only, which indicates after dissociation the hydrogen atoms go towards the more stable fcc position almost spontaneously. Once the preferred location of the dissociated hydrogen atoms are established, it is important to understand their diffusion behavior in the surface. For the diffusion of hydrogen molecules from the fcc sites to the hcp site [Fig 7.10], the activation energy is calculated through nudged elastic band method and the resulting MEP is shown in Fig. 7.11. The NEB map for the diffusion of one hydrogen atom from one of the fcc site to hcp site the activation energy was found to be 0.29 eV/hydrogen atom [Table 7.2] as shown in Fig. 7.11, so the dissociation of hydrogen molecule is the rate limiting step. The results indicate when Ti atom remains in the second

layer of Mg surface then the diffusion of hydrogen is much easier than when it remains in the first layer. As from the energy point of view Ti prefers to remain in the second layer so it can be considered as a good catalyst for hydrogen absorption.

Table 7.2 Calculation of interaction energy of hydrogen and different activation barriers

Surface	Substitution at the first surface			Substitution at the second surface		
	Hydrogen absorption energy (eV)	Activation barrier for dissociation (eV)	Activation barrier for diffusion (eV)	Hydrogen absorption energy (eV)	Activation barrier for dissociation (eV)	Activation barrier for diffusion (eV)
Pure Mg surface	-0.066	0.97	0.26	-	-	-
Ti doped Mg surface	-0.605	Almost nil	0.96	-0.157	0.8	0.29
V doped Mg surface	-0.67	Almost nil	0.73	-0.1326	0.56	0.12
Ni doped Mg surface	-0.37	0.124	0.45	-0.092	0.78	0.22

Similar calculations of hydrogen absorption were performed for the V substituted Mg surface when one of the Mg from the second layer is replaced [Fig 7.12].

In contrast to the previous case, here the molecular dissociation of hydrogen requires less amount of activation energy, which is estimated to be 0.56 eV, as calculated through NEB method. In the second step, for the diffusion of initially absorbed hydrogen, the energy barrier for the migration of hydrogen atom towards more stable fcc positions were estimated.

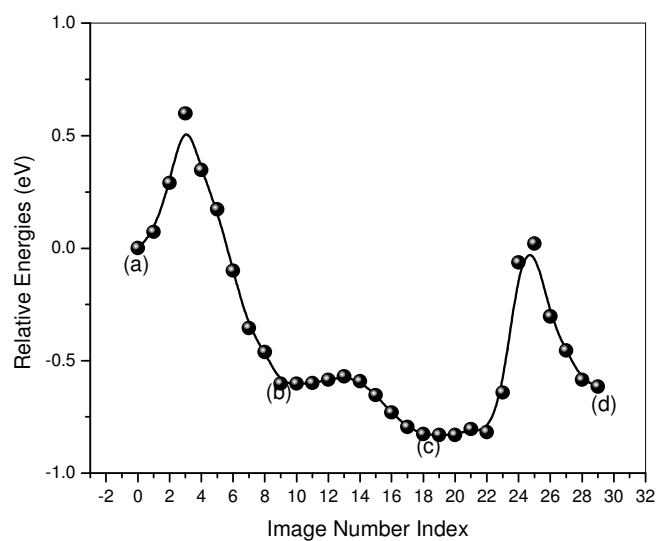


Fig.7.12 NEB profile for hydrogen dissociation and diffusion on the V doped Mg surface when V is in the second layer as represented by initial State (a), after dissociation of hydrogen (b) and (c) and after diffusion of hydrogen (d).

When Ni substitutes one of the Mg atoms from the second layer [Fig. 7.13], the activation energy for the dissociation of hydrogen is higher compared to the first layer. From the NEB calculation the activation energy is found to be 0.78 eV.

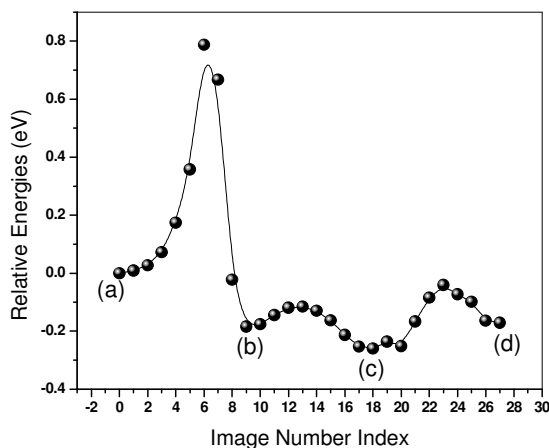


Fig. 7.13 NEB profile for hydrogen dissociation and diffusion on the Ni doped Mg surface when Ni is in the second layer as represented by initial state (a), After dissociation of hydrogen (b) and (c) After diffusion of hydrogen (d).

After the dissociation, the hydrogen atoms can be stabilized into the fcc holes with an activation energy of 0.1 eV. But in this case the activation energy for the diffusion of hydrogen atom from one fcc site to one hcp site decreases further and it is found to be equal to 0.22 eV only. So in this case the dissociation of hydrogen molecule is the rate limiting step. It can be concluded also in the manner that if the surface Ni atom dissociates the hydrogen molecule into hydrogen atom then the bulk Ni atoms are quite efficient to diffuse the hydrogen molecules towards the bulk Mg.

7.1.2.4 Relative stability of Mg surface after substitution of V and Ni

In the previous study one of the important finding that most of the 3d elements prefer to replace one of the Mg atoms from the second layer instead the first layer. While this has an advantage of reducing the diffusion barrier but on the other hand it increases the activation barrier for dissociation (compared to the case where M atom remains at the first layer) for its obvious reasons. So the most desirable situation could be if two dopants can be used simultaneously, each substituting one Mg atoms from the first and second layer.

Based on energetics, it is seen already that both Ni and V atoms prefer to substitute one of the Mg atoms from the second layer than that from the top surface layer. However, the relative stability in the first and second layer differs for different transition metal elements. For V, the difference in energy is almost 0.425 eV and in case of Ni it is 0.13 eV only. The interaction of a hydrogen molecule with doped Mg surface suggest that when the impurity atoms are on the top layer, the dissociative chemisorption of hydrogen molecule occurs spontaneously on the catalytic site and the hydrogen atoms occupy the fcc or hcp holes depending upon the nature of M atom. However, they restrict the movement of hydrogen atoms further, as the diffusion barrier is quite high. Here the diffusion of hydrogen atoms is the rate limiting step and Ni is found to be the best catalyst as it shows lowest activation

barrier for diffusion. The situation is reversed when the M atoms substitute one of the Mg atoms from the second layer. In this case the dissociation of hydrogen molecule is controlled by a high activation barrier but once the hydrogen is absorbed, the mobility of the hydrogen atoms on the surface is easier than the previous case. Here the dissociation process is the rate limiting step. Finally, by comparing all the results, it is inferred that the substitution of V in the Mg lattice will be the best choice considering the requirements of a good hydrogen storage material. So in the present study, by using first principle calculations, the stability of Ni and V doped Mg(0001) surface were determined, when they are doped simultaneously substituting two Mg atom from same or different layers.

Here is the description of the initial structural arrangements of the double substituted Mg surface that were considered in the work. The clean Mg(0001) surface under consideration is composed of 60 Mg atoms (total five layer slab and each layer is consisting of 12 Mg atoms). Now two Mg atoms were substituted by Ni and V atoms, so resulting surface was abbreviated as $Mg_{58}VNi$ and the wt% of doping is estimated to be 7.52 wt%. Now to find out the most stable location for Ni and V on the Mg(0001) surface, the relative stability of different V and Ni substituted Mg surfaces were calculated by placing the doping elements at different locations. The substitutional arrangement was divided into two parts: (A) when Ni and V are not occupying the nearby positions, and (B) when Ni and V substitute two Mg atoms from adjacent positions.

For the first case, four starting geometries were considered, which are shown in Fig. 7.14, (i) Both V and Ni are in the first layer (V1Ni1), (ii) both are in the second layer (V2Ni2) (iii) V is in the first layer and Ni in the second layer (V1Ni2), and (iv) V is in the second layer and Ni in the first layer (V2Ni1).

Similar substitutional pattern with V and Ni at the adjacent sites were also considered in the second case. The stability of configurations was analyzed by the energy gain as:

$$E = E_{\text{Mg/VNi}(0001)} + 2E_{\text{Mg(atom)}} - E_{\text{V}} - E_{\text{Ni}} - E_{\text{Mg}(0001)},$$

where, $E_{\text{Mg/VNi}(0001)}$ is the energy of Ni and V substituted Mg(0001) surface, $E_{\text{Mg(atom)}}$ is the energy of one bulk Mg atom, E_{V} is the energy of V atom in the free state, E_{Ni} is the energy of Ni atom in the free state, and $E_{\text{Mg}(0001)}$ is the energy of clean Mg surface.

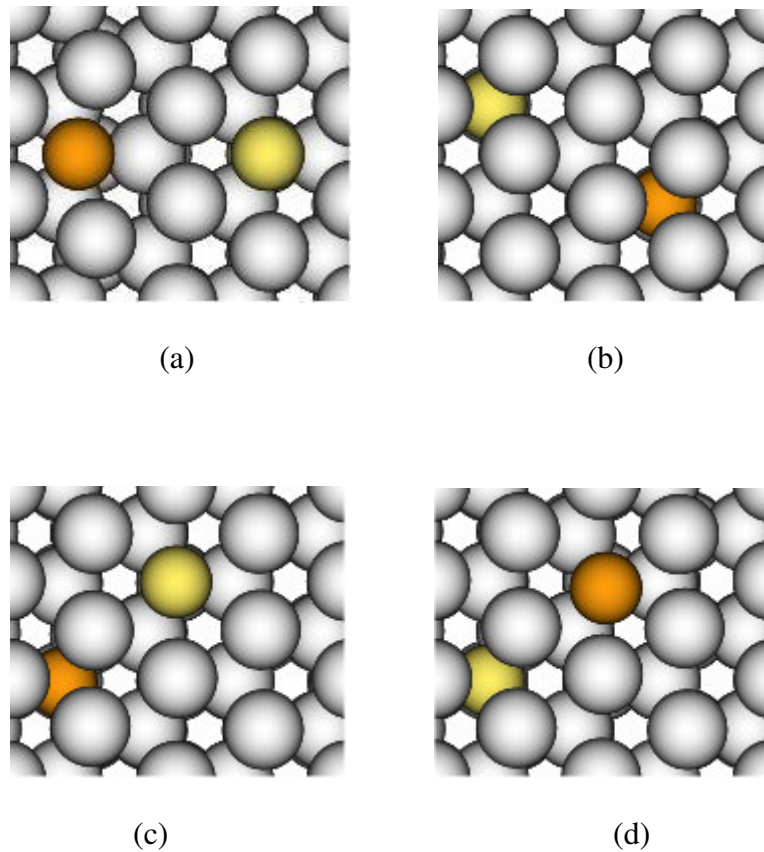


Fig.7.14 V and Ni doped at different layer of Mg(0001) surface, when V and Ni are not occupying the nearby positions. The yellow and orange balls indicate V and Ni atoms, respectively. The figures (a), (b), (c) and (d) indicate V1Ni1, V2Ni2, V1Ni2 and V2Ni1 respectively.

For the first case where the V and Ni atoms are not occupying the adjacent sites the most stable configuration is obtained by substituting two Mg atoms from the second layer. In this context it should be mentioned that when the Mg surface was substituted by V or Ni separately, both favors second layer over top layer. The order of stability for all substitutional patterns is listed in Table 7.3.

Table 7.3 *The substitutional energies for different geometries of V-Ni composite doping on Mg(0001) surface.*

Geometries	Substitutional Energies (eV)	
	No adjacent site	Adjacent site
V1Ni1	-7.961	-8.008
V2Ni2	-8.440	-8.489
V1Ni2	-8.092	-7.790
V2Ni1	-8.308	-8.562

In the second case where Ni and V occupy adjacent sites [Fig. 7.15] in the Mg surface, then the situation is different. In general all configurations are more stable than the previous case except the situation when V remains in the first layer and Ni in the second layer. The most favorable substitutional site is found to be V2Ni1, where V and Ni substitute for two Mg atoms from the second and first layer respectively and they are adjacent to each other. The Ni-V distance for this geometry is 2.32 Å, which is 0.274 Å less than the sum of the atomic radii of Ni and V. Further, the smallest Mg-Mg distance on the top layer adjacent to the Ni atom is found to be 3.02 Å compared to the ideal Mg-Mg distance in same layer of hcp lattice of 3.21 Å. This results in a local dip at the Ni site, and acts as a catalytic center.

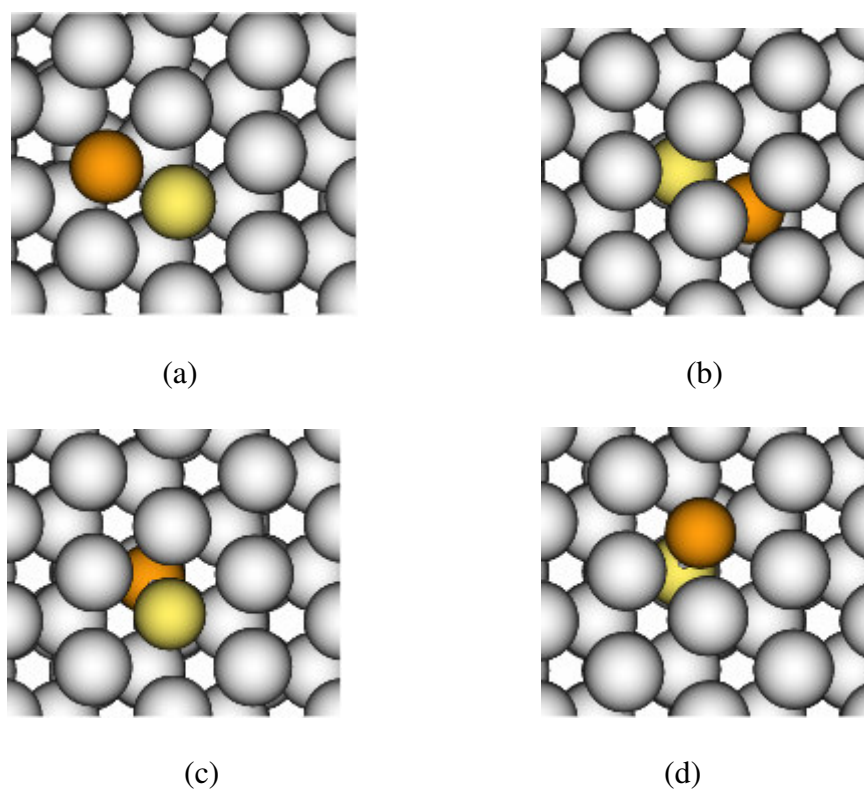


Fig. 7.15 *V and Ni doped at different layer of Mg(0001) surface, when V and Ni substitute two Mg atoms from the adjacent position. The gray, yellow and orange balls indicate Mg, V and Ni atoms, respectively. The figures (a), (b), (c) and (d) indicate V1Ni1, V2Ni2, V1Ni2 and V2Ni1 respectively.*

7.1.2.5 Interaction of hydrogen with most stable Mg₅₈VNi Surface

After establishing the most stable geometry for the V and Ni double substituted Mg surface, the interaction of hydrogen molecule was investigated. The interaction of hydrogen molecule with the Mg surface was carried out in two steps. In the first step, the molecular hydrogen comes close to the Mg surface and dissociated into two H atoms (dissociative chemisorption), and in the second step the hydrogen atoms are diffused along the surface. Both steps require some external energy to cross the activation barrier. The role of a catalyst is to decrease the activation barrier for the dissociation of hydrogen molecule and diffusion of hydrogen atoms. In the present work, V and Ni are used as catalysts to minimize the activation barrier of each process.

To start the calculation of molecular hydrogen dissociation on the Mg surface, it was found that the most favorable location of hydrogen atoms after dissociation is at the top of Ni atom. For this purpose, six different hollow sites were identified nearby the Ni atom where the dissociated hydrogen atoms can be absorbed. The possible locations are shown in the Fig. 7.16.

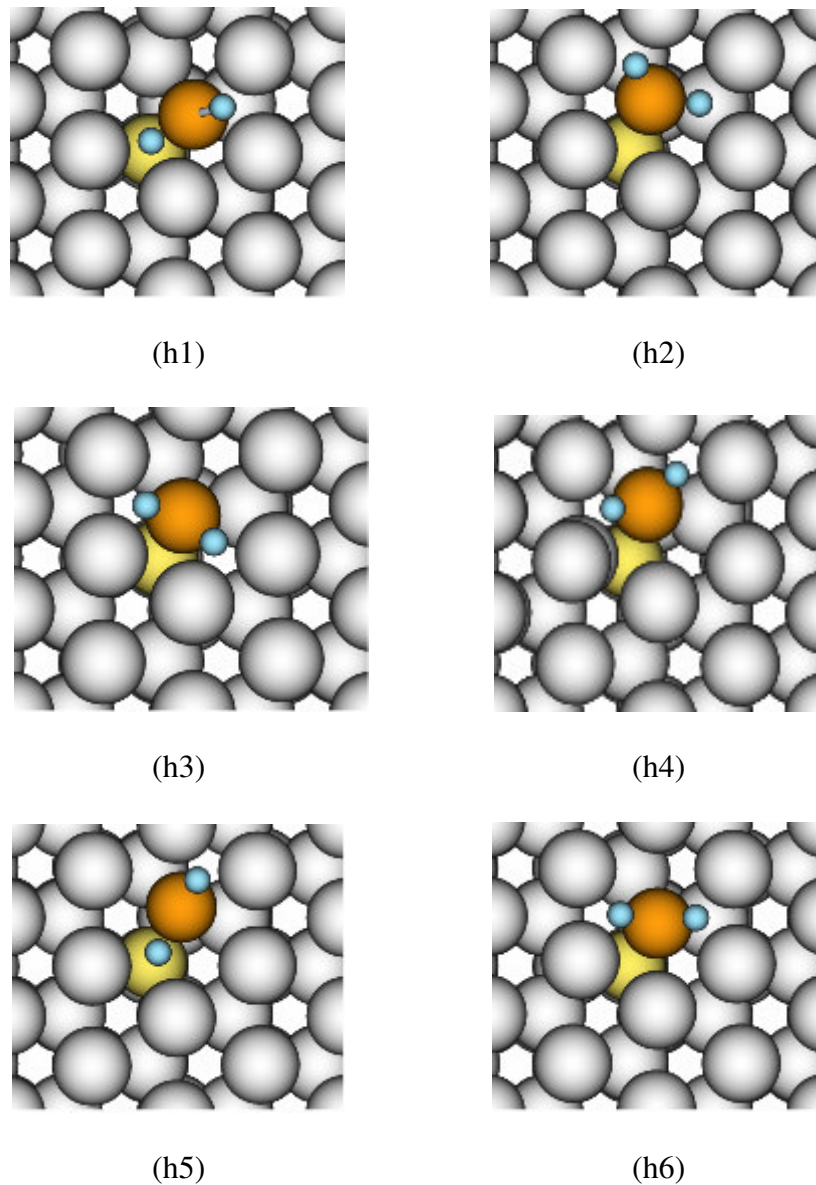


Fig. 7.16 Possible absorption sites of the hydrogen atoms after dissociation on the V and Ni doped Mg(0001) surface. The small balls indicate hydrogen atoms.

Total six possibilities are there. i) Two hydrogen atoms occupy the hcp holes (octahedral site/face) on the surface layer such that one hydrogen atom is nearer the V atom (h1), ii) Two hydrogen atoms occupy the hcp holes on the surface layer such that both the hydrogen atoms are away from the V atom (h2), iii) two hydrogen atoms can occupy fcc holes (tetrahedral site/face) on the surface layer such that both the hydrogen atoms are nearer to the V atom (h3), iv) Two hydrogen atoms occupy the fcc holes on the surface layer such that one hydrogen atom is nearer to the V atom (h4), v) One hydrogen atom occupy the fcc hole and the other hcp hole such that second hydrogen is nearer to the V atom (h5), and vi) One hydrogen atom occupy the fcc hole and the other hcp hole such that second hydrogen is away from the V atom (h6).

The average binding energy was calculated from the following equation:

$$E = (E_{\text{total surface}+2\text{H}} - E_{\text{total surface}} - E_{\text{H}_2})/2,$$

Where, $E_{\text{total surface}+2\text{H}}$ is the total energy of the system after hydrogen absorption, $E_{\text{total surface}}$ is the total energy of the surface and E_{H_2} is the energy of hydrogen molecule. The average binding energy for all the above cases were calculated and listed in Table 7.4.

It was found that in the most stable configuration, the hydrogen atoms are absorbed into two nearby hcp positions and one hydrogen atom is absorbed nearer to the V atom (h1). The next higher energy location is 0.06 eV higher in energy, where one hydrogen atom occupies the fcc hole and the other hcp hole such that second hydrogen is nearer to the V atom (h5). Fig. 7.17 shows the top view of the dissociation of hydrogen molecule and diffusion of hydrogen atoms on the Ni and V doped Mg(0001) surface when the hydrogen molecule is kept at a distance on 3Å from the surface.

Table 7.4 The average binding energies of hydrogen atom when they occupy different holes at the $Mg_{58}VNi$ surface

Number	Abbreviation	Binding Energy (eV)
1	h1	-0.474
2	h2	-0.374
3	h3	-0.348
4	h4	-0.370
5	h5	-0.419
6	h6	-0.377

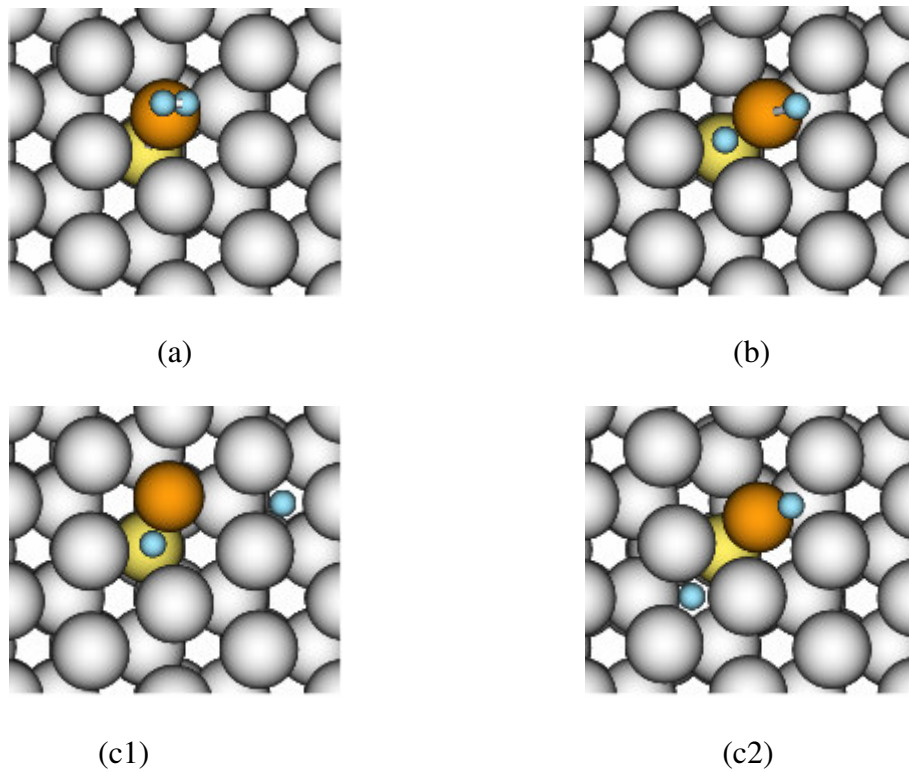


Fig. 7.17 Hydrogen dissociation and diffusion on the most stable $Mg_{58}VNi(0001)$ surface as represented by initial State (a), after dissociation of hydrogen molecule (b) and after diffusion of hydrogen atoms (c1 and c2).

In order to understand the effect on the electronic structures of the system, the projected density of state (PDOS) was plotted and analysed for the most stable configuration.

In principle, the transition metal elements act as good catalyst because of the availability of d electrons for donation and vacant d-states for back donation. Fig. 7.18 shows the PDOS of the Ni, and V before and after interaction with hydrogen.

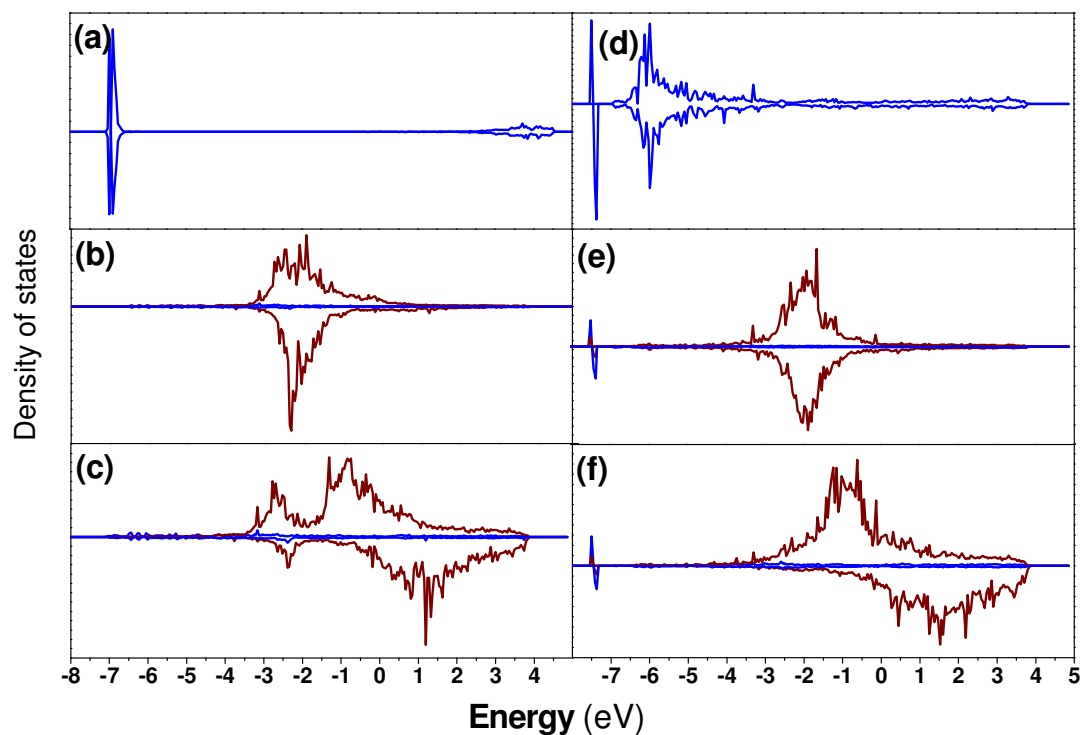


Fig. 7.18 Projected densities of states for H_2 dissociating over Ni and V doped Mg surface as a function of the energy. While figures (a), (b), and (c) represent the PDOS of H, Ni, and V before interaction (initial state), figures (d), (e), and (f) represent the PDOS of H, Ni, V after hydrogen absorption. The s and d orbitals are represented by blue and red lines, respectively.

For comparison, we have also depicted the PDOS of only hydrogen before and after interaction. It is seen (Fig. 7.18a) that, when hydrogen molecule is at a large distance (3 \AA) from the surface, there is no overlap between the Ni-d orbital and H-s orbital, a peak of hydrogen appears at -6.99 eV . The d PDOS of Ni (Fig. 7.18b) (at the top layer of Mg surface, shows a broad peak for d band. With slight variation to this, the d PDOS of V (Fig. 7.18c), which is in the second layer of the Mg(0001) surface, exhibit a dip in the center of the d band, characteristics of bcc metals. It can be noted further that, unlike Ni, the d PDOS of V shows

polarization of the spin channels. After the interaction of hydrogen with the metal surface, two distinct features are observed; (i) the 1s peak of hydrogen gets blue shifted (more negative energy) (Fig. 7.18d), and (ii) the appearance of a new s-band in the Ni and V spectra (Fig 7.18e and 7.18f). Moreover, the d PDOS of V was changed significantly after the interaction with hydrogen, which suggests there is strong influence of V atom also for the dissociation of hydrogen molecule.

After optimization of the most favorable adsorption site for dissociated H atoms on the Ni-V doped Mg surface the activation barrier for the dissociation of hydrogen molecule was calculated along the minimum energy path by NEB method. It was found that the dissociation of hydrogen molecule on the Ni site followed by migration towards the most stable hollow sites requires an activation barrier of 0.098 eV as shown in the Fig 7.19 by solid circles. This is significantly lower in comparison to the undoped Mg surface, where the activation barrier is found to be 0.97 eV [Table 7.2].

The activation barrier for the diffusion of hydrogen atom was calculated by taking 10 replicas including the initial and final state. As here the adsorption sites of two hydrogen atoms are not identical so the diffusion barrier was calculated separately for each of the adsorbed hydrogen. For the first hydrogen atom, which is adsorbed at the hcp site away from the V atom (V-H distance is 4.22 Å) the barrier for diffusion towards the fcc site was shown in the Fig. 7.17(c1). It was found from the NEB map that it needs an activation barrier of 0.41 eV for the diffusion process as shown by the solid triangle in Fig. 7.19.

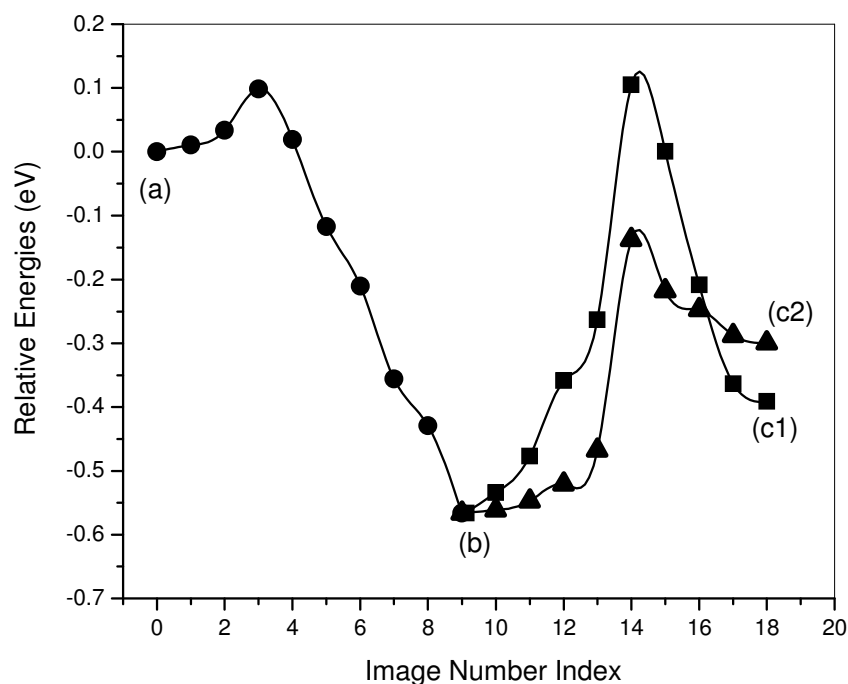


Fig. 7.19 NEB profiles for the dissociation and diffusion of hydrogen on the $Mg_{55}VNi$ surface when Ni atom is at the first layer and V atom is at the second layer. The relative energies of the initial state, after dissociation of hydrogen molecule on the surface, and after diffusion of hydrogen atoms on the surface are marked by (a), (b) and (c), respectively.

The result shows that for the diffusion of first hydrogen atom, the presence of V atom does not influence the activation barrier much. For the diffusion of the second hydrogen atom, i.e., which is closer to the V atom (V-H distance is 1.884 Å towards the fcc site (Fig 7.17(c2)), the activation barrier for diffusing from hcp site towards the fcc site is 0.66 eV (shown by the squares in Fig. 7.19), higher than the previous case.

7.1.3 Summery

Using first principles calculations we have investigated the interaction of hydrogen molecules with clean and M (Ti, V and Ni) doped Mg(0001) surfaces. The calculations were carried out using plane wave based pseudo potential method under the formalism of density

functional theory. First we have calculated the stability of the M atoms on the Mg surface. On the basis of the energetic criteria, we found that all these M atoms prefer to substitute one of the Mg atoms from the second layer than the top surface atom. In the second step we have studied the interaction of a hydrogen molecule with the clean and doped Mg surface. The results show that for M atoms at the surface, the hydrogen molecule undergoes spontaneous dissociative chemisorptions. However, for M atoms in the second layer, it requires to cross an activation barrier to undergo molecular dissociation. Further, to understand the mobility of hydrogen atoms on the surface we have calculated the diffusion energy barriers for the M doped surface. Contrary to the molecular dissociation behavior, it is found that the mobility of hydrogen atoms on the surface is easier if the M atoms are placed in the second layer in comparison to that in the top surface layer. It is believed that the results of the present study provides useful information based on the first principles calculations for synthesizing Mg based materials for hydrogen storage with optimal performance.

To understand the effect of impurity concentration in hydrogen dissociation and diffusion, an extensive first-principles investigation was performed over doubly substituted Mg surface and the findings were compared to those of single substitution. The calculations were carried out using density functional theory within the plane-wave pseudopotential approach employing projector-augmented wave potentials and generalized gradient approximation of Perdew-Burke-Ernzerhof exchange-correlation functional. Unlike single substitution, where the impurity atoms always prefer to replace one of the Mg atoms from the second layer, in the case of double substitution, when Ni and V atoms are doped simultaneously, the most stable configuration shows that Ni and V prefer to substitute Mg atoms from the first and second layers, respectively. The stabilization of Ni on the surface layer results in significant reduction in the dissociation barrier of the hydrogen molecule on the doped Mg surface.

7.2 Hydrogen Adsorption and Desorption Properties of Ti Doped Mg Clusters

An effective way to improve the efficiency of Mg hydrogen storage material is to reduce the particle size, where defects, large surface areas, and small diffusion path length help to improve the thermodynamics and kinetics of the sorption processes [280-282]. Typically, by ball milling, it is possible to get particle size as small as 20 nm. As the nano size Mg shows improved kinetics of hydrogen absorption, so the effect of finite size and doping was underscored for the hydrogen absorption- desorption properties of magnesium. Unfortunately, using first principles calculations, it is impossible to calculate such a large finite system due to the constraint of present day computers. However, it was found that for a Mg cluster consisting of more than 20 atoms, the hydrogenation leads to a rutile type inner core, similar to that of bulk [283-285]. Therefore, the Mg₅₅ cluster, which was used in the present work to study the hydrogenation behavior, is expected to provide useful information about the electronic and energetic barrier similar to that of larger size nanocrystals produced by ball milling.

The primary objective of this study is to underscore the feasibility of Mg based nanoclusters as hydrogen storage system. Further, it is of special interest to understand the role of Ti as a catalyst for the hydrogenation. Mg₅₅ cluster was used as a model to relatively larger size nanocrystals and doped it with Ti. After establishing the atomic and electronic structure of the Mg₅₅ cluster and the preferred location of Ti in the TiMg₅₄ cluster, the hydrogenation behavior of these clusters was investigated. These results were analysed in terms of stability, adsorption and dissociation barrier of H₂ molecule on the clean and doped Mg₅₅ to understand the role of doping towards designing nanoscale magnesium based alloys for hydrogen storage materials.

Along with the Mg₅₅ cluster, the smaller Ti doped Mg clusters (TiMg_n, n = 1-9) were also studied for their size depended stability. The hydrogen adsorption behavior was evaluated for the most stable cluster in that smaller series. Finally, these results were compared with previously studied Mg(0001) surface to emphasize the difference in hydrogenation behavior between a finite size cluster and extended substrates.

7.2.1 Computational methodology

In the present work we have used density functional theory (DFT) [210, 211] as employed in the Vienna *ab initio* Simulation Package (VASP) [275], and the projector augmented wave (PAW) method [234]. The PAW method is an all-electron frozen core method, which combines the features of both the ultra-soft pseudopotentials and augmented plane wave methods. The exchange correlation contributions were included using the generalized gradient approximation (GGA) proposed by Perdew–Burke–Ernzerhof (PBE). Wave functions were expanded using a plane wave basis set with a cutoff energy of 400 eV. The Brillouin zone was sampled at the gamma point. The magnetic moments at the local sites were calculated by projecting the wave functions on spherical waves within atomic spheres and integrating the resulting local spin-polarized densities of states up to the Fermi level. For the geometry optimization, the forces were minimized up to 0.05 eV/Å. The geometry optimizations were run starting from several initial candidate geometries with out imposing any symmetry constraints

We have also seen the interaction of hydrogen with the most stable TiMg₈ cluster. By varying the distance of hydrogen molecule from a face of TiMg₈ cluster in parallel and perpendicular geometry, the interaction diameter and the angular dependence was found out.

The nudged elastic band (NEB) [286] method was employed to find out the minimum energy path (MEP) and the corresponding energy barrier for the dissociation of hydrogen molecules on the clean Mg₅₅ and TiMg₅₄ cluster. The method involves the optimization of chain of images, obtained by linear interpolation, between the initial and final state. In most of the cases total number of images used is equal to 10, which is sufficient to map the minimum energy path (MEP) accurately. Each image is allowed to move in the direction perpendicular to the hyper tangent. Hence the energy is minimized in all direction except the direction of reaction path.

In order to check the stability of each cluster and the diffusion of H atoms on the Mg₅₅ cluster, we have performed *ab-initio* molecular dynamic simulations using the Nosé algorithm [287]. For this purpose each system was heated at higher temperatures (exact values are given in the text below) and kept for 5ps with a time step of 1fs. Although we understand that 5ps is not sufficient for accurate statistical analysis but it certainly provides meaningful qualitative information to understand the system. MD run was performed at 300 K on the most stable structures in the TiMg_n for sufficiently longer time to confirm its stability.

7.2.2 Results & discussion

7.2.2.1 Optimization of the geometry of Mg₅₅ cluster and Ti doped Mg₅₅ cluster

To begin with the electronic properties of Mg clusters were taken into consideration. The ground state electronic configuration of Mg is 3s², and there is a considerable energy difference between the filled 3s and vacant 3p orbital. As a result, two magnesium atoms interact through weak van der Waals force with low binding energy of 0.025 eV. In contrast, the binding energy of the bulk Mg with hcp packing is reported to be 1.51 eV/atom [236]. Mg

atom has filled $3s^2$ orbital and vacant $3p$ orbital in the ground state having considerable energy difference. So when two Mg atoms interact, two molecular orbital are formed and both are filled. As more and more Mg atoms interact, filled molecular orbital based on $3s$ (HOMO) and empty molecular orbital based on $3p$ (LUMO) are formed. The gap between HOMO and LUMO (i.e., the band gap) decreases as number of Mg atom increases. After a certain n value, Δ becomes close to zero and $3s$ and $3p$ band overlaps with each other. At this stage there will be a possible hybridization of $3s$ and $3p$ band and the electrons shows partial directional character which gives raise to electronic spin moment. At around $n = 20$, the band gap becomes zero and the spin moment arises. From the literature it is found that that small clusters of Mg show stability according to the prediction of the electronic shell model, where as the larger clusters follow the geometrical model. Among the different geometrical structures of the large Mg cluster, the icosahedral packings are most favorable, which also supports the experimental findings. The icosahedral structure of Mg₅₅ shows definite spin moment and its electronic structure is quite different than the bulk Mg. Icosahedral structure is having five fold axis of symmetry so this cannot be realized in the bulk phase. As the physical and chemical properties of the cluster are dependent on their geometrical structure, so in the present study Mg₅₅ was taken as the representative material to study the behavior of nano structured.

The ground state geometry of the Mg₅₅ cluster was found to form a compact icosahedron. This is in good agreement with the previous prediction by Köhn et al [50]. The Mg₅₅ cluster has a core of 13 atom icosahedron with one atom at the centre. The outer layer consists of 42 atoms, of which 12 atoms are at vertices of the inner icosahedron and additional 30 atoms are at the centre of the 30 edges. So, in this type of structure there are four different sets of Mg atoms. One Mg atom is at the center (Mg1), 12 Mg atoms are at the

middle layer (Mg2), and two types of Mg atoms (12 and 30 atoms) at the top layer (Mg3 and Mg4) as shown in Fig. 7.20.

The binding energy of Mg55 cluster is 1.016 eV/atom, which is 67 % of the cohesive energy of bulk cohesive energy. Most importantly, the equilibrium structure of the Mg₅₅ cluster shows total spin moment of 8 μ B. In this context it should be mentioned that the unusual appearance of the magnetic moment in Mg₅₅ cluster can be attributed to the *s-p* hybridization, which starts from *n* = 18 onwards, a signature of its metallic behavior [284].

After establishing the ground state geometry and electronic structure of pure Mg₅₅ cluster, we next consider the most preferred substitutional site for an impurity Ti atom in Mg₅₅ cluster. For this purpose four different locations were considered: Ti substitutes one Mg (i) from the center (Ti1), (ii) at the middle layer (Ti2) and (iii) & (iv) two different positions at the top layers (Ti3 and Ti4). To illustrate the locations in detail, they were represented in Fig. 7.20.

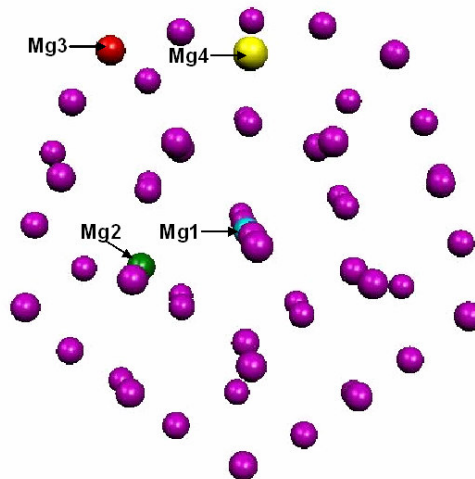


Fig. 7.20 The equilibrium structure of the Mg₅₅ cluster. Blue, green, red and yellow colors represent center Mg atom (Mg1), one of the 12 Mg atoms at the middle layer (Mg2), one of the 12 Mg atoms at the surface at the top of 12 vertices (Mg3), and one of the Mg atoms at the center of 30 edges of the icosahedron (Mg4), respectively.

Once the geometries are optimized, the binding energies, substitutional energies and total spin moments for each structure were calculated and a summary of these results are listed in Table 7.5. The binding energies and substitutional energies of different substituted Mg₅₅ clusters were calculated by the following equation:

$$BE(\text{TiMg}_{54}) = E(\text{TiMg}_{54}) - E(\text{Ti}) - 54E(\text{Mg})$$

$$E_{\text{sub}} = E(\text{Mg}) + E(\text{TiMg}_{54}) - E(\text{Mg}_{55}) - E(\text{Ti})$$

Where BE(TiMg₅₄) is the BE energy of the Ti atom substituted Mg₅₅ cluster, E(TiMg₅₄) is the total energy of the Ti atom substituted Mg₅₅ cluster, E(Ti) is the energy of Ti atom in the free state, E(Mg) is the energy of the Mg atom in the free state and E_{sub} is the substitutional energy.

Table 7.5 The binding energies, substitutional energies and magnetic moments of Mg₅₅ cluster and Ti substituted (four different locations) Mg₅₅ cluster.

	Binding Energy (eV)	Magnetic Moment (μ_B)	Substitutional Energy (eV)
Mg ₅₅	-55.88	8.00	0
Ti1	-58.44	16.00	-2.55
Ti2	-59.41	6.00	-3.53
Ti3	-58.23	10.00	-2.53
Ti4	-58.62	8.00	-2.74

It is clear from this table that Ti prefers to replace one Mg atom from the middle layer. Further, a comparison of the spin density distribution between Mg₅₅ and TiMg₅₄ clusters (shown in the Fig. 7.21) show that, not only the local spin moment of Ti is higher, but it further induces higher spin moments on its nearest Mg atoms.

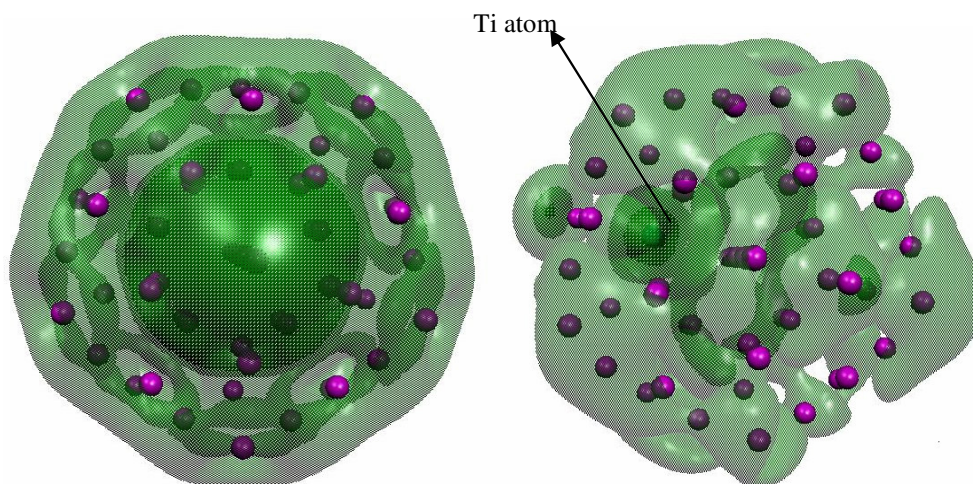


Fig. 7.21 The spin density distribution of (a) Mg_{55} and (b) $TiMg_{54}$ cluster (Ti remains at the middle layer). Dark and light colors represent higher and lower values, respectively.

Thus the substitution of Ti can activate the neighboring Mg at the surface by changing the spin density around it, which in turn can enhance the dissociation of hydrogen molecule. Further to ascertain the enhanced activity of the surface Mg atoms in presence of Ti in the middle layer, the change in the density of states of the particular Mg atom in $TiMg_{54}$ cluster were plotted in Fig 7.22, and compared it with the clean Mg_{55} .

It is seen that, though there is no appreciable change at the deeper energy levels, but significant changes were observed around the highest occupied molecular orbital (HOMO). When Ti is doped at the middle layer then the adjacent Mg atom shows a finite density of state at the HOMO level, which is responsible for catalyzing the dissociation of hydrogen molecule.

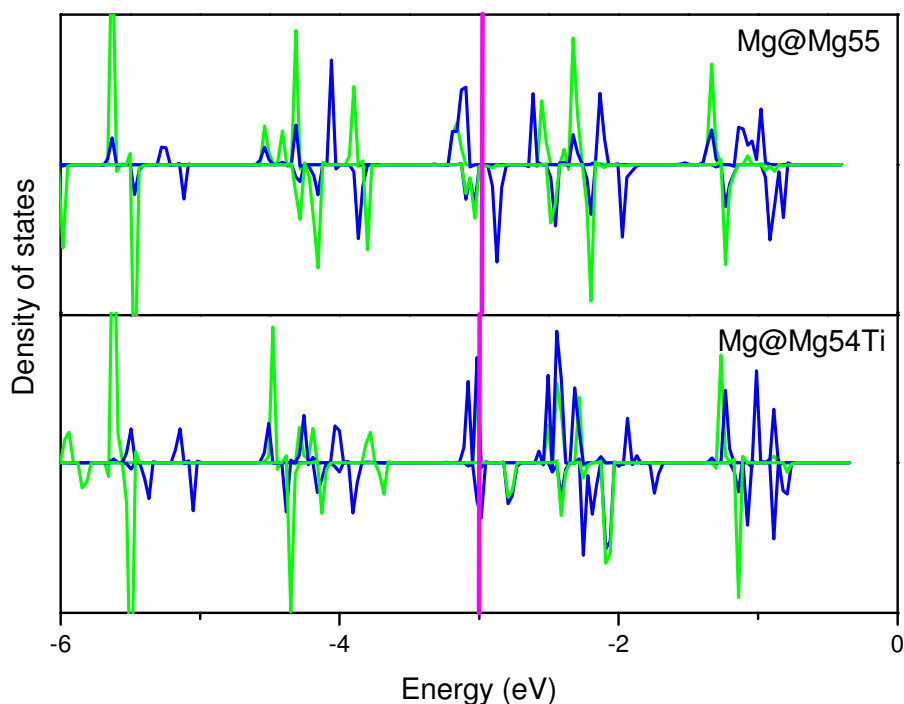


Fig. 7.22 The density of state of one of the surface Mg atom for Mg_{55} cluster and $TiMg_{54}$ cluster (Ti remains at the middle layer). Green and blue colors indicate the contribution from *s* and *p* orbital, respectively. The pink line indicates the Fermi level.

7.2.2.2 Interaction of hydrogen with Mg_{55} and $TiMg_{54}$ clusters

Coming to the hydrogenation behavior of Mg_{55} and $TiMg_{54}$ clusters, the focus was given on two aspects: (i) the effect of finite size of Mg_{55} cluster in comparison to the periodic surface and (ii) the effect of Ti substitution on the hydrogenation behavior. Table 7.6 shows the interaction energy of hydrogen atom with pure Mg_{55} and $TiMg_{54}$ clusters where Ti substitutes Mg from different layers. For comparison, the dissociation barrier of hydrogen in case of periodic Mg surfaces calculated using same methodology is shown in the parenthesis.

Table 7.6 Interaction energies of hydrogen with Mg₅₅ and TiMg₅₄ clusters. The numbers in the parenthesis corresponds to the same for periodic surface.

System	H ₂ absorption energy (eV)	Magnetic Moment (μ _B)	Activation Energy (eV)
Mg1	-0.217	4	0.72 (0.96)
Mg2	-0.218	4	0.72
Ti1	-0.198	12	0.68
Ti2	-0.164	4	0.58 (0.8)
Ti3	-0.704	8	Nil
Ti4	-0.571	6	Nil

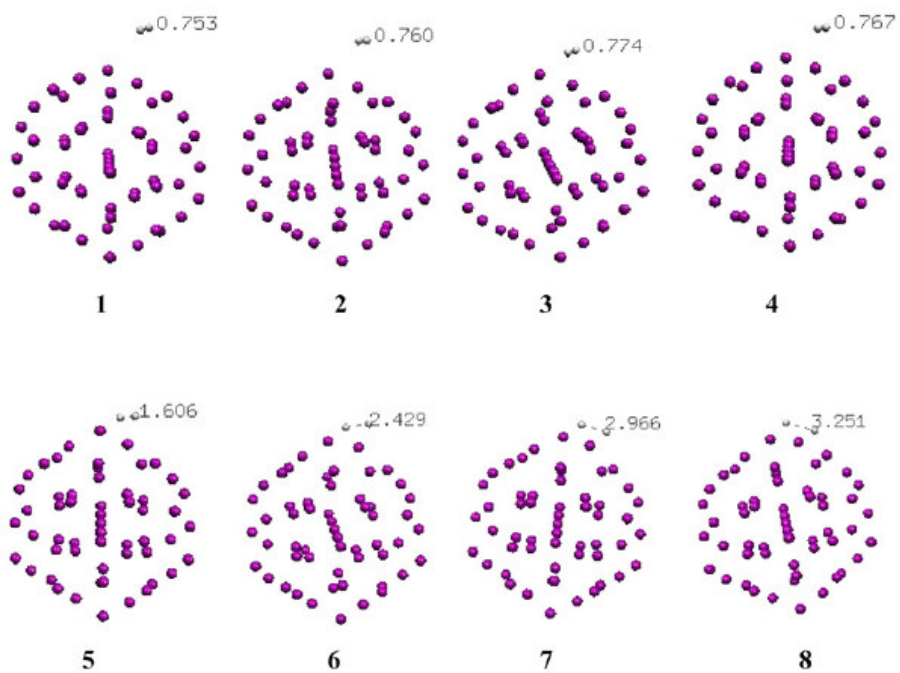
It was found that for all the cases the hydrogen molecule interacts *via* dissociative chemisorptions. The hydrogen adsorption energy was calculated by the following equation:

$$H = [E(\text{TiMg}_{54}\text{H}_2) - E(\text{TiMg}_{54}) - E(\text{H}_2)]/2$$

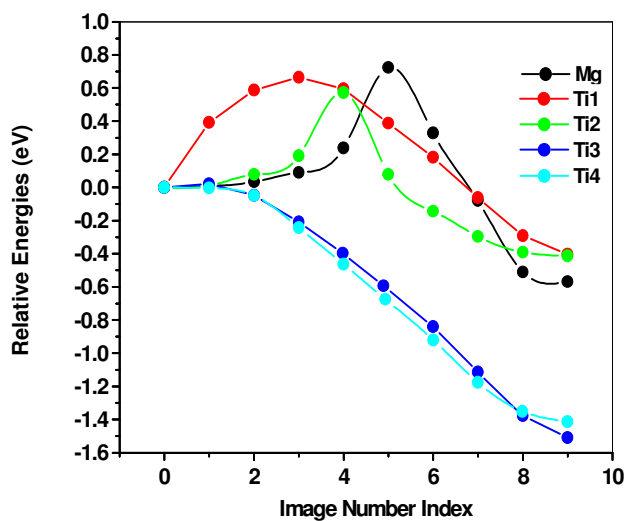
Where H is the adsorption energy, E(TiMg₅₄H₂) is the total energy of the system after interaction with hydrogen, E(TiMg₅₄) and E(H₂) are the total energy of doped Mg cluster and hydrogen molecule before dissociation. When hydrogen molecule approaches to the Mg₅₅ cluster, after dissociation it can bind either one of the 12 Mg atoms that forms corner of the triangle on the surface or one of the 30 Mg atoms placed over the edges of the inner icosahedron. In both cases, the interaction energy is found to be similar (0.218 eV/atom). Now for Ti substituted Mg clusters, the binding energy of hydrogen is found to be the highest when Ti remains at the top layer (Ti3 & Ti4). This is because of direct Ti- H bond formation, which is much stronger than Mg-H bond. But when Ti is placed at the middle layer (Ti2) or at the center (Ti1), the binding energy of hydrogen is found to be 0.164 and 0.198 eV, respectively. Thus, the incorporation of Ti in Mg₅₅ cluster reduces the strength of Mg-H bond, which is a desirable property for easy diffusion and desorption of hydrogen.

After optimizing the geometry of the hydrogenated Mg_{55} cluster, the minimum energy reaction path was investigated using the NEB method. For this purpose, total 10 images were used including the initial and final positions. The images are given in Fig. 7.23(a), where it shows that as the hydrogen molecule comes closer to the Mg_{55} cluster the H-H bond length increases and finally the hydrogen molecule gets dissociated. The H-H bond length distance for each of the images during the hydrogenation reaction, has been shown in the the figure. The activation energy for the dissociation of hydrogen on Mg_{55} cluster was estimated to be 0.72 eV [Fig. 7.23(b)]. It is of worth to mention that earlier in our work for a clean Mg(0001) surface the activation energy was found to be 0.97 eV. The smaller dissociation barrier of Mg_{55} cluster is attributed to its finite size or the large surface to volume ratio. To compare the dissociation barriers of hydrogen with Ti substituted Mg_{55} cluster, the MEP were investigated by placing the Ti at four different positions as mentioned before. The energy profiles through 10 image sites are shown in Fig. 7.23.

It is found that when Ti replaces one of the Mg atoms from the top layer, the dissociation of hydrogen occurs spontaneously without any effective barrier. However, when Ti substitutes Mg from the middle layer or center, the dissociation barrier of the hydrogen molecule is found to be 0.58 and 0.68 eV, respectively. The variation of the dissociation barrier of hydrogen molecule is due to the influence of Ti and can be explained from the electronic density of electronic state spectrum as shown in Fig. 7.24.



(a)



(b)

Fig.7.23 (a) The images of Mg_{55} through out the reaction path. The bond distance of H-H bond was indicated on each image showing the dissociation of the hydrogen molecule towards hydrogen atoms. (b) NEB profiles for the dissociation of hydrogen molecule on pure Mg_{55} cluster and $TiMg_{54}$ clusters when Ti atom remains at four different positions.

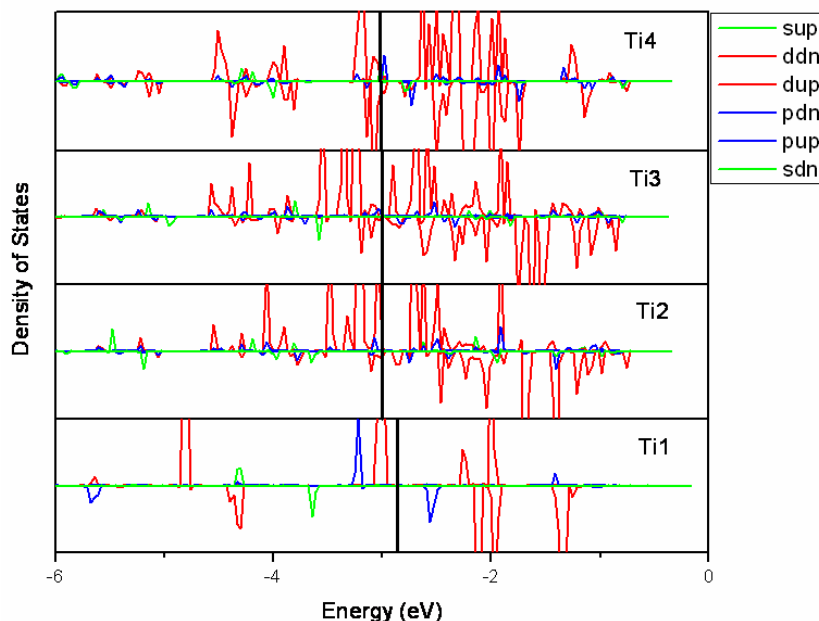


Fig. 7.24 The density of state of Ti atom of $TiMg_{54}$ cluster when Ti atom remains at four different positions. The sup, ddn etc represents s spin up, d spin down respectively.

In case of pure Mg_{55} cluster, the density of state shows polarization of up and down spins with total magnetic moment of $8\mu_B$, which increases its activity compared to the Mg bulk, and results in the lower activation energy of 0.72 eV. When Ti is at the surface, the d orbital of Ti interacts directly with the hydrogen and the dissociation occurs spontaneously. In the second case where Ti replaces Mg from the center, the PDOS spectrum reveals significant contribution of Mg energy levels in the formation of the HOMO energy state. Thus the influence of Ti is expected to be less, which results in small decrease in the activation barrier compared to Mg_{55} cluster. But when Ti is at the middle layer, it can activate the surface Mg atom adjacent to it, which was verified both from the spin density distribution and density of state plot. Moreover, it is seen that the d-orbital of Ti is localized on the HOMO, so the Ti can influence the dissociation of hydrogen more and indeed a considerable decrease in the activation barrier was found.

After calculating the activation energy for the dissociation of hydrogen molecule of different clusters, the *ab-initio* molecular dynamics simulations was performed to see the

effect of temperature on the cluster stability and on the diffusion behavior of adsorbed hydrogen atoms. In this context it should be mentioned that diffusion of hydrogen atoms on the substrate plays the key role for the final desorption step. The hydrogenated HMg_{55}H cluster was heated at 100K, 200K and 300K separately for 5ps with 1fs time step using the Nose algorithm. The Mg-H(2) distance [Fig. 7.25] was monitored with respect to the time for all the cases.

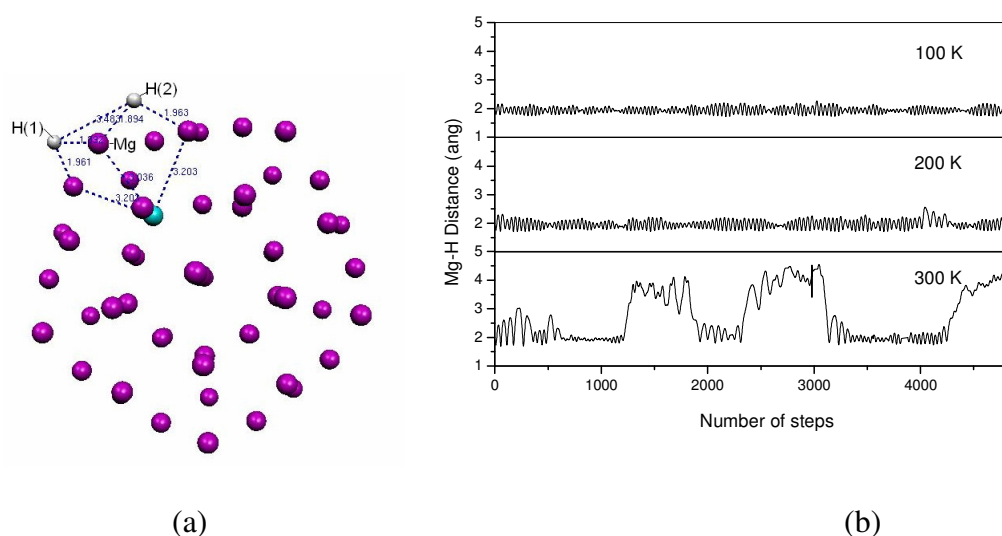


Fig. 7.25 Molecular Dynamics Calculation at 100 K, 200 K and 300 K on HMg_{55}H cluster. (a) The equilibrium structure of HMg_{55}H and (b) variation of Mg-H(2) distance at different temperatures.

Interestingly, it can be noted that whereas there is no appreciable change in the Mg-H distances when it is heated at 100 and 200K (only the Mg-H bond vibration was observed due to the increased thermal energy), but when the system is heated at 300K, the Mg-H bond distances increases significantly and the H atom starts toggling between two adjacent Mg atoms. It may be important to note that as the coverage is very small, so the possibility of two hydrogen atoms coming in proximity and forming H_2 molecule for desorption is negligible. However, for desorption of hydrogen molecule, the first step is the onset of hydrogen atom diffusion and therefore, it is inferred that at room temperature the hydrogen atoms will start

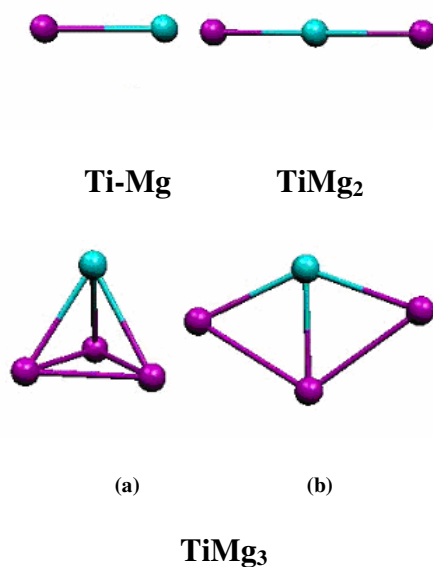
diffusion on the Mg nanoclusters, which will lead to desorption at slightly higher temperatures.

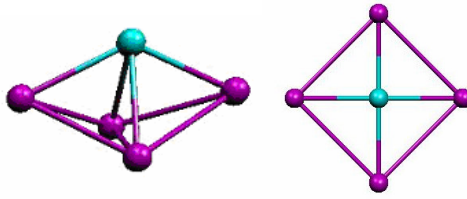
7.2.2.3 Geometry and stability of smaller Ti doped Mg Clusters (TiMg_n, n = 1-9)

To obtain the equilibrium geometries of all TiMg_n (n = 1-9) clusters a large numbers configuration for each cluster were optimized without any symmetry constrain. Fig. 7.26 shows few low lying isomers (within 1 eV) those were obtained from these calculations. From the optimized geometries it was seen that Ti atom occupies the most coordinated site by replacing Mg. So in all the studied structures, the Ti atom is considered as the center atom with which all the Mg atoms get coordinated. The binding energies of the clusters were calculated as:

$$BE = E_t - (nE_{Mg} + E_{Ti}),$$

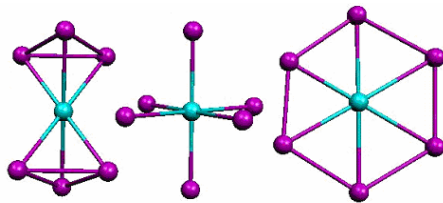
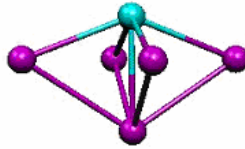
where, E_t is the total electronic energy of a cluster and E_{Mg} and E_{Ti} are the correction energies for Mg atom and Ti atom respectively.





(a)

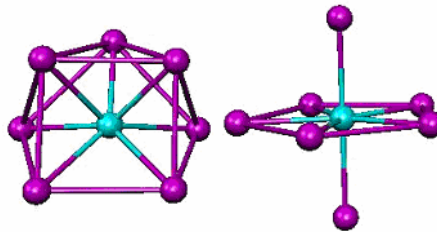
(b)



(a)

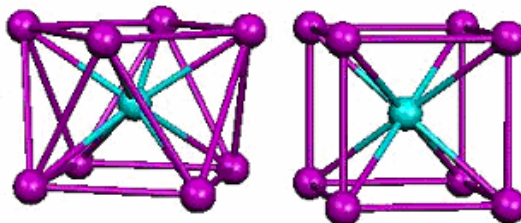
(b)

(c)



(a)

(b)



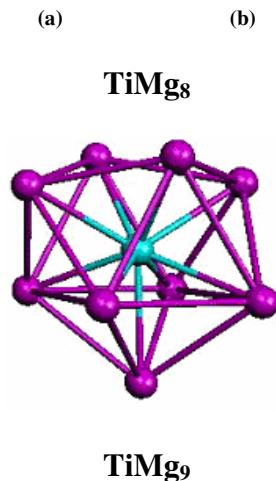


Fig. 7.26 *The optimized geometries of TiMg_n clusters.*

To start the discussion on the geometries of these clusters, let us first consider the three dimers. Mg-Mg, Ti-Ti and Ti-Mg are having bond distances 3.50 Å, 1.89 Å and 2.86 Å respectively. Their binding energies are -0.043 eV, -3.60 eV and -0.80 eV respectively which are close to the literature value. It is noted that Mg-Mg bond distance is much higher (3.50 Å) compared to Ti-Mg distance. The TiMg₂ cluster form linear structure where Ti is placed at the center. In TiMg₂ cluster the Ti-Mg distance is 3.00 Å and the binding energy is found to be -1.311 eV. Though Mg₃ cluster is having a triangular geometry but after Ti doping, the triangular geometry, and linear geometry with Ti at the corner are found to be much higher in energy.

Both TiMg₃ and TiMg₄ optimizes in the non-planar structures rather than a planar structure and the binding energies are found to be -2.587 eV and -3.618 eV respectively, which are 0.241 eV and 0.864 eV more stable than their respective planar values. The non-planar geometry of TiMg₃ is trigonal pyramidal type, where Ti caps the triangle formed by three Mg atoms. In the metastable planer structure of TiMg₃ the Ti and Mg atoms form a tetragon together. The equilibrium structure of TiMg₄ is a capped trigonal pyramid (TP). The Ti atom along with three Mg atoms form one trigonal pyramid, of which one of the triangular

faces containing Ti atom gets capped with the remaining Mg atom. In this structure, two Ti-Mg distances are 2.816 Å and other two are 2.834 Å. In the metastable square planar structure of TiMg₄, Ti atom remains at the center and four Mg atoms get attached with the Ti to form a square with Ti-Mg bond length of 2.896 Å and the Mg-Mg distances are 4.095 Å.

The equilibrium structure of TiMg₅ is a distorted octahedral structure with binding energy of -4.43247 eV. In that structure, Ti atom resides at one of the apex and the Ti-Mg bonds are found to be 2.82 Å. The Mg atom which resides at the opposite vertex of Ti can form bond with other Mg atoms and the bond distances are 3.14 Å. The other two metastable structures of TiMg₅ are trigonal bi pyramid and planar structure and in both the cases Ti is the center atom.

The most stable isomer of TiMg₆ forms trigonal anti prism, where all the Ti-Mg bond distances are equal to 2.91 Å, showing the symmetrical nature of the structure. The other two close lying isomers are octahedron and planar hexagonal structure, which are 0.1 eV and 0.95 eV higher in energy respectively than the equilibrium trigonal anti prism geometry. Several initial configurations were considered for TiMg₇ cluster. It is found that the lowest energy isomer favors a tetragonal antiprism with one corner vacancy. It can be viewed as the central Ti connecting with a square and triangle in opposite sides as shown in Fig. 7.26. Another isomer which forms pentagonal bipyramid motif is 0.06 eV higher in energy. The most stable isomer of the TiMg₈ cluster forms by filling the vacancy of the TiMg₇ cluster i.e.; it forms tetragonal antiprism structure. The structure is highly symmetric as all the Ti-Mg distances are 2.68 Å and all the Mg-Mg distances in the same square faces are 3.2 Å. The second higher energy isomers of TiMg₈ are body centered cubic structure where Ti resides at the body centered position with edge length of 3.127 Å and Ti-Mg distances of 2.708 Å. For, TiMg₉ cluster, the lowest energy isomer is found to form by fusing TiMg₄ and TiMg₅ clusters

as shown in Fig. 7.26. By this process several number of triangular Mg faces are generated so the structure becomes stabilized. Few other isomers were also considered starting with different configurations. But after optimization either they relaxes into the same ground state structure or optimizes into metastable structures which are significantly higher in energy (more than 1 eV) in comparison to the ground state isomer.

The average binding energy of TiMg_n clusters was calculated as

$$E_b = [E_{\text{TiMg}_n} - (nE_{\text{Mg}} + E_{\text{Ti}})]/(n+1),$$

Where, E_{TiMg_n} is the total energy of the corresponding TiMg_n cluster, E_{Mg} and E_{Ti} are the energy of Mg and Ti atom respectively in the free state. Fig. 7.27 shows the variation of binding energy as a function of Mg atom in TiMg_n clusters. In general, the binding energy increases smoothly with number of Mg atoms. The additional humps in the binding energy curve observed for TiMg_6 and TiMg_8 reflects their higher stability over others in this series.

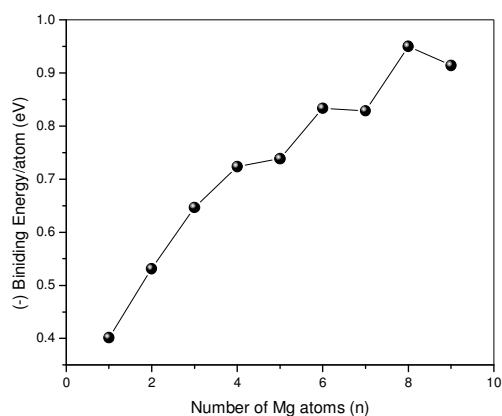


Fig. 7.27 The variation of binding energy/atom with increasing number of Mg atom

Magic clusters are those, which show higher stability than their neighbors. Based on the total energies one can search for stable clusters by calculating the second energy difference, which is being calculated as,

$$\Delta_2 E(n) = [E(\text{TiMg}_{n-1}) + E(\text{TiMg}_{n+1}) - 2E(\text{TiMg}_n)],$$

Where, $E(\text{TiMg}_n)$ is the total energy of cluster TiMg_n . $\Delta_2 E(n)$ represents the relative stability of a cluster, with n number of Ti-Mg bond, with respect to its neighbors. As seen in the Fig. 7.28, TiMg_6 and TiMg_8 clusters show higher stability compared to other clusters.

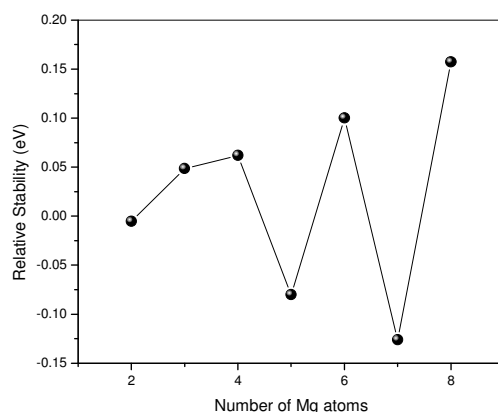


Fig. 7.28 The variation of second difference in energy with the increasing number of Mg atom.

7.2.2.4 Hydrogenation on TiMg_8 cluster

To understand the hydrogenation behavior of doped Mg clusters TiMg_8 cluster was used as model. The reason for choosing TiMg_8 is two fold: (i) It is one of the most stable clusters in this series, and (ii) Ti atom is symmetrically covered by Mg atoms. It should be worth mentioning that in our previous work on Ti doped Mg surface it was found that the most stable location of Ti is in the second layer instead of top layer [262, 263]. Even in case of TiMg_{54} cluster it was found that Ti atom stabilizes in the second layer of the icosahedron structure [284]. Thus we believe that in the range of such small clusters, TiMg_8 is a good choice to compare the results between finite and infinite systems. In order to further confirm the stability of TiMg_8 cluster, the *ab-initio* molecular dynamics simulations was performed

using the Nose algorithm [287]. The TiMg_8 cluster was heated up to 300K and equilibrated for 10 ps and it is found that the structure is quite stable.

Once the stability of TiMg_8 cluster has got established, its hydrogenation behavior was studied. First, the minimum distance of interaction of hydrogen molecule was calculated when it approaches in i) perpendicular and ii) parallel direction on the plane of the TiMg_8 cluster as shown in Fig.7.29.

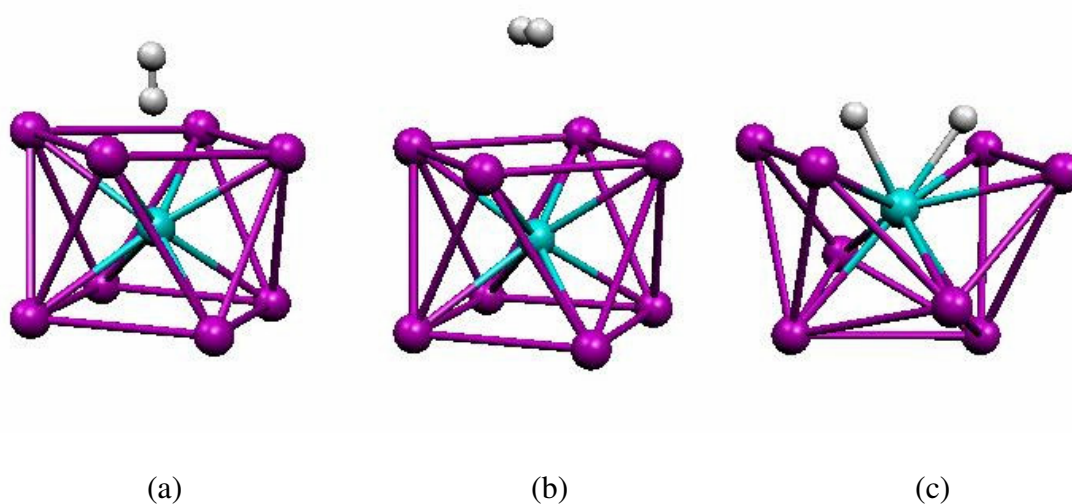


Fig. 7.29 Interaction of hydrogen molecule with the TiMg_8 cluster in the perpendicular and parallel direction and the final geometry after interaction.

In the first case, when the hydrogen molecule approaches in perpendicular orientation with respect to the face of TiMg_8 , the starting distances of hydrogen molecule was varied as 2 Å, 1 Å, 0.5 Å, 0.2 Å and 0.1 Å. It was found that the dissociation of H-H bond occurs only when the starting distance from the surface plane is 0.1 Å or less. Otherwise the hydrogen molecule is repelled up to a distance of 3.5 Å from the plane. In the second case, when the H-H bond is in parallel orientation to the plane of TiMg_8 surface, was studied at various distances like 2 Å, 1 Å and 0.5 Å. In this case it is found that the dissociation hydrogen molecule occurs at a distance of 0.5 Å from the surface, otherwise the hydrogen molecule

gets repelled and the parallel geometry changes to the perpendicular geometry. From the above results it can be concluded that hydrogen molecule can dissociatively interact with the TiMg₈ cluster from a larger distance if it comes parallel to one of plane of the cluster.

The binding energy/hydrogen atom was calculated as:

$$E = (E_{\text{TiMg}_8+2\text{H}} - E_{\text{TiMg}_8} - E_{\text{H}_2})/2,$$

where, $E_{\text{TiMg}_8+2\text{H}}$ is the total energy of TiMg₈ system after interaction with hydrogen, E_{TiMg_8} is the energy of TiMg₈ system and E_{H_2} is the energy of hydrogen molecule. The binding energy of hydrogen on TiMg₈ cluster is estimated to be 0.152 eV. Remarkably, this is in good agreement to the case for extended surface. It was found that when Ti is doped in the second layer of Mg surface, the interaction energy of hydrogen on the Mg surface is 0.157 eV found in our earlier study. After optimizing the starting distance of hydrogen for interacting with TiMg₈ cluster, the angular dependence was considered next. For this purpose the approach angle of hydrogen molecule was increased slowly from 90° by placing at 0.5 Å distance from the surface. The results suggest that the hydrogen molecule only interacts from a distance of 0.5 Å, if the angle of interaction is 120° or more.

In order to explore the activation energy for hydrogen interaction on TiMg₈ cluster, the minimum energy path (MEP) was calculated using Nudge Elastic Band (NEB) method. For this purpose 10 images were considered including the initial and the final state. It is found that considerable activation barrier is there for the dissociation of hydrogen molecule as shown in the Fig. 7.30 and the value is found to be 0.86 eV. It can be noted that in case of a Mg(0001) surface with one Ti atom at the second layer then the activation barrier is almost same as found above, so such type of surfaces can be modeled as TiMg₈ cluster.

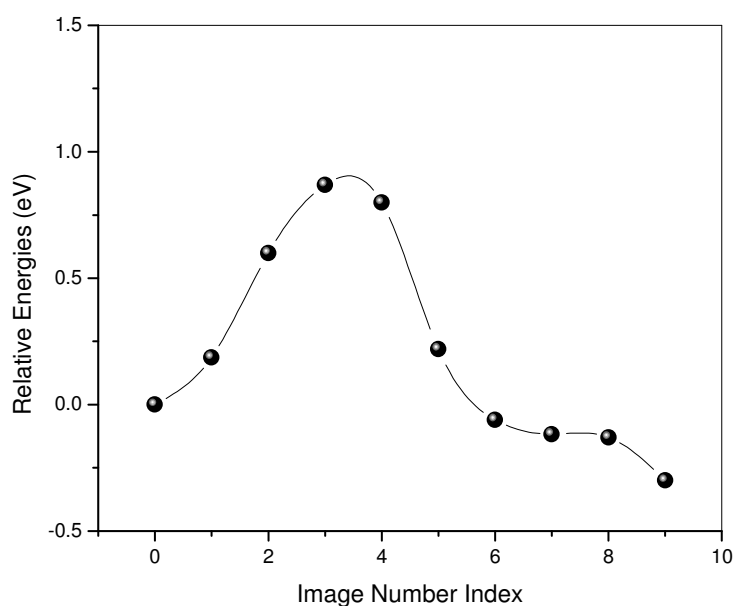


Fig. 7.30 NEB profile for the dissociation of hydrogen molecule on the $TiMg_8$ cluster.

7.2.2.5 Comparison of hydrogen absorption behavior of the Mg clusters with Mg(0001) surface

Lastly the structure and behavior of $TiMg_8$ cluster was compared with the Ti doped Mg surface. It is known from the previous study that Ti metal stabilizes itself in the second layer rather than the surface layer. Now when they interact with hydrogen molecule, in both the cases, the hydrogen molecule undergoes dissociative chemisorption and the binding energies are also quite comparable. It was found that in both the cases, the geometry of interaction is quite similar as after interaction, the H-Ti, Mg-Mg, and Mg-H distances are quite similar. It is worth noted that the activation barrier for the interaction of hydrogen, which was calculated from the NEB calculation, is close to that of surface, indicating that the $TiMg_8$ can be considered as a finite geometrical model of Ti doped Mg surface where Ti remains in the second layer.

7.2.3 Summary

Using first principle calculations, the hydrogen absorption properties of Mg cluster to reveal the effect of finite size was studied. The calculations clearly show that Mg₅₅ cluster has less activation barrier for dissociation of hydrogen molecule than bulk Mg, hence enabling hydrogen dissociation at lower temperatures. The effect of Ti doping on the hydrogen absorption properties also was established, and it is found that when Ti is substituted in the Mg₅₅ cluster then it preferably goes at the middle layer and it can decrease the dissociation barrier further by activating the surface Mg atom. The overall decrease in the activation barrier in this case is 40 % compared to pure Mg bulk. The *ab-initio* molecular dynamics calculations show that, at 300 K the Mg-H is elongated sufficiently and starts a flip-flop motion on the surface, which can be viewed as the onset of hydrogen diffusion, a preliminary step for desorption. As currently, high desorption temperatures are a major impediment; hence the projected shift toward more favorable operation temperatures is crucial for the application of Mg as a reversible hydrogen storage material. We believe that the above results can provide a good theoretical support towards the attempts of the experimentalist to reduce the size of Mg for hydrogen storage material with optimal performance. We have also carried out calculations based on Density Functional Theory to find the structures and relative stabilities of TiMg_n (n = 1-9) clusters. We have seen that TiMg₈ cluster, with staggered bcc conformation, is the most stable system in the series. We have also found the interaction behavior of hydrogen with the TiMg₈ system. The hydrogen molecule can interact with the TiMg₈ cluster from a shorter distance, if it comes parallel to one of the square faces. The interaction energy of hydrogen for the studied system is close to that of the Ti doped Mg surface, when Ti atom is doped in the second layer. So for that type

of surface, the local structure around the doped Ti atom can be modeled as TiMg_8 cluster as it shows behavior similar to that.

7.3 Conclusion

Here the interaction behavior of a hydrogen molecule on the $\text{Mg}(0001)$ surface doped with three different transition metal atoms ($M = \text{Ti}, \text{V}, \text{and Ni}$) was reported. This work was divided into two parts: in the first part the stability of these M atoms at different layers of the Mg surface was investigated, and in the second part the interaction of molecular hydrogen with these doped surfaces was calculated. To understand the hydrogen storage efficiency of these materials, the energy barriers for the dissociation of molecular hydrogen and subsequent diffusion of dissociated hydrogen when the M atoms are at the top surface and in the bulk was also calculated.

On the basis of stability criteria, the substitutional energies of all the M elements are found to be negative, indicating that M atom doping is thermodynamically favorable. More importantly, it is seen that all the M atoms prefer to substitute one of the Mg atoms from the second layer than that from the top surface layer. However, the relative stability in the first and second layer differs for different transition metal elements. For Ti and V the difference in energy is almost 0.52 and 0.425 eV respectively and in case of Ni it is 0.13 eV only.

The interaction of a hydrogen molecule with doped Mg surface suggest that when the impurity atoms are on the top layer, they are good catalyst for hydrogen absorption as the dissociative chemisorption of hydrogen molecule occurs spontaneously on the catalyst site and the hydrogen atoms occupy the fcc or hcp holes depending upon the nature of M atom. However, they restrict the movement of hydrogen atoms further, as the diffusion barrier is quite high. Here the diffusion of hydrogen atoms is the rate limiting step. The situation is

reversed when the M atoms substitute one of the Mg atoms from the second layer. In this case the dissociation of hydrogen molecule is controlled by a high activation barrier but once the hydrogen is absorbed the mobility of the hydrogen atoms on the surface is easier than the previous case. Here the dissociation process is the rate limiting step. Finally, by comparing all the results, it is inferred that the substitution of V in the Mg lattice will be the best choice considering the requirements of a good hydrogen storage material.

In the later part of the study, the hydrogen dissociation and diffusion mechanism on the Mg(0001) surface doped with V and Ni atoms was investigated. The efficiency of catalytic behavior of these transition elements was compared between single and double substitution. All calculations were performed with density functional theory using plane-wave pseudopotential approach. The results showed that when the Mg surface was doped by one Ni or V atoms, the most stable configuration showed that the impurity atoms prefer to substitute one of the Mg atoms from the second layer. This results in very negligible effect on the hydrogen dissociation barrier. Unlike this, when both V and Ni are doped simultaneously, the most stable configuration shows that V and Ni are placed in the second and first layer respectively. The stabilization of Ni in the first layer enhances the direct interaction of hydrogen which results in significant lowering of the dissociation energy barrier, the most desirable property of hydrogen storage. The presence of V atom at the subsurface layer not only stabilizes Ni at the surface layer but additionally facilitate dissociative chemisorptions of the hydrogen molecule on the catalytic site of Mg(0001) surface. Its effect on the diffusion of hydrogen molecule through the Mg(0001) surface was also seen. After dissociation of hydrogen molecule into two hydrogen atoms at the catalytic site in the Mg(0001) surface, two hydrogen atoms show different activation barriers for diffusion depending upon their positions. The hydrogen atom, which is away from the V atom shows a lower diffusion barrier compared to the other hydrogen atom due to the lower influence of the V atom.

Finally it can be concluded that by increasing the impurity concentration it is possible to stabilize the dopant on the top layer, which results in significant reduction of the hydrogen molecule dissociation barrier on the Mg surface.

Using first principle calculations, the hydrogen absorption properties of Mg cluster to reveal the effect of finite size was studied. The calculations clearly show that Mg₅₅ cluster has less activation barrier for dissociation of hydrogen molecule than bulk Mg, hence enabling hydrogen dissociation at lower temperatures. The effect of Ti doping on the hydrogen absorption properties also was established, and it is found that when Ti is substituted in the Mg₅₅ cluster then it preferably goes at the middle layer and it can decrease the dissociation barrier further by activating the surface Mg atom. The overall decrease in the activation barrier in this case is 40 % compared to pure Mg bulk. The *ab-initio* molecular dynamics calculations show that at 300 K the Mg-H is elongated sufficiently and starts a flip-flop motion on the surface, which can be viewed as the onset of hydrogen diffusion, a preliminary step for desorption. As currently, high desorption temperatures are a major impediment; hence the projected shift toward more favorable operation temperatures is crucial for the application of Mg as a reversible hydrogen storage material.

In the present study we have carried out calculations based on Density Functional Theory to find the structures and relative stabilities of TiMg_n (n = 1-9) clusters. We have seen that TiMg₈ cluster, with staggered bcc conformation, is the most stable system in the series. We have also found the interaction behavior of hydrogen with the TiMg₈ system. The hydrogen molecule can interact with the TiMg₈ cluster from a shorter distance, if it comes parallel to one of the square faces. The interaction energy and the activation barrier for dissociation of hydrogen on TiMg₈ cluster, is close to that of the Ti doped Mg surface, when

Ti atom is doped in the second layer. So for that type of surface the local structure around the doped Ti atom can be modeled as TiMg_8 cluster.

Hydrogen Storage in Carbon Based Systems

Introduction

Among the various solid state options available for hydrogen storage, carbon nanostructures have been studied extensively due to its light weight, diversity in structures, good thermal stability and mechanical property, large surface area and interesting hydrogen storage properties. Nanotubes, nano scrolls, nano fibers, fullerenes and graphene sheets are among the different well studied structures of carbon [288-290]. Initially, some of the results indicate that carbon nanotube can adsorb 5-10 wt. % of hydrogen at low temperature and atmospheric pressure [96]. After wards it has been established that pure carbon nanotubes do not adsorb much amount of hydrogen at ambient conditions and the irregularities in many of the results may be due to the metallic impurities in carbon nanostructures, structural defects and the water vapor coming out from the carbon systems [292, 293]. Hydrogen molecules bind with the carbon nanotube in the molecular form, by pure van der Waal interactions and the interaction energy is ~ 0.1 eV/hydrogen molecule which is very low for the room temperature hydrogen storage [294-296]. Though many scientists consider that pure carbon

nanostructure can not meet the required gravimetric goal for vehicular application, unless it is designed with very large surface area [1, 291], but still decorated carbon nanostructures, with suitable modification are being studied as prospective hydrogen storage materials. Thus, hydrogen storage in carbon nanostructures is still an important issue and deserves more attention. Carbon nanostructures can be modified by decorating with Transition metals (TM) and alkali metals and by creating defects to modify its hydrogen storage properties [102, 297-301]. It has been predicted using density functional theory that a single ethylene molecule can form a stable complex with two transition metals, thus adsorbing ten H₂ molecules and lead to a high storage capacity of ~14 wt. % [300]. In transition metal decorated carbon nanostructure, the TM-carbon binding takes place through a charge-transfer mechanism and the TM remains in the cationic state. So the hydrogen molecules can get absorb on the cationic transition metal element giving some electronic charge. By this way the transition metals can facilitate the multiple site hydrogen adsorption, provide a good binding energy (0.2 - 0.7 eV) for room temperature adsorption and also facilitate the hydrogen adsorption- desorption kinetics as it binds the hydrogen in the molecular form. A very well known carbon nanostructure, which has been reported for its interesting hydrogen adsorption behavior is C₆₀ fullerene. The highest hydrogen storage capacity is reported in the fullerene cage is 13 wt. %, where the pentagonal faces of the fullerene are capped by twelve Li atoms [301]. This system has average adsorption energy of $E_b = -0.075$ eV/H₂. Another important modification is heteroatom (B/N/P/N) substituted carbon nanostructure. As the heteroatoms are having higher redox potential than that of the C atom so they can activate the carbon surface by tuning the electronic properties of the carbon material. The Studies also shows that heteroatom substituted carbon nano-tubes and fullerene molecule shows lower dissociation energy compared to the unsubstituted one [302, 303].

Graphene is two dimensional carbon nanostructure, which is being studied extensively. The potential of graphene as hydrogen storage materials through doping is already explored. The interesting properties of graphene are: (1) a large surface for hydrogen adsorption, (2) economical and scalable production, and (3) the strongest material ever measured [304].

In the present chapter, the hydrogen adsorption properties of alkali and alkaline earth metal doped corannulene system, Ti doped SiC nano structures and metallo carbohedrene separately have been described separately with introductions. According to the work plan this chapter of the thesis is divided into four sections.

8.1 Hydrogen adsorption on the corannulene based systems

8.2 Hydrogen adsorption on SiC nanostructures

8.3 Hydrogen adsorption on metallocarbohedrene

8.4 Conclusion

In the remaining part of the chapter, the sections will be described separately.

8.1 Hydrogen adsorption behavior of alkali and alkaline earth metal doped corannulene

In this section, we discuss the hydrogen storage properties of alkali and alkaline earth metal doped corannulene. Transition metal doped fullerene shows a great potential towards hydrogen storage. But due to high cohesive energy, doped transition metals can cluster together, thus decreases the hydrogen storage capacity [301, 305]. The metal adsorption energy should be larger than the cohesive energy of the metal for atomic dispersion. Recently Chandrakumar *et. al.* [102] has proposed alkali metal doped fullerene as a new class of hydrogen storage material as they show high gravimetric density due to electrostatic mediated ion–molecular interaction. Other than CNTs and C₆₀, corannulene is one of the simplest

curved carbon structures and can be represented as one third of a C₆₀ fullerene molecule with hydrogen termination. As corannulene is commercially available, relatively easy to synthesize [306, 307], and has a small curvature, this can give an interesting topological comparison with fullerene. Moreover, both concave and convex surfaces of corannulene molecule are exposed to react with an incoming molecule, which can be used as a prototype to explore the dependence of curvature for hydrogen uptake on single layer carbon nanostructures. Recently Scanlon *et. al.* [308] has shown the interaction of molecular hydrogen with corannulene *via* computational and experimental methods. In general, it is found that the binding of hydrogen molecule with corannulene yields very small amount of energy. However, alkali metal ion adsorption on the corannulene is found to improve its binding capacity towards molecular hydrogen. This is attributed to the induce dipole moment on the H-H bond and widening the exposed area for hydrogen adsorption [309-311].

In the present work, a systematic investigation based on density functional theory has been carried out to compare the Hydrogen adsorption behavior of different alkali (Li⁺, Na⁺ and K⁺) and alkaline earth metal (Be²⁺, Mg²⁺ and Ca²⁺) doped corannulene (C₂₀H₁₀) systems and explored their prospects as hydrogen storage material. For this purpose, first the best locations of the doped metal ions on the corannulene ring have been identified by placing them at different sites and understood the interaction between the alkali or alkaline earth metal ion and the π orbital of the corannulene ring. In the second step, the interaction of hydrogen molecule with doped corannulene has been investigated. The energy released during the process of hydrogen binding with doped corannulene was correlated by estimating the charge transfer. Finally, these results have been analyzed in terms of stability, number of hydrogen molecules absorbed and the interaction energies of hydrogen molecule. In the remaining part of the section will describe the following.

8.1.1. Theoretical Methodology

8.1.2. Results and Discussion

8.1.3. Summary of the work

8.1.1 Theoretical Methodology

During this work, all the calculations were performed using the LCAO-MO approach under the framework of functional theory [210, 211] as implemented in the GAMESS software [312]. In particular, the electronic and geometry optimizations were carried out using the hybrid exchange correlation energy functional, commonly known as B3-LYP, where the notation B3 implies three parameters Becke exchange functional and the LYP indicates correlation functional as described in reference 313. A standard split-valence basis set with polarization functions (6-31G(d,p)) was employed for this purpose. To obtain the most stable adsorption site of each metal ion on the corannulene ring, several possible configurations have been considered and the optimization was carried out without any symmetry constraint. The atomic charge distribution was carried out through Mulliken population analysis. The binding energy of the metal ion-corannulene complex is calculated as;

$$E(\text{BE}) = E(\text{cmpx}) - (E(\text{cor}) + E(\text{cat}))$$

Where $E(\text{cmpx})$ is the total energy of the corannulene-cation complex, $E(\text{cor})$ is the energy of the corannulene molecule and $E(\text{cat})$ is the energy of the cation.

Once the most stable adsorption site is established, interaction of molecular hydrogen with the doped corannulene ring was investigated. The hydrogen molecules were added one after another to investigate the variation in the binding energy as a function of hydrogen molecule uptake number. The interaction energy for each hydrogen molecule is defined as,

$$IE = E(\text{cmpxh}) - (E(\text{cmpx}) + E(\text{H}_2))$$

Where, $E(\text{cmpxh})$ is the hydrogen-corannulene-metal complex and $E(\text{H}_2)$ is the energy of the hydrogen molecule. The initial geometries and all the figures presented in this article have been prepared using the graphical software, MOLEKEL 4.0 [314].

8.1.2 Results and Discussion

8.1.2.1 Doping of alkali (Li^+ , Na^+ , K^+) and alkaline earth metal (Be^{2+} , Mg^{2+} , Ca^{2+}) ions on the corannulene ring

8.1.2.1.1 Geometries

Corannulene, a bowl-shaped molecule, consists of a pentagonal central ring surrounded by five hexagonal rings and is the simplest example of intrinsically curved π system with C_{5v} symmetry. The optimized structure of corannulene molecule is shown in Fig. 8.1.

Due to its curvature, it has two non-identical surfaces, one is concave and the other is convex. The depth of the curvature of the corannulene ring can be measured by adding up the bond angles of the central pentagonal site. It is found that the inner C site has an angle of 353.914° , which is close to the literature value [315]. The interaction of bare corannulene ring with molecular hydrogen is very weak (the details of the results have been discussed later). Therefore, although it can absorb few hydrogen molecules on the ring but they are not stable in the ambient temperature. On the other hand, it is known that metal ions have great affinity for hydrogen adsorption [106, 316]. Thus it is of interest to verify if the hydrogen capacity of corannulene can be improved by functionalizing it with metal ions. Previous studies have shown that transition metals undergo clustering on the C_{60} surface. On the other hand, it has been established that, the alkali and alkaline earth metals do not form cluster on the C_{60}

surface as the binding is strong enough to avoid clustering. Following the same strategy, here also the ring has been functionalized with different alkali and alkaline earth metal ions.

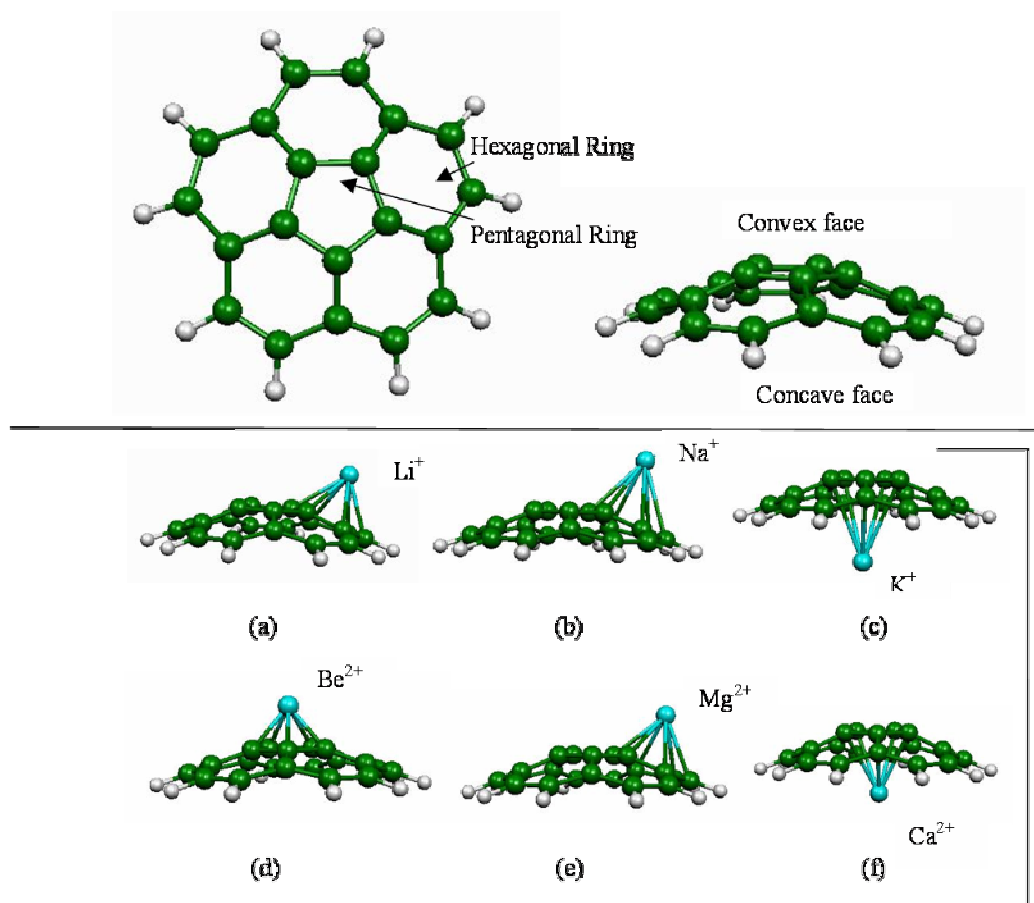


Fig. 8.1 *Optimized geometries of the corannulene molecule and metal-corannulene complexes.*

As a first step it is important to understand the most preferred geometries of metal ion doped corannulene molecule. When alkali and alkaline earth metal ions are placed on the ring, they have a choice to adsorb either on the convex or the concave surface. Moreover, they have an option to occupy the five or six member ring site. In this context it should be mentioned that, the metal ion was also placed on the bridged site (on the C-C bond), but the initial results showed no local minima on that site, and hence the metal atom goes to the adjacent hexagonal/pentagonal site. Here four different positions had been considered for doping of an alkali or alkaline earth metal ion on the corannulene ring:

1. Convex surface of central five member ring
2. Concave surface of central five member ring
3. Convex surface of side six member ring
4. Concave surface of side six member ring

It is found that the most preferred adsorption site of each metal ion on the corannulene ring is related to their respective ionic radii. From the literature it is known that the ionic radii of the metal ions studied in this work are in the order of $Be < Mg < Li < Na < Ca < K$. On the basis of the lowest energy isomers of all systems studied in this work, it is seen [Fig. 8.1] that while the metal ions with smaller radii prefer the convex surface, the ions with larger radii stabilize on the concave surface. In general, the dipole of corannulene points towards the outer surface. So it is expected that the positively charged metal ions will stabilize themselves on the convex surface. If the metal ion is large, then the geometrical factor becomes predominant over polarization. Dunbar has reported that for alkali metal ions, the binding to the convex face is slightly favored than the concave face and the binding energy difference between these two faces decreases as the size of the metal ion increases. This is in agreement with the previous report where Li cation was found to favor the convex side of the ring. Frash *et al.* reported similar results showing complexation of Li ion on the convex side of corannulene ring. In line with these results, in the present work also, a similar structure for Li ion adsorption was found on the corannulene ring with a binding energy of 2.13 eV. For Na ion, similar to Li, it is found to favor a hexagonal ring on the convex surface of the corannulene. Unlike the case of Li and Na ions, K ion being a larger cation, prefers the five member ring on the concave surface. The alkaline earth metal ions also follow the same trend, where smaller and larger ions favor convex and concave surfaces, respectively. For example while Be and Mg ions, being smaller in size, prefer to adsorb on the convex side

occupying five and six member rings, respectively, on the other hand Ca, which is larger in size, prefers to be on the six member ring of the concave surface. Basis set superposition error (BSSE) calculations were carried out for all the stable configurations. Although there are variations in the total energies for each metal ion-corannulene complexes but importantly the trend in the stability pattern remain same. The largest correction was found for K^+ -corannulene complex. In general, the energy correction was found to vary upto 8.283 kcal/mole depending upon the nature of the metal ion and the adsorption site.

8.1.2.1.2 Stability and charge analysis

On the basis of previous results, it is envisaged that when alkali (Li^+ , Na^+ , K^+) and alkaline earth metal (Be^{+2} , Mg^{+2} , Ca^{+2}) ions are adsorbed on the corannulene ring, a charge transfer complex is formed. The binding strength of different metal cations through π -cation interaction is found to vary depending on the extent of charge transfer and the size of the metal cations as shown in Fig. 8.2.

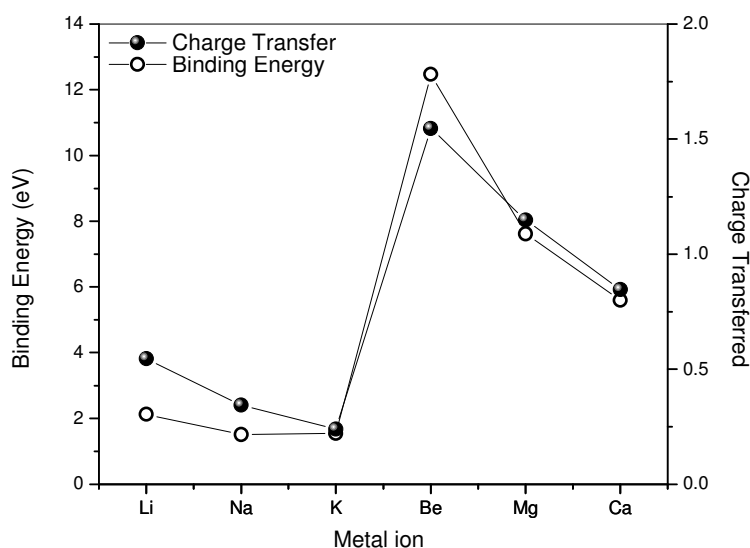


Fig 8.2 Comparison of binding energies and charge transfer of alkali and alkaline earth metal ions with corannulene molecule.

The charge distribution for all these systems is carried out using Mulliken population analysis. A summary of the point charge distribution and the binding energies are presented in Table 8.1.

Table 8.1 Doping of charged alkali and alkaline metal atoms at different positions. In this table 1, 2, 3, 4 locations are Convex surface of central five member ring, Concave surface of central five member ring, Convex surface of side six member ring and Concave surface of side six member ring, respectively.

Metal Atom		1	2	3	4
Li ⁺	Charge transfer	0.4821	0.5024	0.5457	0.5313
	BE (eV)	-2.100	-2.0435	-2.1305	-2.0217
Na ⁺	Charge transfer	0.3015	0.3441	0.3432	0.3372
	BE(eV)	-1.4803	-1.4612	-1.5102	-1.4068
K ⁺	Charge transfer	0.204	0.2391	0.2264	0.2413
	BE(eV)	-1.1551	-1.5428	-1.4585	-1.4585
Be ⁺²	Charge transfer	1.5465	1.4561	1.5021	Unstable
	BE(eV)	-12.4734	-12.253	-9.7018	Unstable
Mg ⁺²	Charge transfer	1.0561	1.1018	1.1487	1.1279
	BE(eV)	-5.5930	-7.0312	-7.619	-7.0938
Ca ⁺²	Charge	0.682	0.8461	0.7366	0.8388
	BE(eV)	-5.4149	-5.5918	-5.3523	-5.6054

It is clear from Fig. 8.2 that for alkali & alkaline earth metal series, the binding energy is directly proportional to the amount of charge transfer. For the alkali metal ions, the charge transfer to the corannulene ring decreases in the order of Li⁺ > Na⁺ > K⁺ and the binding energy follow the same order. For alkaline earth metal series, the binding energy of Be²⁺ with corannulene ring is very high (-12.47 eV), which is attributed to the large charge transfer. For

Mg^{2+} and Ca^{2+} , the binding energies are 7.61 and 5.59 eV, respectively. In fact, the binding energy of each metal ion with the corannulene ring is quite high reflecting the stability of the ions on the ring.

8.1.2.2 Interaction with hydrogen molecule

Initially the interaction of hydrogen molecule was optimized on the clean corannulene molecule. To underscore an energy landscape of hydrogen adsorption on the corannulene, the hydrogen-corannulene complex has been optimized by placing the hydrogen at various places (on top of the five and six membered rings on the concave and convex surfaces) and different orientations (perpendicular and parallel). The results suggest that the hydrogen molecule prefers to bind corannulene molecule in perpendicular orientation [Fig. 8.3] irrespective of the concave or convex side.

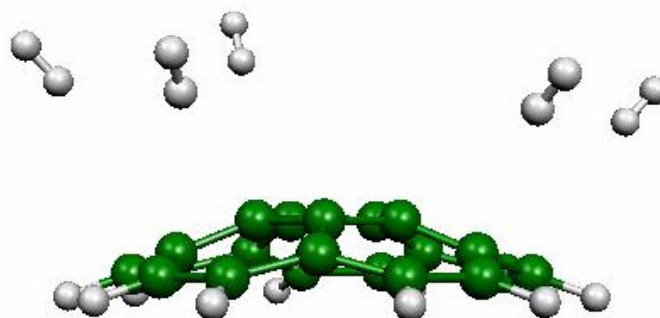


Fig. 8.3 *Binding of hydrogen molecule with clean corannulene ring in the perpendicular orientation.*

The binding energy varies depending upon the site and side of adsorption. Moreover, to take care of the dispersion interaction properly, the interaction energy between hydrogen and corannulene has been calculated using M062X as implemented in the GAMESS. The results show that for one hydrogen molecule interaction on the pentagonal ring of corannulene, the difference in binding energy between the concave and convex surface is 3.3

$\times 10^{-3}$ Ha (0.09 eV). Furthermore, when five hydrogen molecules are adsorbed on five hexagonal rings of the convex and concave surfaces, the total interaction energy is estimated to be 7.2×10^{-3} Ha (1.44×10^{-3} Ha/hydrogen molecule) and 16.5×10^{-3} Ha. (3.3×10^{-3} Ha/hydrogen molecule), respectively. Thus it is inferred that the adsorption energy of hydrogen molecule on the concave surface is larger than that of convex surface, which is also in line with previous results [306, 318]. Theoretically, one corannulene molecule can absorb ten hydrogen molecules. This corresponds to hydrogen storage capacity of 13.16 wt. %, which is significantly high. However, the lower binding energy of hydrogen can lead to desorption at lower temperature. Therefore, corannulene molecule can store hydrogen only at cryogenic temperature. To overcome this problem the molecule should be fictionalized in such a way that hydrogen can be stored upto working temperature. Previously, many theoretical and experimental works reported the improvements of hydrogen storage properties of metal doped carbon systems [319-321]. In the present work the corannulene molecule has been functionalized by alkali and alkaline earth metal ions. The hydrogen adsorption behavior of metal ion doped corannulene molecule has been carried out, which is considered as molecular model of single sheet graphene nanostructure. After establishing the most preferred location of the metal ions on the ring, hydrogen molecules were added one by one sequentially. This way the maximum number of hydrogen uptake by a metal ion doped corannulene as well as the variation of hydrogen binding with pre hydrogen loaded doped corannulene has been found out.

8.1.2.2.1 Interaction of hydrogen molecules with bare metal ions

Before starting the discussion about the hydrogen storage properties of metal ion doped corannulene, it is important to understand how bare metal ions interact with hydrogen molecules. On interaction with metal ion, the hydrogen molecule prefers to bind in with both

the ends as shown in Fig. 8.4. Most importantly, during adsorption the hydrogen molecule does not dissociate. This is the main feature of alkali metal–hydrogen binding where the molecular identity is retained. In this context it should be mentioned that in case of transition metal atoms, the first hydrogen molecule undergoes dissociative chemisorption. The difference in the adsorption behavior is attributed to higher binding energy of transition metal hydrides [322]. Moreover, the number of hydrogen molecules attached with the metal ions strongly depends upon the size of the metal ions. Be^{2+} being the smallest metal ion can absorb only four hydrogen molecules as shown in Fig. 8.4. Li^+ and Mg^{2+} absorb six hydrogen molecules whereas the other larger metal ions (Na^+ , K^+ , and Ca^{2+}) absorb eight hydrogen molecules each.

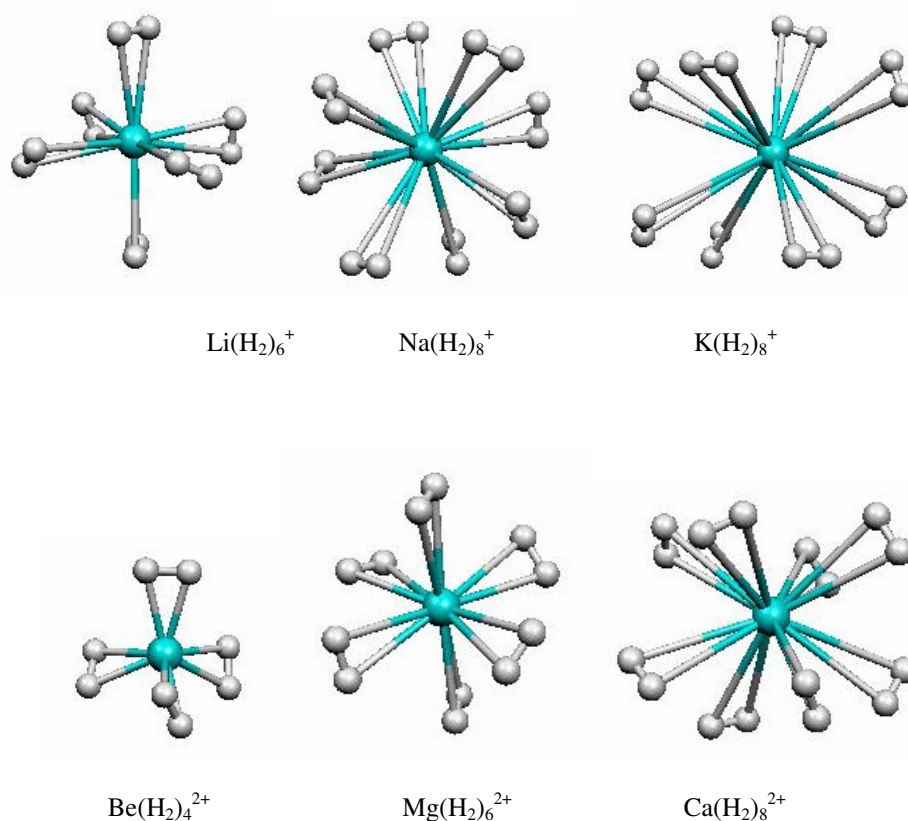


Fig. 8.4 Optimized geometry of metal ions-hydrogen complexes.

The binding energies of metal ion- hydrogen complexes are shown in Fig. 8.5. In this case the hydrogen molecules are attached with the metal ions one after another until the binding is saturated. It is seen that the binding energy/hydrogen molecule decreases with increasing number of absorbed hydrogen. From the increase in the total interaction energy, the maximum number of hydrogen molecule uptake by each metal ion can be established. For example, in case of Be^{2+} it is found that after adsorption of four hydrogen molecules the total binding energy does not change appreciably by further addition of hydrogen and the binding energy/hydrogen molecule is estimated to be 1.34 eV. Similarly, in case of Mg^{2+} it is seen that it can absorb maximum eight hydrogen molecules with an average binding energy/hydrogen molecule of 0.57 eV. Comparing the trend in binding energies, it is seen that in general the alkaline earth metal ions are found to bind more strongly with hydrogen compared to the alkali metal ions. This is because of their higher charge, which can polarize the hydrogen molecule better. Again, in a particular series, it is observed that with the increase in the size of the metal ion, the distance between the metal atom and hydrogen increases. This reduces the polarization of the hydrogen molecule resulting in the decrease of the interaction energy. From the results of the calculation, it was seen that the interaction energy between hydrogen and metal ions decreases in the order of $\text{Be} > \text{Mg} > \text{Ca} > \text{Li} > \text{Na} > \text{K}$. Further, it is clear from Fig. 8.5 that as the hydrogen molecules interact with the metal ions in the molecular form so the binding energy is rather small.

Subsequently, it is found that when metal ion interacts with molecular hydrogen, due to the electrostatic nature of interaction, the charge of the metal ion reduces. In fact the field generated by the positively charged cation polarizes the hydrogen molecule. As a result, the charge-induced dipole moment enhances the adsorption of hydrogen at ambient conditions. The differences in the point charge on the metal ions due to hydrogen adsorption are shown

in Fig. 8.6. From this figure it is seen that there is steady decrease in the charge of the metal ions as more and more hydrogen molecules are attached to it.

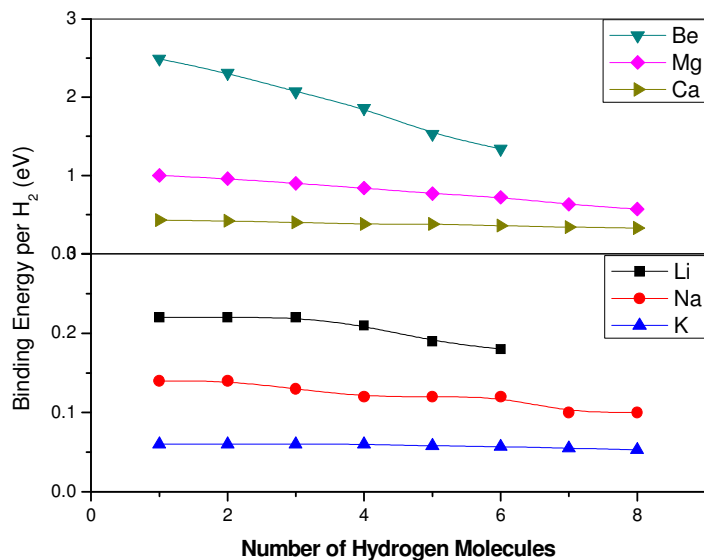


Fig. 8.5 Binding energy of hydrogen molecules with the bare metal ions.

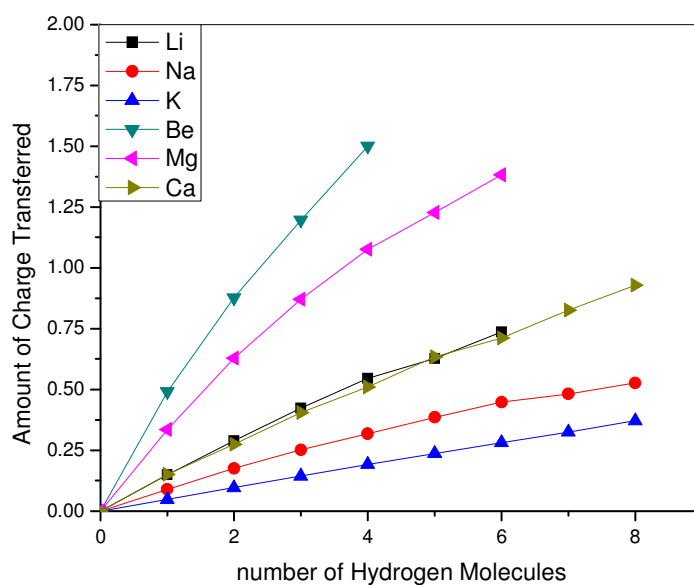
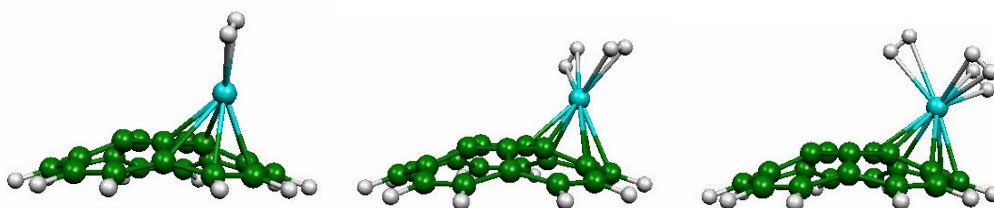


Fig. 8.6 Charge transfer by the metal atoms after interaction with hydrogen molecules.

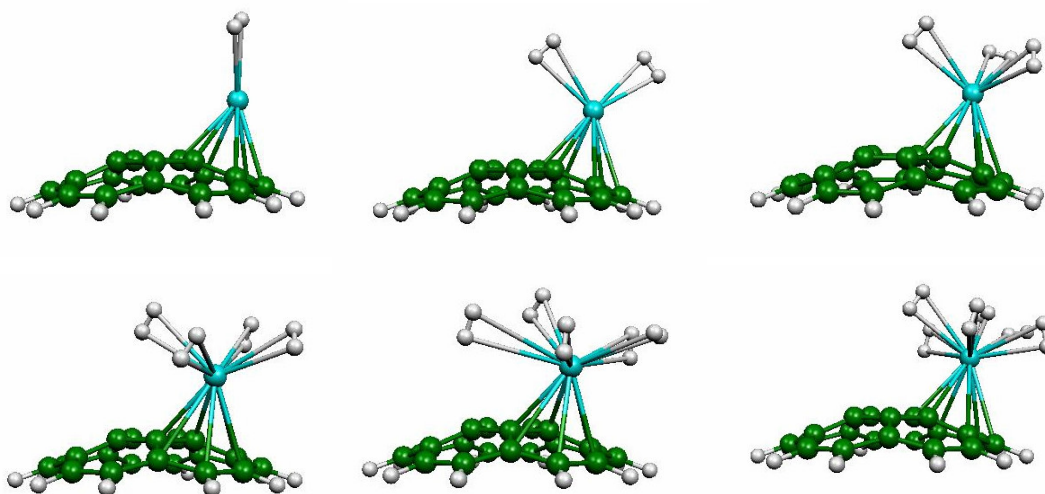
8.1.2.2.2 Interaction of hydrogen molecules with metal ion decorated corannulene complexes

Now coming to the final hybrid system, the metal ion decorated corannulene complexes for hydrogen storage. Based on these results, i.e., low metal-hydrogen interaction energy and very high metal-corannulene binding energy, it can be inferred that the complex system will be able to desorb hydrogen molecules without breaking the metal ion corannulene bond. That means the system gives ideal platform for efficient storage of molecular hydrogen. From our previous results it is seen that when metal ions interact with corannulene, the charge on the metal ions decreases. This has been attributed to the transfer of finite electronic charges from the corannulene molecule to the metal ions.

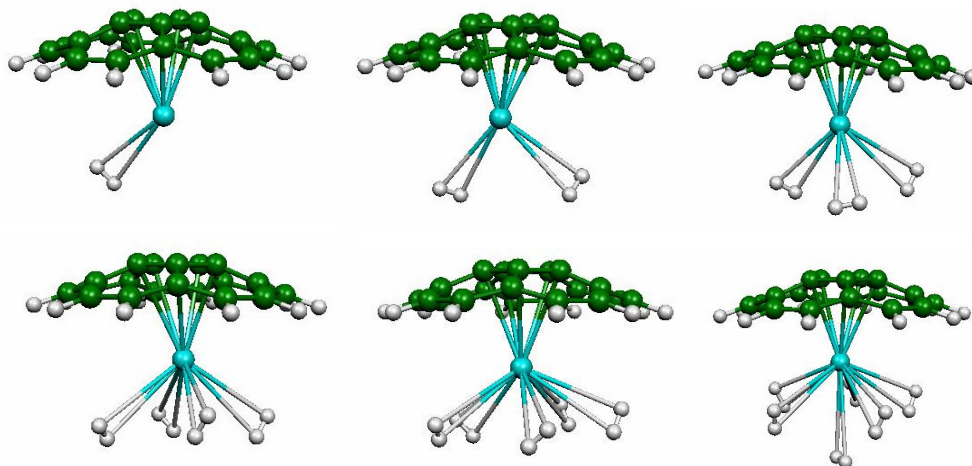
When a metal ion decorated corannulene interacts with hydrogen molecule, the binding energy depends on the residual charge on the metal ions. Higher the residual charge more is the binding energy. As the charge on the metal ion reduces after adsorption on the corannulene so the binding of hydrogen and the number of hydrogen uptake will be less. While the Be^{2+} -corannulene can absorb only two molecules of hydrogen, the Li^+ , Mg^{2+} , Ca^{2+} -corannulene complexes can absorb three, four and four molecules of hydrogen, respectively. The other complexes formed by Na^+ and K^+ ions can absorb six hydrogen molecules each. To make the understanding better, the optimized structure of metal ion doped corannulene rings can be depicted after interaction with different number of hydrogen molecules in Fig. 8.7.



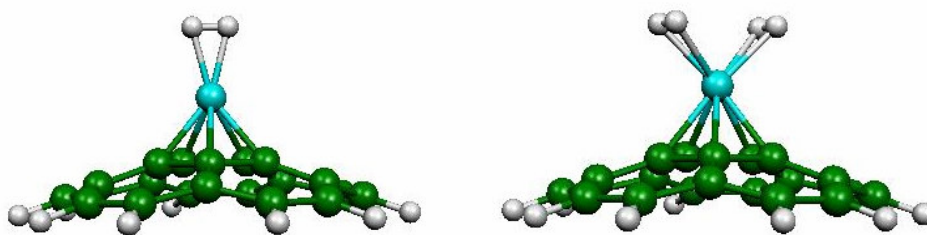
Li^+



Na⁺



K⁺



Be²⁺

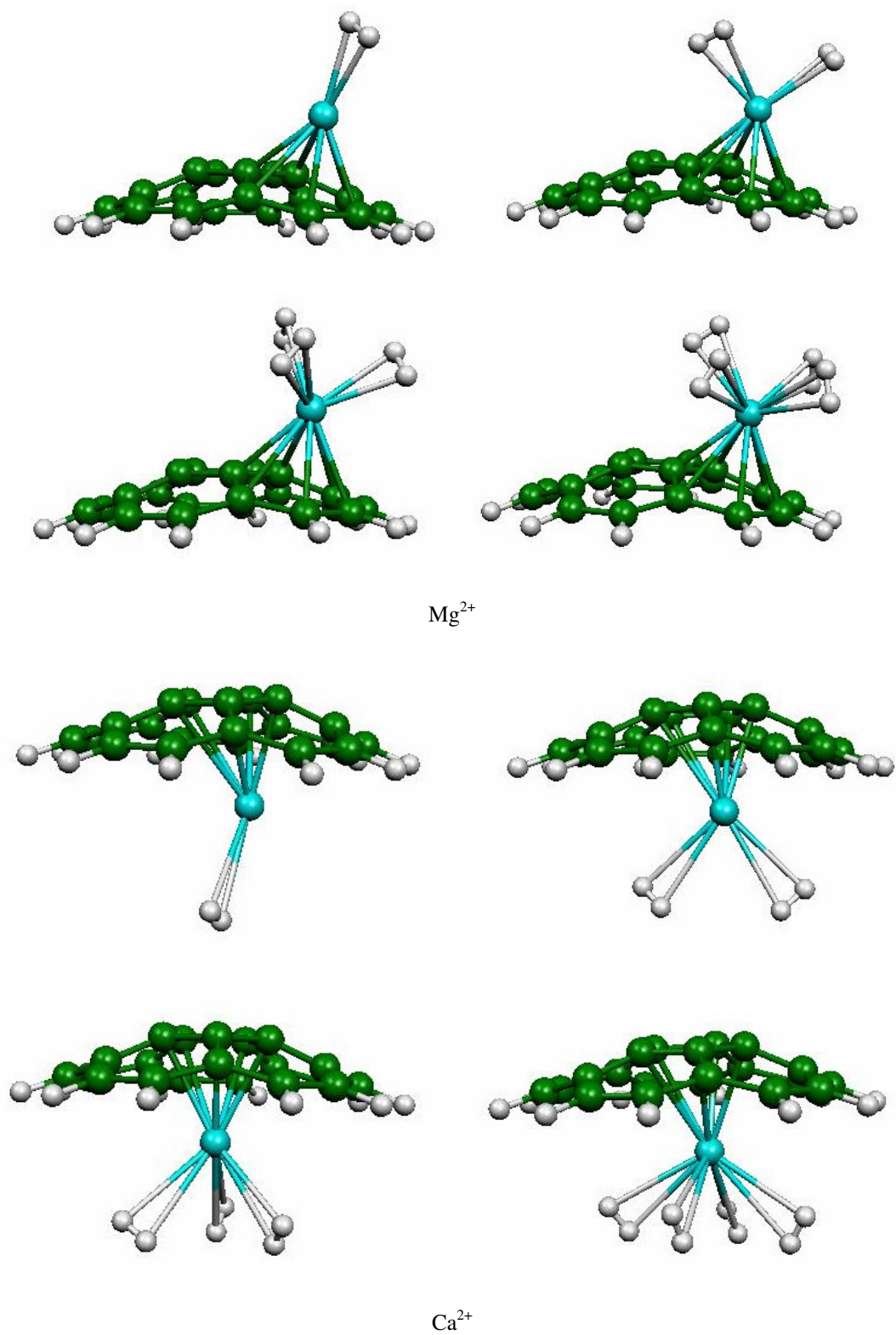


Fig. 8.7 *Optimized geometries of the hydrogenated alkali and alkaline metal doped corannulene.*

In Fig. 8.8 shows the binding energy/hydrogen molecule, when the hydrogen molecules are added one after another in the metal doped corannulene complexes.

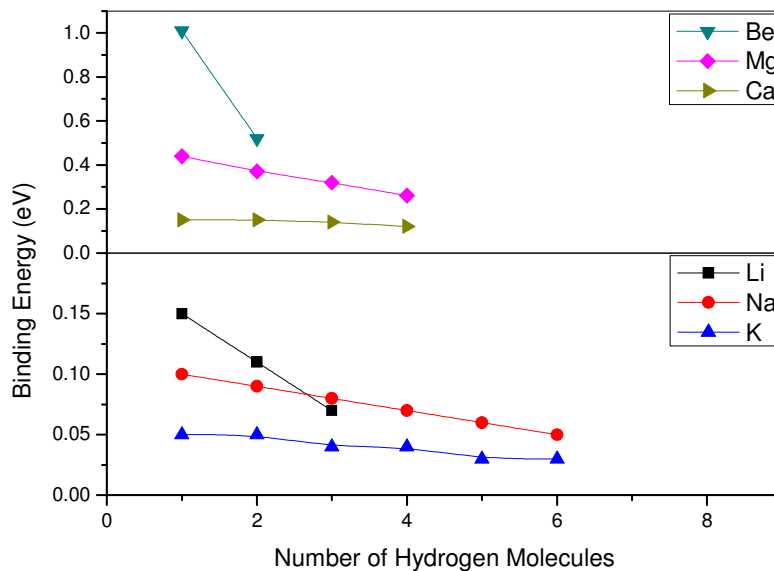


Fig. 8.8 Binding energy of hydrogen molecules with the metal ion-corannulene complexes.

It is seen from the figure that here also the interaction of hydrogen molecules are stronger for alkaline metal ions compared to the alkali metal ions. Again, after interaction with the hydrogen molecule, the charge of the metal ion is found to reduce as represented in Fig. 8.9.

So from the above discussion two general inferences can be made; (i) as the size of the cation becomes larger, it can hold more hydrogen, (ii) as the residual charge on the metal ion increases the interaction energy becomes higher. So combining these two effects it can be concluded that sodium ion doped corannulene ring can be considered as the best hydrogen absorbing material in this series.

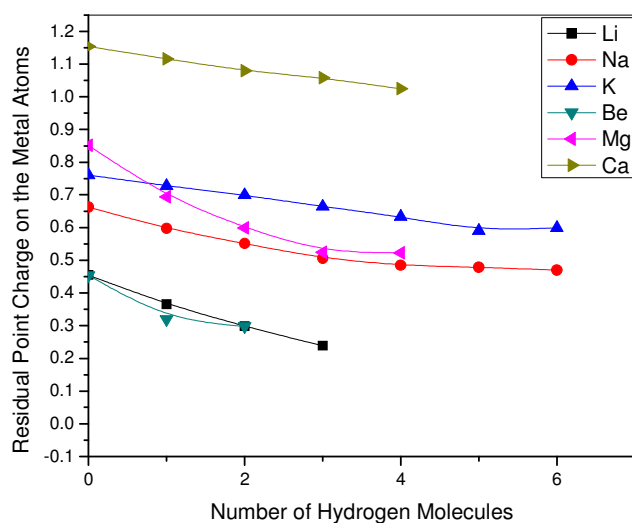


Fig. 8.9 Charge on the metal atoms in corannulene-metal ion complexes after interaction with hydrogen molecules.

8.1.3 Summary

In this section of the thesis, the hydrogen adsorption properties of alkali (Li^+ , Na^+ and K^+) and alkaline (Be^{2+} , Mg^{2+} , Ca^{2+}) earth metal ion doped corannulene molecules have been reported. The calculations are carried out at the B3LYP level of theory under the LCAO-MO approach. For the adsorption of metal ions on the corannulene ring, it is found that the adsorption site of the metal ions depends on its ionic radii. While the smaller size cations show higher binding energy on the convex plane, the larger ions prefer to bind through concave side. The interaction of hydrogen molecules with bare and doped corannulene molecule reveal that while the clean surface of the molecule interacts with hydrogen very weakly, the binding strength is significantly improved after decorating the molecule by alkali or alkaline earth metal ions. The binding energies of hydrogen molecules depend upon the residual charge of the metal ions. Based on the results it can be inferred that Na ion doped corannulene molecule gives optimal performance for the Hydrogen adsorption of alkali and

alkaline earth metal ions doped corannulene molecules. Thus it is expected that the information obtained here will help towards designing higher capacity hydrogen storage materials based on extended carbon nanostructures.

8.2 Hydrogen Storage on SiC Nanostructures

Apart from the carbon nanostructure, another very promising carbon like hydrogen storage alternative is Si/SiC nanostructure [323-325]. Si being in the same group with the carbon it shows properties quite similar to that of C. Again, as the polarizability of Si is more than C, so it is expected that, due to stronger van der Waal's interaction, SiC/Si nanotubes can bind hydrogen more strongly compared to the pure carbon nanotube. It is known that, in the bulk phase SiC exhibits more than 250 crystalline forms. α -SiC is the most common high temperature polymorph (forms at a temperature above 1700°C) and is having Wurtzite structure (lattice parameters $a = 3.073 \text{ \AA}$, $b = 10.053 \text{ \AA}$). β -SiC forms below 1700°C and it is having diamond like Zinc Blende structure (lattice parameter $a = 4.36 \text{ \AA}$). Though in the bulk structure of SiC, Si and C atoms are sp^3 hybridized, but in the EELS spectra of experimentally synthesized single SiC-NT, an extra strong pre-edge adsorption peak is seen, which is a prove of π bonding between Si and C atom [326]. The result indicates that though in the bulk structure the Si remains in sp^3 hybridized state, but actually during the bonding between Si and C atom in SiC nanotube, Si shows similar multi-facet character as C atom and Si can exist in sp^2 hybridised state also. Due to this multi-facet character, SiC can exhibit multidimensional structures including different forms, viz nanotubes, nanorods, nanoclusters, nanowires, nanofiber, nanobelts etc [326-331].

Though the theoretical proposal of graphene [332-334], was made in the year 1956, but only after almost 60 years, in 2004, Geim and co-workers [335-338] made the successful isolation of this two-dimensional (2D) crystal, which opens up a new horizon of 2D nano-

material. Graphene like hydrocarbon can be fully hydrogenated (one hydrogen atom with each of the C atom resulting in sp^3 C atom) giving rise to different conformers among which the chair conformer is most stable one reported so far [339-341], and subsequently the compound has also been synthesized in the laboratory [342]. Thus it is expected that, similar to the graphene structure Si and C atom can arrange alternatively giving rise to SiC sheet and subsequently it can be hydrogenated forming graphane like structure. Xu *et. al.* [343] has investigated the electronic and magnetic properties of the semi-hydrogenated SiC sheet by means of the DFT calculation and found that, the different magnetic properties of the semihydrogenated SiC sheets can be introduced if one can control the atoms on which H atoms are adsorbed. The phonon dispersion calculations on the fully hydrogenated SiC honeycomb structure shows that between the chair-like and boat-like configurations, both are dynamically quite stable, and the chair-like conformer is energetically more favored relative to the boat-like one [344].

In our present study we have studied different possible stable conformers of fully hydrogenate graphane like silicon carbide (SiHCH) and found out their relative stabilities. We have done molecular dynamic simulation on the most stable conformer to see the effect of temperature.

During this study, we have also explored Ti doped two dimensional SiC sheet and (10, 0) single walled SiC nanotube for the hydrogen storage. Further, the results of Ti functionalized SiC sheet and SiC nanotube has been compared to see the effect of curvature on the hydrogen adsorption properties. In earlier study Mpourmpakis *et. al.* [345] has proposed that pure SiC nanotube can improve the hydrogen storage properties by increasing the binding energy with hydrogen molecule by 20 % compared to pure carbon nanotube. The hydrogen storage capacity of the SiC nanotube found to be more compared to the iso-

diameter carbon nanotube, especially at low pressure. But still at 5 MPa pressure at 175 K, SiC can absorb only 2.82 wt. % of hydrogen, which is quite less than the required value. It is known that for optimum performance as a hydrogen storage material, the ideal form of binding between the host material and adsorbed hydrogen molecules should be intermediate between physisorption and chemisorption energy (ideal energy range is 0.2-0.8 eV) [346]. In that particular case the molecular bond of hydrogen does not break but rather elongates slightly, as a result the material can desorb molecular hydrogen at an ambient temperature. Among the different form of SiC nanotubes, the zigzag form is direct band gap semiconductor compared to the SiC bulk, which is actually an indirect band gap semiconductor. Small diameter SiC nanotubes are more stable than the SiC nanowires but less stable than the bulk materials. From the first principle molecular dynamics simulation it has been found that the SiC nanotubes are more stable than nanowires below a critical diameter of about 1.6 nm, above which the nanowires are more stable [347]. From that calculation it has also been found that the SiC nanotubes are stable upto a temperature of 1620 K beyond which melting takes place. Coming to the structural aspects of Si_xC_y nanotube, the first principle calculation reveals that the nanotube is not stable when $x > y$, i.e., the limiting condition is $x = y$. Again for $x = y$ the nanotube is more stable when the Si and C atoms are arranged alternatively [348-351]. The zigzag SiC nanotube is found to be stable than its armchair counterpart though the deference is very minute [349].

Eventually in the present study, the graphene like two dimensional SiC sheet and (10, 0) single walled SiC nanotube have been investigated for the hydrogen storage. Further, the results of Ti functionalized SiC sheet and SiC nanotube has been compared to see the effect of curvature on the hydrogen adsorption properties.

8.2.1 Computational details

All calculations have been performed with density functional theory (DFT), [210, 211] within the plane-wave pseudo potential approach as implemented in the Vienna *ab-initio* Simulation Package (VASP) [275]. The Perdew-Burke-Ernzerhof (PBE) functional [217] was used for the calculation of the exchange-correlation energy. The electron-ion interactions are described with projector augmented wave (PAW) method [234], expanded up to a default plane-wave cutoff energy.

For the SiC graphene-like sheet calculation, the sheet has been modeled by alternatively arranged 16 C and 16 Si atoms. Two-dimensional periodic boundary condition has been employed in the layered plane with a vacuum region (15 Å) between sheets to ensure there was no interaction between SiC graphene-like sheets. In order to establish the accuracy of the present method few test calculations have been performed on SiC graphene-like sheet using several sets of k points according to the Monkhorst-Pack scheme [276] so as to ensure the convergence of the total energy. Finally the k points were taken as 5X5X1. The SiC (10, 0) nanotube has been modeled by 80 alternative Si and C atoms (40 Si atoms and 40 C atoms). The vacuum space is kept as 20 Å to avoid any intermolecular interaction between two nanotubes. The total energy has been calculated using 1X1X3 k-point meshes. The energy convergence for the self-consistent calculation was set to 10^{-4} eV, and the structure was relaxed using a conjugate-gradient (CG) algorithm until the atomic forces were less than 10^{-3} eV/Å.

8.2.2 Results and Discussion

8.2.2.1 Calculations on SiC graphene Like Sheet

8.2.2.1.1 Geometric optimization and energetic calculations of SiC sheet

In a previous theoretical calculation it is reported that the most stable structure of planar SiC forms graphene-like structure with alternative SiC bond and the bonding in such structure is of sp^2 type [348]. In this calculation also similar structure was optimized without any symmetry constraint. In the optimized geometry, which is shown in Fig. 8.10(a), all the Si-C bonds are found to be identical and the Si-C bond distance is found to be 1.78 Å.

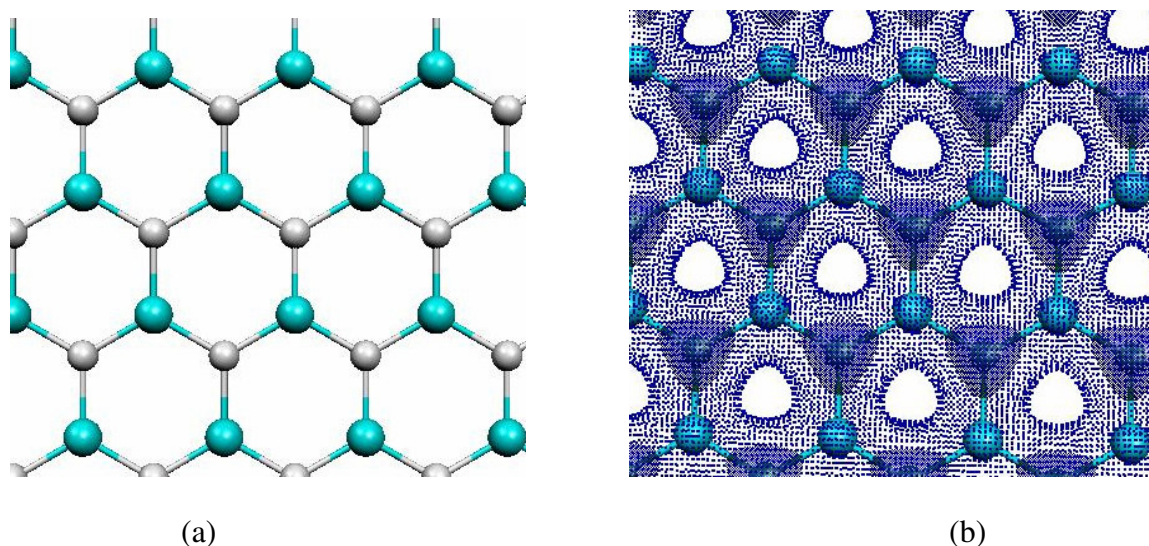


Fig. 8.10 (a) The structure of SiC sheet with alternative Si (bigger atom) and C atoms (smaller atom). (b) The charge density distribution on the SiC sheet. The darker color and lighter color indicate higher charge and lesser charge respectively. Figure shows higher charge on the C atom and lower charge on the Si atom.

In this context it should be noted that the Si-C bond length in the bulk SiC is reported to be 1.89 Å, and each of the atom is bonded through sp^3 hybridization. The stabilization energy/atom (5.815 eV/atom) of this SiC sheet is calculated as $E_b = (E_{\text{total}} - 16E_{\text{Si}} - 16E_{\text{C}})/32$,

where E_{total} is the total energy after optimization, E_{Si} and E_{C} are the correction factors for Si and C atoms, respectively.

From the charge density distribution of the SiC sheet [Fig. 8.10(b)], it is seen that a considerable amount of electronic charge is transferred from Si to C site. The presence of these point charges on the SiC sheet influence the hydrogen storage properties. The total and split density of states (DOS) of the SiC sheet is plotted in Fig. 8.11. The energy gap between the valence and conduction band is found to be 2.42 eV. It is found that the upper energy levels of the valence band (near fermi energy) is primarily contributed by the p -orbital of carbon atoms, and the p orbitals of Si atoms form the lower energy of the conduction band.

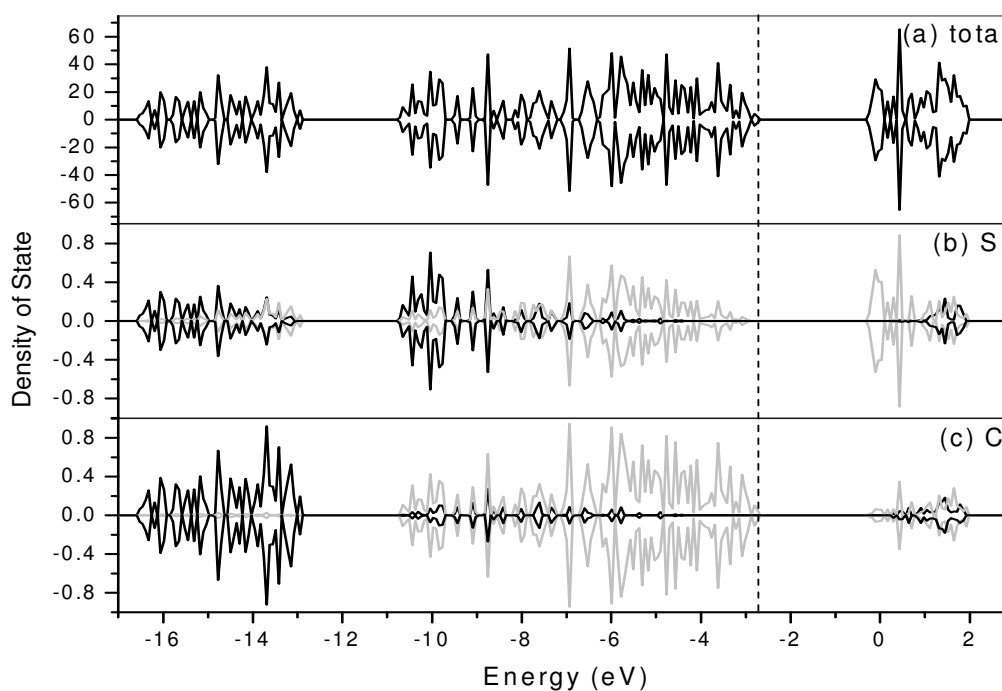


Fig. 8.11 (a) The total density of state (DOS) of the graphene like SiC sheet. (b) The DOS of the Si atoms. (c) The DOS of the C atoms. The darker and the lighter color in the DOS of Si & C atoms represent the s - and p -orbital respectively.

8.2.2.1.2 Hydrogenation properties of the SiC sheet

The hydrogenation of SiC sheet gives rise to various conformers (with formula unit SiHCH) depending upon the position of the hydrogen atoms on the sheet. We have identified eight different types of orientation of hydrogen atoms in which each of the Si and C atoms of the sheet is bonded to one H atom. After optimizing the three structures without any symmetry constrained we found that they form stable chair, boat and stirrup, puckered and twist conformers of SiHCH and all of them are having symmetrical zigzag 2D structures, some of them resemble in structure to those of graphane [340, 341]. In the chair conformer, the hydrogen atoms are arranged alternatively up and down on both the sides of the sheet, where as in the boat conformation hydrogen atoms are added pair wise (2 up–2 down) on both sides of the sheet. However, in stirrup SiHCH conformer, the H atoms of one SiC hexagon, alternates in three on either side of the SiC plane (3 up–3 down). And we call other two types of conformers as the puckered and twist conformer. From the Si-C bond lengths and HSiC and HCSi bond angles we can confirm that due to hydrogen uptake in the atomic form the Si and C atom goes towards the sp^3 hybridized form in all the conformers.

For the chair conformer [Fig. 8.12] the starting geometry has been taken as the hydrogen atoms attached alternatively ups and downs. In the fully optimized structure of the chair conformer, all the HSiC and HCSi angles are almost equal and slightly lower than the sp^3 angle (109.5°). The Si and C atoms of Si-C bonds connect the H atoms lying on opposite side of the sheet and therefore are of equal length (1.87 \AA). The Si-H and C-H distances are found to be 1.50 \AA and 1.11 \AA respectively.

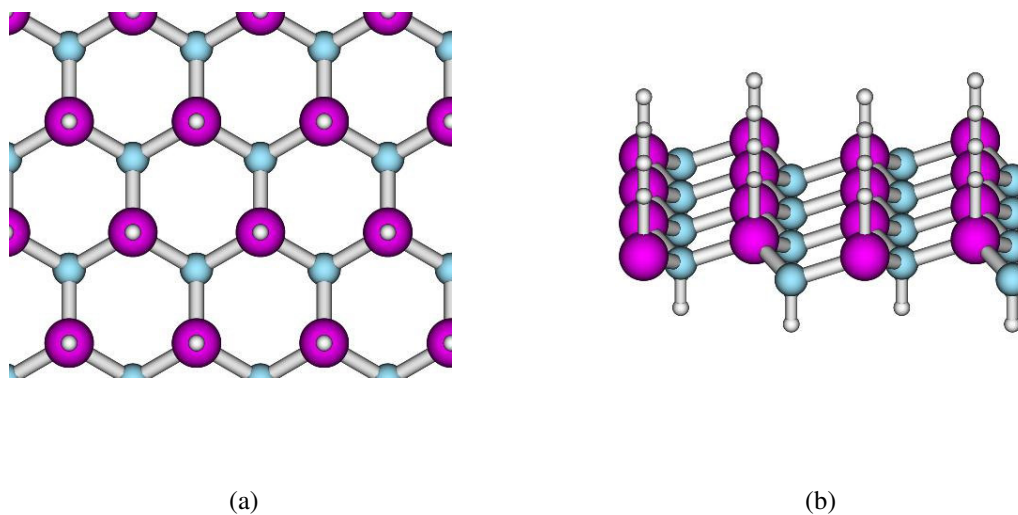


Fig. 8.12 *The chair conformer of SiCH (The bigger and smaller atoms are Si and C respectively). (a) The top view and (b) the side view*

In the stating geometry of the stirrup conformation [Fig. 8.13], three hydrogen atoms are attached at the top side where three hydrogen atoms are attached at the down side in the SiC honeycomb structure. In stirrup conformation also like the boat conformer all the H-Si-C and H-C-Si are consistently lower than the sp^3 angle and the H-Si-C angles are higher than the H-C-Si angles.

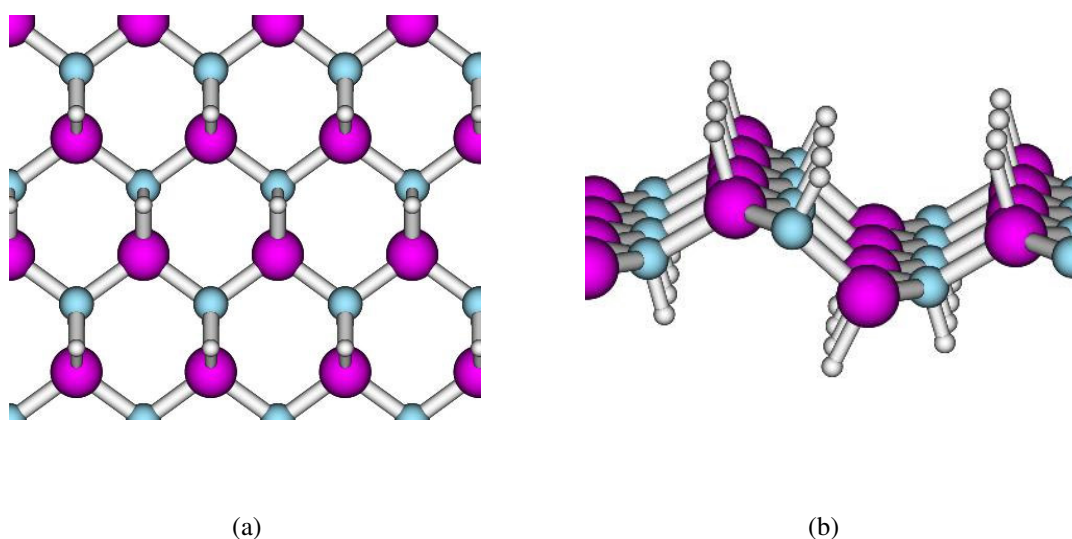


Fig. 8.13 *The stirrup conformer of SiCH. (a) The top view and (b) the side view*

Unlike the boat structure, the Si-C bond distances in the stirrup conformer are higher for the bonds joining the H atoms lying on the opposite side of the plane (1.92 Å) compared to that in the same sides of the sheet (1.91 Å) and both the distances are higher compared to the Si-C distance in the chair conformer. The Si-H and C-H distances are found to be similar to that of chair and boat conformer.

In the initial geometry of the twist conformation [Fig. 8.14] the hydrogen atoms are attached as two up, two down followed by one up and one down on the honeycomb structure of the SiC sheet. Here also all the Si-C-H and C-Si-H angles are less than the ideal sp^3 angle and two types of Si-C distances are there, 1.89 and 1.90 Å respectively. The Si-H and the C-H distances are found to be 1.50 Å and 1.10 Å respectively.

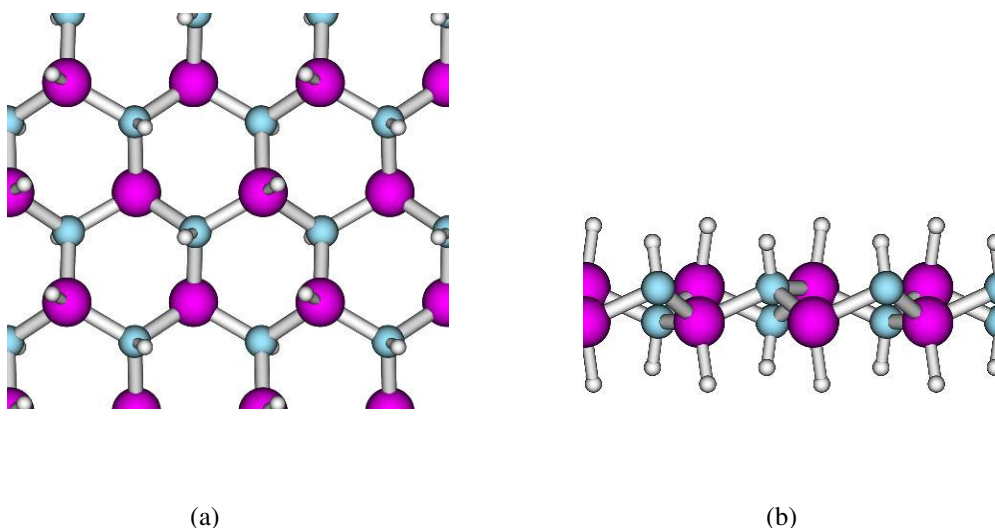


Fig. 8.14 *The twist conformer of SiCH. (a) The top view and (b) the side view*

The initial geometry of the puckered conformation [Fig. 8.15] is taken as 3 ups, 1 down, 1 up and 1 down hydrogen atoms attached on the SiC sheet. The Si-C distances in the puckered conformer are found to be 1.89 Å. The C-H and Si-H distances are found to be 1.11 and 1.50 Å respectively.

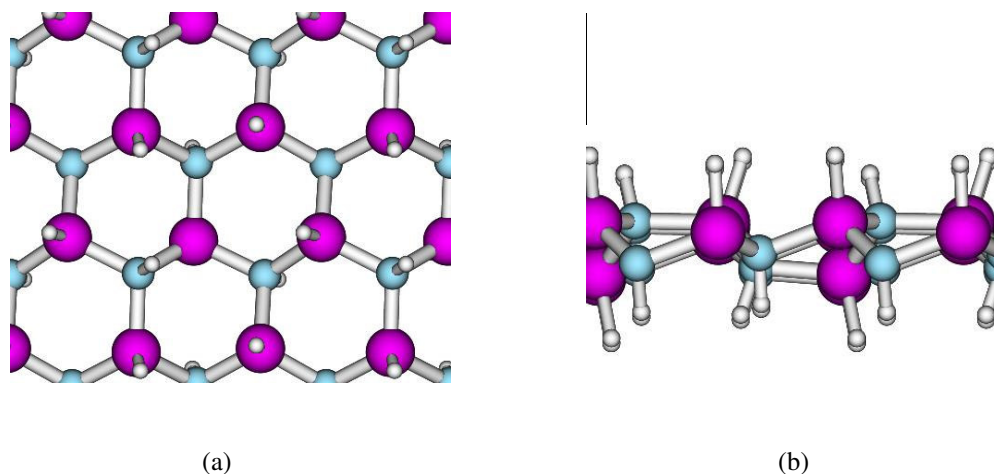


Fig. 8.15 *The puckered conformer of SiCH. (a) The top view and (b) the side view.*

The starting geometry of the boat conformer [Fig. 8.16] consists of honeycomb SiC sheet where the hydrogen atoms are attached as 2 up, 1 down, 2 up, one down fashion. In boat conformer, the H-C-Si angles are higher than the H-C-Si angles in chair. There are two types of SiC distances. The bonds connecting the H atoms lying on the same side of the sheet are larger (1.92 \AA) than the bonds joining H atoms on opposite sides of the sheet (1.88 \AA). The Si-H and the C-H bond distances are found to be 1.50 \AA and 1.11 \AA respectively which are equal to the chair conformation.

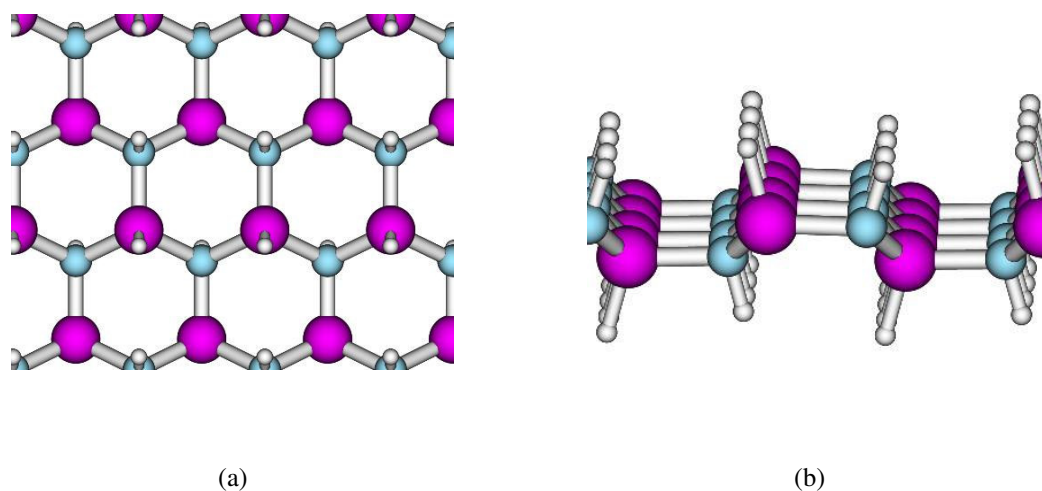


Fig. 8.16 *The boat conformer of SiCH. (a) The top view and (b) the side view*

From the above discussion it is clear that the H atoms bonded differently in the different conformers of SiHCH and depending upon their bonding nature the stability of the conformers varies.

The binding energy (BE) of the three SiHCH conformers has been calculated by the following equation:

$$BE = \frac{E_{total} - n \times E_{Si} - n \times E_C - 2n \times E_H}{4n}$$

Where n is the number of Si/C atoms used for the optimization. We find that the most stable conformer of SiHCH is chair conformer with a binding energy of -4.37 eV. The stability of the boat conformer is slightly lower than chair and the binding energy is found to be -4.36 eV while the stirrup conformer is calculated to have a BE of -4.32 eV. The other two conformers namely twist and puckered are having almost similar binding energy of -4.35 eV. So from the binding energy calculation we find that depending upon the arrangements of the hydrogen atoms on the SiC honeycomb sheet, the resultant structure gives rise to different SiCH conformers and the binding energy also strongly depends on the nature of the conformer.

The interlayer bonding between two layers of all the conformers is found to be negligible, which is similar to that of the conformers of graphane. This proves that all the C and Si atoms are saturated that's why they show minimum interaction between two layers.

The total densities of state (DOS) of all the conformers are plotted in Fig. 8.17. The figure shows that the hydrogenation of graphene like SiC sheet leads to opening of the band gap, with a concomitant increase in the intrinsic stability of the single sheet 2D material. The chair structure is found to have a band gap of 3.7 eV. Among the conformers considered here, the puckered conformer has the highest value (4.2 eV) among the three conformers. The boat conformer found to have higher band gap (3.9 eV) than the chair conformer.

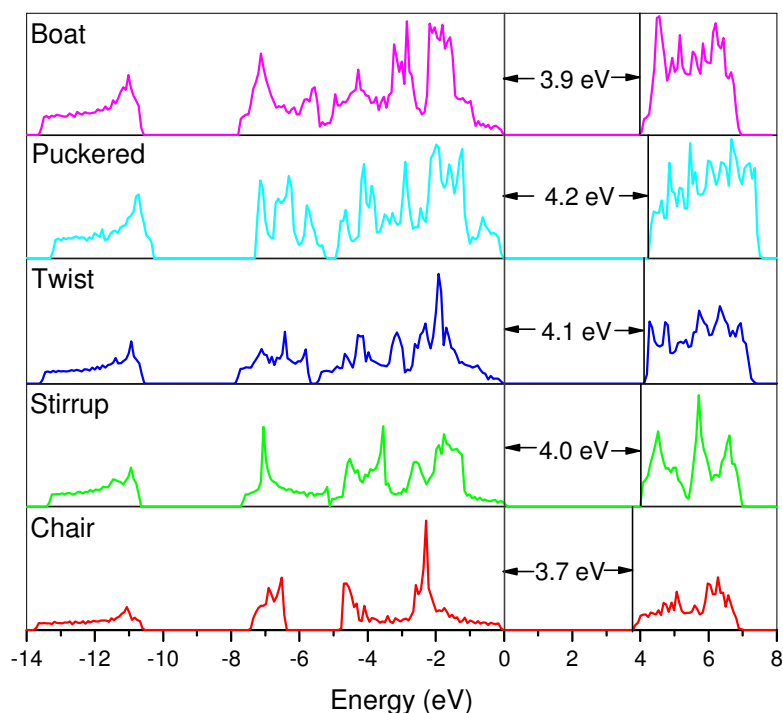


Fig. 8.17 The density of states of different conformers of fully hydrogenated SiC honeycomb structure.

In order to calculate the charge distribution between the C and H atoms of the stirrup conformer, we have deployed the Mulliken population analysis scheme in the single point calculation with the optimized structures of all the conformers. It has been found that in all the conformer the Si atoms give electrons gaining positive charge where as the carbons take electron and become negatively charge in the graphane like SiC sheet. The charge on the Si, C and hydrogen atoms depends on the nature of the conformers. The chair structure shows an electronic charge state of 0.46 electrons for the H atoms while the C atoms have a charge state of -0.5 [Table 8.2]. The corresponding Mulliken charges for H atoms are 0.07 (attached with the Si atom) and 0.11(attached with the C atom) respectively. The charges on Si, C and hydrogen atoms for other conformations are shown are shown in Table 8.2. It is to be noted that larger charge transfer from the C to H atoms, as compared to the Si to H atoms, lead to the strong C-H bonds.

Table 8.2 Charge on Si, C and H atom of different SiC conformers

	Charge on Si atom	Charge on C atom	Charge on H atom
Chair	0.46	-0.5	0.07(Si), 0.11(C)
Stirrup	0.48, 0.50	-0.56, -0.54	-0.08, -0.08, 0.13, 0.13
Twist	0.57, 0.57	-0.57,-0.57	-0.1, -0.11, 0.14, 0.14
Puckered	0.51, 0.41	-0.40,-0.56	-0.1,-0.07, 0.13, 0.12
Boat	0.53, 0.52	-0.56, -0.57	0.1, 0.09, 0.13, 0.13

We have performed a 9-ps *ab-initio* molecular dynamics simulation using the Nose algorithm [287] with a 1-fs time step and a 9000 self-consistent-field run on the most stable chair conformer, in order to see the effect of temperature on the Si-H, C-H and Si-C bond. From the high temperature MD simulation, we find that the chair conformation is quite stable at room temperature. In Fig. 8.18 we have plotted the mean square deviation of the Si-H, C-H and C-Si bonds with time step as estimated at 300 K.

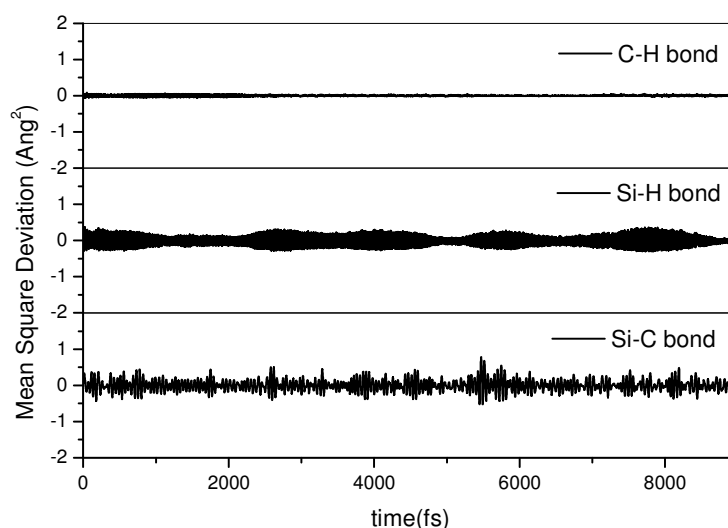


Fig. 8.18 Molecular dynamics simulation showing the average relaxation of C-H, Si-H and Si-C bonds at 300 K with 5-ps time period and 1-fs time step.

The mean square deviation of C-H bond is least, suggests that it is the strongest bond in the graphane like SiC sheet. The average bond distances do not vary considerably throughout the MD run, which does suggest that it is possible to realize the chair conformer of the hydrogenated SiC sheet at room temperature (300 K).

8.2.2.1.3 Addition of Ti atom on the SiC sheet

After establishing the structure and energetics of SiC sheet, attempt has been made to add Ti atom on it. For the interaction of Ti atom, four different possible sites have been considered: i) on the top of the Si atom, ii) on the top of the C atom, iii) at the hollow hexagonal site and iv) at the bridged position as indicated in Fig. 8.19(a). A full geometry optimization is carried out without any constraint. The results reveal that that Ti atom is not stable on the bridge site. Among the other three positions the most stable location of Ti is on the top of Si atom by pushing it down the plane [Fig. 8.19(b) & 8.19(c)].

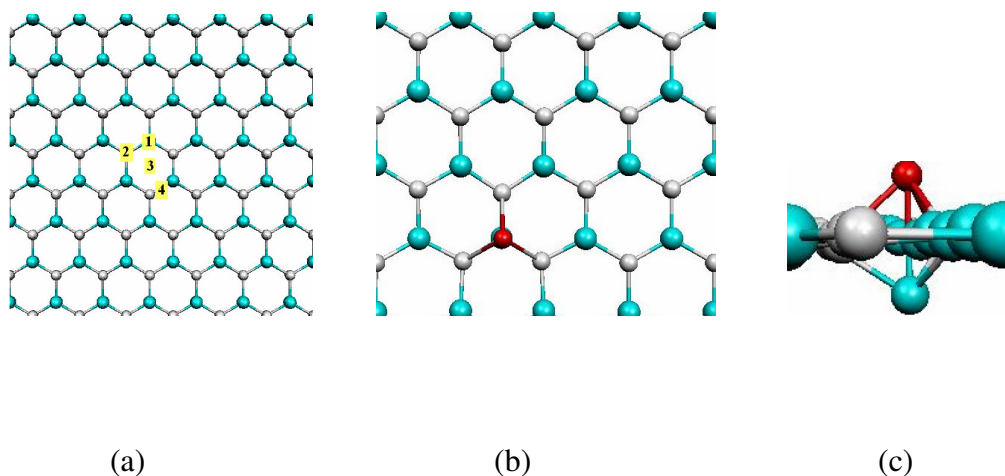


Fig. 8.19 Ti doped SiC graphene like sheet. (a) Different probable positions for Ti doping. [1) on top of the Si atom, 2) on top of the C atom, 3) at the hexagonal site and 4) at the bridged position] (b) The top view of the SiC sheet after doping with Ti atom. (c) Side view of the SiC sheet after doping with Ti atom.

The binding energies of the Ti atom on the Si atom, on the C atom and at the hollow site are found to be 2.74 eV, 1.90 eV and 2.12 eV, respectively. To underscore the preferred

site of the Ti on the sheet, the Ti-Si and Ti-C dimmers have been optimized. The binding energies are found to be 2.82 eV and 4.85 eV with bond distances of 2.43 Å and 1.70 Å respectively. From the figure it is seen that the SiC sheet is distorted from planarity after the addition of Ti in such a way that the doped Ti can bind with Si atom along with three neighboring C atoms, thus improving the stability of the system. When the Ti atom is on the Si atom the Ti-Si bond distance is 2.56 Å where as Ti-C bond distance is 1.98 Å. After Ti doping on the Si atom, the planarity of the system is disturbed due to the fact that the Si atom goes towards the sp^3 hybridization. Though Si and C atoms are isovalent but the most stable state of C is sp^2 and Si is sp^3 . [351] In this case also it is most likely that when Si atom binds with Ti atom forming Si-Ti bond and changes its own hybridization from sp^2 to the most stable sp^3 . From the charge analysis it can be seen that the point charge on the Ti atom 3.31e compared to 4.0 for valence electrons in the neutral state. This indicates that Ti atom transfers 0.7 electronic charges to the SiC sheet and becomes partially cationic in nature. Fig. 8.20 shows the projected density of state of the Ti decorated SiC sheet.

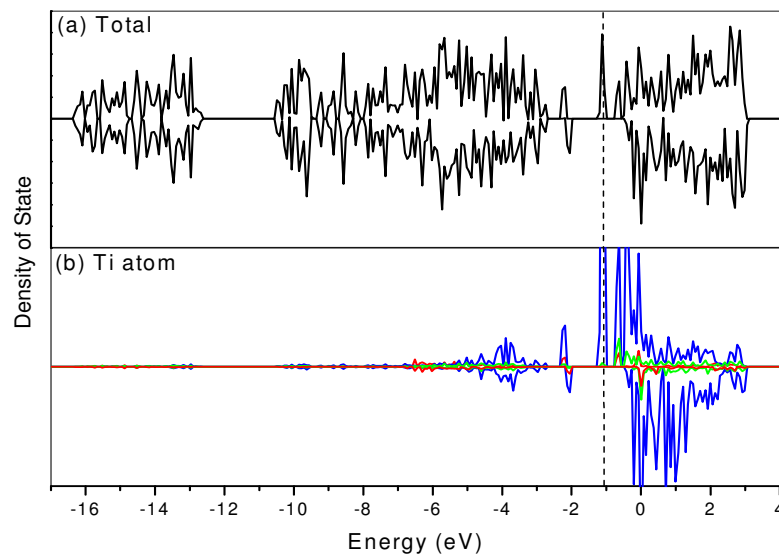


Fig. 8.20 (a) The total density of state (DOS) of the Ti doped SiC sheet. (b) The DOS of the Ti atoms. Red, green and blue colors indicate the s-DOS, p-DOS and d-DOS respectively.

We have found earlier that the SiC sheet itself is having a band gap of 2.42 eV [Fig. 8.11(a)] indicating its semiconducting nature. It is clear from Fig. 8.20(a) that the band gap closes after doping with Ti atom. The projected density of state (PDOS) of the Ti atom on the SiC sheet shows that after doping with Ti atom there is a significant contribution of Ti d-orbital in the unoccupied level. The appearance of the energy states (particularly d orbital) of Ti within the gap of SiC sheet induces the reactivity of the system. Based on the population analysis and DOS it can be concluded that Ti is having a large number of unoccupied d states and it remains in the cationic state and it can accept more electrons from other atoms. Just below the Fermi level also there are hybrid orbitals, which in turn help to increase the reactivity of the system.

8.2.2.1.4 Interaction of hydrogen molecule with the Ti added SiC sheet

The interaction of hydrogen molecules with the Ti decorated SiC sheet (here after will be denoted as Ti@SiC_sh) have been studied. The optimized geometries of the hydrogenated Ti decorated SiC sheet are shown in Fig. 8.21. After adding the hydrogen molecules one by one, we found that that one Ti atom can take upto maximum four hydrogen molecules, which is shown in figure 8.21. The interaction energy (shown in Table 8.3) between the hydrogen molecules and the Ti@SiC_sh is calculated by adding one hydrogen molecule at a time by the following equation:

$$E_n = [E(\text{SiCTiH}_{2n}) - E(\text{SiCTi}) - nE(\text{H}_2)]/n$$

Where $E(\text{SiCTiH}_{2n})$ is the total energy of the hydrogenated Ti@SiC_sh, $E(\text{SiCTi})$ is the energy of Ti@SiC_sh, n is the number of hydrogen molecules and $E(\text{H}_2)$ is the energy of the hydrogen molecule.

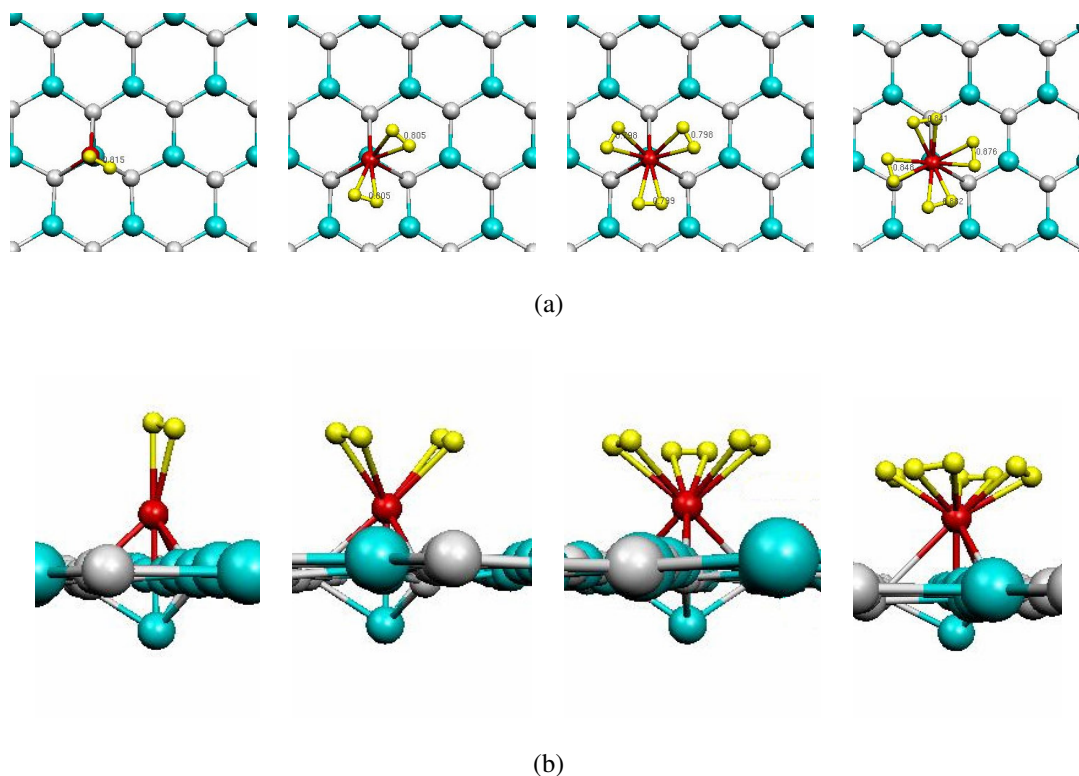


Fig. 8.21 Pictorial diagram showing the interaction of hydrogen molecules one by one with *Ti@SiC_sh*. (a) top view (b) side view.

It is found that the Ti doped SiC sheet interacts with the first hydrogen molecule weakly with a binding energy of 0.62 eV. It can be noted from Fig. 8.21 that, although the molecular bond of hydrogen is elongated, but it does not dissociate. After the first hydrogen molecule interaction, the H-H bond length is elongated to 0.85 Å. It should be mentioned that this is in contrast with the Ti doped C and BN nanotube, where the first hydrogen molecule is dissociated to hydrogen atoms. This result in higher temperature of hydrogen desorption [352]. For the subsequent interaction of three hydrogen molecules, the average interaction energy/hydrogen molecule decreases slowly as shown in the Table 8.3. After the adsorption of total four hydrogen molecules, the average interaction energy is found to be 0.37 eV, which is within the energy window of 0.2 to 0.7 eV desired for an ideal hydrogen storage material.

Table 8.3 *The average interaction energy/hydrogen molecule and the charge on the Ti atom, when the hydrogen molecule interacts one by one with Ti@SiC_sh*

Number of Hydrogen Molecule	Interaction energy/hydrogen molecule (eV)	Positive charge on the Ti atom
1	0.62	0.57
2	0.51	0.54
3	0.44	0.52
4	0.37	0.31

Let now discuss the chemical nature of interaction between the Ti and hydrogen molecules. It is known that for such kind of interactions, Kubas complex is formed by the hybridization between σ or σ^* orbital of hydrogen and d-orbital of Ti metal. From the charge analysis it can be seen when hydrogen atoms are added one by one, the cationic charge on the Ti atom decreases gradually and when four hydrogen atoms are added the cationic charge is reduced from 0.57 to 0.31.

8.2.2.2 Calculations on Single walled SiC (10, 0) nanotube

8.2.2.2.1 Geometry optimization

Now rolling up the SiC sheet then SiC nanotube will form. From the literature it is reported that zigzag SiC nanotube is a direct band gap semiconductor and it is more stable when C and Si atoms are arranged alternatively. Moreover, the relative stability of the nanotube and the nanowires of SiC depend on the diameter. It is reported that below 1.6 nm diameter, nanotubes of SiC are more stable than nanowires [347]. In the present study, single walled nanotube (10, 0) with diameter about 1 nm has been considered, where Si and C atoms are arranged alternatively and the relaxed structure of this tube is shown in Fig. 8.22.

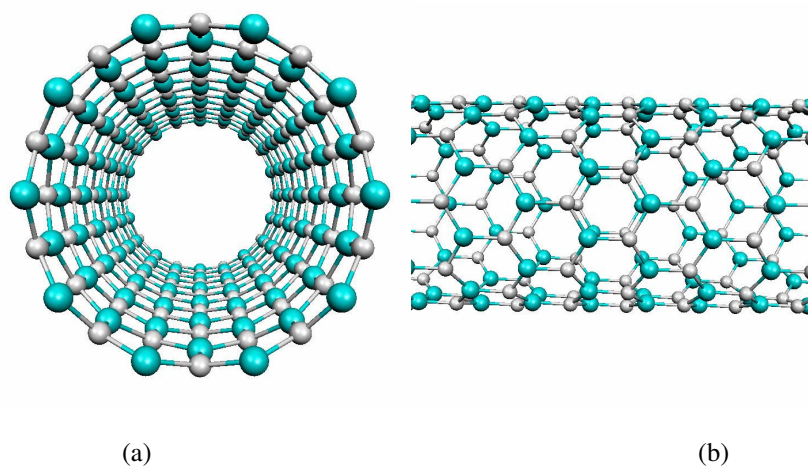


Fig. 8.22 *SiC (10,0) zigzag nanotube. (a) Transverse view (b) Longitudinal view.*

The binding energy/atom of SiC nanotube is found to be 5.85 eV/atom and the Si-C distance is found to be 1.79 Å in agreement with the earlier study [353]. In accordance with the other hetero atomic nanotubes, in this case also more electronegative carbon atoms move towards outer direction of the tube, whereas more electropositive Si atoms move inward direction forming a rippled ring surface. In the present case the tube diameter of the SiC tube containing C atom is 9.97 Å and containing Si atom is 9.80 Å [354]. From the charge density distribution of SiC nanotube it is found that there is transfer of electronic charge from Si to C site. The density of state of SiC nanotube has been plotted in Fig. 8.23. The band gap is found to be 2 eV in accordance with the earlier literature value [351]. It is found that the upper energy levels of the valence band (near fermi energy) is primarily contributed by the *p*-orbital of carbon atoms, and the *p* orbitals of Si atoms form the lower energy of the conduction band. It is worth to mention here that in comparison to the sheet, the nanotube is showing broadening of bands, which is due to enhanced delocalization of electrons.

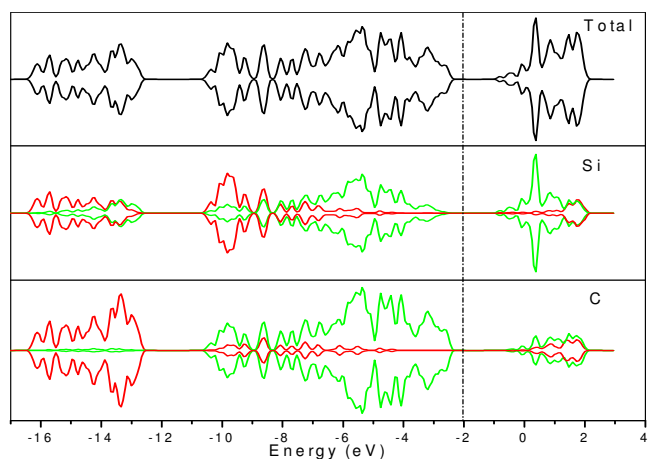


Fig. 8.23 (a) The total density of state (DOS) of SiC nanotube. (b) The DOS of the Si atoms. (c) DOS of the C atoms. The red color and green color and in the PDOS of Si & C atoms represents the *s*- and *p*-orbital respectively.

8.2.2.2.2 Addition of Ti atom on the SiC nanotube

The Ti atom can approach the SiC nanotube at different sites. In case of SiC (10, 0) nanotube the Ti atom preferentially goes towards the hexagonal site [Fig. 8.24] with a binding energy of -2.49 eV.

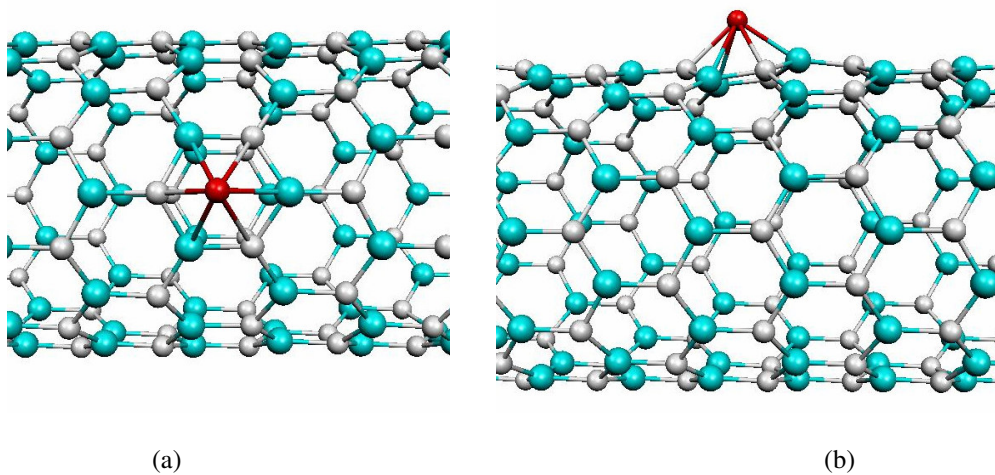


Fig. 8.24 Doping of Ti atom on the SiC nano tube.

When the Ti atom is on the top of the Si atom or C atom the binding energies are found to be -2.36 and -2.29 eV respectively. In this case after Ti doping, the distortion of the structure is

quite less as compared to the SiC sheet. As in this case the hexagonal site is found to be the most stable one so for further calculations this site has been taken into consideration.

Fig. 8.25 shows the projected density state of the Ti doped SiC (10, 0) nanotube.

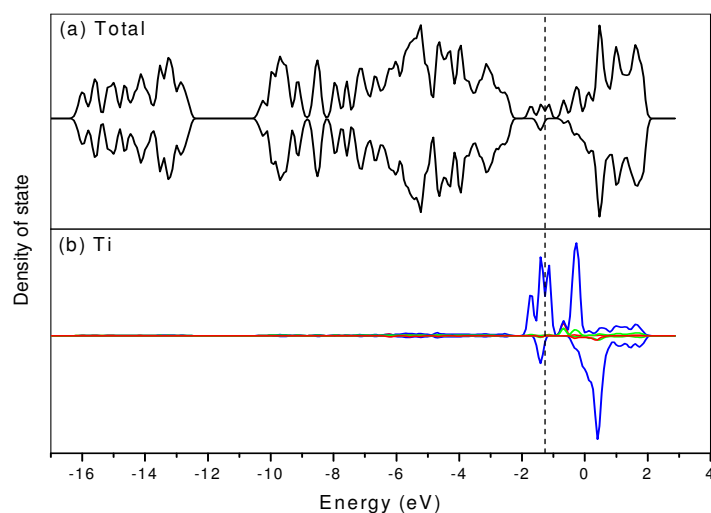


Fig. 8.25 (a) Total density of state (DOS) of the Ti doped SiC (10, 0) nanotube. (b) The DOS of the Ti atom. (Red, green and blue colors indicate the s-DOS, p-DOS and d-DOS respectively).

In this case also it is found that when Ti is added to the SiC nanotube, due to the presence of d-orbital of Ti, the system becomes more reactive and at the Fermi level there is a finite density of states contributed by the Ti d-orbital. From the charge distribution it is seen that the Ti atom has a point charge of 3.28 e (by transferring 0.72 electrons to the SiC tube) as compared to 4 valence electrons in the neutral state, which is comparable with the Ti atom on the SiC sheet.

8.2.2.2.3 Interaction of hydrogen molecules with the Ti added SiC nanotube

Coming to the hydrogen adsorption behavior, the Ti atom can absorb four hydrogen molecules as shown in Fig. 8.26.

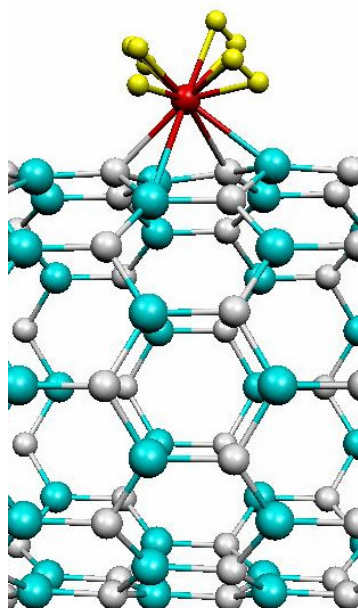


Fig. 8.26 *The optimized geometry of Ti doped SiC nanotube when it interacts with four hydrogen molecules.*

The first hydrogen adsorption energy is found to be 0.84 eV. In contrast to the previous case (Ti doped SiC sheet), here the first hydrogen molecule gets dissociated upon interaction with the Ti atom and the H-H bond distance is elongated upto 0.97 Å. Subsequently, when the second hydrogen molecule is absorbed, it remains in the molecular form only, and the average interaction energy is found to be 0.72 eV. Finally, after adsorption of four hydrogen molecules, the average interaction energy/hydrogen molecule is estimated to be 0.65 eV. For the comparison purpose it can be stated here that the average interaction energy of four hydrogen molecules with Ti@SiC_sh is 0.37 eV. So if the SiC sheet is rolled, the Ti can interact with hydrogen molecules more strongly. The point charge on the Ti atom after interaction with four hydrogen molecules is found to be 3.97 e as compared to 4 valence electrons indicating the charge neutralization by interacting hydrogen molecules. Thus during the adsorption of Ti atom on the SiC nanotube there was some electronic charge transferred from the Ti atom to the tube. Now after the Ti doped SiC nanotube interacts with the hydrogen molecule the Ti atom regained the charge from the hydrogen molecules.

From the above discussions it is understood that the Ti atom shows different hydrogen adsorption behavior, when it is doped on the SiC sheet and SiC nanotube. The projected DOS of Ti d-orbitals for the two cases give the insight about the interaction behavior of Ti atom with SiC as well as with the hydrogen molecules. Earlier it has been seen the binding energy of the Ti atom is more in the SiC sheet (2.74 eV) than that of the SiC nanotube.

From the projected DOS [Fig. 8.27] it is seen that when the Ti atom interacts with the SiC sheet then two major bands are formed below the Fermi level. The first one (designated by 1) is formed by the d_{z^2} orbital of Ti atom where as the other band is contributed by all the d-orbitals of Ti atom (designated by 2).

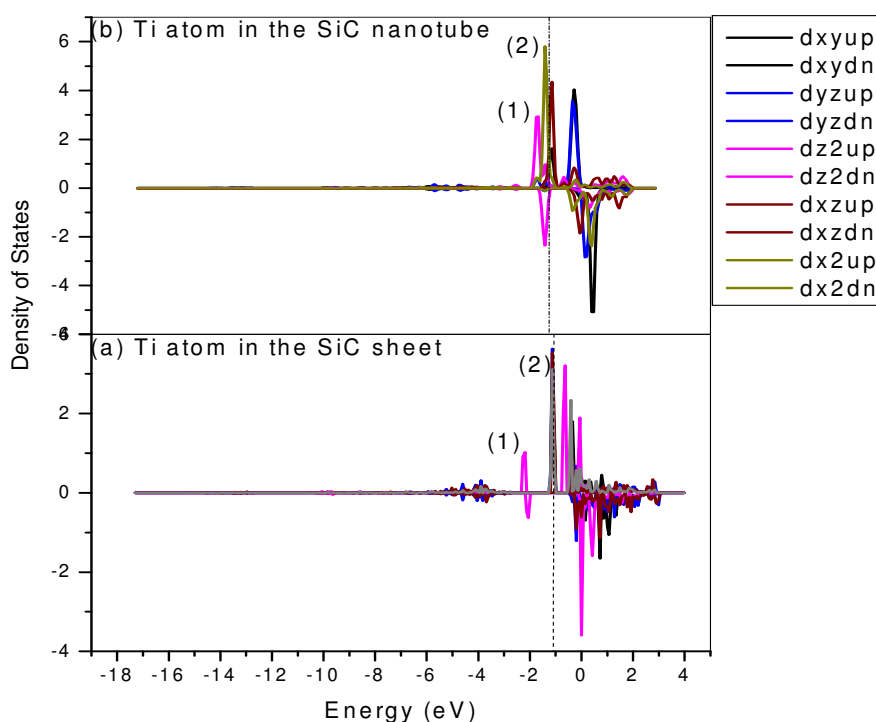


Fig. 8.27 The projected density of state of the Ti d-orbital. (a) Ti atom is doped on the Si atom of SiC sheet. (b) Ti atom is doped in the hexagonal site of SiC nanotube.

As all the d-orbitals of Ti atoms are involved for the bonding with SiC sheet so the binding energy is more in this case and the available orbitals for the interaction with

hydrogen molecule is less, which is reflected in the lower average hydrogen interaction energy value of 0.37 eV. When Ti atom is doped on the SiC nanotube the bonding d-orbitals are d_{z^2} and $d_{x^2-y^2}$. All the other d-orbitals are available for the bonding with incoming hydrogen molecule. So in this case the Ti atom interacts more strongly with the hydrogen molecule with an average binding energy of 0.65 eV.

8.2.3 Summary

In the present study the different conformer of fully hydrogenated Graphene like SiC sheet has been investigated and the chair conformer found to be the most stable one. Molecular dynamic study showed that the structures are quite stable at room temperature and the desorption of hydrogen from the sheet is difficult. To improve the hydrogen storage properties the SiC graphene like sheet has been doped with the Ti atom. The results show that the most stable adsorption site of Ti atom on the SiC sheet is on top of the Si atom. The binding energy is estimated to be 2.74 eV. In contrast, Ti favors a hexagonal site on the SiC nanotube with binding energy of 2.49 eV. Consequently, different atomic sites lead to different orbital interactions of Ti atom in both the cases. Further hydrogenation studies of these Ti decorated nano structures 2.74 reveals that in both cases Ti can absorb upto four H_2 molecules with average binding energy of 0.37 eV and 0.65 eV, respectively. This is within the energy window of an ideal hydrogen storage material. However, while Ti decorated SiC sheet adsorbs all four hydrogen molecule in molecular form, the SiC nanotube dissociates the first hydrogen molecule and thereafter adsorb three hydrogens in molecular form. Based on these results it is inferred that these results provide fundamental insights into the hydrogen adsorption properties of Ti doped SiC and that drive towards the way for further investigations on the potential applications of transition metal decorated-SiC nanostructures as hydrogen storage material.

8.3 Interaction of Hydrogen with Metallo-Carbohedrenes

Among the other carbon nanostructures, transition metal doped fullerene shows a great potential towards hydrogen storage. But due to high cohesive energy, doped transition metals can cluster together, thus decreases the hydrogen storage capacity [301, 355, 356]. The metal adsorption energy should be larger than the cohesive energy of the metal for atomic dispersion. Metal carbide is one of such system where metal and C atoms are bound strongly. Among the metal carbide systems, metallocarbohedrene with chemical formula of M_8C_{12} (M = transition metal atoms) clusters appear outstandingly stable. Unlike transition metal decorated carbon fullerene, which suffers from the metal clustering, metallocarbohedrenes are stable systems with transition metal atoms as part of the carbon nanostructures.

In 1992 Castleman and his group [357] first discovered metallocarbohedrene and characterized by mass spectrometry [Fig. 8.28]. Metallocarbohedrenes or Met-cars are atomic clusters in the form of polyhedra with the composition M_8C_{12} , at the vertices of which there are carbon and transition metal atoms (Ti, V, Zr, Hf, Fe, Cr, Mo). If the transition metal atom is Ti, then it forms titenocarbohedrene which is the most well studied metallo carbohedrene. These clusters can exist mostly in two isomeric forms: a fullerene-like cage structure, formed by 12 C—M—C—C—M pentagons (a pentagonal dodecahedron with T_h symmetry), [358] and the tetracapped tetrahedrons of metal atoms (T_d symmetry) as optimized by Dance [359] from DFT calculations. From further experimental and theoretical findings, T_d symmetry is considered as the most abundant isomer of met-car. Energetically the tetracapped tetrahedron (T_d) was found more stable than the pentagonal dodecahedron (T_h) by a considerable amount

and apart from an initial small energy bump transformation from the T_h form to the T_d isomer proceeds barrier less along a reaction path constrained with the D_2 symmetry [360].

Guo & Castleman, Science 255, 1411-13 (1992)

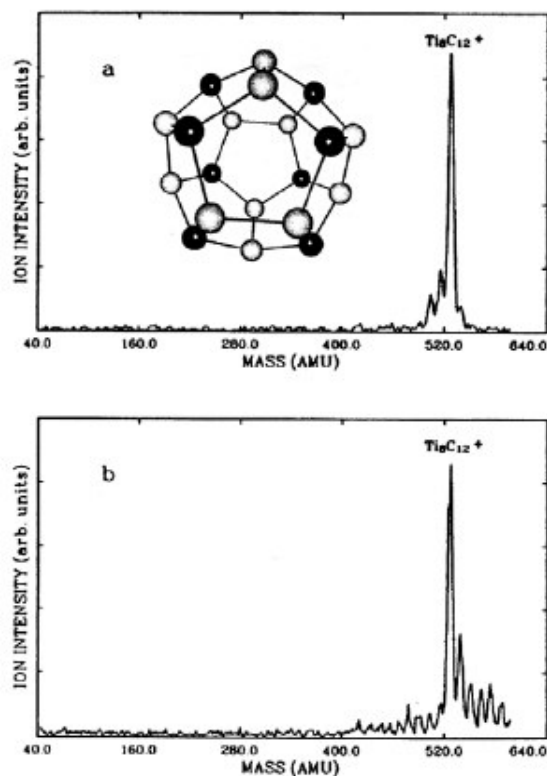


Fig. 8.28 *Discovery of metallocarbohedrene by mass spectrometric study by Guo & Castleman*

Here we report a first principles study of hydrogen storage behavior of metal-carbohedrene clusters consisting of transition metal and carbon atoms. In the present work, we considered T_d geometry of met-car as our model system to study the hydrogen adsorption on the M_8C_{12} ($M = Sc, Ti, \text{ and } V$) clusters. In the first part we have used pure met-car cluster for hydrogen adsorption. It is seen that each corner Ti atoms can bind three molecules of hydrogen, and each Ti atoms on the face site can bind with one molecule of hydrogen. In the next step 12 carbon atoms adsorb hydrogen in the atomic form. This process is not

spontaneous, and needs activation energy to dissociate the H-H bond. After saturating the met-car with hydrogen, we have investigated the desorption behavior using the molecular dynamics simulation.

8.3.1 Theoretical methodology

In the present work we have used density functional theory (DFT), [210, 211] as employed in the Vienna *ab-initio* Simulation Package (VASP), [275] and the projector augmented wave (PAW) method [234]. The PAW method is an all-electron frozen core method, which combines the features of both the ultra-soft pseudopotentials and augmented plane wave methods. The exchange correlation contributions were included using the generalized gradient approximation (GGA) proposed by Perdew–Burke–Ernzerhof (PBE) [217, 218]. Wave functions were expanded using a plane wave basis set with a cutoff energy of 400 eV. The Brillouin zone was sampled at the gamma point. For the geometry optimization, the forces were minimized up to 0.001 eV/Å. The geometry optimizations were run starting from several initial candidate geometries with out imposing any symmetry constraints. The nudged elastic band (NEB) [286] method has been employed to find out the minimum energy path (MEP) and the corresponding energy barrier for the dissociation of hydrogen molecules on the C-C bond of Ti_8C_{12} cluster. The method involves the optimization of chain of images, obtained by linear interpolation, between the initial and final state. In most of the cases total number of images used is equal to 10, which is sufficient to map the minimum energy path (MEP) accurately. Each image is allowed to move in the direction perpendicular to the hyper tangent. Hence the energy is minimized in all direction except the direction of reaction path. In order to check the stability of cluster and desorption of H atoms from Ti_8C_{12} cluster, we have performed *ab-initio* molecular dynamic simulations using the Nosé algorithm [287]. For this purpose each system was heated at higher temperatures (exact

values are given in the text below) and kept for 7ps with a time step of 1fs. Although we understand that 7ps is not sufficient for accurate statistical analysis but it certainly provides meaningful qualitative information to understand the system.

8.3.2 Results and discussion

8.3.2.1 Geometry and energetics

Metallocarbohedrenes or Met-cars are “supermagic” cluster of transition metal atom and carbon with the composition of M_8C_{12} , where M represents the transition metal atom. In the present study we have considered T_d geometry of three met-car group clusters (Ti_8C_{12} , Sc_8C_{12} , and V_8C_{12}) with spin singlet as a model system to investigate the hydrogen adsorption behavior. A typical geometrical configuration of the Met-Car clusters with T_d symmetry is shown in Fig. 8.29. The structural parameters and energetics of these clusters are summarized in Table 8.4.

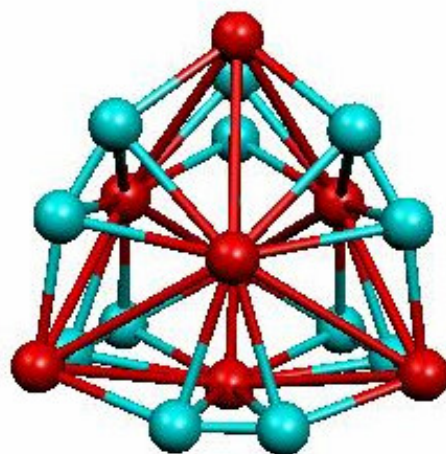


Fig. 8.29 The geometry of Ti_8C_{12} cluster. The red balls and the blue balls represent Ti and carbon atoms respectively.

Table 8.4 *The structural parameters and energetics of Sc₈C₁₂, Ti₈C₁₂, V₈C₁₂ clusters*

	Sc ₈ C ₁₂	Ti ₈ C ₁₂	V ₈ C ₁₂
Binding Energy	5.94 eV/atom	6.49 eV/atom	6.13 eV/atom
C-C bond length	1.31 Å	1.34 Å	1.36 Å
M-C_{side on} distance	2.38 Å	2.24 Å	2.18 Å
M-C_{end on} distance	2.18 Å	1.97 Å	1.87 Å
M-M bond length	5.27 Å 2.99 Å	4.89 Å 2.80 Å	4.62 Å 2.66 Å

It has been found that the stability of the M₈C₁₂ clusters decreases in the order Ti₈C₁₂ > V₈C₁₂ > Sc₈C₁₂. The higher stability of Ti₈C₁₂ and Sc₈C₁₂ clusters in comparison to that of V₈C₁₂ is in line with the experimental observations [361]. From the geometry of these clusters, it is seen that the cage size follow the trend in the atomic size of metal atoms. For example, the atomic radius of Sc, Ti and V atoms are 2.09 Å, 2.00 Å, 1.92 Å respectively, and similarly the cage size varies in the order of Sc₈C₁₂ > Ti₈C₁₂ > V₈C₁₂. To underscore the chemical bonding in these clusters, we have analyzed the total and split density of states for a representative Ti₈C₁₂ cluster as shown in the Fig. 8.30.

It can be seen from Fig. 8.30 that in the density of state of Ti₈C₁₂ four distinct regions can be identified. It is seen that the HOMO energy level (shown by 1) is formed by the filled Ti-3d and C-2p orbital, and the LUMO is formed by the empty Ti-3d orbital. The other states deep in the energy level are C p & s orbitals (shown by 2, 3, and 4 respectively). Similar DOS spectrums are also observed for Sc₈C₁₂ and V₈C₁₂ clusters with a small difference that for Sc₈C₁₂, the energy bands are narrower than Ti₈C₁₂. This has been attributed to the minimum

overlap between orbitals of different atoms, which is also reflected in the lower binding energy of the Sc_8C_{12} cluster.

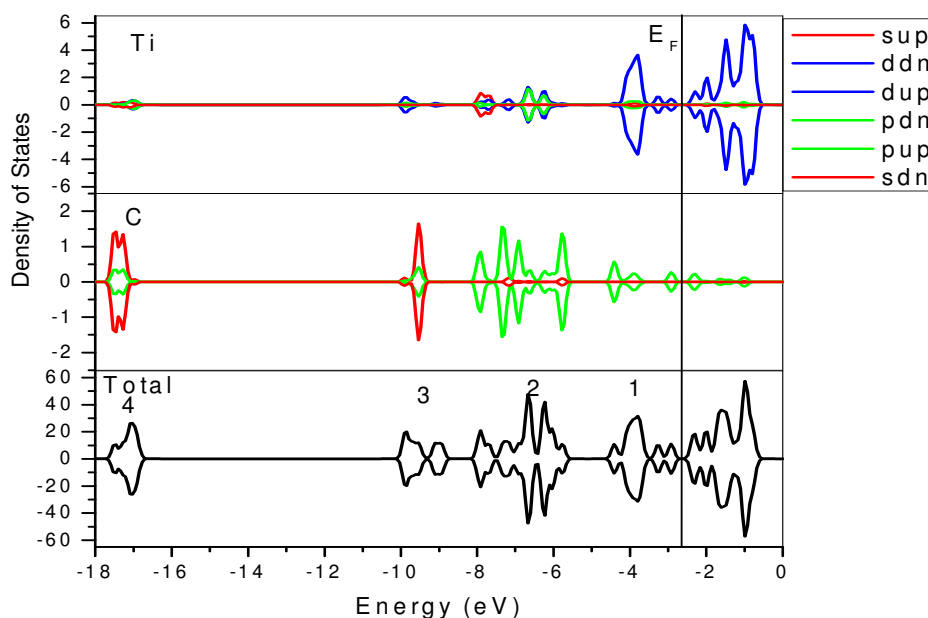


Fig. 8.30 Density of state of Ti_8C_{12} cluster. In the projected density of state of Ti and C atom the red, green and blue indicates the s, p & d orbitals.

8.3.2.2 Interaction of hydrogen molecules with M_8C_{12} cluster

Based on the geometrical orientations, it is envisaged that hydrogen molecule can approach the Ti_8C_{12} cluster from three different directions: (i) four corner Ti atoms (cTi), (ii) four side centered Ti atoms (sTi), and (iii) hydrogenation of C-C bonds. We have investigated all these options by allowing interaction of one hydrogen molecule at a time. These interactions reveal that each side centered Ti atoms can bind one hydrogen molecule non-dissociatively with interaction energy of -0.25 eV. Moreover, the hydrogen molecule forms ‘T’ shaped complex with Ti, very similar to what has been predicted for Kubas complex [Fig. 8.31]. In contrast, the corner Ti atoms bind with three hydrogen molecules. While the first hydrogen molecule is found to bind with 0.44 eV energy, the average interaction energy of the second and third hydrogen molecules is estimated to be 0.39 eV and 0.37 eV,

respectively. Thus, four corner Ti atoms can bind $4 \times 3 = 12$ hydrogen molecules. To understand the mechanism of hydrogen interaction with these clusters, it is of interest to investigate the nature of bonding. For Ti_8C_{12} , it is seen that the side centered Ti atom uses the in-plane metal orbitals ($d_{x^2-y^2}$ and d_{xy}) for making a σ bond with acetylenic π orbital and the outer plane orbitals (d_{xz} , d_{yz} , d_z^2) remain free. On the other hand, the corner Ti atoms form pyramidal structure by forming the σ bond with three C atoms [362]. The charge distribution analysis indicates that the side centered and corner Ti atoms have 3.6 and 3.1 (compared to 4 number of valence electrons) electronic charge, respectively. As the Ti atoms are in cationic state so it can accept electrons from other atoms. Moreover, it is expected that the corner Ti atoms will bind with more number of hydrogen as compared to side centered Ti atom.

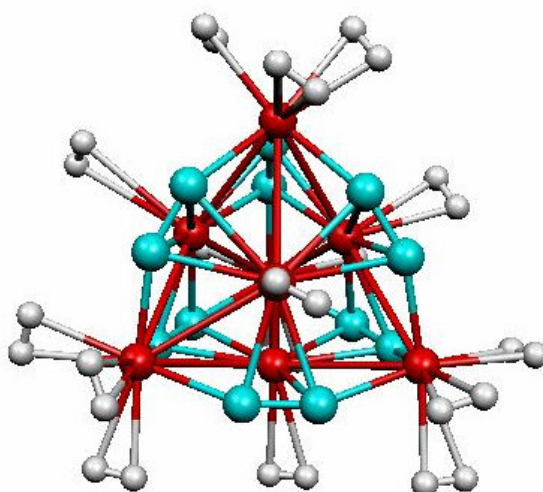


Fig. 8.31 16 hydrogen molecules absorbed in Ti_8C_{12} cluster. Each corner and side centered Ti atoms absorbs three and one hydrogen molecules respectively.

The optimized geometry of the hydrogenated Ti_8C_{12} cluster is shown in Fig 8.31. Fig. 8.32 shows the change in density of state of Ti_8C_{12} before and after interaction with the molecular hydrogen. It is seen from the figure that after interaction with hydrogen two extra bands appear between -8 to -10.5 eV, leaving the other energy bands almost unaltered. We

see that for the binding with hydrogen molecule there is significant contribution of Ti-3d orbital in the unoccupied level. When hydrogen molecules are added one after another on the corner Ti atom, the vacant d orbital of Ti gets gradually filled up due to the transfer of electron from the hydrogen molecule towards the vacant d-orbital of Ti atom. As a result, the unoccupied energy levels of Ti are depopulated and the H-1s peak grows which can be seen in Fig. 8.32.

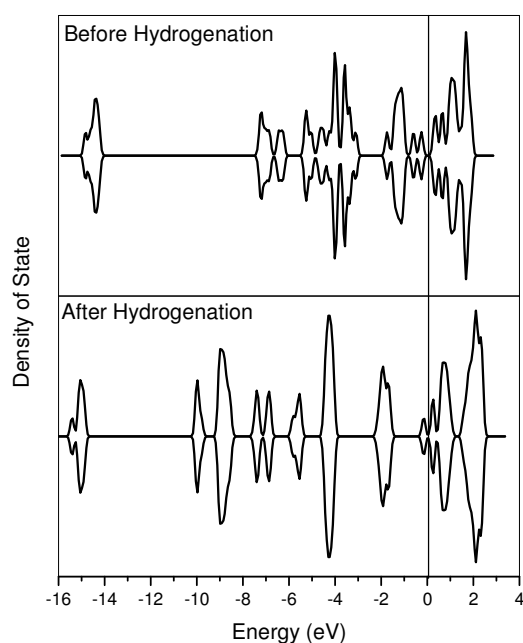


Fig. 8.32 Comparison of density of states between Ti_8C_{12} and $16H_2@Ti_8C_{12}$. For comparison purpose the Fermi energy has been set at zero.

After interaction with one, two and three hydrogen molecules, the positive charge on the Ti atoms is found to be 0.83, 0.63 and 0.58 respectively. Due to the transfer of electron from the H_2 molecule to the Ti atom, the positive charge on the Ti atom decreases gradually. Thus, 8-Ti atoms of Ti_8C_{12} cluster can bind total 16 hydrogen molecules with average interaction energy of -0.32 eV per H_2 molecule.

In the next step, we attempt to attach more H_2 molecules with Ti_8C_{12} cluster via C atoms. But in this case, the hydrogen molecule undergoes dissociative adsorption. Thus, total

12 hydrogen atoms can be attached with 12 C atoms of the Ti_8C_{12} cluster. The binding energy of each hydrogen atom is calculated as

$$\Delta E = \frac{1}{n} [E(M_8C_{12}H_n) - E(M_8C_{12}) - nE(H)]$$

Where, n is the number of hydrogen atom attached, $E(M_8C_{12}H_n)$ is the total energy of the hydrogenated met-car, $E(H)$ is the energy of hydrogen atom and $E(M_8C_{12})$ is the total energy of the met-car. For Ti_8C_{12} cluster the interaction energy is estimated to be 2.59 eV. The optimized geometry of the Ti_8C_{12} cluster after hydrogenation is shown in Fig. 8.33(a). From the elastic band calculation, it is found that an activation barrier of 2.2 eV is required for the dissociation of H-H bond for the hydrogenation of C atoms. In this context it should be mentioned that one can avoid the high activation barrier of H-H bond dissociation by considering a spillover mechanism, where intra-molecular Ti atoms can act as catalyst [363], which lowers the activation barrier of hydrogen adsorption.

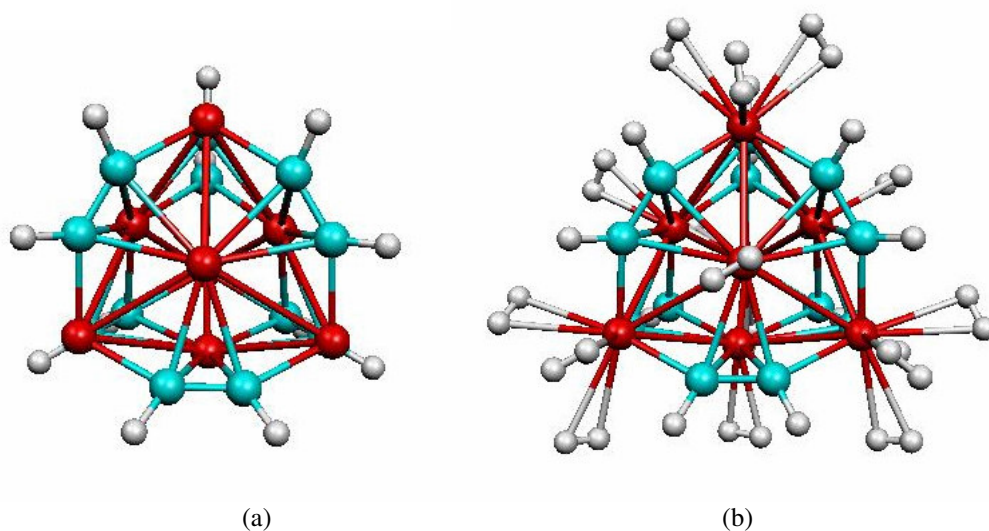


Fig. 8.33 Geometry of Ti_8C_{12} cluster after addition of hydrogen on the C sites. (a) and (b) represents the geometry of the cluster after addition of hydrogen on the C atom, and geometry of the cluster after full coverage with hydrogen respectively.

After establishing the hydrogenation behavior of Ti_8C_{12} cluster, we have investigated the hydrogen adsorption of Sc_8C_{12} and V_8C_{12} clusters. For Sc_8C_{12} , the side centered Sc atoms

adsorb one hydrogen molecule with binding energy of 0.15 eV. This is smaller than Ti_8C_{12} cluster. The corner Sc atoms bind the hydrogen molecule weakly (interaction energy 0.28 eV) compared to the Ti atom, though it can bind one more hydrogen molecule. For V_8C_{12} cluster, the side centered and corner V atoms bind one and two hydrogen molecules with binding energy of 0.23 eV, and 0.46 eV, respectively. We note that although the interaction energy is more than Ti atoms, but the total number of hydrogen molecules attached with V atoms is smaller. The interaction energy of hydrogen atom with C in Sc_8C_{12} and V_8C_{12} cluster are 2.78 eV and 2.48 eV respectively. The higher interaction energy of hydrogen with C in case of Sc_8C_{12} is higher due to the smaller C-C bond distance (1.31 Å). Upon hydrogenation the strain gets released and as a result the overall geometry becomes stabilized. Based on these results, the total hydrogen storage capacity of Ti_8C_{12} , Sc_8C_{12} , and V_8C_{12} clusters is estimated to be 15.06, 20.00 and 12.33 wt. % respectively.

8.3.2.3 Hydrogen desorption behavior

One important factor for a good hydrogen storage material is the desorption profile of the adsorbed hydrogen. In fact, to be a good hydrogen storage material, not only desorption kinetics should be fast enough, but also the material should be stable at higher temperature. To verify these aspects, we have investigated the thermal stability and desorption behavior of Ti_8C_{12} cluster by using the ab-initio molecular dynamics simulation using Nöse algorithm. To start with, the hydrogenated Ti_8C_{12} cluster ($\text{Ti}_8\text{C}_{12}, 16\text{H}_2$) is heated at different temperatures (100 K, 150 K, 200 K, 300 K and 500 K) followed by equilibration for 7000 steps with 1 fs time scale. The results [Fig. 8.34] reveal that while at 100 K, and 200 K, one and three hydrogen molecules are evaporated respectively; at 300 K four hydrogen molecules are desorbed. Most importantly, above 300 K, the hydrogen molecules tend to dissociate and attach with the nearest C atoms via spillover mechanism.

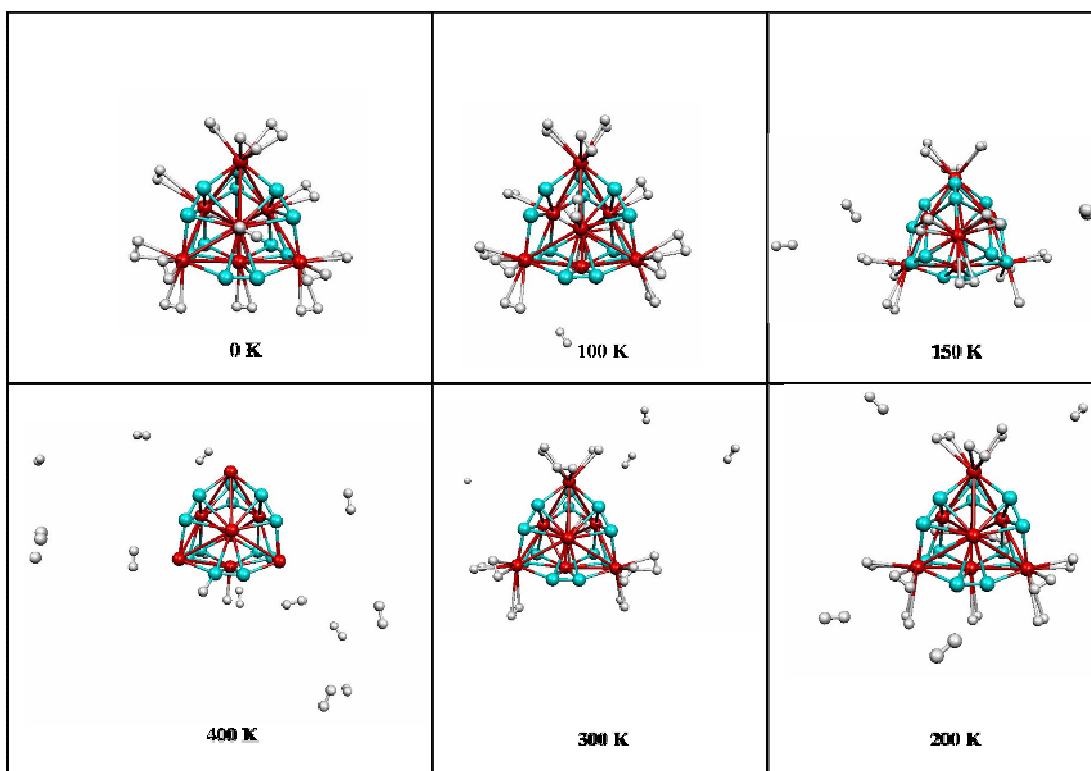


Fig 8.34 Few snapshots of the hydrogenated Ti_8C_{12} clusters during MD simulations at 0 K, 100 K, 150 K, 200 K, 300 K and 500 K.

Finally at 400 K, the hydrogen spillover towards the C atom occurs spontaneously which leads to the formation of $Ti_8C_{12}H_{12}$ cluster, where 12 hydrogen atoms are chemisorbed with C atoms. In other words, if we cool the $Ti_8C_{12}H_{12}$ cluster and keep in hydrogen atmosphere, it can take up 16 H_2 molecules giving rise to $[Ti_8C_{12}H_{12}, 16H_2]$ complex, with total hydrogen storage capacity of 15.06 wt. % for Ti_8C_{12} . However, previous calculations suggest that H atoms are bonded with C atoms via a strong covalent bond. Therefore, desorption of these chemisorbed H atoms are difficult and needs very high temperature. In this situation, the $Ti_8C_{12}H_{12}$ complex can be considered as a host material, which adsorbs and desorbs 16 hydrogen molecules, leading to 10.96 wt. % of reversible hydrogen storage capacity. To verify this conjecture, the interaction of hydrogen molecules with $Ti_8C_{12}H_{12}$ complex was carried out in the similar way as described for Ti_8C_{12} cluster. The interaction

energy of hydrogen with the corner Ti atom of $\text{Ti}_8\text{C}_{12}\text{H}_{12}$ is found to be 0.25 eV which is slightly less than the Ti_8C_{12} cluster. The interaction energy of hydrogen with the side centered Ti atom is found to be 0.20 eV for the $\text{Ti}_8\text{C}_{12}\text{H}_{12}$ cluster. With the help of the molecular dynamic simulation we checked the reversibility. We find that $[\text{Ti}_8\text{C}_{12}\text{H}_{12}, 16\text{H}_2]$ desorbs three molecular hydrogen at 50 K and all hydrogen molecules attached to Ti atoms are desorbed at 300 K. At that temperature, the overall structure of the $\text{Ti}_8\text{C}_{12}\text{H}_{12}$ cluster remains stable with 12 hydrogen atoms attached with carbon atoms. The adsorption desorption process is discussed pictorially in Fig. 8.35

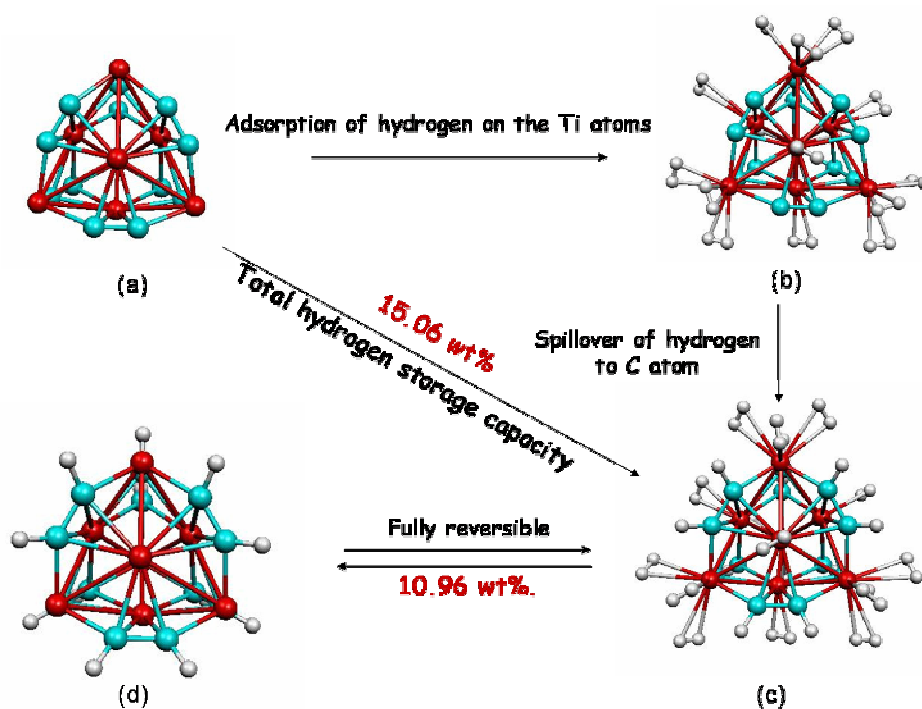


Fig 8.35 Flow sheet for hydrogen adsorption desorption in the Ti_8C_{12} cluster.

8.3.3 Summary

In this study we have investigated the hydrogen storage properties of selected metallo-carbohedrene (M_8C_{12} , $\text{M} = \text{Sc}, \text{Ti}, \text{V}$). The hydrogen storage capacities of these metallo-carbohedrenes have been compared. All calculations were performed with density functional

theory using plane-wave pseudo potential approach. The results revealed that when the M = Ti, the cluster can take up total 16 hydrogen molecule by physisorption where the hydrogen molecules gets absorbed reversibly on the Ti atoms. Each of the C atoms can bind one hydrogen atom by chemisorption. Though the total hydrogen storage capacity found to be 15.06 wt % but the reversible capacity is 10.96 wt %. In case of Sc_8C_{12} the total hydrogen storage capacity is much higher (20 %), as it can adsorb 30 hydrogen molecules by physisorption. The results show that the interaction energy of the hydrogen molecules with cluster is lower compared to the Ti_8C_{12} cluster. For V_8C_{12} the hydrogen storage capacity decreases and the total hydrogen storage capacity found to be 12.33 wt % only.

8.4 Conclusion

In this chapter different carbon and carbon based nano structure has been studied for their hydrogen storage properties. Most of the earlier researches reveal that the pure carbon nanostructures bind hydrogen very weakly for practical hydrogen storage application. In our study we have tried to alter the hydrogen storage properties of corannulene, which is a simple representative of curved carbon nanostructure. The alkali (Li^+ , Na^+ and K^+) and alkaline (Be^{2+} , Mg^{2+} , Ca^{2+}) earth metal ion doped corannulene molecules show that all the metal ions can bind with the corannulene ring through the charge transfer complex formation. Moreover, the preference of adsorption site is dependent on the size of the cations; while the larger size cations prefer to bind on the concave surface, the smaller cations stabilizes on the convex surface. During this work significant improvement of hydrogen binding was found on the metal ion doped corannulene molecules in comparison to the clean corannulene system. The Na^+ doped corannulene is found to be the best candidate among all metal ions considered here.

Pure SiC nanostructure exhibits better binding ability than the corresponding carbon nanostructure due to the polarity in Si-C bond. The fully hydrogenated SiC sheet shows that depending upon the hydrogen adsorption sites it can form different conformers. The chair conformer is found to be the most stable one. Due to the poor reversibility in the system the sheet has been further modified by the Ti atom and the results have been compared with Ti doped SiC tube. The interaction of this Ti decorated sheet with hydrogen suggests that each Ti atom can bind up to four hydrogen molecules (all hydrogens are adsorbed in the molecular form) with an average binding energy of 0.37 eV, which is less than that of Ti doped SiC nanotube (0.65 eV). The differences come due to different bonding nature of the Ti atom with SiC sheet and nanotube. The problem with transition metal doping is that, the transition metal can form cluster and one of the ways out is embedment of the transition metal atoms in the carbon structure. We have investigated one such model system, metallocarbohedrene for its hydrogen storage properties. The results show that Ti_8C_{12} cluster can absorb 15.06 wt. % of hydrogen at low temperature.

Conclusion and Scope for Future Work

During the present thesis, different experimental techniques have been used for the determination of hydrogen storage capacities, pressure composition isotherms, and critical thermodynamic and kinetic properties of solid state hydrogen storage materials. During the course of the work, several transition metal based alloys have been identified, modified by proper substitution and the results provide a suitable database for the appropriate choice of hydrogen storage materials. Further the theoretical calculations in the thesis provide proper understanding of physical and chemical properties for efficient hydrogen storage materials, which can give insight for experimental studies. In order to further explore new materials with higher hydrogen storage capacities, theoretical modeling has been carried out on carbon based system using electronic structure theory.

Several transition metal based hydrogen storage materials, which are proposed to be the practical small scale hydrogen storage solution in the present day scenario, were investigated during the present work. The hydrogen content, equilibrium pressure at given temperature and the hydrogen desorption behavior determines the thermodynamic properties of the metal hydrides. The optimized system development for a given application is not possible without selecting a hydride with suitable hydrogen absorption desorption properties.

It has been found that the hydrogen storage properties of metal hydrides can be tailored in a wide range by means of substitution. The discovery of the approach of combining different hydrides, which react with each other during hydrogen release by forming a stable compound, show a great promise for the development of novel suitable hydrogen storage material systems with elevated gravimetric storage densities. However, so far, the ideal storage material with low reaction temperatures, ideal thermodynamics and on-board reversible hydrogen storage density of more than 6 wt. % H₂ has not been found.

This thesis contributes significantly to the development of hydrogen storage materials based on Ti-V-Fe and Ti-V-Cr systems (Chapter III, IV). From the hydrogen storage studies on Ti_{1-x}VFe_x series we could conclude that, by varying the concentration of Fe, the hydrogen storage properties and activation of the alloys can be modified drastically. Ti_{0.85}VFe_{0.15} shows the maximum hydrogen storage capacity of 3.7 wt. % within this series. Both Zr and Ce substitution found to improve the hydrogen storage properties. It has been found in Ti-V-Cr series that, TiVCr shows TiH₂ phase separation on cycling, but a small amount of Zr substitution for Ti is found to have beneficial effects on the hydrogen absorption properties as it restrains TiH₂ phase separation and decreases hysteresis. The Ti₂VCr alloy in Ti-V-Cr series shows a maximum hydrogen storage capacity of 4.37 wt. % at room temperature.

One more transition metal based system, which has been explored during the present study, is Zr-Fe-V based Laves phase alloy for hydrogen storage (Chapter V). The systematic improvement of the hydrogen storage capacity of ZrFe₂ Laves phase compound was done by the V substitution for Fe. Though ZrFe₂ forms unstable hydride, with the increase in the V concentration the stability of the hydrides increase. The formation enthalpy of the hydride of ZrFe_{1.2}V_{0.8} is found to be -41.8 KJ/ mole, which is close to the enthalpy value required for the room temperature absorption-desorption of hydrogen.

Unfortunately, so far all the known conventional metal hydrides with more or less ideal reaction enthalpies and hydrogen equilibrium pressures above 1 bar at room temperature suffer from a rather limited reversible hydrogen storage capacity and it is not possible to realise a solid storage hydrogen tank with these materials, though such tank systems still have advantages for the storage of small quantities of hydrogen. For large scale vehicular applications, it is required to develop novel hydrogen storage materials based on light weight elements. For the applications of these novel material systems it is important to further adapt thermodynamic properties as well as the temperatures of operation towards the practical requirements of the system.

In the present thesis, the light weight hydrogen storage materials for the large scale applications have been studied computationally, and also newer materials have been proposed as future candidate material (Chapter VII, VIII). The interaction behavior of a hydrogen molecule with Mg(0001) surface, doped with three different transition metal atoms ($M = \text{Ti}$, V , and Ni) was reported. On the basis of stability criteria, it is seen that all the M atoms prefer to substitute one of the Mg atoms from the second layer than that from the top surface layer. By comparing the dissociation and diffusion activation barrier for hydrogen on Ti, V and Ni metal doped Mg(0001) surface it is inferred that the substitution of V in the Mg lattice will be the best choice considering the requirements of a good hydrogen storage material. Finally we found that by increasing the impurity concentration it is possible to stabilize the dopant on the top layer, which results in significant reduction of the hydrogen molecule dissociation barrier on the Mg surface. The hydrogen absorption properties of Mg cluster also has been studied to reveal the effect of finite size on the hydrogen absorption desorption properties. The calculations clearly illustrate that Mg_{55} cluster dissociate hydrogen at lower temperature by decreasing the activation barrier for dissociation of hydrogen molecule than bulk Mg. It has been also found that if the Ti atom is substituted in the cluster it goes at the middle layer and

decrease the dissociation barrier further by activating the surface Mg atom. The *ab-initio* molecular dynamics calculations show that at 300 K the Mg-H is elongated sufficiently and starts a flip-flop motion on the surface, which can be viewed as the onset of hydrogen diffusion, a preliminary step for desorption.

Different carbon and carbon based nano structures have also been studied in this thesis for their hydrogen storage properties. The alkali (Li^+ , Na^+ and K^+) and alkaline (Be^{2+} , Mg^{2+} , Ca^{2+}) earth metal ion doped corannulene molecules show that all the metal ions bind with the corannulene ring through charge transfer complex formation. The adsorption site of the alkali & alkaline earth metal is dependent on the size of the cation. Significant improvement of hydrogen binding energy has been reported on the metal ion doped corannulene molecule in comparison to the clean corannulene system and Na^+ doped corannulene is proposed as the best candidate.

The hydrogen absorption study has been done on the SiC sheet. The results show that depending upon the hydrogen adsorption sites, fully hydrogenated SiC sheet, can form different conformers, among which the chair conformer is found to be the most stable one. The sheet has been further modified by the doping Ti atom on that and hydrogen interaction suggests that each Ti atom can bind up to four hydrogen molecules (all hydrogen are adsorbed in the molecular form) with an average binding energy of 0.37 eV, which is less than that of Ti doped SiC nanotube (0.65 eV). The differences come due to different bonding nature of the Ti atom with SiC sheet and nanotube. The problem with transition metal doping is that, the transition metal can cluster together and one of the ways out is embedment of the transition metal atoms within the carbon structure. We have investigated one such model system, metallocarbohedrene for its hydrogen storage properties. The results show that Ti_8C_{12}

cluster can absorb 15.06 wt. % of hydrogen at low temperature and the compound can be tailored further to stabilize hydrogen near room temperature.

During this thesis, I have tried to make significant contribution towards the development of material for hydrogen storage and the fundamental understanding of interaction of hydrogen with different materials. The present work can be extended by different other modifications experimentally, for the verification of the theoretical data by experimental methods. Efforts have been already started in this direction. However, hydrogen storage studies are to be continued, using both experimental and theoretical tools, to find newer materials with suitable thermodynamics and kinetics properties, which can store higher amount of hydrogen.

REFERENCES

- [1] L. Schlapbach and A. Züttel, “Hydrogen storage materials for mobile applications”, *Nature*, **414**, 353 (2001).
- [2] Pius Fatona, “Renewable Energy Use and Energy Efficiency-A Critical Tool for Sustainable Development, Sustainable Growth and Applications in Renewable Energy Sources”, Edited by Majid Nayeripour and Mostafa Kheshti, Publisher: InTech, Published: December 02, 2011.
- [3] N. N. Greenwood, A. Earnshaw, “Chemistry of the Elements”, Oxford; Boston, Butterworth-Heinemann (1997).
- [4] “The Hydrogen Economy: Opportunities, Costs, Barriers, and R&D Needs, Committee on Alternatives and Strategies for Future Hydrogen Production and Use”, National Research Council, National Academy of Engineering, National Academy of Sciences.
- [5] W. Grochala, P. P. Edwards, “Hydrides of the Chemical Elements for the Storage and Production of Hydrogen”, *Chemical Reviews*, **104**, 1283 (2004).
- [6] S. A. Sherif, N. Zeytinoglu, T. N. Veziroglu, “Liquid hydrogen: Potential, problems, and a proposed research program”, *International Journal of Hydrogen Energy*, **22**, 683 (1997).
- [7] W. Peschka, “Hydrogen: The future cryofuel in internal combustion engines” *International Journal of Hydrogen Energy*, **23**, 27 (1998).
- [8] S. M. Aceves, J. Martinez-Frias, O. Garcia-Villazana, “Analytical and experimental evaluation of insulated pressure vessels for cryogenic hydrogen storage”, *International Journal of Hydrogen Energy*, **25**, 1075 (2000).

- [9] D. Browning, P. Jones, K. Packer, "An investigation of hydrogen storage methods for fuel cell operation with man-portable equipment", *Journal of Power Sources*, **65**, 187 (1997).
- [10] H. Ewe, H. Selbach, "The Storage of Hydrogen", United Kingdom, Plenum Press (1987).
- [11] J. Wolf, "Liquid-hydrogen technology for vehicles", *MRS Bulletin*, **27**, 684 (2002).
- [12] Darren P Broom, "Hydrogen Storage Material. The Characterisation of their Hydrogen Storage Properties", Springer, 2001.
- [13] K. H. J. Buschow, P. C. P. Bouten, A. R. Miedema, "Hydrides formed from intermetallic compounds of two transition metals: a special class of ternary alloys", *Report Prog. Phys*, vol. **45**; (1982).
- [14] George G. Libowitz, "The solid state chemistry of binary metal hydrides", *The Physical Inorganic Chemistry Series*, (ed) W. A. Benjamin, 1905.
- [15] Puru Jena, "Materials for Hydrogen Storage: Past, Present, and Future", *Journal of Physical Chemistry Letters*, **2**, 206 (2011).
- [16] S. Corre, M. Bououdina, D. Fruchart, G. Adachi, "Stabilisation of high dissociation pressure hydrides of formula $\text{La}_{1-x}\text{Ce}_x\text{Ni}_5$ ($x=0-0.3$) with carbon monoxide". *Journal of Alloys and Compounds*, **275**, 99 (1998).
- [17] S. Corre, Ph. D. Thesis. University Joseph Fourier, Grenoble, 1999
- [18] E. M. B. Heller, A. M. Vredenberg, D. O. Boerma, "Hydrogen uptake kinetics of Pd coated FeTi films", *Applied Surface Science*, **253**(2), 771 (2006).
- [19] S. Kulshreshtha, O. Jayakumar, K. Bhatt, "Hydriding characteristics of palladium and platinum alloyed FeTi", *Journal of Material Science*, **28**, 4229 (1993).

- [20] M. Bououdina, J. L. Soubeyroux, D. Fruchart, P. De. Rango, “Structural studies of Laves phases $Zr(Cr_{1-x}Ni_x)_2$ with $0 \leq x \leq 0.4$ and their hydrides”, *Journal of Alloys and Compounds*, **257**, 82 (1997).
- [21] M. Bououdina, J. L. Soubeyroux, P. De. Rango, D. Fruchart, “Phase stability and neutron diffraction studies of the laves phase compounds $Zr(Cr_{1-x}Mo_x)_2$ with $0.0 \leq x \leq 0.5$ and their hydrides”, *International Journal of Hydrogen Energy*, **25**(11), 1059 (2000).
- [22] Billur Sakintuna, Farida Lamari-Darkrim, Michael Hirscher, “Metal hydride materials for solid hydrogen storage: A review”, *International Journal of Hydrogen Energy*, **32**, 1121 (2007).
- [23] M. Bououdina, D. Grant, G. Walker, “Review on hydrogen absorbing materials—structure, microstructure, and thermodynamic properties”, *International Journal of Hydrogen Energy*, **31**(2) 177 (2006).
- [24] M. Bououdina, J. L. Soubeyroux, D. Fruchart, P. De. Rango, “Study of the hydrogenation/dehydrogenation processes of $ZrCr_{0.7}Ni_{1.3}$, a Laves phase-rich multi-component system, by in-situ neutron diffraction under hydrogen gas pressure”, *Journal of Alloys and Compounds*, **327**(1-2), 185 (2001).
- [25] H. Iba, E. Akiba, “The relation between microstructure and hydrogen absorbing property in Laves phase-solid solution multiphase alloys”, *Journal of Alloys and Compounds*, **231**, 508 (1995).
- [26] James J. Reilly, Richard H. Wiswall, “Higher hydrides of vanadium and niobium”, *Inorganic Chemistry*, **9**(7), 1678 (1970).
- [27] K. Nomura and E. Akiba, “Hydrogen Absorbing Desorbing Characterisation of the Ti-V-Fe alloy system”, *Journal of Alloys and Compounds*, **231**, 513 (1995).

- [28] Hongge Pan, Rui Li, Yongfeng Liu, Mingxia Gao, He Miao, Yongquan Lei, Qidong Wang, “Structure and electrochemical properties of the Fe substituted Ti–V-based hydrogen storage alloys”, *Journal of Alloys and Compounds*, **463**, 189 (2008).
- [29] Jing Mi, Xiumei Guo, Xiaopeng Liu, Lijun Jiang, Zhinian Li, Lei Hao, and Shumao Wang, “Effect of Al on microstructures and hydrogen storage properties of $\text{Ti}_{26.5}\text{Cr}_{20}(\text{V}_{0.45}\text{Fe}_{0.085})_{100-x}\text{Al}_x\text{Ce}_{0.5}$ alloy”, *Journal of Alloys and Compounds*, **485**, 324 (2009).
- [30] X.B. Yu, Z.X. Yang, S.L. Feng, Z. Wu, N.X. Xu, “Influence of Fe addition on hydrogen storage characteristics of Ti–V-based alloy” *International Journal of Hydrogen Energy*, **31**, 1176 (2006).
- [31] M. Jing, L. Fang, L. Xiaopeng, , J. Lijun, L. Zhinian, W. Shumao, “Enhancement of cerium and hydrogenstorage property of a low-cost Ti-V based BCC alloy prepared by commercial ferrovanadium” *Journal of Rare Earths*, **28**(5), 781 (2010).
- [32] J.-L. Bobet, B. Chevalier and D. Fruchart, “Replacement of Vanadium by Ferrovanadium in Ti-Based BCC Alloys for Hydrogen Storage”, *Solid State Phenomena*, **170**, 144 (2011).
- [33] Jeong-Hyun Yoo, Gunchoo Shim, Sung-Wook Cho, and Choong-Nyeon Park, “Effects of desorption temperature and substitution of Fe for Cr on the hydrogen storage properties of $\text{Ti}_{0.32}\text{Cr}_{0.43}\text{V}_{0.25}$ alloy”, *International Journal of Hydrogen Energy*, **32**, 2977 (2007).
- [34] Z. Hang, X. Xiao, K. Yu, S. Li, C. Chen, L. Chen, “Influence of Fe content on the microstructure and hydrogen storage properties of $\text{Ti}_{16}\text{Zr}_5\text{Cr}_{22}\text{V}_{57-x}\text{Fe}_x$ ($x = 2-8$) alloys”, *International Journal of Hydrogen Energy*, **35**(5), 8143 (2010).
- [35] M. Okada , T. Kuriwa, T. Tamura, H. Takamura, A. Kamegawa, “Ti–V–Cr b.c.c. alloys with high protium content”, *Journal of Alloys and Compounds*, **330**, 511 (2002).

- [36] Masachika Shibuya, Jin Nakamura, Hirotohi Enoki, Etsuo Akiba, "High-pressure hydrogenation properties of Ti–V–Mn alloy for hybrid hydrogen storage vessel", *Journal of Alloys and Compounds*, **475**, 543 (2009).
- [37] Z. Dehouche, M. Savard, F. Laurencelle, J. Goyette, "Ti–V–Mn based alloys for hydrogen compression system", *Journal of Alloys and Compounds*, **400**, 276 (2005).
- [38] Y. Nakamura and E. Akiba, "Hydrogenation properties of Ti–V–Mn alloys with a BCC structure containing high and low oxygen concentrations", *Journal of Alloys and Compounds*, **509**, 1841 (2011).
- [39] J. Topler, H. Buchner, H. Saufferer, K. Knorr, W. Prandl, "Measurements of the Diffusion of Hydrogen Atom in Mg and Mg₂Ni by Neutron Scattering", *Less Common Metals*, **88**, 397 (1982)
- [40] C. Suryanarayana, "Mechanical alloying and milling", *Progress in Material Science*, **46**, 1 (2001).
- [41] T. Klassen, W. Oelerich, R. Bormann, "Nanocrystal line Mg-based Hydrides: Hydrogen Storage for the. Zero-Emission Vehicle", *Material Science Forum*, **360-362**, 603 (2001).
- [42] T. Klassen, W. Oelerich, R. Bormann, "Nanocrystalline Mg-based hydrides: hydrogen storage for the zero-emission vehicle", *Journal of Metastable and Nanocrystalline Materials*. **10**, 603 (2001).
- [43] A. Zaluska, L. Zaluski, J. O. Ström-Olsen, "Synergy of hydrogen sorption in ball-milled hydrides of Mg and Mg₂Ni", *Journal of Alloys and Compounds*, **289**, 197 (1999).
- [44] J. Huot, S. Boily, E. Akiba, R. Schulz, "Direct synthesis of Mg₂FeH₆ by mechanical alloying", *Journal of Alloys and Compounds*, **280**, 306 (1998).

- [45] A. Zaluska, L. Zaluski, & J. O. Strom-Olsen, "Structure, catalysis and atomic reactions on the nano-scale: a systematic approach to metal hydrides for hydrogen storage" *Applied Physics A-Materials Science & Processing*, **72**, 157 (2001).
- [46] I.P. Jain, Chhagan Lal, Ankur Jain, "Hydrogen storage in Mg: A most promising material", *International Journal of Hydrogen Energy*, **35**(10), 5133 (2010).
- [47] J. Chen, "Hydriding and dehydriding properties of amorphous magnesium-nickel films prepared by a sputtering method", *Chemistry of Materials*, **14**, 2834 (2002).
- [48] S. Orimo, H. Fujii, "Materials science of Mg-Ni based new hydrides", *Applied Physics a-Materials Science & Processing*, **72**, 167 (2001).
- [49] W. Oelerich, T. Klassen, R. Bormann, "Metal oxides as catalysts for improved hydrogen sorption in nanocrystalline Mg-based materials", *Journal of Alloys and Compounds*, **315**, 237 (2001).
- [50] J. Huot, G. Liang, R. Schulz, "Mechanically alloyed metal hydride systems", *Applied Physics A-Materials Science & Processing*, **72**, 187 (2001).
- [51] G. Liang, J. Huot, S. Boily, A. Van Neste, R. Schulz, "Hydrogen storage properties of the mechanically milled MgH₂-V nanocomposite". *Journal of Alloys and Compounds*, **291**, 295 (1999)
- [52] H. G. Schimmel, "Towards a hydrogen-driven society?" Thesis, Delft University of Technology 2004.
- [53] A. R. Yavari, J. F. R. de Castro, G. Vaughan, G. Heunen, "Structural evolution and metastable phase detection in MgH₂-5%NbH nanocomposite during in-situ H-desorption in a synchrotron beam" *Journal of Alloys And Compounds*, **353**, 246 (2003).

- [54] H. G. Schimmel, "The vibrational spectrum of magnesium hydride from inelastic neutron scattering and density functional theory", *Materials Science and Engineering B-Solid State Materials for Advanced Technology*, **108**, 38 (2004).
- [55] P. Wang, H. F. Zhang, B. Z. Ding, & Z. Q. Hu, "Direct hydrogenation of Mg and decomposition behavior of the hydride formed", *Journal of Alloys and Compounds*, **313**, 209 (2000)
- [56] Xiangdong Yao, Chengzhang Wu, Aijun Du, Gao Qing Lu, Huiming Cheng, Sean C. Smith, Jin Zou, and Yinghe He, "Mg-Based Nanocomposites with High Capacity and Fast Kinetics for Hydrogen Storage", *Journal of Physical Chemistry B*, **110** (24), 11697 (2006)
- [57] K. Higuchi, "In situ study of hydridingdehydriding properties in some Pd/Mg thin films with different degree of Mg crystallization", *Journal of Alloys and Compounds*, **295**, 484 (1999).
- [58] L. Zaluski, A. Zaluska, & J. O. Strom-Olsen, "Nanocrystalline metal hydrides", *Journal of Alloys and Compounds*, **253**, 70 (1997).
- [59] K. Higuchi, "Remarkable hydrogen storage properties in three-layered Pd/Mg/Pd thin films". *Journal of Alloys and Compounds*, **330**, 526 (2002).
- [60] R. A. Varin, L. Guo, S. Li, C. Chiu, & A. Calka, "Nanostructured and nanocomposite light metal based compounds for hydrogen storage", *NATO Science Series, II: Mathematics, Physics and Chemistry*, **146**, 67 (2004).
- [61] T. Czujko, R. Varin, J. Bystrzycki, Z. Bojar, & T. Kaldonski, "Nanostructurization of magnesium and Mg₂Ni intermetallic phase-related hydrogen storage materials", *Biuletyn Wojskowej Akademii Technicznej*, **52**, 107 (2003).

- [62] H. Fujii, S.-I. Orimo, “Hydrogen storage properties in nanostructured magnesium- and carbon-related materials. *Physica B: Condensed Matter* (Amsterdam, Netherlands)” **328**, 77 (2003).
- [63] T. Vegge, L. S. Hedegaard-Jensen, J. Bonde, T. R. Munter, & J. K. Norskov, “Trends in hydride formation energies for magnesium-3d transition metal alloys” *Journal of Alloys and Compounds*, **386**, 1 (2005).
- [64] S. V. Alapati, J. K. Johnson, D. S. Sholl, “Identification of Destabilized Metal Hydrides for Hydrogen Storage Using First Principles Calculations”, *Journal of Physical Chemistry B*, **110**, 8769 (2006).
- [65] J. J. Liang & N. Khosrovani, “Theoretical perspective on improving kinetics in Mg hydrogen storage” *Preprints of Papers-American Chemical Society, Division. Fuel Chemistry*. **49**, 152 (2004).
- [66] J. J. Liang, “Theoretical insight on tailoring energetics of Mg hydrogen absorption/desorption through nano-engineering” *Applied Physics A: Materials Science & Processing*, **80**, 173 (2005).
- [67] F. W. Bach, M. Schaper, C. Jaschik, “Magnesium Alloys”, *Material Science Forum*, **419** Pts 1 and 2, 1037 (2003).
- [68] F. L. Darkrim, P. Malbrunot, G. P. Tartaglia, “Review of hydrogen storage by adsorption in carbon nanotubes”, *International Journal of Hydrogen Energy*, **27**, 193 (2002).
- [69] R. Chahine, T. K. Bose, “Low-pressure adsorption storage of hydrogen”, *International Journal of Hydrogen Energy*, **19**, 161 (1994).
- [70] A.C. Dillon, K.E.H. Gilbert, J. L. Alleman, T. Gennett, K.M. Jones, P.A. Parilla, M.J. Heben, “Carbon Nanotube Material for Hydrogen Storage”, Proceedings of 2001 DOE Hydrogen Program Review.

- [71] S. Hynek, W. Fuller, J. Bentley, “Hydrogen storage by carbon sorption”, *International Journal of Hydrogen Energy*, **22**, 601 (1997).
- [72] M. A. de la Casa-Lillo, F. Lamari-Darkrim, D. Cazorla-Amorós, A. Linares-Solano, “Hydrogen Storage in Activated Carbons and Activated Carbon Fibers”, *Journal of Physical Chemistry B*, **106**(42), 10930 (2002).
- [73] A. V. Talyzin, S. Klyamkin, “Hydrogen adsorption in C₆₀ at pressures up to 2000 atm” *Chemical Physics Letters*, **397**, 77 (2004).
- [74] A. V. Talyzin, U. Jansson, “Comparative Raman Study of Some Transitional Metal Fullerides”, *Thin Solid Films*, **429**, 96 (2003).
- [75] A. V. Talyzin, U. Jansson, A. V. Usatov, V. V. Burlakov, V. B. Shur and Y. N. Novikov, “Comparative Raman study of the Ti complex Cp₂Ti(η²-C₆₀), C₆H₅CH₃ and Ti_xC₆₀ films”, *Physics of the Solid State*, **44**, 506 (2002).
- [76] A. V. Talyzin, H. Hogberg, U. Jansson, “Deposition and characterisation of Nb_xC₆₀ fulleride”. *Thin Solid Films*, **405**, 42 (2002).
- [77] A. S. Gurav, Z. Duan, L. Wang, M. J. Hampden-Smith, T. T. Kodas, “Synthesis of fullerene-rhodium nanocomposites via aerosol decomposition”, *Chemistry of Materials*, **5**, 214 (1993).
- [78] V. Lavrentiev, H. Naramoto, H. Abe, S. Yamamoto, K. Narumi, S. Sakai, “Chemically Driven Microstructure Evolution in Cobalt–Fullerene Mixed System” *Fullerene, Nanotube Carbon Nanostructures*, **12**, 51925 (2004).
- [79] M. Kalbác, L. Kavan, M. Zúkalová, L. Dunsch, “Doping of C₆₀ fullerene peapods with lithium vapor: Raman spectroscopic and spectroelectrochemical studies”, *Chemistry*, **14**(20), 6231 (2008).

- [80] E. Zurek, J. Autschbach, N. Malinowski, A. Enders, K. Kern, “Experimental and Theoretical Investigations of the Thermodynamic Stability of Ba-C60 and K-C60 Clusters”, *ACS Nano*, **2**, 1000 (2008)
- [81] U. Zimmermann, N. Malinowski, U. Näher, S. Frank, T. P. Martin, “Multilayer Metal Coverage of Fullerene Molecules”, *Physical Review Letters*, **72**, 3542 (1994)
- [82] T. P. Martin, N. Malinowski, U. Zimmermann, U. Näher, H. J. Schaber, “Metal coated fullerene molecules and clusters”, *Journal of Chemical Physics*, **99**, 4210 (1993).
- [83] X. L. Wang, J. P. Tu, “Characterization and hydrogen storage properties of Pt-C60 compound”, *Applied Physics Letters*, **89**, 064101 (2006).
- [84] J. Lan, D. Cao, W. Wang, “Li₁₂Si₆₀H₆₀ Fullerene Composite: A Promising Hydrogen Storage Medium”, *ACS Nano*, **3**, 3294 (2009).
- [85] M. Li, Y. Li, Z. Zhou, P. Shen, Z. Chen, “Ca-Coated Boron Fullerenes and Nanotubes as Superior Hydrogen Storage Materials” *Nano Letters*, **9**, 1944 (2009).
- [86] D. Saha, S. Deng, “Hydrogen adsorption on partially truncated and open cage C60 fullerene”, *Carbon*, **48**, 3471 (2010).
- [87] A. Oberlin, M. Endo, T. Koyama, “Filamentous growth of carbon through benzene decomposition”, *Journal of Crystal Growth*, **32**, 335 (1976).
- [88] D. J. Browning, M. L. Gerrard, J. B. Lakeman, I. M. Mellor, R. J. Mortimer, M. C. Turpin, “Studies into the storage of hydrogen in carbon nanofibers: Proposal of a possible reaction mechanism”, *Nano Letters*, **2**, 201 (2002).
- [89] A. Chambers, C. Park, T. K. Baker, N. M. J. Rodriguez, “Hydrogen Storage in Graphite Nanofibers”, *Physical Chemistry B*, **102**, 4253 (1998).

- [90] Angela D. Lueking, Ralph T. Yang, Nelly M. Rodriguez, R. Terry K. Baker “Hydrogen Storage in Graphite Nanofibers: Effect of Synthesis Catalyst and Pretreatment Conditions”, *Langmuir*, **20**(3), 714 (2004).
- [91] Q. Wang, J. K. J. Johnson, “Molecular simulation of hydrogen adsorption in single-walled carbon nanotubes and idealized carbon slit pores”, *Journal of Chemical Physics*, **110**, 577 (1999).
- [92] T. D. Jarvi, J. Sun, L. F. Conopask, S. Satyapal, “Prepr. Interaction of Hydrogen With Nanoporous Carbon Materials”, Symposium of American Chemical Society, Division, Fuel Chemistry, **44**, 962 (1999).
- [93] S. Iijima, “Helical microtubules of graphitic carbon”, *Nature*, **354**, 56-58 (1991).
- [94] M. W. Maddox, K. E. Gubbins, “Molecular simulation of fluid adsorption in buckytubes and MCM- 41”, *International Journal of Thermophysics*, **15**, 1115 (1994).
- [95] M. W. Maddox, K. E. Gubbins “Molecular simulation of fluid adsorption in buckytubes”, *Langmuir*, **11**, 3988 (1995).
- [96] A. C. Dillon, K. M. Jones, T. A. Bekkedahl, C. H. Kiang, D. S. Bethune, M. J. Heben, “Storage of hydrogen in single-walled carbon nanotubes”, *Nature*, **386**, 377 (1997).
- [97] C. Liu, Y. Y. Fan, M. Liu, H. T. Cong, H. M. Cheng, M. S. Dresselhaus, “Hydrogen storage in single-walled carbon nanotubes at room temperature”, *Science*, **286**, 1127 (1999).
- [98] Y. F. Yin, T. Mays, B. McEnaney, “Molecular simulations of hydrogen storage in carbon nanotube arrays”, *Langmuir*, **16**, 10521 (2000).
- [99] C. J. Lee, S. C. Lyu, H. W. Kim, C. Y. Park, C. W. Yang, “Large-scale production of aligned carbon nanotubes by the vapor phase growth method”, *Chemical Physics Letters*, **359**, 109 (2002).

- [100] S. M. Lee, K. H. An, W. S. Kim, Y. H. Lee, Y. S. Park, G. Seifert, T. Frauenheim, "Hydrogen storage in carbon nanotubes", *Synthetic Metals*, **121**, 1189-1190 (2001).
- [101] M. T. Bowers "cluster ions: carbon, met-cars, and .sigma.-bond activation", *Accounts of Chemical Research*, **27**, 324 (1994).
- [102] K. R. S. Chandrakumar, S. K. Ghosh, "Alkali-metal-induced enhancement of hydrogen adsorption in C-60 fullerene: An ab initio study" *Nano Letter*, **8**, 13 (2008).
- [103] J. Niu, B. K. Rao, P. Jena, "Binding of hydrogen molecules by a transition-metal ion," *Physical Review Letters*, **68**, 2277 (1992).
- [104] L. Gagliardi, P. K. Pyykko, "How Many Hydrogen Atoms Can Be Bound to a Metal? Predicted MH₁₂ Species" *Journal of the American Chemical Society*, **126**, 15014 (2004).
- [105] P. Chen, X. Wu, J. Lin, K. L. Tan, "High hydrogen uptake by alkali-doped carbon nanotubes under ambient pressure and moderate temperatures". *Science*, **285**, 91 (1999).
- [106] Giannis Mpourmpakis, Emmanuel Tylianakis, and George E. Froudakis, "Carbon Nanoscrolls: A Promising Material for Hydrogen Storage", *Nano Letters*, **7**, 1893 (2007).
- [107] B. Bogdanovic, M. Schwickarde, "Ti-doped alkali metal aluminium hydrides as potential novel reversible hydrogen storage materials", *Journal of Alloys and Compounds*, **253**, 1 (1997).
- [108] H. I. Schlesinger, H. C. Brown, A. E. Finholt, J. R. Gilbreath, H. R. Hockstra, E. K. Hyde, "Sodium Borohydride, its hydrolysis and use as reducing agent and its generation of hydrogen", *Journal of the American Chemical Society*, **75**(1), 215, 1953.
- [109] Ping Chen, Zhitao Xiong, Jizhong Luo, Jianyi Lin & Kuang Lee Tan, "Interaction of hydrogen with metal nitrides and imides", *Nature*, **420**, 302 (2002).

- [110] Weifang Luo, “(LiNH₂–MgH₂): a viable hydrogen storage system”, *Journal of Alloys and Compounds*, **381**(1–2), 284, (2004).
- [111] D. A. J. Rand & R. M. Dell, “Hydrogen Energy Challenges and Prospect”, Copyright: 2008, ISBN: 978-1-84755-802-2, DOI:10.1039/9781847558022 pp 167
- [112] O. V. Komova, V. I. Simagina, G. V. Odegova, Yu. A. Chesalov, O. V. Netskina and A. M. Ozerova, “Low-temperature decomposition of ammonia borane in the presence of titania”, *Inorganic Materials*, **47**(10), 1101 (2011).
- [113] C.N. Hinshelwood, R.E. Burk, “The thermal decomposition of ammonia upon various surfaces”, *Journal of Chemical Society*, **127**, 1105 (1925).
- [114] D.A. Cooper and E.B. Ljungstrom, “Decomposition of NH₃ over Quartz Sand at 840-960°C”, *Energy & Fuels*, **2**, 716 (1988).
- [115] N. L. Rosi, J. Eckert, M. Eddaoudi, D. T. Vodak, J. Kim, M. O’Keeffe, O. M. Yaghi, “Hydrogen Storage in Microporous Metal-Organic Frameworks”, *Science*, **300**, 1127 (2003).
- [116] J. L. C. Rowsell, Omar M. Yaghi, “Strategies for Hydrogen Storage in Metal-Organic Frameworks”, *Angewandte Chemie*, **44**, 4670 (2005).
- [117] T. Riis, G. Sandrok, Ø. Ulleberg, P. J. S. Vie, “Hydrogen Storage – Gaps and Priorities”, http://ieahia.org/pdfs/HIA_Storage_G&P_Final_with_Rev.pdf, (2005).
- [118] J.A.T. Jones, B. Bowman, P.A. Lefrank, “Electric Furnace Steelmaking”, in The Making, Shaping and Treating of Steel, R.J. Fruehan, Editor., *The AISE Steel Foundation*, Pittsburgh. Page 525 (1998).
- [119] R Checchetto, G. Trettel and A. Miotello, “Sievert-type apparatus for the study of hydrogen storage in solids”, *Measurement Science and Technology*, **15**, 127 (2004).
- [120] . D. Cullity, “Elements of X-ray diffraction”, *Addison-Wilson Publishing Comp. Inc.*, USA (1959).

- [121] H. P. Klug and L. E. Alexander, "X-ray diffraction procedures", *Wiley-Interscience Publication*, New York (1974).
- [122] L. V. Azaroff and M. J. Buerger, "The Powder Method in X-ray Crystallography", *McGraw-Hill Book Comp.*, New York (1958).
- [123] A.R. West, "Solid State Chemistry and its Application", *John Wiley & Sons*, Singapore, (1989).
- [124] R. W. Cahn, P. Haasen and E. J. Kramer, "Material Science and Engineering: Characterisation of Materials", *VCH Publisher Inc.*, New York (1991).
- [125] S. J. B. Reed, "Electron Microprobe Analysis (2nd Ed.)", *Cambridge University Press*, (1993).
- [126] J. M. Gütllich, "The Principle of the Mössbauer Effect and Basic Concepts of Mössbauer Spectrometry". <http://pecbip2.univ-lemans.fr/webibame/>.
- [127] Mössbauer Spectroscopy Group, "Introduction to Mössbauer Spectroscopy" Royal Society of Chemistry (RSC) website.
- [128] P. W. Atkins, "Physical Chemistry", 5th ed. *W. H. Freeman*, New York (1994).
- [129] P. J. Haines, and F. W. Wilburn, "Differential thermal analysis and differential scanning calorimetry. In Thermal Methods of Analysis", (P. J. Haines, ed.). pp. 63–122. *Blackie Academic and Professional, London*. (1995).
- [130] P. A. Redhead, "Thermal desorption of gases", *Vacuum*, **12**, 203 (1962).
- [131] T. Kuriwa, T. Tamura, T. Amemiya, T. Fuda, A. Kamegawa, H. Takamura, M. J. Okada. "New V-based alloys with high protium absorption and desorption capacity", *Journal of Alloys and Compounds*, **293-295**, 433 (1999).
- [132] "Hume-Rothery Rules". Van Nostrand's Scientific Encyclopedia. John Wiley & Sons, Inc. 2002.

- [133] A. Kagawa, E. Ono, T. Kusakabe, Y. Sakamoto, “Absorption of hydrogen by vanadium-rich VTi-based alloys”, *Journal of Less-common Metals*, **64**, 172 (1991).
- [134] E. Akiba, H. Iba, “Hydrogen absorption by Laves phase related BCC solid solution”, *Intermetallics* **6**, 461 (1998).
- [135] S. W. Cho, C. S. Han, C. N. Park, E. Akiba. “Hydrogen storage characteristics of Ti–Zr–Cr–V alloys”, *Journal of Alloys and Compounds*, **289**, 244 (1999).
- [136] S. W. Cho, H. Enoki, E. Akiba, “Effect of Fe addition on hydrogen storage characteristics of $\text{Ti}_{0.16}\text{Zr}_{0.05}\text{Cr}_{0.22}\text{V}_{0.57}$ alloy”, *Journal of Alloys and Compounds*, **307**, 304 (2000).
- [137] X. B. Yu, J. Z. Chen, Z. Wu, B. J. Xia, N. X. Xu, “Effect of Cr content on hydrogen storage properties for Ti-V-based BCC-phase alloys”, *International Journal of Hydrogen Energy*, **29**, 1377 (2004).
- [138] X. B. Yu, Z. Wu, B. J. Xia, N. X. Xu, “Enhancement of hydrogen storage capacity of Ti–V–Cr–Mn BCC phase alloys”, *Journal of Alloys and Compounds*, **372**, 272 (2004).
- [139] Y. Nakamura, E. Akiba, “Hydriding properties and crystal structure of NaCl-type mono-hydrides formed from Ti–V–Mn BCC solid solutions”, *Journal of Alloys and Compounds*, **345**, 175 (2002).
- [140] Y. Yan, Y. Chen, H. Liang, X. Zhou, C. Wu, M. Tao, “Effect of Ce on the structure and hydrogen storage properties of $\text{V}_{55}\text{Ti}_{22.5}\text{Cr}_{16.1}\text{Fe}_{6.4}$ ”, *Journal of Alloys and Compounds*, **429**, 301 (2007).
- [141] C.L. Wu, Y.G. Yan, Y.G. Chen, M.D. Tao, X. Zheg, “Effect of rare earth (RE) elements on V-based hydrogen storage alloys”, *International Journal of Hydrogen Energy*, **33**, 93 (2008).

- [142] X.P. Liu, F. Cuevas, L.J. Jiang, M. Latroche, Z.N. Li, S.M. Wang, “Improvement of the hydrogen storage properties of Ti–Cr–V–Fe BCC alloy by Ce addition”, *Journal of Alloys and Compounds*, **476**, 403, (2009).
- [143] M.I. Jing, X. P. Liu, L.I. Yan, L. Jiang L, L.I. Zhinian, Z. Huang, S.M. Wang, *Journal of Rare Earth* **27**, 154 (2009).
- [144] X.P. Liu, L. Jiang, Z. Li, Z. Huang, S. Wang, “Improve plateau property of Ti₃₂Cr₄₆V₂₂ BCC alloy with heat treatment and Ce additive”, *Journal of Alloys and Compounds*, **471**, L36 (2009).
- [145] S. Basak, K. Shashikala, P. Sengupta, S.K. Kulshreshtha, “Hydrogen absorption properties of Ti–V–Fe alloys: Effect of Cr substitution”, *International Journal of Hydrogen Energy*, **32**, 4973 (2007).
- [146] Z. Hang, L. Chen, X. Xiao, S. Li, C. Chen, Y. Lei, Q. Wang, “The effect of Cr content on the structural and hydrogen storage characteristics of Ti₁₀V_{80-x}Fe₆Zr₄Cr_x (x = 0–14) alloys”, *Journal of Alloys and Compounds*, **493**, 396 (2010).
- [147] M. Geng, J. Han, F. Feng, D.O. Northwood, “Electrochemical measurements of a metal hydride electrode for the Ni/MH battery”, *International Journal of Hydrogen Energy*, **25**, 203 (2000).
- [148] A. J. Maeland, G. G. Libowitz, and J. F. Lynch, “Hydride formation rates of titanium-based b.c.c. solid solution alloys”, *Journal of Less-Common Metals*, **104**, 361 (1984)
- [149] X. B. Yu, S. L. Feng, Z. Wu, B. J. Xia, N. X. Xu, “Hydrogen storage performance of Ti–V-based BCC phase alloys with various Fe content”, *Journal of Alloys and Compounds*, **393**, 128, (2005).

- [150] Sung-Wook Cho, Etsuo Akiba, Yumiko Nakamura, Hirotohi Enoki, "Hydrogen isotope effects in $Ti_{1.0}Mn_{0.9}V_{1.1}$ and $Ti_{1.0}Cr_{1.5}V_{1.7}$ alloys", *Journal of Alloys and Compounds*, **297**, 253 (2000).
- [151] Junko Matsuda, Yumiko Nakamura, Etsuo Akiba, "Microstructure of Ti–V–Mn BCC alloys before and after hydrogen absorption–desorption", *Journal of Alloys and Compounds*, **509**, 4352 (2011).
- [152] J. L. Pouchou, F. Pichoir, (1986) Basic expression of "PAP" computation for quantitative empa, in J. D. Brown and R. H. Packwood, ed, *11th Intl Congress on X-ray Optics and Microanalysis*, p. 249.
- [153] R. H. Wiswall, J. J. Reilly "Inverse hydrogen isotope effects in some metal hydride systems", *Journal of Inorganic Chemistry*, **11**, 1691 (1972).
- [154] X. Yu, Z. Wu, F. Li, B. Xia, N. Xu, "Body-centered-cubic phase hydrogen storage alloy with improved capacity and fast activation", *Applied Physics Letters*, **84**, 3199 (2004).
- [155] H. Taizhong, Wu. Zhu, X. Baojia, Xu. Naixin, "Effect of stoichiometry on hydrogen storage properties of Ti-Cr-V-Fe based alloys", *Intermetallics*, **13**, 1075 (2005).
- [156] Tamura T, Kazumi T, Kamegawa A, Takamura H, Okada M, "Protium absorption properties and protide formation of Ti-Cr-V alloys", *Journal of Alloys and Compounds*, **356-357**, 505 (2003).
- [157] H. Itoh, H. Arashima, K. Kubo, T. Kabutomori. "The influence of microstructure on hydrogen absorption properties of Ti–Cr–V alloys", *Journal of Alloys and Compounds*, **330–332**, 287 (2002).
- [158] S. N. Klyamkin, A. Y. Kovriga., V. N. Verbetsky, "Effect of substitution on FCC and BCC hydride-phase formation in the $TiCr_2-H_2$ system" *International Journal of Hydrogen Energy*, **24**, 149 (1999).

- [159] M. Uno, K. Takahashi, T. Maruyama, H. Muta, S. Yamanaka, "Hydrogen solubility of BCC titanium alloys", *Journal of Alloys and Compounds*, **366**, 213 (2004).
- [160] Y. Yan, Y. Chen, H. Liang, C. Wu, M. Tao, T. Mingjing, "Effect of Al on hydrogen storage properties of $V_{30}Ti_{15}Cr_{25}Fe_{10}$ alloy", *Journal of Alloys and Compounds*, **426**, 253 (2006).
- [161] H. C. Lin, K. M. Lin, K. C. Wu, H. H. Hsiung, H. K. Tsai, "Cyclic hydrogen absorption-desorption characteristics of TiVCr and $Ti_{0.8}Cr_{1.2}V$ alloys", *International Journal of Hydrogen Energy*, **32**, 4966 (2007).
- [162] S. W. Cho, G. Shim, G. S. Choi, C. N. Park, J. H. Yoo, J. Choi, "Hydrogen absorption-desorption properties of $Ti_{0.32}Cr_{0.43}V_{0.25}$ alloy", *Journal of Alloys and Compounds*, **430**, 136 (2007).
- [163] E. Akiba, M. Okada, "Metallic Hydrides III: Body-centered-cubic solid-solution alloys", *MRS Bulletin Sept*; 699 (2002).
- [164] J-H. Yoo, G. Shim, J-S. Yoon, S-W. Cho, "Effects of substituting Al for Cr in the $Ti_{0.32}Cr_{0.43}V_{0.25}$ alloy on its microstructure and hydrogen storage properties", *International Journal of Hydrogen Energy*, **34**, 1463 (2009).
- [165] J-Y Wang, R-R Jeng, J-K Nieh, S Lee, S-L Lee, H-Y Bor, "Comparing the hydrogen storage alloys-TiVCr and vanadium rich TiCrMnV", *International Journal of Hydrogen Energy*, **32**, 3959 (2007).
- [166] S. Basak, K. Shashikala, S. K. Kulshreshtha, "Hydrogen absorption characteristics of Zr substituted $Ti_{0.85}VFe_{0.15}$ alloy", *International Journal of Hydrogen Energy*, **33**, 350 (2008).
- [167] J. M. Park and J. Y. Lee, "An investigation of the hydrogen site occupancy in the $ErFe_2$ -H system by a hydrogen thermal desorption study", *Scripta Metallurgica* **23**, 1525 (1989).

- [168] K. Shashikala., S. Banerjee, A. Kumar, M. R. Pai., C. G. S. Pillai. “Improvement of hydrogen storage properties of TiVCr alloys by Zr Substitution for Ti”, *International Journal of Hydrogen Energy*, **34**, 6684 (2009).
- [169] W. Chubin., Ju. Xin., Q. Ying., F. Chao., W. Shumao., L. Xiaopeng., J. A. Lijun, “Study on crystal structure and chemical state of TiVCrMn hydrogen storage alloys during hydrogen absorption-desorption cycling”, *International Journal of Hydrogen Energy*, **34**, 8944 (2009).
- [170] G. Sandrock. “A panoramic overview of hydrogen storage alloys from a gas reaction point of view”, *Journal of Alloys and Compounds*, **293–295**, 877(1999).
- [171] X. W. Yang., T. B. Zhang., R. Hu., J. S. Li., X. Y. Xue., H. Z. Fu. “Microstructure and hydrogenation thermokinetics of ZrTi_{0.2}V_{1.8} alloy”, *International Journal of Hydrogen Energy*, **35**, 11981-11985 (2010).
- [172] G. Srinivas, V. Sankaranarayanan, S. Ramaprabhu, “Diffusion of hydrogen in cubic Laves phase Ho_{1-x}Mm_xCo₂ (x = 0, 0.2 and 0.4) alloys”, *International Journal of Hydrogen Energy*, **32**, 2956 (2007).
- [173] M. Kandavel, S. Ramaprabhu, “Hydrogen solubility and diffusion studies of Zr-based AB₂ alloys and sol-gel encapsulated AB₂ alloys particles”, *Intermetallics*, **15**, 968 (2007).
- [174] M. Krishna Kumar, S. Ramaprabhu “Hydrogen absorption characteristics in Mm_xTb_{1-x}Co₂ (x = 0, 0.05, 0.1, 0.15, 0.2)”, *International Journal of Hydrogen Energy*, **32**, 1890 (2007).
- [175] X.Y. Cui, Q. Li, K.C. Chou, S.L. Chen, G.W. Lin, K.D. Xu, “A comparative study on the hydriding kinetics of Zr-based AB₂, hydrogen storage alloys”, *Intermetallics*, **16**, 662 (2008).

- [176] Y. H. Xu, C. P. Chen, X. L. Wang, Y. Q. Lei, X. H. Wang, L. X. Chen, “The influence of relative content of Ti and Zr on the electrochemical behavior of Laves phase alloy”, *International Journal of Hydrogen Energy*, **32**, 1716 (2007).
- [177] F. Stein “Consequences of Crystal Structure Differences between C14, C15, and C36 Laves Phase Polytypes for their Coexistence in Transition-Metal-Based Systems”, *Material Research Society, Symposium Proceeding*, **1295**, 299 (2011).
- [178] F. Stein, M. Palm, and G. Sauthoff: “Structure and Stability of Laves Phases Part II – Structure Type Variations in Binary and Ternary Systems”, *Intermetallics*, **13**, 1056 (2005).
- [179] F. Stein, M. Palm, and G. Sauthoff: “Structure and Stability of Laves Phases Part I – Critical Assessment of Factors Controlling Laves Phase Stability”, *Intermetallics*, **12**, 713 (2004).
- [180] F.C. Frank and J.S. Kasper, “Complex alloy structures regarded as sphere packings. I. Definitions and basic principles”, *Acta Crystallographica*, **12**, 483 (1959).
- [181] F.C. Frank and J.S. Kasper, “Complex alloy structures regarded as sphere packings. II. Analysis and classification of representative structures”, *Acta Crystallographica*, **12**, 483 (1959).
- [182] B. Friauf, The crystal structure of two intermetallic compounds, *Journal of the American Chemical Society*, **49**, 3107 (1927),
- [183] J .B. Friauf, The crystal structure of magnesium di-zincide, *Physical Reviews*, **29**, 34-40 F (1927).
- [184] F. Laves, H. Witte, „Der Einfluß der Valenzelektronen auf die Kristallstruktur ternärer Magnesium-Legierungen“, *Metallwirtschaft*, **15**, 840 (1936).
- [185] D. Shaltiel, “Hydride Properties of AB₂ Laves Phase Compounds”, *Journal of the Less-common Metals*, **62**, 407 (1978)

- [186] Xu Zhang, Qian Li, Kuo-Chih Chou, “Kinetics of hydrogen absorption in the solid solution region for Laves phase $\text{Ho}_{1-x}\text{Mm}_x\text{Co}_2$ ($x = 0, 0.2$ and 0.4) alloys”, *Intermetallics*, **16**, 1258 (2008).
- [187] F. Ghezzi, M. De Angeli, “On the dependence of true hydrogen equilibrium pressure on the granular size distribution of the $\text{Zr}(\text{Fe}_{0.5}\text{Mn}_{0.5})_2$ getter alloy” *Journal of Alloys and Compounds*, **330-332**, 76 (2002)
- [188] Suklyun Hong and C. L. Fu, “Hydrogen in Laves phase ZrX_2 ($X = \text{V}, \text{Cr}, \text{Mn}, \text{Fe}, \text{Co}, \text{Ni}$) compounds: Binding energies and electronic and magnetic structure”, *Physical Review B*, **66** (2002) 094109.
- [189] J. F. Fern´andez, M. Kemali, D. K. Ross and C. S´anchez, “An empirical potential for interstitial hydrogen in some C-15 Laves phase compounds from IINS measurements”, *Journal of Physics: Condensed Matter*, **11**, 10353–10373 (1999).
- [190] Ankur Jain, R.K. Jain, Shivani Agarwal, V. Ganesan, N.P. Lalla, D.M. Phase, I.P. Jain, “Synthesis, characterization and hydrogenation of $\text{ZrFe}_{2-x}\text{Ni}_x$. ($x = 0.2, 0.4, 0.6, 0.8$) alloys”, *International Journal of Hydrogen Energy*, **32**, 3965 (2007).
- [191] Ankur Jain, R.K. Jain, Shivani Agarwal, R.K. Sharma, S.K. Kulshrestha, I.P. Jain, “Structural and Mossbauer spectroscopic study of cubic phase $\text{ZrFe}_{2-x}\text{Mn}_x$ hydrogen storage alloy”, *Journal of Alloys and Compound*, **454**, 31 (2008).
- [192] A. Jain, R. K. Jain, G. Agarwal, I. P. Jain. “Crystal structure, hydrogen absorption and thermodynamics of $\text{Zr}_{1-x}\text{Co}_x\text{Fe}_2$ alloys”, *Journal of Alloys and Compound*, **438**, 106 (2007).
- [193] A. Jain, R. K. Jain, S. Agarwal, I. P. Jain. “Thermodynamics and structural aspects of hydrogen absorption in $\text{Zr}_{1-x}\text{Cr}_x\text{Fe}_2$ alloys”, *International Journal of Hydrogen Energy*, **32**, 2445 (2007).

- [194] Ali H. Reshak, Mikhail Y. Shalaginov, Yasir Saeed, I. V. Kityk, and S. Auluck “First-Principles Calculations of Structural, Elastic, Electronic, and Optical Properties of Perovskite-type KMgH_3 Crystals: Novel Hydrogen Storage Material, [dx.doi.org/10.1021/jp111382h](https://doi.org/10.1021/jp111382h), *Journal of Physical Chemistry B*, (online)
- [195] K. C. Kim, Thermodynamics of Metal Hydrides for Hydrogen Storage Applications using First Principles Calculations, A Thesis Presented to The Academic Faculty.
- [196] C. Tian, W. Zhao, Z. Wang and M. Jin, “Physisorption to Chemisorption Transformation of a H_2 Molecule on B-doped Fullerene C_{59}B ”, *Journal of Theoretical and Computational Chemistry*, **10**(6), 839 (2011).
- [197] Z. Yang and J. Ni, “Hydrogen storage on calcium-decorated BC_3 sheet: A first principles study”, *Applied Physics Letters*, **97**, 253117 (2010).
- [198] Wenhao Q. Sun, C. Wolverton, A. R. Akbarzadeh, and V. Ozolins, “First-principles prediction of high-capacity, thermodynamically reversible hydrogen storage reactions based on $(\text{NH}_4)_2\text{B}_{12}\text{H}_{12}$ ”, *Physical Review B*, **83**, 064112 (2011).
- [199] V Ozolins, A R Akbarzadeh, H Gunaydin, K Michel, Wolverton, and E H Majzoub, “First-principles computational discovery of materials for hydrogen storage”, *Journal of Physics: Conference Series*, **180** (2009) 012076.
- [200] Feng Shi, Amar Bhalla, Chonglin Chen, Gemunu H. Gunaratne, Jiechao Jiang, and Efsthios I. Meletis, “Atomistically-Informed Continuum Model for Hydrogen Storage on Graphene”, *The Electrochemical Society Interface*, Spring 2011.
- [201] N. Park, S. Hong, G. Kim, and S-H Jhi, “Computational Study of Hydrogen Storage Characteristics of Covalent-Bonded Graphenes”, *Journal of the American Chemical Society*, **129**, 8999 (2007).
- [202] Caetano R. Miranda and Gerbrand Ceder, “Ab initio investigation of ammonia-borane complexes for hydrogen storage”, *Journal of Chemical Physics* **126**, 184703 (2007).

- [203] M. L. Born and R. Oppenheimer, "Zur Quantum Theorie der Molekeln" *Annalen der Physik*, **84**, 457 (1927).
- [204] J. C. Slater, "The theory of complex spectra", *Physical Review*, **34**, 1293 (1929).
- [205] J. C. Slater, "Cohesion in Monovalent Metals", *Physical Review*, **35**, 509 (1930).
- [206] Ira Levine, "Quantum Chemistry", Prentice Hall of India Pvt. Ltd. 2001.
- [207] Tim Clark, "A Handbook of Computational Chemistry", John Wiley & Sons, Inc (1985).
- [208] J. B. Foresman & A. Frisch, "Exploring Chemistry with Electronic Structure Method", 2nd Edition Gaussian Inc. (1996).
- [209] C. C. J. Roothaan, "New Developments in Molecular Orbital Theory", *Reviews in Modern Physics*, **23**, 69 (1951).
- [210] P. Hohenburg and W. Kohn, "Inhomogeneous Electron Gas", *Physical Review*, **136** B864 (1964).
- [211] W. Kohn and L. J. Sham, "Self-Consistent Equations Including Exchange and Correlation Effects", *Physical Review*, **140**, A1133 (1965).
- [212] L. H. Thomas, "The calculation of atomic fields", *Proceedings of Cambridge Philosophical Society*, **23**, 542 (1927).
- [213] E. Fermi, "Eine statistische Methode zur Bestimmung einiger Eigenschaften des Atoms und ihre Anwendung auf die Theorie des periodischen Systems der Elemente", *Zeitschrift für Physik A Hadrons and Nuclei*. **48**, 73 (1928).
- [214] D. M. Ceperley and B. J. Alder, "Ground State of the Electron Gas by a Stochastic Method", *Physical Review Letters*, **45**, 566 (1980).
- [215] J. P. Perdew and A. Zunger, "Self-interaction correction to density-functional approximations for many-electron systems", *Physical Review B*, **23**, 5048 (1981).

- [216] J. P. Perdew, J.A. Chevary, S.H. Vosko, K.A. Jackson, M.R. Pederson, D.J. Singh, and C. Fiolhais, "Atoms, molecules, solids, and surfaces: Applications of the generalized gradient approximation for exchange and correlation", *Physical Review B*, **46**, 6671 (1992).
- [217] J. P. Perdew, K. Burke, and M. Ernzerhof, "Generalized Gradient Approximation Made Simple", *Physical Review Letters*, **77**, 3865 (1996).
- [218] J. P. Perdew, K. Burke, and M. Ernzerhof, "Generalized Gradient Approximation Made Simple", *Physical Review Letters*, **78**, 1396 (1997).
- [219] A. D. Becke, "Density-functional exchange-energy approximation with correct asymptotic behavior", *Physical Review A*, **38**, 3098 (1988).
- [220] Lee, Yang, Parr, "Development of the Colle-Salvetti correlation-energy formula into a functional of the electron density", *Physical Review B*, **37**, 785 (1988).
- [221] D. Feller, E. R. Davidson, "Basis Sets for Ab Initio Molecular Orbital Calculations and Intermolecular Interactions", *Reviews on Computation Chemistry*, **1**, 1 (1990).
- [222] E. R. Davidson, D. Feller, "Basis set selection for molecular calculations", *Chemical Reviews*, **86**, 681 (1986).
- [223] F. Jensen, *Introduction to Computational Chemistry*, John Wiley & Sons: Chichester, 1999.
- [224] A. Szabo, N. A. Ostlung, *Modern Quantum Chemistry: Introduction to Advanced Electronic Structure Theory*, McGraw-Hill: New York, (1989).
- [225] S. F. Boys, "Electronic Wave Functions. I. A General Method of Calculation for the Stationary States of Any Molecular System", *Proceeding of the Royal Society (London)*, **542**, A200 (1950).

- [226] U. von Barth, C.D. Gelatt, “Validity of the frozen-core approximation and pseudopotential theory for cohesive energy calculations”, *Physical Review B*, **21**, 2222 (1980).
- [227] D. R. Hamann, M. Schlüter, and C. Chiang, “Norm-conserving pseudopotentials,” *Physical Review Letters*, **43**, 1494 (1979).
- [228] V. Heine, “The concept of Pseudopotentials”, *Solid State Physics*, **24**, 1 (1970).
- [229] G. Kresse, and J. Hafner, “Norm-conserving and ultrasoft pseudopotentials for first-row and transition elements”, *Journal of Physics: Condense Matter*, **6**, 8245 (1994).
- [230] D. Vanderbilt, “Soft self-consistent pseudopotentials in a generalized eigenvalue formalism”, *Physical Review B*, **41**, 7892 (1990).
- [231] P. Blöchl, “Generalized separable potentials for electronic-structure calculations”, *Physical Review B*, **41**, 5414 (1990).
- [232] K. Laasonen, A. Pasquarello, R. Car, C. Lee, and D. Vanderbilt, “Car-Parrinello molecular dynamics with Vanderbilt ultrasoft pseudopotentials”, *Physical Review B*, **47**, 10142 (1993).
- [233] P. E. Blöchl, “Projector augmented-wave method”, *Physical Review B*, **50**, 17953 (1994).
- [234] G. Kresse, and D. Joubert, “From ultrasoft pseudopotentials to the projector augmented wave method”, *Physical Review B*, **59**, 1758 (1999).
- [235] N. W. Ashcroft and N. D. Mermin, *Solid State Physics* (Thomson Learning, Inc., 1976).
- [236] C. Kittel, *Introduction to Solid State Physics* (New York: John Wiley & Sons, Inc., 1996).

- [237] R. S. Mulliken, "Electronic Population Analysis on LCAO-MO Molecular Wave Functions. I", *Journal of Chemical Physics*, **23**, 1833 (1955).
- [238] J. Meister and W. H. E. Schwarz, "Principal Components of Ionicity", *Journal of Chemical Physics*, **98**, 8245 (1994).
- [239] R. Bader, *Atoms in Molecules: A Quantum Theory*, (USA: Oxford University Press, 1994).
- [240] F. L. Hirshfeld, Bonded-atom fragments for describing molecular charge densities, *Theoretical Chemistry Accounts: Theory, Computation, and Modeling (Theoretica Chimica Acta)* **44**, 129 (1977).
- [241] G. Henkelman, A. Arnaldsson, and H. Jonsson, "A fast and robust algorithm for Bader decomposition of charge density", *Computational Materials Science*, **36**, 354 (2006).
- [242] E. Sanville, S. D. Kenny, R. Smith, and G. Henkelman, "An improved grid-based algorithm for Bader charge allocation", *Journal of Computational Chemistry*, **28**, 899 (2007).
- [243] J. Alper, "Water splitting goes Au naturel", *Science*, **299**, 1686 (2003).
- [244] M. Tsuda, W.A. Din˜o, H. Nakanishi nad H. Kasai, "Ab initio study of H₂ desorption from magnesium hydride MgH₂ cluster", *Journal of thePhysical Society of Japan*, **73**, 2628 (2004).
- [245] Y. Fukai, "The Metal-Hydrogen System - Basic Bulk Properties", (Springer- Verlag, Berlin, 1993).
- [246] R. Griessen and T. Riesterer, "*Hydrogen in Intermetallic Compounds I*", ed. By L. Schlapbach, *Topics Appl. Phys.*, Vol 63 p. 219. (Springer, Berlin, 1988).

- [247] B. Bogdanovic , K. Bohmhammel , B. Christ , A. Reiser ,K. Schlichte , R. Vehlen and U. Wolf, “Thermodynamic investigation of the magnesium–hydrogen system”, *Journal of Alloys and Compounds*, **282**, 84 (1999).
- [248] A.S. Arico, P. Bruce, B. Scrosati, J.M. Tarascon and W. Van Schalkwijk, “Nanostructured materials for advanced energy conversion and storage devices”, *Nature materials*, **4**, 366 (2005).
- [249] M. Tsuda, W.A. Dino, H. Kasai and H. Nakanishi, “Magnetized/charged MgH₂-based hydrogen storage materials”, *Applied Physics Letters*, **86**, 21309 (2005).
- [250] N. Hanada, T. Ichikawa and H. Fujii, “Catalytic Effect of Nanoparticle 3d-Transition Metals on Hydrogen Storage Properties in Magnesium Hydride MgH₂ Prepared by Mechanical Milling”, *Journal of Physical Chemistry B*, **109**, 7188 (2005).
- [251] S. R. Johnson, P.A. Anderson, P. P. Edwards, I. Gameson, J.W. Prendergast, M. Al-Mamouri, D. Book, I. R. Harris, J. D. Speight and A. Walton, *Chemical Communication*, DOI: 10.1039/b5030852823 (2005).
- [252] M. Y. Song, D.R. Mumm, S. N. Kwon, S. H. Hong and J. S. Bae, “Hydrogen-storage properties of Mg–10 wt.% (Fe₂O₃, Ni, MnO) alloy prepared by reactive mechanical grinding”, *Journal of Alloys and Compounds*, **416**, 239 (2006).
- [253] P. Vermeulen, R. A. H. Niessen and P. H. L. Notten, “Hydrogen storage in metastable Mg_yTi(1 – y) thin films”, *Electrochemical Communication*, **8**, 27 (2006).
- [254] W.P. Kalisvaart, H.J.Wondergem, F. Bakker and P.H.L.Notten, “Mg–Ti based materials for electrochemical hydrogen storage”, *Journal of Material Research*, **22**, 1640 (2007).
- [255] S. Rousselot, M.-P. Bichat, D. Guay and L. Roue', “Structure and electrochemical behaviour of metastable Mg₅₀Ti₅₀ alloy prepared by ball milling”, *Journal of Power Sources*, **175**, 621 (2008).

- [256] J.F.R. De Castro, S.F. Santos, A.L.M. Costa, A.R. Yavari, W.J. Botta and T.T. Ishikawa, "Structural characterization and dehydrogenation behavior of Mg-5 at.%Nb nano-composite processed by reactive milling", *Journal of Alloys and Compounds*, **376**, 251 (2004).
- [257] J. Charbonnier, P. de Rango, D. Fruchart, S. Miraglia, L. Pontonnier, S. Rivoirard, N. Skryabina and P. Vulliet, "Hydrogenation of transition element additives (Ti, V) during ball milling of magnesium hydride", *Journal of Alloys and Compounds*, **383**, 205 (2004).
- [258] G. Barkhordarian, T. Klassen and R. Bormann, "Catalytic Mechanism of Transition-Metal Compounds on Mg Hydrogen Sorption Reaction", *Journal of Physical Chemistry B*, **110**, 11020 (2006).
- [259] V.V. Bhat, A. Rougier, L. Aymard, X. Darok, G. Nazri and J.M. Tarascon, "Catalytic activity of oxides and halides on hydrogen storage of MgH₂", *Journal of Power Sources*, **159**, 107 (2006).
- [260] G. Liang, "Synthesis and hydrogen storage properties of Mg-based alloys", *Journal of Alloys and Compounds*, **370**, 123 (2004).
- [261] N. B. Arboleda Jr., H. Kasai, K. Nobuhara, W. A. Dino and H. Nakanishi, "Dissociation and Sticking of H₂ on Mg(0001), Ti(0001) and La(0001) Surfaces", *Journal of Physical Society of Japan*, **73**, 745 (2004).
- [262] M. Pozzo, D. Alfè, A. Amieiro, S. French and A. Pratt, "Hydrogen dissociation and diffusion on Ni- and Ti-doped Mg(0001) surfaces", *The Journal of Chemical Physics*, **128**, 094703 (2008).
- [263] A. J. Du, S. C. Smith, X. D. Yao and G. Q. Lu, "The role of Ti as a catalyst for the dissociation of hydrogen on a Mg(0001) surface", *Journal of Physical Chemistry B*, **109**, 18037, (2005).

- [264] A. J. Du, Sean C. Smith, X. D. Yao and G. Q Lu, "Hydrogen spillover mechanism on a Pd-doped Mg surface as revealed by ab initio density functional calculation", *Journal of the American Chemical Society*, **129**, 10201, (2007).
- [265] T Vegge, Locating the rate-limiting step for the interaction of hydrogen with Mg(0001) using density-functional theory calculations and rate theory, *Physical Review B*, **70** (3) 035412 (2004).
- [266] X. G. Li, P Zhang, C. K. Chan, First-principles calculation of Mg(0001) thin films: Quantum size effect and adsorption of atomic hydrogen, *Physica B: Condensed Matter*, **390** (1/2), 225 (2007).
- [267] N Jacobson, B Tegner, E Schroder, P Hyldgaard, B. I. Lundqvist, Hydrogen dynamics in magnesium and graphite, *Computational Material Science*, **24** (1/2), 273 (2002).
- [268] G. X. Wu, J. Y. Zhang, Y. Q. Wu, Q. Li, K. C. Chou, X. H. Bao, First-principle calculations of the adsorption, dissociation and diffusion of hydrogen on the Mg(0001) surface, *Acta Physico-Chimica Sinica*, **24** (1) 55 (2008).
- [269] J. K. Norskov, A. Houmoller, P. K. Johansson and B. I. Lundqvist, "Adsorption and dissociation of H₂ on Mg surfaces", *Physical Review Letters*, **46**, 257 (1981).
- [270] G. Barkhordarian, T. Klassen, R. Bormann, "Effect of Nb₂O₅ content on hydrogen reaction kinetics of Mg", *Journal of Alloys and Compounds*, **364** (1/2), 242 (2004).
- [271] P. T. Sprunger, E. W. Plummer, "An experimental study of the interaction of hydrogen with the Mg(0001) surface", *Chemical Physics Letters*, **187** (6) 559 (1991).
- [272] C. X. Shang, M Bououdina, Y Song, Z. X. Guo, "Mechanical alloying and electronic simulations of (MgH₂+M) systems (M=Al, Ti, Fe, Ni, Cu and Nb) for hydrogen storage", *International Journal of Hydrogen Energy*, **29** (1) 73 (2004).

- [273] W Oelerich, T Klassen, R Bormann, “Comparison of the catalytic effects of V, V₂O₅, VN, and VC on the hydrogen sorption of nanocrystalline Mg”, *Journal of Alloys and Compounds*, 322 (1/2) (2001), pp. L5–L9
- [274] W Oelerich, T Klassen, R Bormann, D. Uuml, “Mg-based hydrogen storage materials with improved hydrogen sorption”, *Materials Transactions*, **42** (8) (2001), pp. 1588–1592
- [275] G. Kresse and J. Furthmuller, “Efficient iterative schemes for ab initio total-energy calculations using a plane-wave basis set”, *Physical Review B*, **54**, 11169 (1996).
- [276] H. J. Monkhorst and J. D. Pack, “Special points for Brillouin-zone integrations”, *Physical Review B*, **13**, 5188 (1976).
- [277] JC-PDS Card number 35-0821.
- [278] The surface energy of (unrelaxed) surface (σ_{unreal}) was calculated according to the equation: $\sigma_{\text{unreal}} = \frac{1}{2}(E_{\text{surface}} - nE_{\text{bulk}})$, where E_{surface} is the total energy of the surface and E_{bulk} is the total energy of the bulk. The total surface energy $\sigma = \sigma_{\text{unreal}} + E_{\text{real}}$; E_{real} is the relaxation energy.
- [279] J. Charbonnier, P. de Rango, D. Fruchart, S. Miraglia, L. Pontonnier, S. Rivoirard, N. Skryabina, P. Vulliet, “Hydrogenation of transition element additives (Ti, V) during ball milling of magnesium hydride”, *Journal of Alloys and Compounds*, **383**, 205 (2004).
- [280] A.S. Arico, P. Bruce, B. Scrosati, J.M. Tarascon, W. Van Schalkwijk, “Nanostructured materials for advanced energy conversion and storage devices”, *Nature Materials*, **4**, 366 (2005).
- [281] Peter Larsson, C. Moysé’s Araujo, J. Andreas Larsson, Puru Jena, and Rajeev Ahuja”, Role of catalysts in dehydrogenation of MgH₂ nanoclusters”, *Proceedings of the National Academy of Sciences*, **105**, 8227 (2008).

- [282] Rudy W. P. Wagemans, Joop H. van Lenthe, Petra E. de Jongh, A. Jos van Dillen and Krijn P. de Jong, "Hydrogen storage in magnesium clusters: Quantum chemical study", *Journal of the American Chemical Society*, **127**, 16675 (2005).
- [283] V. Kumar, Y. Car, "A density functional molecular dynamics study of the bonding and stability of Mg_n clusters (n=2–13)" *Zeitschrift für Physik D Atoms, Molecules and Clusters*, **19**, 177 (1991)
- [284] T. P. Martin, T. Bergmann, H. Gohlich and T. Lange, "Evidence for icosahedral shell structure in large magnesium clusters", *Chemical Physics Letters*, **176**, 343 (1991).
- [285] Paulo H. Acioli* and Julius Jellinek, "Electron Binding Energies of Anionic Magnesium Clusters and the Nonmetal-to-Metal Transition", *Physical Review Letters*, **89**, 213402 (2002).
- [286] H. Jónsson, G. Mills, K. W. Jacobsen, "Nudged Elastic Band Method for Finding Minimum Energy Paths of Transitions, in Classical and Quantum Dynamics in Condensed Phase Simulations", Ed. B. J. Berne, G. Ciccotti and D. F. Coker, 385 (World Scientific, 1998).
- [287] S. Noše. "A molecular dynamics method for simulations in the canonical ensemble", *Molecular Physics*, **52**, 255 (1984).
- [288] Y. Yürüm, A. Taralp, T. Nejat Veziroglu, "Storage of hydrogen in nanostructured carbon materials", *International Journal of Hydrogen Energy*, **34**, 3784 (2009).
- [289] H. Cheng, A. C. Cooper, G. P. Pez, M. K. Kostov, P. Piotrowski, S. J. Stuart, "Molecular Dynamics Simulations on the Effects of Diameter and Chirality on Hydrogen Adsorption in Single Walled Carbon Nanotubes", *Journal of Physical Chemistry B*, **109**, 3780 (2005).

- [290] H. Cheng, G. P. Pez, A. C. Cooper, “Mechanism of Hydrogen Sorption in Single-Walled Carbon Nanotubes”, *Journal of the American Chemical Society*, **123**, 5845 (2001).
- [291] M. Hirscher, M. Becher, M. Haluska, F. von Zeppelin, X. Chen, U. D. Weglikowska, S. Roth, “Are carbon nanostructures an efficient hydrogen storage medium?”, *Journal of Alloys and Compounds*, **356–357**, 433 (2003).
- [292] A. D. Lueking, R. T. Yang, “Hydrogen spillover to enhance hydrogen storage—study of the effect of carbon physicochemical properties”, *Applied Catalysis A*, **265**, 259 (2004).
- [293] R. Strobel, J. Garcia, P. T. Moseley, L. Jorissen, G. Wolf, “Hydrogen storage by carbon materials”, *Journal of Power Sources*, **159**, 781 (2006).
- [294] J. Li, T. Furuta, H. Goto, T. Ohashi, Y. Fujiwara, S. Yip, “Theoretical evaluation of hydrogen storage capacity in pure carbon nanostructures”, *Journal of Chemical Physics*, **119**, 2376 (2003).
- [295] Y. H. Kim, Y. F. Zhao, A. Williamson, M. J. Heben, S. B. Zhang, “Nondissociative Adsorption of H₂ Molecules in Light-Element-Doped Fullerenes,” *Physical Review Letters*, **96**, 016102 (2006).
- [296] R. C. Lochan, M. Head-Gordon, “Computational studies of molecular hydrogen binding affinities: the role of dispersion forces, electrostatics, and orbital interactions”, *Physical Chemistry & Chemical Physics*, **8**, 1357 (2006).
- [297] E. Klontzas, A. Mavrandonakis, E. Tylianakis, and G. E. Froudakis, “Improving Hydrogen Storage Capacity of MOF by Functionalization of the Organic Linker with Lithium Atoms”, *Nano Letters*, **8**, 1572 (2008).

- [298] W. Q. Deng, X. Xu, and W. A. Goddard, “New alkali doped pillared carbon materials designed to achieve practical reversible hydrogen storage for transportation”, *Physical Review Letters*, **92**, 166103 (2004).
- [299] X. Nikitin, Z. Li, H. Zhang, H. Ogasawara, Dai, and A. Nilsson, “Hydrogen storage in carbon nanotubes through the formation of stable C-H bonds”, *Nano Letters*, **8**, 162 (2008).
- [300] E. Durgun, S. Ciraci, W. Zhou, and T. Yildirim, “Transition-Metal-Ethylene Complexes as High-Capacity Hydrogen-Storage Media”, *Physical Review Letters*, **97**, 226102 (2006).
- [301] Q. Sun, P. Jena, Q. Wang, and M. Marquez, First-Principles Study of Hydrogen Storage on $\text{Li}_{12}\text{C}_{60}$, *Journal of the American Chemical Society*, **128**, 9741 (2006).
- [302] T. Badzian, E. Badzian, A. Breval, Piotrowski, “Nanostructured, nitrogen-doped carbon materials for hydrogen storage”, *Thin Solid Film*, **398**, 170 (2001).
- [303] M. Sankaran, B. Viswanathan, “The role of heteroatoms in carbon nanotubed for hydrogen storage”, *Carbon*, **44**, 2816 (2006).
- [304] C. Lee, X. Wei, J. W. Kysar, and J. Hone, “Measurement of the Elastic Properties and Intrinsic Strength of Monolayer Graphene”, *Science*, **321**, 385 (2008).
- [305] Q. Sun, Q. Wang, P. Jena, Y. Kawazoe, “Clustering of Ti on a C_{60} Surface and Its Effect on Hydrogen Storage”, *Journal of the American Chemical Society*, **127**, 14582 (2005).
- [306] Sygula, P. W. Rabideau, “A Practical Large Scale Synthesis of the Corannulene System”, *Journal of the American Chemical Society*, **122**, 6323 (2000).
- [307] L. T. Scott, M. M. Hashemi, D. T. Meyer, H. B. Warren, “Corannulene. A convenient new synthesis”, *Journal of the American Chemical Society*, **113**, 7081 (1991).

- [308] L. G. Scanlon, P. B. Balbuena, Y. Zhang, G. Sandi, C. K. Back, W. A. Feld, J. Mack, M. A. Rottmayer, and J. L. Riepenhoff, "Investigation of Corannulene for Molecular Hydrogen Storage via Computational Chemistry and Experimentation", *Journal of Physical Chemistry B*, **110**, 7688 (2006).
- [309] Y. Zhang, L. G. Scanlon, M. A. Rottmayer, P. B. Balbuena, "Computational investigation of adsorption of molecular hydrogen on lithium-doped corannulene", *Journal of Physical Chemistry B*, **110**, 22532 (2006).
- [310] M. V. Frash, A. C. Hopkinson, D. K. Bohme, "Corannulene as a Lewis Base: Computational Modelling of Protonation and Lithium Cation Binding", *Journal of the American Chemical Society*, **123**, 6687 (2001).
- [311] D. Caraiman, G. K. Koyanagi, L. T. Scott, D. V. Preda, D. K. Bohme, "Fullerometallic Ion Chemistry: Reactions of $C_{60}Fe^+$ and $C_{20}H_{10}Fe^+$ in the Gas Phase", *Journal of the American Chemical Society*, **123**, 8573 (2001).
- [312] M. W. Schmidt, K. K. Baldrige, J. A. Boatz, S. T. Elbert, M. S. Gordon, J. H. Jensen, S. Koseki,; N. Matsunga, K. A. Nguyen, S. J. Su, M. Dupuis, J. A. Montgomery, "General Atomic and Molecular Electronic Structure System", *Journal of Computational Chemistry*, **14**, 1347 (1993).
- [313] C. Lee, W. Yang, R. G. Parr, "Development of the Colle-Salvetti correlation-energy formula into a functional of the electron density", *Physical Review B*, **37**, 785 (1988).
- [314] P. Flükiger, H. P. Lüthi, S. Portmann, J. Weber, MOLEKEL 4.0, *Swiss Center for Scientific Computing, Manno (Switzerland)*, 2000.
- [315] T. Sagara, E. Ganz, "Calculations of Dihydrogen Binding to Doped Carbon Nanostructures", *Journal of Physical Chemistry C*, **112**, 3515 (2008).

- [316] M. Cabria, J. López, J. A. Alonso, “Enhancement of hydrogen physisorption on graphene and carbon nanotubes by Li doping”, *Journal of Chemical Physics*, **123**, 204721 (2005).
- [317] R. C. Dunbar, “Binding of Transition-Metal Ions to Curved π Surfaces: Corannulene and Coronene”, *Journal of Physical Chemistry A*, **106**, 9809 (2002).
- [318] P. A. Denis, Investigation of H₂ Physisorption on corannulene (C₂₀H₁₀), Tetraindenocorannulene (C₄₄H₁₈), Pentaindenocorannulene (C₅₀H₂₀), C₆₀ and Their Nitrogen Derivatives, *Journal of Physical Chemistry C*, **112**, 2791 (2008).
- [319] H. Lee, J. Ihm, M. L. Cohen, S. G. Louie, Calcium-Decorated Graphene-Based Nanostructures for Hydrogen Storage, *Nano Letters*, **10**, 793 (2010).
- [320] W. Wang, Q. Sun, P. Jena, Y. Kawazoe, “Theoretical Study of Hydrogen Storage in Ca-Coated Fullerenes”, *Journal of Chemical Theory and Computation*, **5**, 374 (2009).
- [321] W. Deng, X. Xu, W. A. Goddard, New Alkali Doped Pillared Carbon Materials Designed to Achieve Practical Reversible Hydrogen Storage for Transportation, *Physical Review Letters*, **92**, 166103 (2004).
- [322] T. Yildirim, J. Iñiguez, S. Ciraci, “Molecular and dissociative adsorption of multiple hydrogen molecules on transition metal decorated C₆₀”, *Physical Review B: Condens. Matter Mater. Phys.*, **72**, 153403 (2005).
- [323] G. P. Lithoxoos, J. Samios, Y. Carissan, “Investigation of Silicon Model Nanotubes as Potential Candidate Nanomaterials for Efficient Hydrogen Storage: A Combined Ab Initio/Grand Canonical Monte Carlo Simulation Study”, *Journal of Physical Chemistry C*, **112**, 16725 (2008).
- [324] J. Lan, D. Cheng, D. Cao, W. Wang, “Silicon Nanotube as a Promising Candidate for Hydrogen Storage: From the First Principle Calculations to Grand Canonical Monte Carlo Simulations”, *Journal of Physical Chemical C*, **112**, 5598 (2008).

- [325] T. Ishihara, M. Nakasu, I. Yasuda, H. Matsumoto, "Preparation of Si-carbon nanotube composite by decomposition of tetramethylsilane (TMS) and its hydrogen storage property", *Science and Technology of Advanced Materials*, **7**, 667 (2006).
- [326] X-H Sun, C-P Li, W-K Wong, N-B Wong, C-S Lee, S-T Lee, and B-K Teo, "Formation of Silicon Carbide Nanotubes and Nanowires via Reaction of Silicon (from Disproportionation of Silicon Monoxide) with Carbon Nanotubes", *Journal of the American Chemical Society*, **124**, 14464 (2002).
- [327] P. Pochet, L. Genovese, D. Caliste, I. Rousseau, S. Goedecker, T. Deutsch, "First-principles prediction of stable SiC cage structures and their synthesis pathways", *Physical Review B*, **82**, 035431 (2010).
- [328] X-F. Xu, P. Xiao, X. Xiong, B-Y Huang, "Effects of Ni catalyzer on growth velocity and morphology of SiC nano-fibers", *Transactions of Nonferrous Metals Society of China*, **19**, 1146 (2009).
- [329] Z. W. Pan, H. L. Lai, C. K. Au, X. F. Duan, W. Y. Zhou, W. S. Shi, N. Wong, C. S. Lee, N. B. Wong, S. T. Lee, "Oriented SiC Nanowires: Synthesis and Emission Properties", *Advanced Material*; **12**, 1186 (2000).
- [330] Z. L. Wang, Z. R. Dai, R. P. Gao, Z. G. Bai, J. L. Gole, "Side-by-side silicon carbide-silica biaxial nanowires: Synthesis, structure and mechanical properties", *Applied Physics Letters*, **77**, 3349 (2000).
- [331] W. S. Shi, H. Y. Peng, Y. F. Zheng, N. Wang, N. G. Shang, Z. W. Pan, C. S. Lee, S. T. Lee, "Synthesis of large areas of highly oriented, very long silicon nanowires", *Advanced Materials*, **12**, 1343 (2000).
- [332] P. R. Wallace, "The band theory of graphite", *Physical Review*, **71**, 622 (1947).
- [333] W. McClure, "Diamagnetism of graphite", *Physical Review*, **104**, 666 (1956).

- [334] J. C. Slonczewski, P. R. Weiss, “Band structure of graphide”, *Physical Review*, **109**, 272 (1958).
- [335] K. Geim, K. S. Novoselov, “The rise of Graphene”, *Nature Materials*, **6**, 183 (2007).
- [336] K. S. Novoselov, A. K. Geim, S. V. Morozov, D. Jiang, Y. Zhang, S. V. Dubonos, I. V. Grigoreva, A. A. Firsov, “Electric Field Effect in Atomically Thin Carbon Films”, *Science*, **306**, 666 (2004).
- [337] K. S. Novoselov, D. Jiang F. Schedin, T. J. Booth, V. V. Khotkevich, S. V. Morozov, A. K. Geim, “Two dimensional atomic crystals”, *Proceedings of the National Academy of Sciences*, **102(30)**, 10451 (2005).
- [338] K. S. Novoselov, A. K. Geim, S. V. Morozov, D. Jiang, M. I. Katsnelson, I. V. Grigorieva, S. V. Dubonos, A. A. Firsov, “Two dimensional gas of massless Dirac fermions in graphene” *Nature*, **438**, 197 (2005).
- [339] H. Marcel F. Sluiter and Yoshiyuki Kawazoe, “Cluster expansion method for adsorption: Application to hydrogen chemisorption on graphene”, *Physical Review B*, **68**, 085410 (2003).
- [340] J. O. Sofo, A. S. Chaudhari, and G. D. Barber, “Graphane: a two-dimensional hydrocarbon”, *Physical Review B*, **75**, 153401 (2007).
- [341] A. Bhattacharya, S. Bhattacharya, C. Majumder, and G. P. Das, “The third conformer of graphane: A first principles DFT based study”, *Physical Review B*, **83**, 033404 (2011).
- [342] D. C. Elias, R. R. Nair, T. M. G. Mohiuddin, S.V. Morozov, P. Blake, M. P. Halsall, A. C. Ferrari, D. W. Boukhvalov, M. I. Katsnelson, A. K. Geim, and K. S. Novoselov, *Science*, **323**, 610 (2009).

- [343] B. Xu, J. Yin, Y. D. Xia, X. G. Wan, Z. G. Liu, "Ferromagnetic and antiferromagnetic properties of the semihydrogenated SiC sheet", *Applied Physics Letter*, **96**, 143111 (2010).
- [344] Xin-Quan Wang, Jian-Tao Wang, "Structural stabilities and electronic properties of fully hydrogenated SiC sheet", *Physics Letters A*, **375**, 2676 (2011).
- [345] G. Mpourmpakis, G. E. Froudakis, G. P. Lithoxoos, J. Samios, "SiC Nanotubes: A Novel Material for Hydrogen Storage", *Nano Letters*, **6**, 1581 (2006).
- [346] H. Lee, J. Ihm, M. L. Cohen, S. G. Louie, "Calcium-decorated carbon nanotubes for high-capacity hydrogen storage: First-principles calculations", *Physical Review B*, **80**, 115412 (2009).
- [347] Y. Zhang, H. Huang, "Stability of single-wall silicon carbide nanotubes - molecular dynamics simulations", *Computational Materials Science*, **43**, 664 (2008).
- [348] Y. Miyamoto, B. D. Yu, Computational designing of graphitic silicon carbide and its tubular forms, *Applied Physics Letters*, **80**, 586 (2002).
- [349] M. Menon, E. Richter, A. Mavrandonakis, G. Froudakis, A. N. Andriotis, "Structure and stability of SiC nanotubes", *Physical Review B*, **69**, 115322 (2004).
- [350] M. Zhao, Y. Xia, F. Li, R. Q. Zhang, S. T. Lee, "Strain energy and electronic structures of silicon carbide nanotubes: Density functional calculations", *Physical Review B*, **71**, 085312 (2005).
- [351] A. Mavrandonakis, G. Froudakis, A. N. Andriotis, "From Pure Carbon to Silicon–Carbon Nanotubes: An *Ab-initio* Study", *Nano Letters*, **3**, 1481 (2003).
- [352] S. Bhattacharya, C. Majumder, G. P. Das, "Hydrogen Storage in Ti-Decorated BC₄N Nanotube", *Journal of Physical Chemistry C*, **112**, 17487 (2008).

- [353] J-X. Zhao, Y-H. Ding, "Silicon Carbide Nanotubes Functionalized by Transition Metal Atoms: A Density-Functional Study", *Journal of Physical Chemistry C*, **112**, 2558 (2008).
- [354] A. Gali, "Ab initio study of nitrogen and boron substitutional impurities in single-wall SiC nanotubes", *Physical Review B*, **73**, 245415 (2006).
- [355] F. Tast, N. Malinowski, S. Frank, M. Heinebrodt, I. M. L. Billas, T. P. Martin, "Cage Destruction in Metal-Fullerene Clusters", *Physical Review Letters*, **77**, 3529 (1996).
- [356] S. Yang, M. Yoon, E. Wang, Z. Zhang, "Energetics and kinetics of Ti clustering on neutral and charged C₆₀ surfaces", *Journal of Chemical Physics*, **129**, 134707 (2008).
- [357] B. C. Guo, K. P. Kerns; A. W. Castleman, "Ti₈C₁₂⁺-Metallo-Carbohedrenes: A New Class of Molecular Clusters?", *Science*, **255**, 1411 (1992).
- [358] B. C. Guo, S. Wei, J. Purnell, S. Buzza, A. W. Castleman, "Metallo-Carbohedrenes [M₈C₁₂⁺ (M = V, Zr, Hf, and Ti)]: A Class of Stable Molecular Cluster Ions", *Science*, **256**, 515 (1992).
- [359] I. Dance, "Understanding structure and reactivity of new fundamental inorganic molecules: metal sulfides, metallocarbohedrenes, and nitrogenase", *Chemical Communicationc*, 523-530, (1998).
- [360] I. Dance, "Ti₈C₁₂ - Barrierless Transformation of the T-H isomer to the T-D Isomer", *Journal of the American Chemical Society*, **118**, 6309 (1996).
- [361] J. S. Pilgrim, M. A. Duncan, "Metallo-carbohedrenes: chromium, iron, and molybdenum analogs"; *Journal of the American Chemical Society*, **115**, 6958 (1993).
- [362] Z. Lin, M. B. Hall, "Theoretical Studies on the Stability of M₈C₁₂ Clusters", *Journal of the American Chemical Society*, **115**, 11165 (1993).

- [363] Y. Zhao, Anne C. Dillon, Y-H Kim, M. J. Heben, S. B. Zhang, “Self-catalyzed hydrogenation and dihydrogen adsorption on titanium carbide nanoparticles”, *Chemical Physics Letter*, **425**, 273 (2006).

LIST OF INTERNATIONAL JOURNAL PUBLICATIONS INCLUDED IN THIS THESIS

- (1) **Seemita Basak**, K. Shashikala, P. Sengupta, S. K. Kulshreshtha, “Hydrogen absorption properties of Ti–V–Fe alloys: Effect of Cr substitution”, *International Journal of Hydrogen Energy*, **32**, 4973, (2007).
- (2) **Seemita Basak**, K. Shashikala, S.K. Kulshreshtha, “Hydrogen absorption characteristics of Zr substituted $Ti_{0.85}VFe_{0.15}$ alloy”, *International Journal of Hydrogen Energy*, **33**, 350, (2008).
- (3) K. Shashikala, **Seemita Banerjee**, Asheesh Kumar, M. R. Pai and C. G. S. Pillai; “Improvement of hydrogen storage properties of TiCrV alloy by Zr substitution for Ti”, *International Journal of Hydrogen Energy*, **34**, 6684, (2009).
- (4) **Seemita Banerjee**, C. G. S. Pillai, and C. Majumder, “First-principles study of the H_2 interaction with transition metal (Ti, V, Ni) doped Mg(0001) surface: Implications for H-storage materials” *Journal of Chemical Physics*, **129**, 174703 (2008).
- (5) **Seemita Banerjee**, C. G. S. Pillai, and C. Majumder; “Dissociation and Diffusion of Hydrogen on the Mg(0001) Surface: Catalytic Effect of V and Ni Double Substitution”, *Journal of Physical Chemistry C*, **113**, 10574, (2009).
- (6) **Seemita Banerjee**, C. G. S. Pillai, C. Majumder, “Adsorption and desorption of hydrogen in Mg nanoclusters: Combined effects of size and Ti doping”, *International Journal of Hydrogen Energy*, **35**, 2344, (2010).
- (7) **Seemita Banerjee**, C. G. S. Pillai, C. Majumder, “Hydrogen absorption behavior of doped corannulene: A first principles study” *International Journal of Hydrogen Energy*, **36**, 4976 (2011).

- (8) Asheesh Kumar, K. Shashikala, **Seemita Banerjee**, J Nuwad, Priyanka Das, C. G. S. Pillai, “Effect of cycling on hydrogen storage properties of Ti₂CrV alloy” *International Journal of Hydrogen Energy*, **37**, 3677 (2012).
- (9) **S. Banerjee**, Sandeep Nigam, C. G. S. Pillai, C. Majumder, “Hydrogen Storage on Ti Decorated SiC Nanostructures: A First Principles Study”, *International Journal of Hydrogen Energy*, **37**, 3733 (2012).
- (10) K. Shashikala, Asheesh Kumar, C. A. Betty, **Seemita Banerjee**, P. Sengupta and C. G. S. Pillai, “Improvement of the hydrogen storage properties and electrochemical characteristics of Ti_{0.85}VFe_{0.15} alloy by Ce substitution”, *Journal of alloys and compounds*, **509**, 9079 (2011).
- (11) **Seemita Banerjee**, C. G. S. Pillai, C. Majumder, “High capacity reversible hydrogen storage by metallo-carbohedrenes: An ab initio molecular dynamic simulation study” *Applied Physics Letters*, Available online DOI: 10.1063/1.4792686.